

DESIGN REVIEW REPORT

VOLUME 1 - SECTIONS 1 THROUGH 3

Visible Infrared Spin-Scan Radiometer (VISSR) for a Synchronous Meteorological Spacecraft (SMS)

Contract No. NAS5-21139

For - National Aeronautics and Space Administration
Goddard Space Flight Center
Glen Dale Road
Greenbelt, Maryland 20771

(NASA-CR-143725) VISIBLE INFRARED SPIN-SCAN
RADIOMETER (VISSR) FOR A SYNCHRONOUS
METEOROLOGICAL SPACECRAFT (SMS), VOLUME 1
(SECTIONS 1-3) Design Review Report, period
ending 15 Jul. 1972 (Santa Barbara Research

N76-71542

Unclas
13417



SANTA BARBARA RESEARCH CENTER

SEERC

A Subsidiary of Hughes Aircraft Company

REPRODUCED BY
NATIONAL TECHNICAL
INFORMATION SERVICE
U.S. DEPARTMENT OF COMMERCE
SPRINGFIELD, VA. 22161

316P

1. Report No.	2. Government Accession No.	3. Recipient's Catalog No.	
4. Title and Subtitle Visible Infrared Spin-Scan Radiometer (VISSR) for a Synchronous Meteorological Spacecraft (SMS)		5. Report Date 15 July 1972	6. Performing Organization Code
		8. Performing Organization Report No.	
7. Author(s) SBRC VISSR/SMS Technical Staff		10. Work Unit No.	
9. Performing Organization Name and Address Santa Barbara Research Center 75 Coromar Drive Goleta, California		11. Contract or Grant No. NAS 5-4-34	
		13. Type of Report and Period Covered Design Review Report for Period Ending 15 July 1972	
12. Sponsoring Agency Name and Address GODDARD SPACE FLIGHT CENTER Greenbelt, Maryland 20771 Technical Officer: J. E. Phenix		14. Sponsoring Agency Code	
		15. Supplementary Notes This report comprises the design review package for a design review tentatively scheduled 28-29 August 1972.	
16. Abstract This report follows the Preliminary Design Definition documented in the Preliminary Design Review Report, dated 27 January 1970 and the Second Quarterly Report compiled for the Design Review conducted 4-5 November 1970. This report substitutes for the Eighth, Ninth, and Tenth Quarterly Reports for the Visible Infrared Spin-Scan Radiometer (VISSR). VISSR will be integrated into a synchronous spin-stabilized geostationary satellite to be used to obtain radiometric data for operational weather analysis. The contents of this report reflect the design status of the Protoflight Model scheduled for delivery in October 1972.			
17. Key Words		18. Distribution Statement	
19. Security Classif. (of this report) Unclassified	20. Security Classif. (of this page) Unclassified	21. No. of Pages	22. Price

1a

SANTA BARBARA RESEARCH CENTER

A Subsidiary of Hughes Aircraft Company

75 COROMAR DRIVE • GOLETA, CALIFORNIA

DESIGN REVIEW REPORT

VOLUME 1 – SECTIONS 1 THROUGH 3

Visible Infrared Spin-Scan Radiometer (VISSR)
for a Synchronous Meteorological Spacecraft (SMS)

Contract No. NAS5-21159

for

National Aeronautics and Space Administration
Goddard Space Flight Center
Glen Dale Road
Greenbelt, Maryland, 20771

15 July 1972

CONTENTS

<u>Section</u>	<u>Volume 1</u>	<u>Page</u>
	INTRODUCTION	1-1
	Summary of Objectives	1-1
	System Operating Characteristics	1-2
	System Description	1-4
	Calibration	1-6
2	SYSTEMS ANALYSIS	2-1
	Design Objective Specifications	2-1
	Performance Analysis	2-2
	Sun Exposure Analysis	2-17
	Scan Distortion Analysis	2-21
	VISSR/SMS Electrical Interface Characteristics	2-30
	Scan Mirror Step-Scan Operation	2-30
	VISSR Inflight Sun Calibration Periods	2-41
	Thermal Analysis	2-43
3	OPTICS	3-1
	Optical Requirements	3-1
	General Description	3-1
	Telescope Design	3-3
	Telescope and Thermal Relay System	3-6
	Visible Relay System	3-37
	Optical Resolution	3-47
	Optical Vendors	3-70
	Beryllium Material	3-72
	Telescope Performance Specification	3-74
	Optical Data	3-
	Scattering	3-71
	VISSR/SMS Calibrator	3-84

CONTENT (Con)

<u>Section</u>		<u>Page</u>
3	Optical Component Measurements	3-145
(Cont)	Integrated Multiplier Photosensor (IMP) Measurements . .	3-147
	Optical System Testing	3-163
	Engineering Model Optical System Measurements	3-179
	Engineering Model Optical System Tests	3-187
	Protoflight Model Optical System Tests	3-224

<u>Section</u>	<u>Volume 2</u>	<u>Page</u>
4	MECHANICS	4-1
5	ELECTRONICS	5-1
6	RADIATION COOLER/DETECTOR	6-1
7	SYSTEMS AND ENVIRONMENTAL TEST	7-1
8	INSTRUMENTATION AND CHECKOUT EQUIPMENT	8-1
9	RELIABILITY	9-1

<u>Appendix</u>	<u>Volume 3</u>	<u>Page</u>
A	THERMAL GRADIENT STUDY	A-1
B	ENGINEERING MODEL OPTICAL MEASUREMENT DATA . .	B-1
C	PROTOFLIGHT MODEL OPTICAL MEASUREMENT DATA	C-1

<u>Appendix</u>	<u>Volume 4</u>	<u>Page</u>
D	DESIGN OBJECTIVES SPECIFICATION	D-1
E	ELECTRICAL INTERFACE CHARACTERISTICS	E-1
F	VISSR COMPONENTS AND MATERIAL LIST	F-1
G	VISSR SCANNER THERMAL MODEL NODAL PARAMETERS	G-1
H	ACL NO. 44345-1	H-1
I	VISSR (SMS) TEST PLAN, 19060	I-1
J	VISSR STRUCTURAL MODEL, VIBRATION QUALIFICATION TEST REPORT	J-1

ILLUSTRATIONS

<u>Figure</u>		<u>Page</u>
1-1	VISSR/Spacecraft Spin-Scan Geometry and Picture Data Format Arrangement	1-3
1-2	VISSR Telescope/Scanner Assembly	1-5
2-1	Effective Radiance N and dN/dT as a Function of Target Temperature in the 10.5- to 12.6-Micron Band	2-5
2-2	VISSR Thermal Channel S/N and $NE\Delta T$ as a Function of Target Temperature, T (for an Extended Target)	2-5
2-3	Spectral Distribution of Sun's Energy Outside the Earth's Atmosphere (from the Handbook of Geophysics)	2-6
2-4	Relative Spectral Sensitivity, Visible Channel Enhanced PMT plus Filter	2-6
2-5	VISSR Visible Channel Sine Wave MTF	2-10
2-6	VISSR Thermal Channel Sine Wave MTF	2-11
2-7	Engineering Model VISSR Visible Channel MTF (Square Bar)	2-13
2-8	Engineering Model VISSR Thermal Channel MTF (Square Bar)	2-13
2-9	VISSR Visible Channel Sine Wave MTF at Several Focus Conditions	2-15
2-10	VISSR Thermal Channel Sine Wave MTF at Several Focus Conditions	2-16
2-11	Perfectly Aligned Scan Frame	2-22
2-12	Visible Channel Element Misalignment	2-24
2-13	Thermal Channel Element Misalignment	2-24
2-14	Latitude Step-Scan Axis Misalignment	2-26
2-15	VISSR/SMS Misalignment	2-27
2-16	Spin Axis Misalignment	2-28
2-17	Data Frame with Nutation of the Spin Axis	2-29
2-18	VISSR Scan Drive Logic Block Diagram	2-32
2-19	Summary of Timing Events and Waveform	2-39

ILLUSTRATIONS (Cont)

<u>Figure</u>		<u>Page</u>
2-20	Time Periods During Which a VISSR Radiometric Check-of-Calibration Against the Sun Can Be Performed	2-22
2-21	Thermal Nodal Model	2-24
2-22	VISSR Scanner Nodal Temperatures, No Thermal Control Surface, $\pm 23.5^\circ$ Sun Angle	2-49
2-23	VISSR Scanner Nodal Temperatures, Thermal Control Surface Band Height = 0.6 inch, $\pm 23.5^\circ$ Sun Angle	2-50
2-24	VISSR Scanner Nodal Temperatures, Thermal Control Surface Band Height = 0.6 inch, $\pm 10^\circ$ Sun Angle	2-51
2-25	VISSR Scanner Nodal Temperatures, Thermal Control Surface Band Height = 1.2 inches, $\pm 23.5^\circ$ Sun Angle	2-52
3-1	Optical Schematic, VISSR/SMS Scanner	3-2
3-2	Comparison of Off-Axis Image Blur for Two-Mirror Optical Systems	3-4
3-3	Infrared Field Segment Array	3-8
3-4	Telescope and IR Relay Schematic	3-9
3-5	IR Channel Relay Lens Schematic	3-10
3-6	Primary Optics, On Axis	3-12
3-7	Primary Optics, Off Axis	3-14
3-8	Optics with Relay	3-16
3-9	Optics with Relay	3-17
3-10	Optics with Relay	3-18
3-11	Optics with Relay	3-19
3-12	Image Blur (μr) for 95% Included Energy vs Decentering	3-24
3-13	IR Relay Sketch	3-28
3-14	Spectral Characteristics of VISSR Optical Components (Excluding Bandpass Filter)	3-29
3-15	Spectral Reflectance of Al-SiO (Average Over 0.55 μ -0.75 μ Band)	3-35
3-16	Fiber Transmittance as a Function of Fiber Length	3-38

ILLUSTRATIONS (Cont)

<u>Figure</u>		<u>Page</u>
3-17	Signal vs Bend Arc Length as a Function of Fiber Bend Radii (f/7 Input with f/4 Output)	3-30
3-18	Relative Signal vs Bend Curvature for Arc Length of 180° (f/7 Input with f/4 Output)	3-39
3-19	Entry of Unwanted Ray into Fiber	3-40
3-20	Beam Divergence	3-43
3-21	Fiber Optics - PMT Assembly, VISSR	3-44
3-22	Prism for Attachment to PMT in VISSR	3-46
3-23	Block Details	3-46
3-24	Diffacted Energy as a Function of Aperture, Obscuration, and Wavelength	3-52
3-25	Two-Mirror Configuration	3-53
3-26	Maximum Stress versus Bow-Strip Deformation as a Function of Beryllium Strip Thickness, T_2	3-68
3-27	Maximum Stress versus Bow-Strip Deformation as a Function of Nickel Plating Thickness, T_1	3-68
3-28	Energy Distribution for e^{ax} Distortion Function	3-77
3-29	Solar Calibrator Prism Assembly	3-79
3-30	Ray Path Through Top Prism	3-80
3-31	Solar Calibrator - Top Prism	3-82
3-32	Solar Calibrator Prism Bottom	3-84
3-33	Basis for Calculations of Calibrator Location Relative to Telescope Coordinate	3-86
3-34	Functional Quantity (F) vs Earth Albedo (α_0), Hemispherical Scatter of 1% for VISSR Mirrors	3-93
3-35	Functional Quantity (F) vs Earth Albedo (α_0), Hemispherical Scatter of 2% for VISSR Mirrors	3-93
3-36	VISSR/SMS Calibrator Optical Schematic	3-95
3-37	Spot Diagram 0.0 mr	3-97
3-38	Spot Diagram 2.0 mr	3-98
3-39	Spot Diagram 3.0 mr	3-99

ILLUSTRATIONS (Cont)

<u>Figure</u>		<u>Page</u>
3-40	Spot Diagram 4.0 mr	3-100
3-41	Field Curvature and Astigmatism (43.987 in.)	3-101
3-42	Field Curvature and Astigmatism (43.972 in.)	3-102
3-43	Primary Mirror Deflection vs Radial Position	3-106
3-44	Energy Distribution Combined Effects (Single Pass)	3-109
3-45	Calibrator Optical System Double Pass Energy Distribution	3-110
3-46	Energy Distribution Measurement	3-111
3-47	Interferograms - VISSR Calibrator No. 1 - Class I	3-112
3-48	Square-Wave Modulation, VISSR Calibrator No. 1	3-113
3-49	Calibrator Visible Source Optical Schematic	3-118
3-50	Aperture Element - With Radial Varying Transmittance Function	3-121
3-51	Radiance Profile Across VISSR Calibrator Entrance (Exit) Pupil	3-123
3-52	Aperture Uniformity - Breadboard Visible Source - Revised Design	3-124
3-53	Field Uniformity - Breadboard Visible Source - Revised Design	3-125
3-54	Spectral Radiance Distribution Matching	3-126
3-55	Spectral Radiance vs Current, Strip Element - Secondary Standard of Radiance	3-128
3-56	VISSR Calibrator Exit Pupil - Uniformity Sampling	3-129
3-57	Calibration Block Diagram	3-131
3-58	Radiometric Calibration Accuracy versus Degree of Polarization for Incident Light	3-137
3-59	Radiometric Calibration Accuracy versus Degree of Polarization for Incident Light	3-137
3-60	Radiometric Calibration Accuracy versus Degree of Polarization for Incident Light	3-137
3-61	VISSR Fractional Vignetting vs Lateral Misalignment	3-140

ILLUSTRATIONS (Cont)

Figure		Page
3-62	VISSR Fractional Vignetting vs Angular Misalignment . . .	3-140
3-63	Fraction of VISSR Aperture Being Illuminated as a Function of Distance between Ceter Lines of VISSR and VISSR Calibrator	3-141
3-64	Sampling - VISSR Calibrator No. 1 Aperture	3-144
3-65	Coated Mirror Reflectance, Visible Region	3-145
3-66	Coated Mirror Reflectance, IR Region	3-145
3-67	Spectral Reflectance of Polished Electroless Nickel	3-145
3-68	Relative Spectral Transmittance - Fiber Optics	3-147
3-69	Spectral Transmittance - Relay Lens	3-148
3-70	Spectral Transmittance - Bandpass Filter	3-148
3-71	Spectral Transmittance - Irtran 2 Window	3-148
3-72	Spectral Transmittance - Irtran 2 Window - Extended IR Spectral Region	3-149
3-73	Spectral Response of Bandpass Filter in IMP Test Set . . .	3-150
3-74	Optical Configuration and Calibration of IMP Test Set . . .	3-151
3-75	IMP Serial No. 8 Stability Test	3-154
3-76	IMP Serial No. 4 Stability Test	3-155
3-77	Engineering Model IMP Stability Tests	3-156
3-78	IMP Serial No. 13 Stability Tests	3-159
3-79	IMP Serial No. 9 Stability Tests	3-161
3-80	IMP Output vs Time - Engineering Model Units	3-162
3-81	IMP Output vs Time - Flight Model Units	3-163
3-82	IMP Solar Flashing Tests	3-166
3-83	Scatter Measurement Geometry	3-168
3-84	Hemispherical Scatter, Perkin-Elmer Reference Mirror No. 3	3-173
3-85	Hemispherical Scatter	3-174
3-86	Scan Mirror Reflectance (Scattering)	3-175
3-87	Anodized Beryllium Reflectance (Scattering)	3-175

ILLUSTRATIONS (Cont)

<u>Figure</u>		<u>Page</u>
3-88	Diffuse Reflection of Anodized Beryllium	3-176
3-89	Radiation Cooler Honeycomb Reflectance (Scattering)	3-177
3-90	Cat-A-Lac Black Paint Reflectance (Scattering)	3-178
3-91	Interferograms, On-Axis, Class II Test Configuration	3-180
3-92	Interferograms, 1.6 mr, Off-Axis, Class II Test Configuration	3-180
3-93	Fractional Encircled Energy as a Function of Blur Diameter, Class II Test Configuration	3-182
3-94	Ritchey Test, Scan Mirror	3-183
3-95	Interferograms, On-Axis, Class I Test Configuration	3-184
3-96	Interferograms, 1.6 mr, Off-Axis, Class I Test Configuration	3-184
3-97	Fractional Encircled Energy as a Function of Blur Diameter, Class I Test Configuration	3-185
3-98	Function θ_{CON} Which Converts Class II Fractional Encircled Energy to Class I Fractional Encircled Energy Data	3-186
3-99	Proper Orientation of the Visible and Thermal IGFOVs	3-188
3-100	Orientation of the VISSR Engineering Model Visible and Thermal IGFOVs	3-188
3-101	FOV Measurement Equipment Setup, Simplified Block Diagram	3-190
3-102	RSR Measurement Equipment Setup, Simplified Block Diagram	3-192
3-103	Thermal Channel 1 Relative Spectral Response	3-194
3-104	Thermal Channel 2 Relative Spectral Response	3-194
3-105	MTF Measurement Equipment Setup, Simplified Block Diagram	3-196
3-106	Visible Channel Modulation Transfer Function - Engineering Model	3-197
3-107	Thermal Channel Modulation Transfer Function	3-198
3-108	VISSR Reference Axes	3-201

ILLUSTRATIONS (Cont)

<u>Figure</u>		<u>Page</u>
3-109	PARM-1 to Y Axis Alignment	3-201
3-110	PARM-2 to X Axis Alignment	3-202
3-111	Alignment of VISSR Optical Axis to PARM-1 in YZ Plane	3-203
3-112	Alignment of VISSR Optical Axis to PARM-1 in XY Plane	3-203
3-113	Alignment of VISSR Optical Axis (without Scan Mirror) to PARM-1 in YZ Plane	3-204
3-114	Alignment of VISSR Optical Axis (without Scan Mirror) to PARM-2 in XZ Plane	3-204
3-115	Alignment of SARM-1 to PARM-2 in XZ Plane	3-205
3-116	Alignment of SARM-2 to PARM-2 in XY Plane	3-205
3-117	Alignment of VISSR Optical Axis to PARM-1 in YZ Plane - Primary Encoder	3-206
3-118	Alignment of VISSR Optical Axis to PARM-1 in XY Plane - Primary Mirror	3-206
3-119	Alignment of VISSR Optical Axis to PARM-1 in YZ Plane - Redundant Encoder	3-207
3-120	Alignment of VISSR Optical Axis to PARM-1 in XY Plane - Redundant Encoder	3-207
3-121	Alignment of VISSR Optical Axis With and Without Scan Mirror - Primary Encoder -7°	3-208
3-122	Alignment of VISSR Optical Axis With and Without Scan Mirror - Redundant Encoder +23°	3-208
3-123	Optical Alignment of Thermal Channel No. 1 (TC No. 1) to VISSR Optical Axis - North-South Direction	3-209
3-124	Optical Alignment of Thermal Channel No. 1 (TC No. 1) to VISSR Optical Axis - East-West Direction	3-209
3-125	Reference Mirror Alignment Measurement Equipment Setup, Simplified Block Diagram	3-211
3-126	Scattered Light Using Laser Source	3-212
3-127	Desired and Spurious Energy Paths in P/N 4020 Prism	3-213
3-128	VISSR Material Model	3-217
3-129	VISSR Calibrator Material Model	3-217

ILLUSTRATIONS (Cont)

<u>Figure</u>	<u>Page</u>
3-130 Graphic Illustrations of Focusing Effects	3-220
3-131 Theoretical versus Actual FOV	3-227
3-132 Visible Channel Modulation Transfer Function - Protoflight Model	3-229
3-133 PARM-1 to Y-Axis Alignment	3-230
3-134 PARM-2 to X-Axis Alignment	3-231
3-135 Alignment of VISSR Optical Axis to PARM-1 in YZ Plane .	3-232
3-136 Alitnment of VISSR Optical Axis to PARM-1 in XY Plane .	3-232
3-137 Alignment of VISSR Optical Axis (without Scan Mirror) to PARM-1 in YZ Plane	3-233
3-138 Alignment of VISSR Optical Axis (without Scan Mirror) to PARM-2 in XZ Plane	3-233
3-139 Alignment of SARM-2 to PARM-2 in XZ Plane	3-234
3-140 Alignment of SARM-2 to PARM-2 in XY Plane	3-234
3-141 Spectral Transmittance of Mylar (0.00025 inch)	3-236
3-142 Spectral Transmittance of Mylar (0.00025 inch)	3-236
3-143 Spectral Transmittance of Saran (0.0005 inch)	3-237
3-144 Spectral Transmittance of Saran (0.0005 inch)	3-237
3-145 Plastic Film Measurement Setup	3-238
3-146 Engineering Model Modulation Modification upon Insertion of Plastic Protective Cover	3-239

TABLES

<u>Table</u>		<u>Page</u>
2-1	Thermal Model Nodal Description	2-45
3-1	Summary of Three Optical Designs Characteristics	3-5
3-2	System Input Data Readout	3-15
3-3	Surface-by-Surface Readouts	3-20
3-4	Surface-by-Surface Readouts	3-21
3-5	Tangential Fan for Reduced Length	3-22
3-6	Image Size vs Decentering	3-24
3-7	Optical Coating Specifications for VISSR Optics	3-34
3-8	Aluminum Optical Constants	3-35
3-9	Thermal Expansion Coefficients per °C, Single Crystal Beryllium	3-55
3-10	Thermal Gradients and Optical Effects in VISSR Fore-Optics Elements	3-60
3-11	Tabulation of Factors Affecting Spatial Resolution, θ_{ID} , Image Size (mr)	3-69
3-12	Optical Vendors	3-71
3-13	Beryllium Material Factors	3-72
3-14	Polished Kanigen Nickel-Plated Beryllium versus Bare Beryllium	3-73
3-15	Square Bar Modulation Transfer	3-78
3-16	Optical System Parameters	3-96
3-17	Image Blur	3-103
3-18	Energy Distribution, Optical System (Class I and II)	3-103
3-19	Wavefront Deformation (Class I and II)	3-104
3-20	Modulation Transfer	3-104
3-21	Visible Source Optical System Parameters	3-120
3-22	NDF Wheel Elements, Nominal Transmittance	3-122
3-23	Schott Glass Transmittance	3-126
3-24	FAV Quartz Iodine Lamp Filament Temperature vs Current	3-127

TABLES (Cont)

<u>Table</u>		<u>Page</u>
3-25	VISSR Calibrator No. 1 Field Uniformity	3-142
3-26	VISSR Calibrator No. 1 Field Uniformity Data (6/12/72). .	3-143
3-27	Fiber Optics Assembly Transmittance and Crosstalk	3-147
3-28	Anode Radiant Sensitivity and Signal/Noise-in-Signal Ratio	3-157
3-29	Summary for Flight Profile Testing of SMS/VISSR IMP Units	3-164
3-30	Summary of Scattering Measurements - VISSR Optics	3-172
3-31	FOV Data, North-South Scan	3-191
3-32	FOV Data, East-West Scan	3-191
3-33	Spatial Frequencies	3-199
3-34	Tabulation of Focal Position as a Function of Temperature	3-215
3-35	VISSR Telescope Partial Derivatives	3-219
3-36	VISSR Calibrator Partial Derivatives	3-219
3-37	FOV Data, North-South Scan, Run 1	3-225
3-38	FOV Data, North-South Scan, Run 2	3-225
3-39	FOV Data, East-West Scan, Run 1	3-226
3-40	FOV Data, East-West Scan, Run 2	3-226

Section 1

INTRODUCTION

This report describes the effort concerning the Visible Infrared Spin-Scan Radiometer (VISSR) for a Synchronous Meteorological Spacecraft (SMS) through the contractual period ending 1 July 1972. The work is being accomplished for the National Aeronautics and Space Administration, Goddard Space Flight Center, under Contract NAS 5-21139 and comprises delivery of an Engineering Model, Protoflight Model, and two Flight Models together with ancillary equipment.

The VISSR preliminary design was accomplished under a separate contract (NAS 5-21088) and was reported in the Preliminary Design Review Report, dated 27 January 1970. The VISSR Second Quarterly Report, dated September 1970, contained data compiled for the Detailed Design Review conducted in November 1970. This report provides a recapitulation of design data for the Design Review tentatively scheduled for the latter part of August 1972.

SUMMARY OF OBJECTIVES

VISSR operates as an integral part of a synchronous spin-stabilized geostationary satellite with an operational life of three years. VISSR provides both day and night mapping capability with a satellite subpoint resolution of one-half mile in daylight and five miles at night. Cloud altitude is determined by infrared radiometric measurement of cloud top temperature. VISSR instrumentation provides a substantial improvement in resolution in the visible region and extends measurement capabilities to the infrared region when compared to the previous smaller ATS Spin-Scan Cameras.

A secondary design objective provides capability for future growth in the infrared region. The primary consideration in this area is for temperature

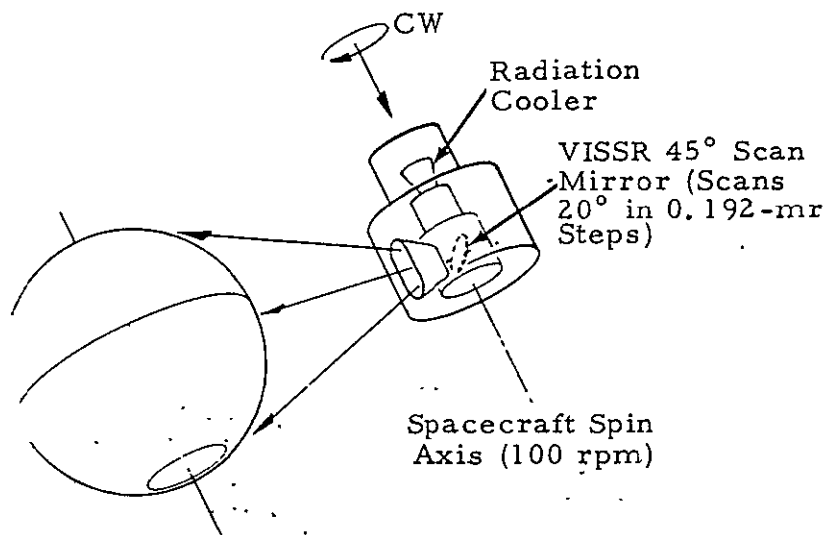
profile measurements requiring additional infrared channels with different spectral and field-of-view characteristics.

Appendix D to this report delineates VISSR design objectives and parameters, and provides required and expected values for each parameter.

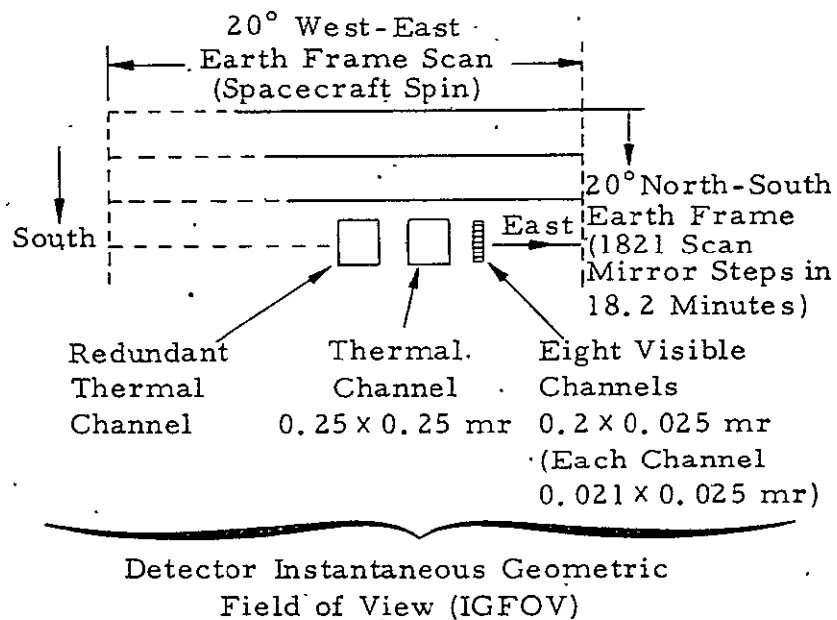
SYSTEM OPERATING CHARACTERISTICS

The VISSR arrangement as used in the synchronous spin-stabilized geostationary satellite is shown in Figure 1-1. As indicated in this figure, the mapping raster is formed by a combination of the satellite spin motion and a step action of the scanner optics. One raster line, corresponding to the earth's west-east axis, is formed for each revolution of the spinning satellite (100 rpm), and the scanner positions each successive line in the north-south axis. Each north-south axis scan step corresponds to the instrument's instantaneous geometric field of view (IGFOV). This 0.192-mr step corresponds to the thermal channel 5-mile resolution when related to the satellite's 22,000 statute mile distance from the earth and considering there is a 1-mile overlap between successive scan lines. The one-half mile resolution in the visible region is obtained by using a linear array of eight detectors aligned so that they sweep out the same scan line path. The IGFOV of each visible channel is 0.025×0.021 mr, allowing 20% underlap between detectors for fabrication considerations. The earth is covered in the north-south plane with successive latitude steps until 20° coverage is attained ($\pm 10^\circ$ about the nominal radiometer optical axis). Following the normal frame, the scanner retraces to the original start position at a rate approximately ten times faster than the normal step scan period. The VISSR instrumentation permits the following four modes of scanning.

1. Normal Frame - This covers the entire earth with a $\pm 10^\circ$ frame, and consists of 1821 latitude steps in 18.2 minutes. It automatically retraces to the original start position in 1.71 minutes to make a complete scan cycle in 19.93 minutes. Each normal frame is initiated by ground command.
2. Variable Frame - Selected frame sector and position within the normal earth view are acquired by ground command.



(A) Spin-Scan Geometry



(B) Picture Data Format (Not to Scale)

Figure 1-1. VISSR/Spacecraft Spin-Scan Geometry and Picture Data Format Arrangement

3. Single-Line - Interruption of the scan step sequence at any selected north-south position makes a single-line scan. Scan position is determined by command timing.
4. Rapid Forward Scan - A rapid forward scan (ten times normal scan rate) is initiated by command to permit rapid positioning of the scan to any selected position within the normal frame.

SYSTEM DESCRIPTION

The scanner assembly consists of a telescope and a separate electronics module. The telescope is a 16-inch diameter aperture optical system which includes an object-space scan mirror for accomplishing the step north-south scan. The assembly includes a radiation cooler and detectors with supporting electronics. It is approximately 60 inches long and 25.5 inches in diameter, and weighs 143.4 pounds. The electronics module occupies approximately 450 in.³ and weighs 13 pounds. It contains the circuitry for interfacing the scanner electronics with the spacecraft electronics, and includes the circuitry necessary for conditioning the scanner signal channels and logic circuitry concerned with the scan drive and calibration sequence. The nominal electrical power required by the radiometer is 22 watts.

The mechanical-optical layout of the telescope is shown in Figure 1-2. Referring to this figure, radiation is received by the primary optics via the 45° object-space scan mirror. It is an elliptically shaped plane mirror which is tilted about its minor axis to obtain the north-south scan steps. The mirror is servo-positioned using a torque motor drive together with a digital encoder for completing the servo loop. A redundant identical assembly is on the opposite side of the mirror. The servo electronics include the logic necessary to step position the mirror at 0.096-mr steps (0.192-mr optical steps) in the required sequence to make the selected scan mode.

Energy from the scan mirror is collected by a Ritchey-Chretien optical system. The 16-inch diameter optics has a 114.7-inch focal length. The system includes a baffle that extends from the primary mirror center section to minimize the effects of scattered radiation. Energy in the visible region

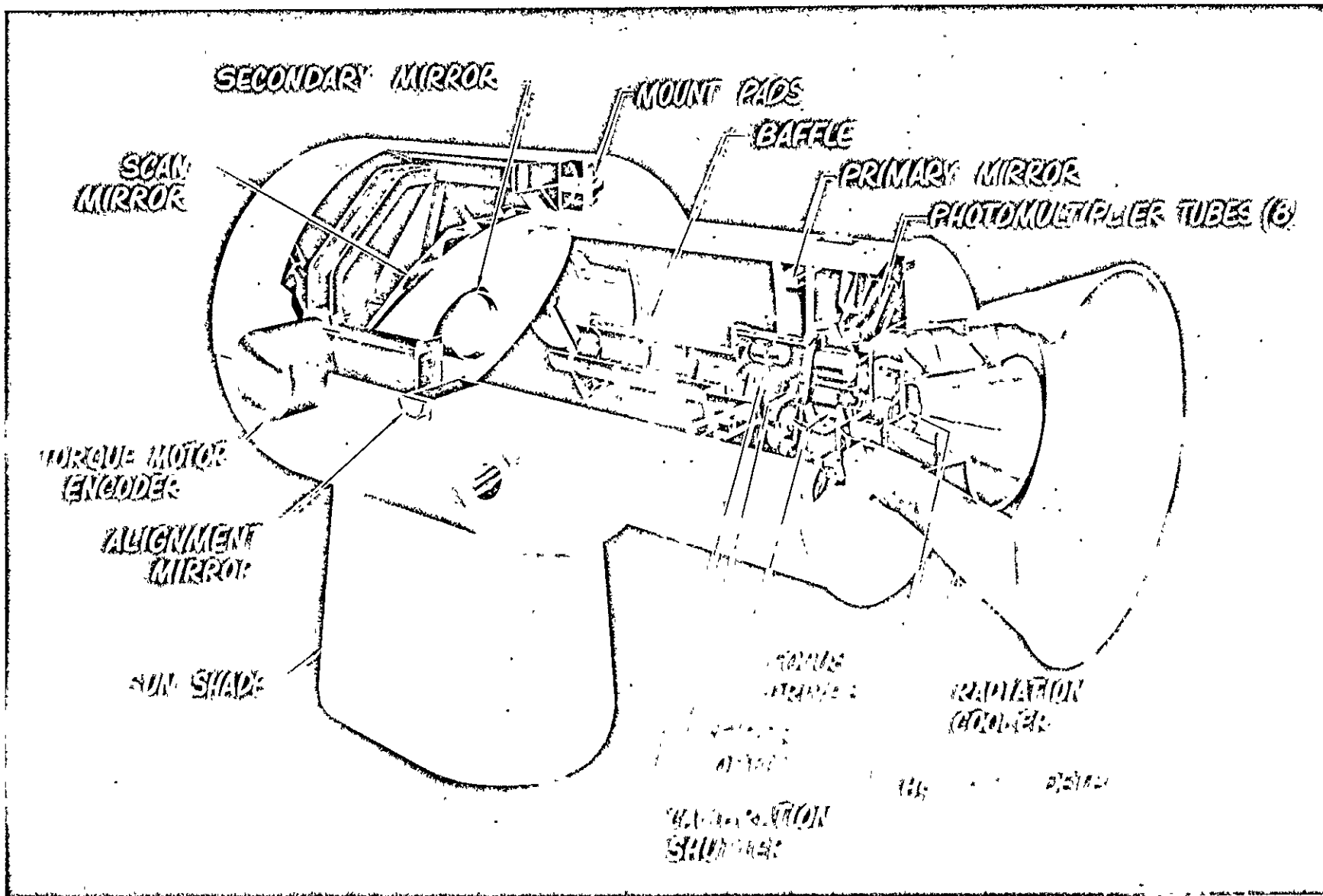


Figure 1-2. VISSR Telescope/Scanner Assembly

is detected at the prime focus using eight fiber optics arranged at the focal plane to form the defining 0.2×0.025 mr (field stop) linear array (each fiber is 0.025×0.021 mr). The other ends of the individual fibers are optically integrated with the eight photomultiplier tubes having the desired 0.55- to 0.75-micron response. In addition, the prime focal plane is relayed to the radiation cooler cold plate using two germanium relay lenses. The relay configuration also is used to increase the overall optical speed to $f/1.28$ relative to the thermal detectors. The 0.005×0.005 inch HgCdTe long-wavelength detector is mounted on the radiation cooler cold plate together with the identical redundant detector. An optical filter between the final relay lens and the detectors restricts the energy to the 10.5- to 12.6-micron wavelength bandpass.

A radiation cooler is used to cool the intrinsic long-wavelength detectors (HgCdTe) in the thermal channel to a nominal temperature of 90°K , the controlled temperature value selected for optimum performance of the particular detector in the scanner. The cooler has actually demonstrated low-temperature performance to 81°K . It uses two cold stages plus an ambient shield. The outside shield is 18 inches in diameter.

CALIBRATION

Both the visible and the thermal channels use the sun as one method of inflight calibration. Saturation of the thermal channel electronics when looking at the sun is avoided by placing the preamplifier in a precision attenuate mode. The second section of the preamplifier is automatically attenuated by a 400 factor immediately when the sun is sensed by the first preamplifier section. It provides a calibration signal that is approximately 50% full scale. Operation is limited to approximately 25 days before and after both the vernal and autumnal equinox. In the visible channels, the sun is viewed with a reduced size "side-looking" collecting prism. The size (approximately 10^{-5} of the aperture area) is made to provide a signal equivalent to a 50% albedo calibration point. The prism is mounted so that its field of view (FOV) leads

the normal FOV in the west-east plane by 15° . This avoids the recovery problem following the primary FOV look into the sun. In addition, three facets are on the prism that increase the effective north-south FOV from $\pm 10^\circ$ to $\pm 26^\circ$ to assure the sun is scanned within the normal scan displacement. This optical arrangement permits an inflight calibration of the visible channels each frame every day of the year (except during solar eclipse).

A second inflight calibration method of the thermal channel is provided using an ambient blackbody shutter arrangement actuated by command. The shutter, whose temperature is monitored, is placed in the FOV near the filter-detector assembly. Therefore, it does not detect possible gain changes caused by the primary optical system. The calibration shutter operates by command, occurring only on the third scan line of the first full frame scan following the command.

The inflight calibration sequence includes an electronic gain calibration. The method uses a precision staircase voltage waveform applied to each of the signal channel preamplifier inputs. The waveform is automatically applied on the first and fourth scan lines of each full frame scan.

The angular position of the radiometer's optical axis at the different timing events occurring during the scan cycle is as follows:

- 0° - Earth Center Look
- 10° - Earth Scan Ends
- 35° - Scan Line Step Initiate
- 330° (-30°) - DC Restore Initiate
- 348° (-12°) - DC Restore Complete
- 350° (-10°) - Earth Scan Begins
- [DC restore initiate is 304° (-56°)
whenever the sun is located in the
330° to 348° angular sector.]

Section 2

SYSTEMS ANALYSIS

DESIGN OBJECTIVE SPECIFICATIONS

The design objective specification was initially written during the preliminary design phase of the VISSR program for the purpose of formalizing and detailing the VISSR design requirements. It was used as the basis for the detail design of the VISSR.

The specification defines the overall VISSR (system) design requirements necessary to accomplish satisfactory operational performance in the SMS application. In addition, the specification defines the requirements for the VISSR subassemblies. These subassembly requirements include: 1) the design approach to be taken, 2) the subassembly design parameter to be used, and 3) the special test and handling provisions to be incorporated.

Following the VISSR Detailed Design Review (held in November 1970), the specification was released as a formal controlled document. The released document has been revised periodically to reflect the results of NASA change orders and directives, VISSR/SMS interface changes, VISSR test data information and analysis updating. The latest issue of the Visible Infrared Spin-Scan Radiometer (VISSR) Design Objective Specification SBRC No. 19100 is attached as Appendix D.

PERFORMANCE ANALYSIS

Thermal Channel Sensitivity

Noise Equivalent Radiance (NEN) Calculations. - For a scanning (non-chopping) radiometer using a detector whose noise equivalent power (NEP) is specified for the electrical bandwidth of the radiometer - the NEN of the radiometer (for an extended source) can be expressed as :

$$NEN = \frac{NEP(A_d, \Delta f_n) \cdot \gamma}{A_o T_o \Omega} \text{ watt-cm}^{-2}\text{-sterad}^{-1} \quad (2-1)$$

where NEP ($A_d, \Delta f_n$) is the noise equivalent power of the radiometer detector, in watts, when the detector has an area of $A_d \text{ cm}^2$ and is operated in the effective noise bandwidth, Δf_n (Hz) of the radiometer.

γ is the preamplifier and load resistor degradation factor which includes the effects of both preamplifier noise and signal loading.

A_o is the effective entrance aperture area in cm^2 .

T_o is the effective "transmission" factor of the radiometer optics and includes all mirrors, lenses, and filters.

Ω is the solid angle FOV of the radiometer in steradians.

Listed in the following are the parameter values of equation (2-1) used to compute the NEN value of the VISSR thermal channel. Also listed are the VISSR design parameters and conditions on which these values are based.

$NEP^{(1)} = 2.0 \times 10^{-10}$ watts, based on 1) a detector area equal to $1.7 \times 10^{-4} \text{ cm}^2$ and 2) an effective electrical bandwidth whose lower cutoff frequency is determined by using dc restoration every 600 msec with a restore loop time constant of 30 msec and whose upper cutoff frequency is determined by a simple 2-pole filter having a -3db break frequency at 26 kHz.

$A_d = (D \times f/\# \times \theta)^2 = 1.7 \times 10^{-4} \text{ cm}^2$. Based on: 1) an entrance aperture diameter D , of 16 inches (40.6 cm); 2) an effective $f/\#$ of 1.29; and 3) an IGFOV, θ , 0.25-mr square.⁽²⁾

(1) The equivalent detector D^* value, referenced to g-r noise, is $1.46 \times 10^{10} \text{ cm (Hz)}^2/\text{watt}$ for an assumed 1/f noise break frequency at 2 kHz.

(2) Changed from 0.2-mr square by NASA directive to achieve an improved NEAT.

- Δf_n = 50.4 kHz. Based on: 1) an information bandwidth equal to 26 kHz⁽³⁾; 2) a low-pass filter rolling off at 12 db/octave; 3) use of dc restoration to set the low-frequency cutoff characteristics; 4) an information gathering period, T_1 = 0.07 sec; 5) a restore network time constant, T_2 = 0.03 sec; and 6) a detector 1/f noise break frequency at 2 kHz.
- γ = 1.3. Based on breadboard tests of the type of preamplifier to be used in the VISSR thermal channel design and a detector responsivity of 3.6×10^3 volts/watt.
- A_o = $(\pi/4D^2 \times 0.84) = 1090 \text{ cm}^2$. Based on: 1) an entrance aperture diameter of 16 inches (40.6 cm); and 2) a central obscuration of 16%.
- T_o = $(R_m^3 \times T_r \times T_f \times T_c) = 0.43$. Based on: 1) three reflecting mirror surfaces with a reflectivity $R_m = 0.96$ in the 10.5- to 12.6-micron band; 2) an optical relay system with an effective transmission $T_r = 0.85$; 3) an effective filter transmission of 0.65; and 4) a first-stage cooler window transmission $T_c = 0.88$.
- Ω = $\theta^2 = 6.25 \times 10^{-8}$ steradian based on an IGFOV of 0.25-mr square.

Using the above parameter values in equation (2-1) yields an NEN for the VISSR thermal channel of:

$$\underline{\underline{NEN(10.5-12.6) = 0.89 \times 10^{-5} \text{ watt-cm}^{-2}\text{-sterad}^{-1}}} \quad (2-2)$$

Temperature Resolution and S/N. - The noise equivalent temperature differential (NE ΔT) of a radiometer operating in the spectral band $\Delta\lambda$, and viewing a blackbody target scene at a temperature T_o , can be expressed as:

$$NE\Delta T = NEN \left[\frac{dN(\Delta\lambda)}{dT} \right]_{T_o}^{-1} \quad (2-3)$$

where $\left[\frac{dN(\Delta\lambda)}{dT} \right]_{T_o}$ is the thermal derivative of the target scene radiance in the spectral band evaluated at the scene temperature T_o .

The radiometer S/N output can be expressed simply as

$$S/N = N(\Delta\lambda)T_o[NEN]^{-1} \quad (2-4)$$

(3) Information bandwidth selection based on original (nominal) 0.2-mr square IGFOV.

The values of $\frac{dN(\Delta\lambda)}{dT}_T$ and $N(\Delta\lambda)_T$ for $\lambda = 10.5$ to 12.6 microns are plotted in Figure 2-1 as a function of T .

The expected $NE\Delta T$ and S/N values for the VISSR thermal channel are shown in Figure 2-2 as a function of target scene temperature for the $NE\Delta T$ value calculated in equation (2-2).

It can be seen from Figure 2-2 that for a scene temperature of 200° and $300^\circ K$, the radiometer $NE\Delta T$ values are approximately 1.2° and $0.32^\circ K$, respectively, for an extended target. The S/N values at $200^\circ K$ and $300^\circ K$ scene temperatures are approximately 25:1 and 210:1, respectively.

Visible Channel Sensitivity

Effective Albedo Radiance. - The spectral distribution of the sun's energy outside the earth's atmosphere is shown in Figure 2-3. The effective radiance value in the VISSR visible channel for an albedo of 100% is obtained by multiplying the values of Figure 2-3 with the spectral response of the VISSR visible channel, integrating the resulting product over wavelength and then dividing by π . Performing these calculations for the VISSR visible channel spectral response shown in Figure 2-4 yields a radiance value of

$$N(100\% \text{ albedo}) = 9.4 \times 10^{-3} \text{ watt-cm}^{-2}\text{-sterad}^{-1} \quad (2-5)$$

The effective irradiance at the VISSR aperture in the spectral band of a visible channel for an albedo of 0.5% can be expressed as:

$$H(0.5\% \text{ albedo}) = 4.7 \times 10^{-5} \times \Omega \text{ watt/cm}^2 \quad (2-6)$$

where Ω is the solid angle FOV of a VISSR visible channel in steradians.

For $\Omega = 5 \times 10^{-10}$ steradians

$$H = 2.35 \times 10^{-14} \text{ watt/cm}^2$$

Signal-to-Noise. - The S/N of a VISSR visible channel can be expressed as:

$$S/N = \sqrt{\frac{HAT_o}{\Delta f_n}} \cdot \sqrt{F(S, \sigma, n, k)} \quad (2-7)(4)$$

(4) This equation assumes that the noise from any amplifier following the PMT will not degrade the PMT S/N . This is true for the VISSR down to S/N values of approximately unity.

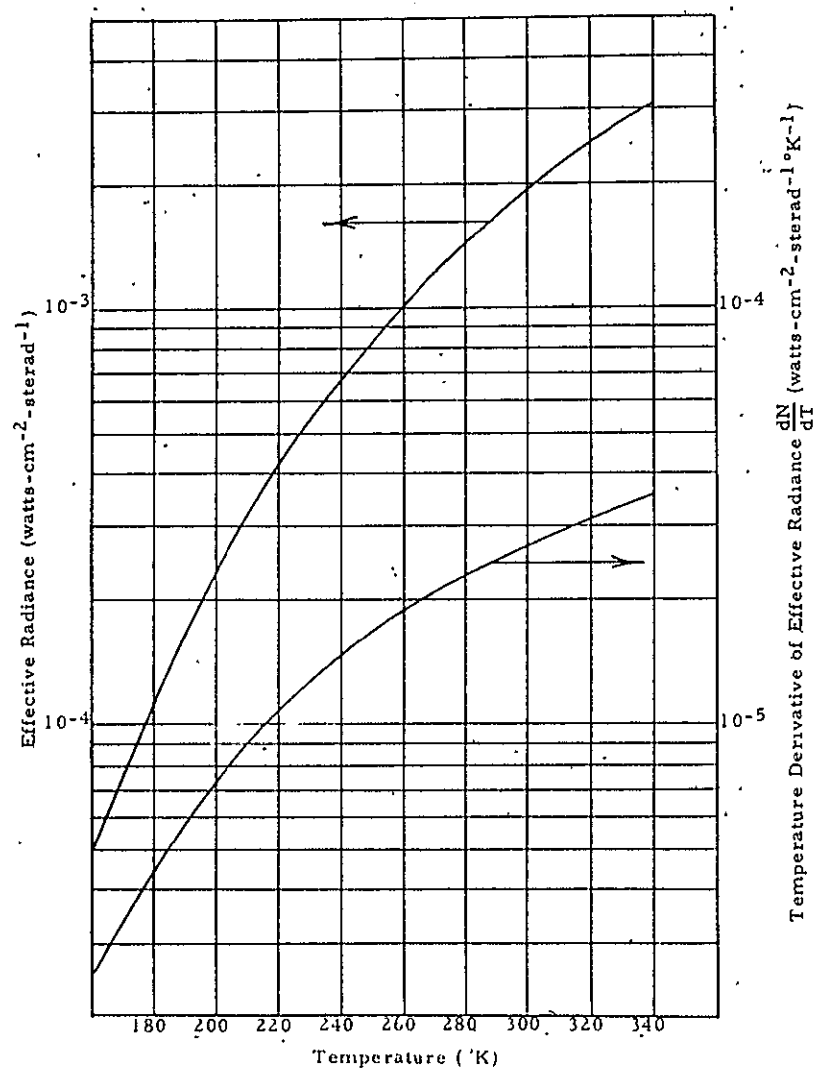


Figure 2-1. Effective Radiance N and dN/dT , as a Function of Target Temperature in the 10.5- to 12.6-Micron Band

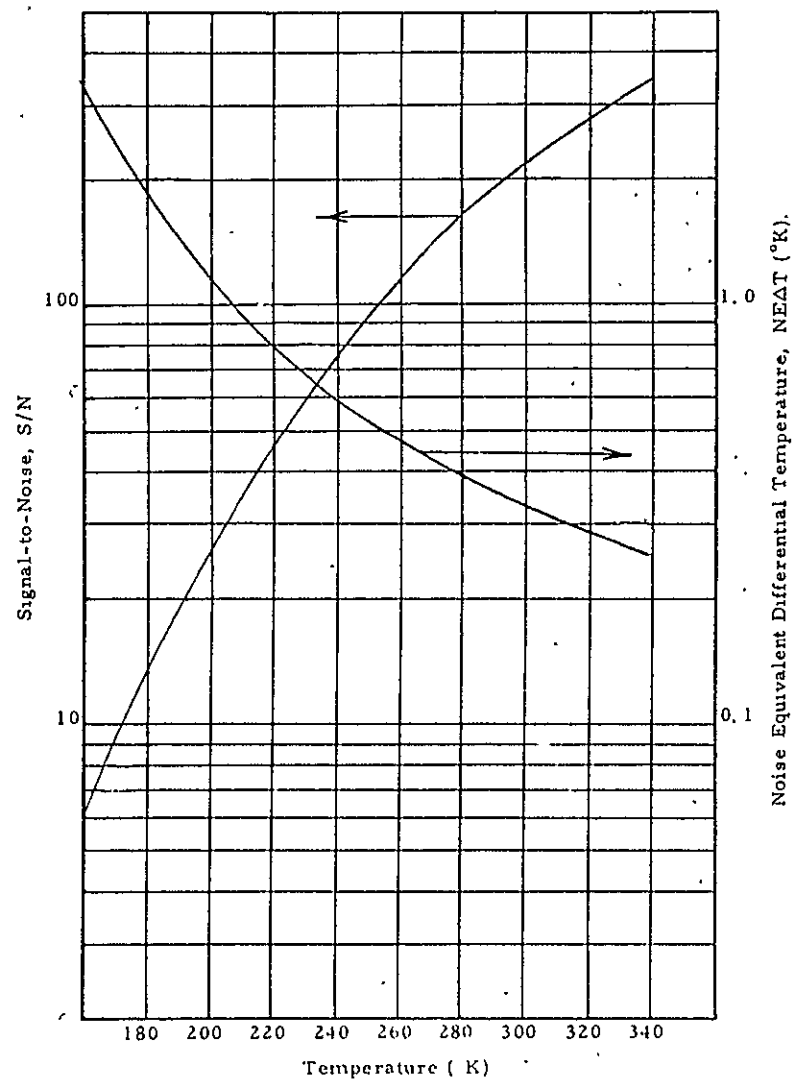


Figure 2-2. VISSR Thermal Channel S/N and NEAT as a Function of Target Temperature, T (For an Extended Target)

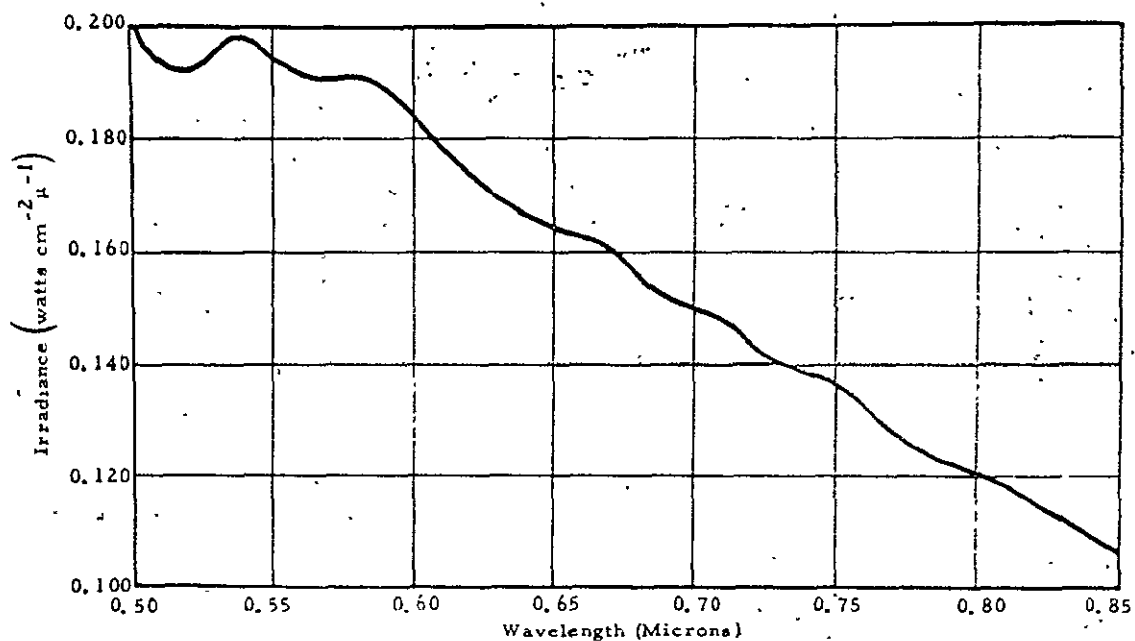


Figure 2-3. Spectral Distribution of Sun's Energy Outside the Earth's Atmosphere (From the Handbook of Geophysics)

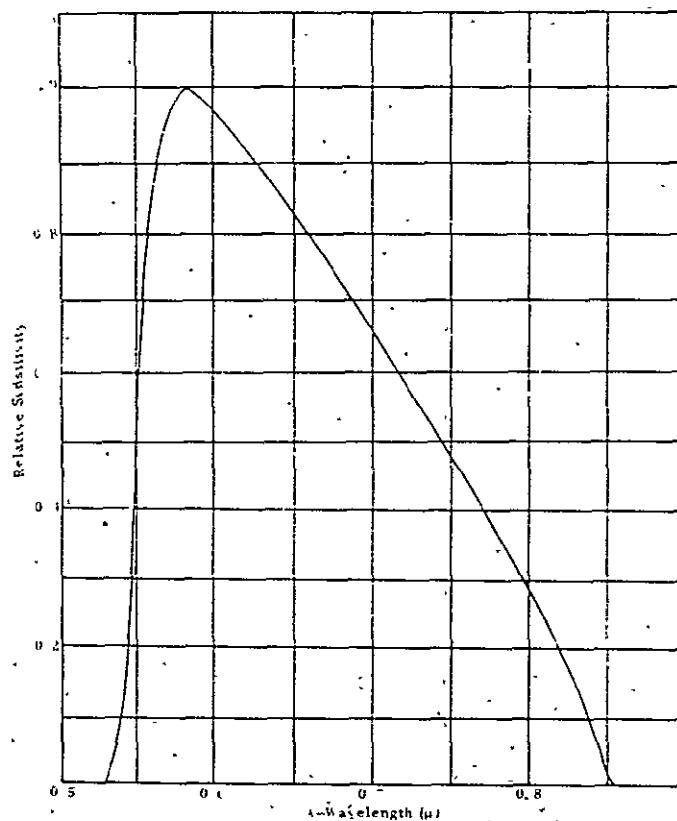


Figure 2-4. Relative Spectral Sensitivity, Visible Channel Enhanced PMT plus Filter

where H is the effective irradiance at radiometer aperture (watt/cm²)
 A is the collecting aperture of the radiometer (cm²)
 T_o is the effective optical train efficiency
 Δf_n is the effective noise bandwidth (Hz)
 $F(S, \sigma, n, k)$ is the effective normalized detectivity of the PMT used in the channel, in (Hz/watt), and is a function of 1) the peak radiant sensitivity, S (amps/watt), of the photocathode surface in the spectral band of interest; 2) the gain, σ , of each current amplifying stage of the PMT; 3) the number of current amplifying stages, n , and the noise factor, k , for each stage.

Listed in the following are the values for the parameters of equation (2-7) used to compute the S/N value of a VISSR visible channel for an albedo of 0.5%. Also listed are the VISSR design parameters and conditions on which these values were based.

$H = 2.35 \times 10^{-14}$ watt/cm². [See equation (2-6).]

$A = 1090$ cm². (See Thermal Channel.)

$T_o = (R_m^3 \times T_{AO}) = 0.42$. Based on: 1) three reflecting mirror surfaces with a reflectivity of $R_m = 0.87$ in the 0.55- to 0.75-micron band; 2) transmission of the visible channel aft optics of 0.75; and 3) the visible channel filter transmission 0.85.

$\Delta f_n = 258$ kHz. Based on: 1) an information bandwidth equal to the reciprocal of twice the IGFOV dwell time, $t_{dwell} = 2.4 \times 10^{-6}$ sec; and 2) a low-pass filter rolling off at 12 db/octave.

$F(S, \sigma, n, k) = 1.5 \times 10^{17}$ Hz/watt. (See SBRC Specification 18858 and Figure 2-4.)

Using the above parameter values in equation (2-7) yields an S/N in a VISSR visible channel for an albedo of 0.5% of

$$S/N_{(0.5\% \text{ albedo})} = 2.5$$

It should be noted that since the S/N only increases as the square root of the irradiance, the S/N for an albedo of 100% will be

$$S/N_{(100\% \text{ albedo})} = 35$$

ATS-1 Spin-Scan Camera S/N Comparison. - The S/N values for the ATS-1 Spin-Scan Camera (2-nmi circular IGFOV) were calculated for comparison with the calculated VISSR S/N values (0.5-nmi square IGFOV). The following parameters were used to calculate the S/N value for the ATS-1 Spin-Scan Camera for a 0.5% albedo.

$H = 2.27 \times 10^{-13}$ watt/cm². Based on: 1) a 0.1-mr circular IGFOV, and 2) a 0.48- to 0.58-micron spectral band (from Spin-Scan Camera Final Report).

$T_o = 0.6$. Based on: 1) a PMT cathode responsivity of 66.5×10^{-3} amp/watt and an effective system cathode responsivity of 39.8×10^{-3} amp/watt at 0.52 micron (from Spin-Scan Camera Final Report).

$A_o = 104$ cm². Based on Spin-Scan Camera design data.

$\Delta f_n = 236$ kHz. Based on a single-pole filter having a 150-kHz cutoff frequency.

$F(S, \sigma, n, k) = 1.5 \times 10^{17}$ Hz/watt. Based on: 1) a PMT cathode responsivity of 66.5×10^{-3} amp/watt at 0.52 micron, 2) a first dynode stage gain of 4.6, and 3) subsequent dynode gains of 2.3 (from EMR PMT data).

Using the above parameter values yields an S/N value for the Spin-Scan Camera for an albedo of 0.5% of

$$S/N(0.5\% \text{ albedo}) = 3.0$$

and for an albedo of 100%

$$S/N(100\% \text{ albedo}) = 42$$

Spatial Resolution

Sine Bar Pattern Scene. - The VISSR relative response,⁵ $V(f)$, to a sine bar pattern scene of a given spatial frequency can be expressed as follows:

$$V(f) = O(f) \times F(f) \times E(f) \quad (2-8)$$

where $O(f)$ is the relative frequency response of the radiometer optics
 $F(f)$ is the relative frequency response of the radiometer IGFOV (field stop)

⁵ Voltage output versus radiation input.

$E(f)$ is the relative frequency response of the radiometer electronics

f is the frequency being considered expressed in the time domain in Hz.

and the transformation of frequency from the space domain (cycles/radian) to the time domain (Hz) is accomplished by using the radiometer scan rate (radian/sec).

The diffraction pattern for the VISSR 16-inch aperture with 0.4 obscuration has been calculated by using the following equations.⁶

$$I(P) = \frac{I_0}{(1 - \epsilon^2)^2} \left[\frac{2J_1(Ka\omega)}{Ka\omega} - \epsilon^2 \frac{2J_1(K\epsilon a\omega)}{K\epsilon a\omega} \right]^2 \quad (2-9)$$

and
$$I_0 = \frac{H\pi^2 a^4 (1 - \epsilon^2)^2}{\lambda^2} \text{ watts sterad}^{-1} \quad (2-10)$$

where H is the uniform irradiance upon the aperture in watts cm^{-2}

a is the entrance aperture radius in cm

λ is the wavelength of the light in cm

ϵ is the ratio of obscuration radius to aperture radius

$$K = \frac{2\pi}{\lambda}$$

$\omega = \sin \theta$ where θ is the angular direction between any point P and the geometric image point

J_1 = Bessel function of the first kind.

This diffraction pattern has been convolved with itself along a line to determine the line spread function. The angular spread of the line spread function has been converted to the time domain by using the scan rate of 10.45 radians per second. The resulting frequency response for a VISSR visible channel and the VISSR thermal channel is given in Figures 2-5 and 2-6.

⁶ M. Born and E. Wolf, "Principles of Optics," Pergamon Press, New York, N. Y. (1959).

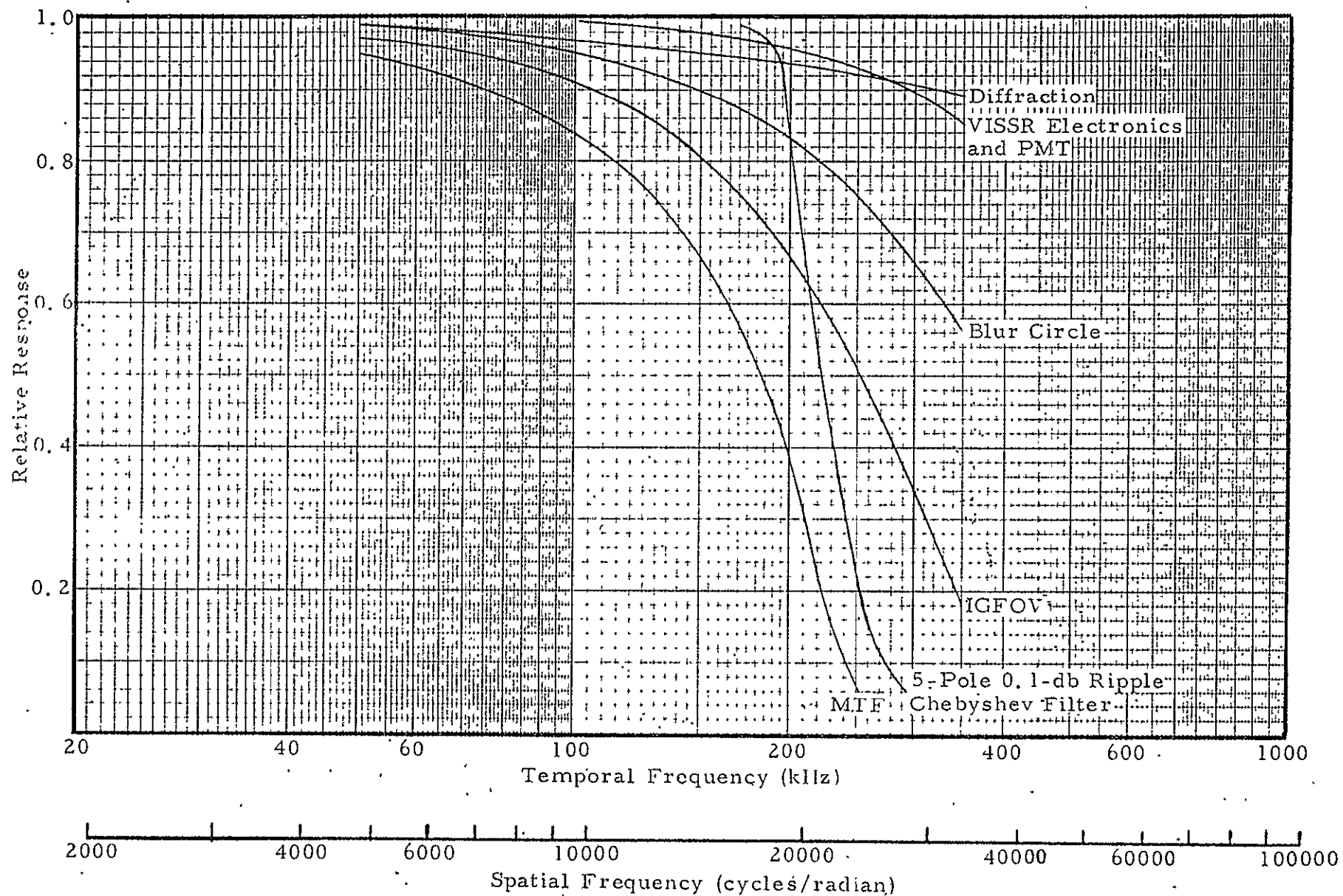


Figure 2-5. VISSR Visible Channel Sine Wave MTF

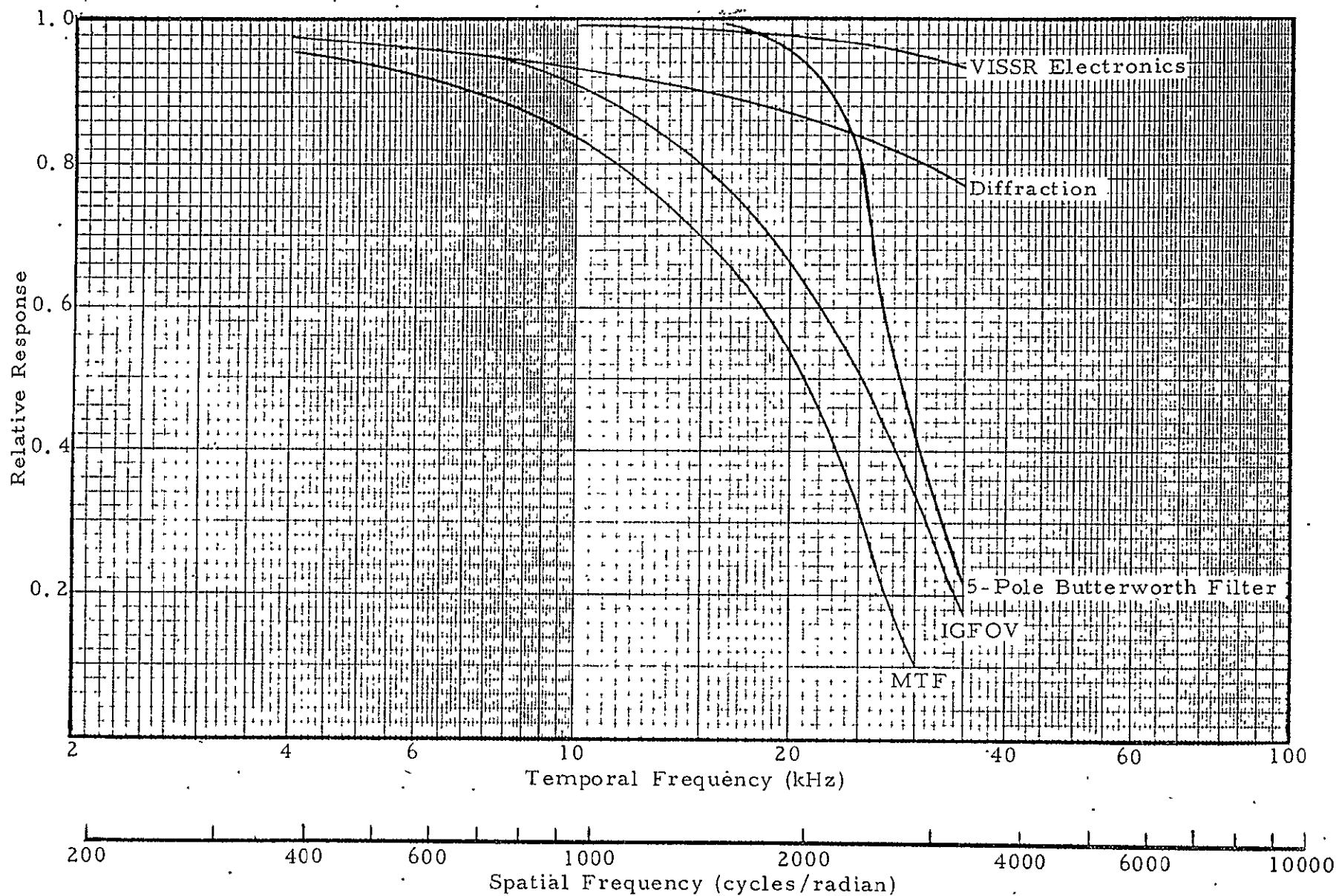


Figure 2-6. VISSR Thermal Channel Sine Wave MTF

The effects of aberrations in the VISSR thermal channel are relatively small compared to the channel IGFOV and can be neglected. However, aberrations in the VISSR visible channels are significant compared to the IGFOVs and must be taken into account (see Optics). In determining the relative frequency response of the VISSR visible channel optics due to aberrations, the blur circle has been assumed to have an energy distribution which is cosine in shape.

The frequency response of a VISSR visible channel IGFOV and the VISSR thermal channel IGFOV has been determined from a $\frac{\sin x}{x}$ pattern converted to the time domain. The results are shown in Figures 2-5 and 2-6.

The electronic frequency response of the VISSR thermal and visible channels (including the frequency response of the PMTs) is also plotted in Figures 2-5 and 2-6 together with the expected spacecraft electronic filtering. For the thermal channels, a 5-pole 26-kHz (at -3 db point) Butterworth filter was assumed for the spacecraft. For the visible channels, a 5-pole, 0.1-db ripple, 210-kHz (at -3 db point) Chebyshev filter was assumed.

The response curves shown in Figures 2-5 and 2-6 have been appropriately combined to show the resultant frequency response (MTF) for the VISSR visible and thermal channels.

For a spatial frequency having a period equal to twice the dwell time of the VISSR IGFOVs (visible channel = 2×10^4 cycles/radian; thermal channel = 2×10^3 cycles/radian), the MTFs for the VISSR visible and thermal channels are 0.33 and 0.50, respectively.

Measured Square-Bar MTF. - An example of the square-bar optical MTF measured for the engineering model VISSR visible and thermal channels is shown in Figures 2-7 and 2-8, respectively. The effects of the spacecraft filter cutoff frequency characteristics (early design) on the VISSR visible channel are also shown in Figure 2-7. At a 900-rpm MTF wheel rotation, the electrical frequencies generated (for the corresponding spatial frequencies generated by the VISSR calibrator) are sufficiently low so as not to be greatly

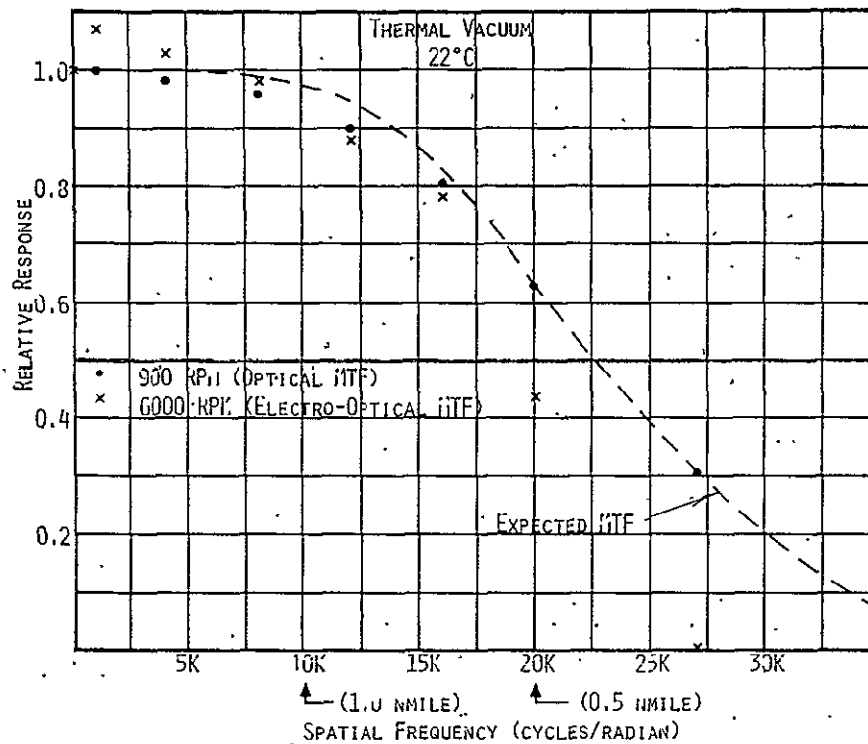


Figure 2-7. Engineering Model VISSR Visible Channel MTF (Square Bar)

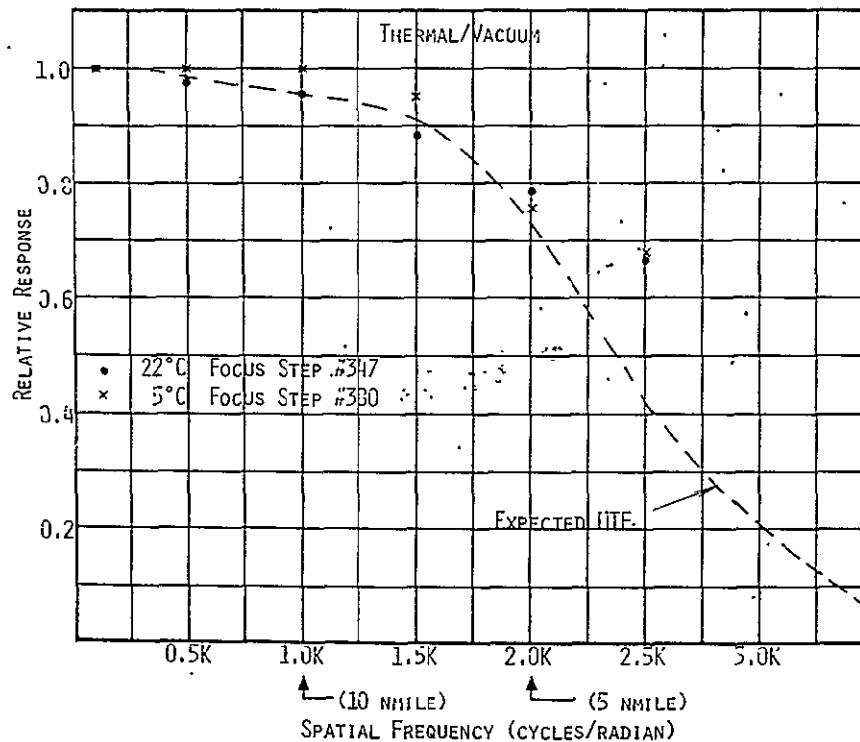


Figure 2-8. Engineering Model VISSR Thermal Channel MTF (Square Bar)

affected by the simulated spacecraft filter (part of the VISSR Test Console). At 6000-rpm MTF wheel rotation, the proper electrical/spatial frequency relationship (for 100-rpm spacecraft spin rate) exists.

The higher than expected square-bar optical MTF values for the VISSR thermal channel at high spatial frequencies are due to the fact that the expected square-bar MTF response is based on a 0.25-mr square IGFOV, whereas the actual thermal channel IGFOV in the engineering model VISSR is approximately 0.20-mr square.

Blur Circle Effect on MTF/Ground Resolution. - An analysis was conducted to determine the change in VISSR MTF as the VISSR optical blur circle size increased above the minimum size attainable under optimum focus conditions.

The purpose for conducting the analysis was to provide the necessary technical information on which a decision could be based for establishing the maximum defocusing that could be tolerated before refocusing would become necessary.

The IGFOV assumed for the VISSR visible channels was the nominal 25 μ r (0.5-nmi ground resolution). For the thermal channel, the nominal 250- μ r IGFOV (5-nmi ground resolution) was assumed.

The spacecraft electrical filtering assumed for the analysis was a 5-pole, 0.1-db ripple, 210-kHz (at -3 db point) Chebyshev filter for the VISSR visible channels and a 5-pole, 26-kHz (at -3 db point) Butterworth filter for the VISSR thermal channels. Also included in the analysis was the expected electrical characteristics of the VISSR electronics.

The results of the analysis are summarized in Figures 2-9 and 2-10; which show the sine wave MTF of the VISSR visible and thermal channels, respectively, for several increases in blur circle size above optimum focus condition. The optimum focus condition includes the effects of diffraction and an expected, uncorrectable 20- μ r diameter blur circle.

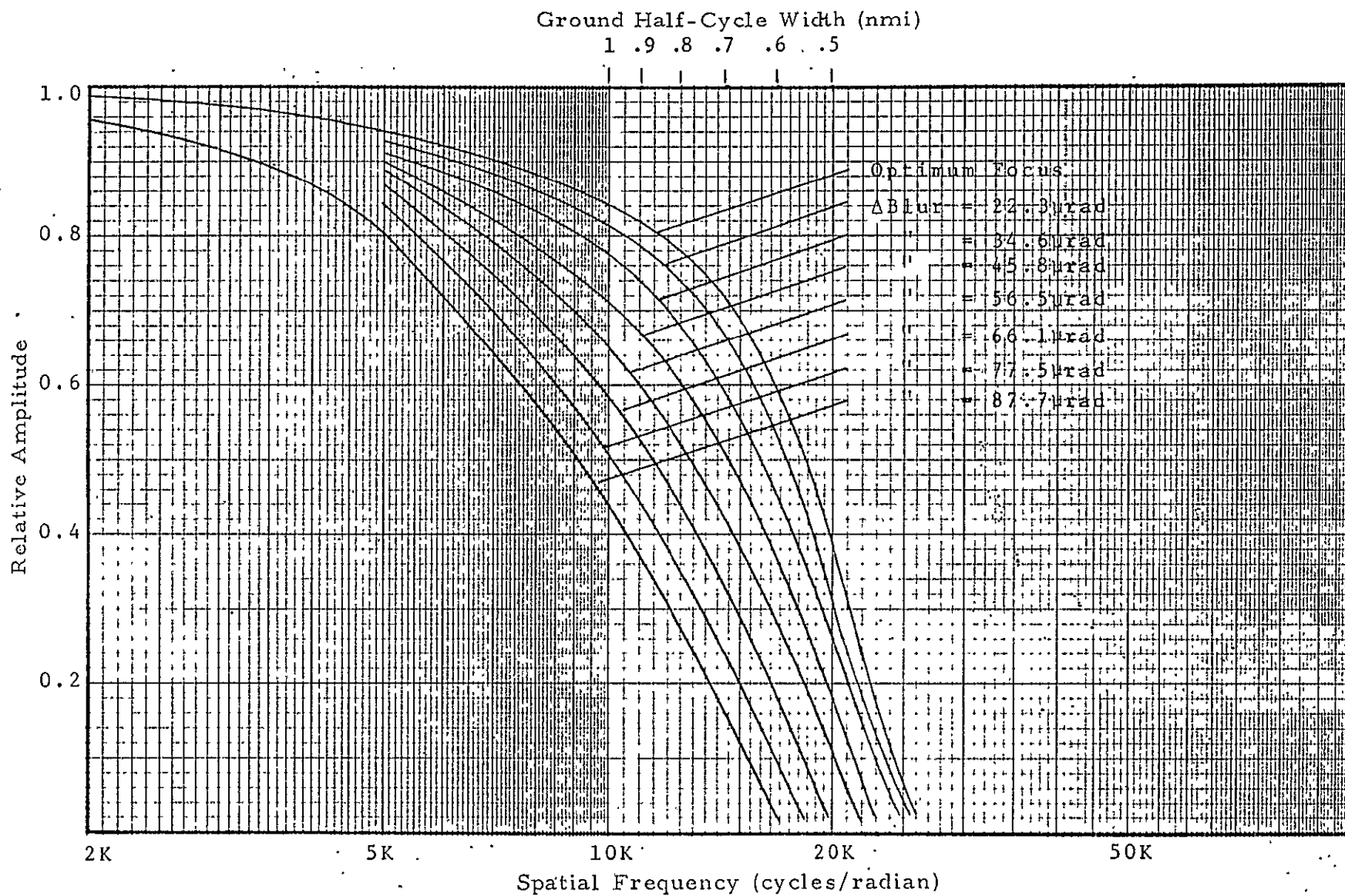


Figure 2-9. VISSR Visible Channel Sine Wave MTF at Several Focus Conditions

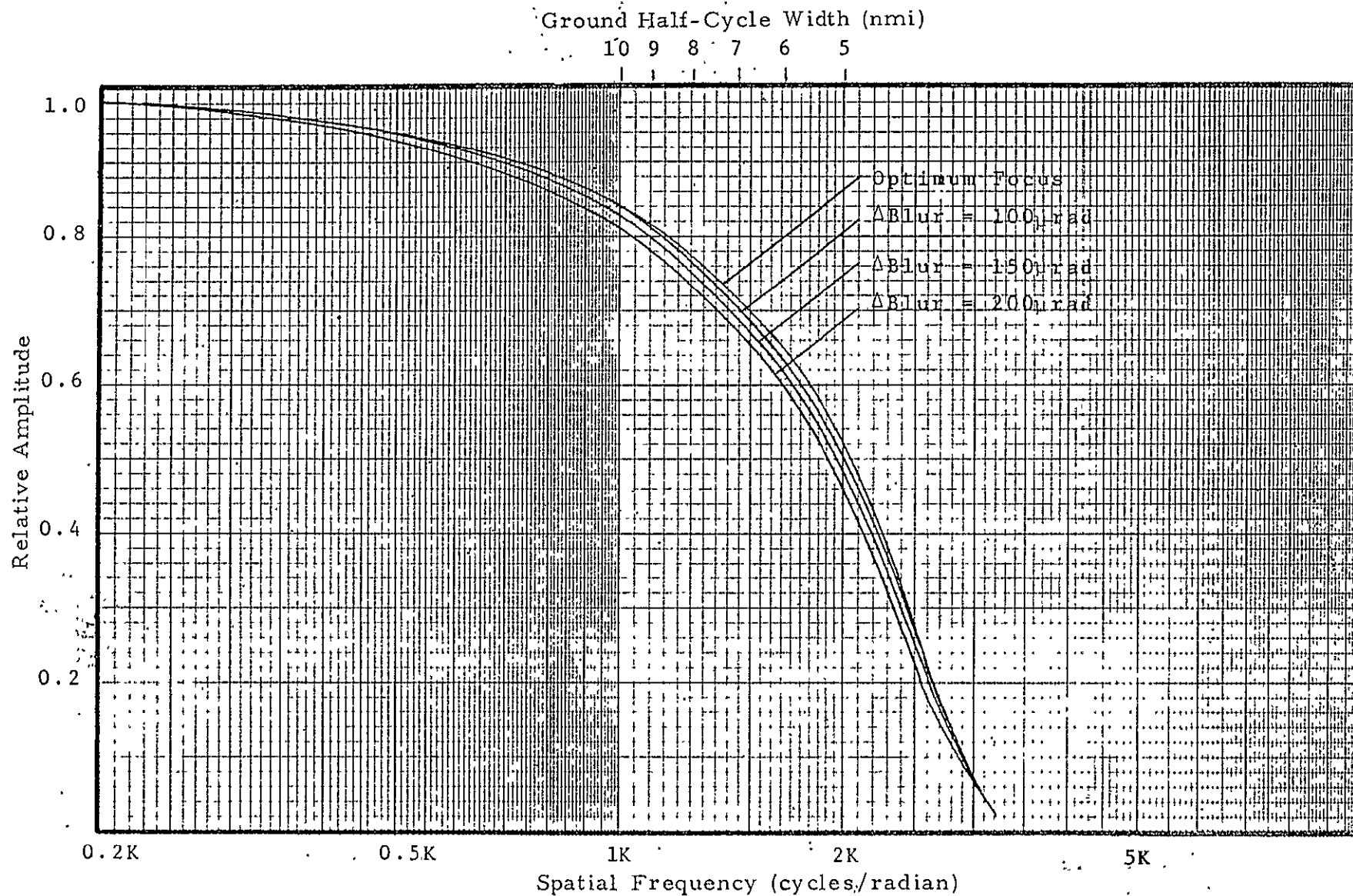


Figure 2-10. VISSR Thermal Channel Sine Wave MTF at Several Focus Conditions

As would be expected (and shown in Figures 2-9 and 2-10), the relative change in MTF for a given change in blur circle size is significantly greater for the visible channels compared to the thermal channels.

If the value of MTF at 20,000 cycles/radian (0.5-nmi ground half-period) at optimum focus condition is used as the basis for evaluating the effects of blur circle size of the VISSR visible channels (see Figure 2-9), then it can be seen that for a blur circle diameter increase of approximately 35 μ r, a decrease in ground resolution of 10% (to 0.55 nmi) results. Similarly, for a blur circle diameter increase of approximately 45 μ r, a decrease in ground resolution of 20% (to 0.6 nmi) results.

For the VISSR thermal channels (see Figure 2-10) a blur circle increase of 200 μ r can be tolerated with less than a 10% decrease in ground resolution.

SUN EXPOSURE ANALYSIS

Effects of Sun Exposure on the VISSR Photomultiplier Tubes

Cathode Radiant Power Density. - The cathode radiant power density expected to impinge on a VISSR PMT photocathode surface when the sun is in the FOV of the VISSR can be expressed as:

$$PD_C = N_S \cdot A_O \cdot \Omega \cdot K(\Delta\lambda) \cdot T_O / A_C \quad (2-11)$$

where N_S is the solar radiance value = 2.03×10^3 watts/cm²/steradian

A_O is the effective collecting aperture of the VISSR = 1090 cm²

Ω is the instantaneous geometric FOV of a VISSR visible channel = 5×10^{-10} steradian

$K(\Delta\lambda)$ is the fractional amount of sun radiance in the spectral band of interest = 0.68. The value of 0.68 takes into account the fact that from radiance transmission consideration the upper wavelength cutoff of the visible channel is set by the visible channel's (glass) aft optics and not the photocathode responsivity which sets the upper wavelength spectral response of the visible channel.

T_O is the effective visible channel transmission up to the visible channel photocathode surface = 0.55

A_c is the effective area of the photocathode surface over which the collected solar radiation is spread ("first bounce" area when PMT enhancement is used) = $3.0 \times 10^{-2} \text{ cm}^2$.

Using the above values in equation (2-11) yields:

$$PD_c = 1.39 \times 10^{-2} \text{ watts/cm}^2 \quad (2-12)$$

This value is approximately 0.1 the value of direct sunlight (0.14 watt/cm^2). In addition, the radiant power is lacking in UV content due to the lower wavelength cutoff (0.55 micron) of the VISSR visible channel filter.

The low level of radiant power density on the photocathode surface ensures against any significant heating or the creation of hot spots. Therefore, no degradation of the PMT is expected due to the heating effects of direct solar radiation.

PMT manufacturers state generally that when a nonpowered PMT is exposed to a relatively high level of radiation, particularly when the radiation is high in UV content, a temporary increase in tube dark noise will result when the PMT is subsequently operated. The length of time the dark noise persists is dependent on the magnitude and length of exposure. For the VISSR PMTs, the above normal dark noise would persist for approximately 24 hours following full exposure to direct sunlight (when nonpowered) for an extended period of time. For the lower level of radiation that will actually be experienced by the VISSR, particularly since the radiation will be void of UV content, no noise problem is expected to exist.

Cathode Current Density. - When PMT enhancement is used to improve the photocathode responsivity of a PMT, the area of the photocathode surface receiving the "first bounce" of the collected radiation will have the highest photocathode current density. The current density increase factor (due to using enhancement) will be approximately 1.5.⁷ Therefore, the maximum

⁷ J. B. Oke and R. E. Shield, "A Practical Multiple Reflection Technique for Improving the Quantum Efficiency of Photomultiplier Tubes," Applied Optics 1, 617 (1968).

photocathode current density expected for a VISSR PMT when the sun is in the FOV of the VISSR can be expressed as:

$$ID_C = 1.5 PD_C (\text{eff}) \cdot R \quad (2-13)$$

where $PD_C (\text{eff})$ is the effective radiant power density at the photocathode surface in the spectral (responsivity) band of interest
 $(0.55 \text{ to } 0.75\mu) = 4.55 \times 10^{-3} \text{ watt/cm}^2$

R is the effective average (non-enhanced) responsivity of the PMT photocathode in the spectral band of interest = $3.5 \times 10^{-2} \text{ amp/watt}$

Using the above values in equation (2-13) yields:

$$ID_C = 2.4 \times 10^{-4} \text{ amp/cm}^2 \quad (2-14)$$

This value exceeds the maximum limit value specified by EMR, 10^{-6} amp/cm^2 (specified as being conservative) for the average cathode current density (averaged over seconds). Therefore, the VISSR PMTs should not be operated (powered) when the sun might be in the FOV of the VISSR for more than just a short period of time.

When the SMS is operating in a spin-stabilized mode at a nominal 100 rpm, the duty cycle of the VISSR FOV crossing the sun is 1.53×10^{-3} (maximum when crossing a 0.55° sun diameter). Therefore, the average cathode current density will be:

$$\begin{aligned} ID_C(\text{ave}) &= 2.4 \times 10^{-4} \times 1.53 \times 10^{-3} \\ &= 3.7 \times 10^{-7} \text{ amps/cm}^2 \end{aligned} \quad (2-15)$$

which is below the (conservative) maximum limit value specified by EMR by a safety factor of 2.7.

Anode Current Density. - For an average PMT photocathode enhancement value of 2, the total cathode current expected for a VISSR PMT when the sun is in the FOV of the VISSR will be:

$$I_C(\text{peak}) = 2.9 \times 10^{-5} \text{ amp} \quad (2-16)$$

When the SMS is in a spin stabilized mode the average cathode current will be:

$$I_c(\text{ave}) = 4.4 \times 10^{-8} \text{ amp} \quad (2-17)$$

For a VISSR PMT gain of 1×10^4 ,⁸ the peak and average values of PMT anode current will be:

$$I_a(\text{peak}) = 2.9 \times 10^{-1} \text{ amp} \quad (2-18)$$

$$I_a(\text{ave}) = 4.4 \times 10^{-4} \text{ amp} \quad (2-19)$$

The values of $I_a(\text{peak})$ and $I_a(\text{ave})$ shown assume no current limiting in the PMT circuitry. Without current limiting the values of $I_a(\text{peak})$ and $I_a(\text{ave})$ will exceed the maximum limit values specified by the PMT manufacturer.⁹ For this reason, PMT anode current limiting of (short duration, pulse) signals above those produced by the maximum scene albedo has been incorporated in the VISSR PMT circuit design.

Tests conducted on a PMT with the anode current limiting circuit shows that after the application of 50 sun amplitude pulses of 1 to 2 msec duration, which are applied at a rate of 1 per 600 msec, the decrease in PMT gain immediately after the 50th pulse is applied is approximately 2.5%. Recovery of the PMT to within 1% of the pre-exposure tube gain occurs approximately 2.5 minutes after exposure to the last "sun" pulse and to within less than 0.5% of the pre-exposure gain after approximately 8 minutes.

Since the maximum width of the sun pulse "seen" by the VISSR channels during a line-scan will be approximately 0.9 msec (at 0.55° sun diameter), the maximum gain change after scanning the sun during a normal full-frame mode of operation is expected to be less than the above measured value.

⁸From stability considerations the PMTs will be operated at a current gain which is only high enough to ensure that the remaining channel gain required can be achieved with a dc amplifier.

⁹Specified as 1×10^{-3} amp and 1×10^{-6} amp, respectively, by EMR for the 541E.

Temperature Effects of Imaged Solar Radiation in the VISSR Scanner

During the process of maneuvering the SMS to achieve proper orientation and stabilization in orbit, the VISSR optical aperture may inadvertently be pointed directly toward the sun. When the optical axis of the VISSR is aligned closely with the sun, the collected solar radiation is concentrated ("imaged") onto small areas of the radiometer. The high radiation flux densities impinging on and being absorbed by these areas can quickly give rise to localized hot-spots. In addition, although localized hot-spots are not as severe for large off-axis angles, the continuous sun input into the VISSR aperture can result in an average over-temperature condition of the scanner.

The effects of solar heating of the VISSR for a non-spinning spacecraft and for a spinning spacecraft rotating at a constant 4-rpm rate about the Z-axis of the spacecraft were investigated. The following conclusions were reached based on the results of the investigation:

1. To assure that the average scanner temperature will not exceed 45°C for the non-spinning case, the VISSR should not be oriented with the sun closer than 55° to the VISSR optical axis.
2. No VISSR temperature problems are expected to be encountered for spacecraft spin rates as low as 4 rpm.

SCAN DISTORTION ANALYSIS

It is desired from data reduction and data analysis considerations to achieve a VISSR scan frame which is essentially distortion-free. A perfectly aligned scan frame consisting of 1821 thermal lines of 0.25-mr width¹⁰ is shown in Figure 2-11. At each scan step position of the scan mirror, eight visible lines are scanned in addition to each thermal line.¹⁰ With a rotation rate of 100 rpm, one line of the 20° square frame is scanned in approximately

¹⁰ With a nominal 0.192-mr scan step, approximately a 25% overlap will occur between adjacent thermal channel scan lines. For the visible channels, approximately a 20% overlap will occur between end channels (of the channel array) each scan step. Visible channels within the channel array will have approximately a 20% underlap due to cladding of the fiber optics.

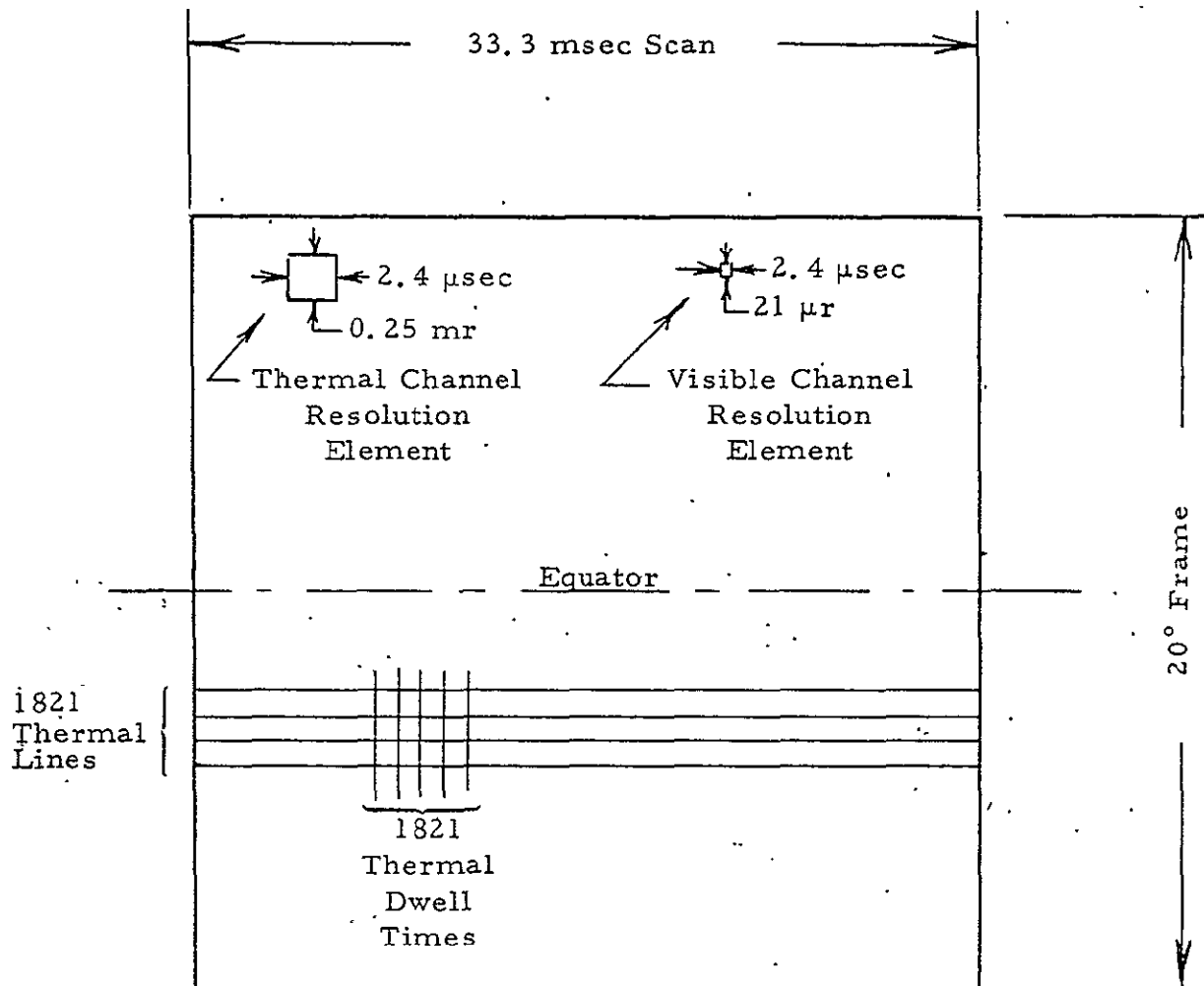


Figure 2-11. Perfectly Aligned Scan Frame

33.3 msec. For a perfectly aligned scan frame, an undistorted one-for-one correspondence will exist between each mosaic element in the scan frame facsimile and each element in the $20^\circ \times 20^\circ$ frame of the earth as seen from synchronous orbit.

As a result of 1) optical alignment errors in the VISSR, 2) axial misalignment between the VISSR and the SMS, and 3) misalignment between the SMS spin axis and the earth north-south center line, a certain amount of scan distortion is expected to exist in the VISSR data frame. The following is a summary of an analysis conducted to determine the type and magnitude of data frame distortion that is expected will exist due to optical alignment errors in the VISSR. Also presented is the type of scan distortion that will

result due to VISSR/SMS misalignment and misalignment between the SMS and the earth north-south center line.

Detector Element Mounting Misalignments

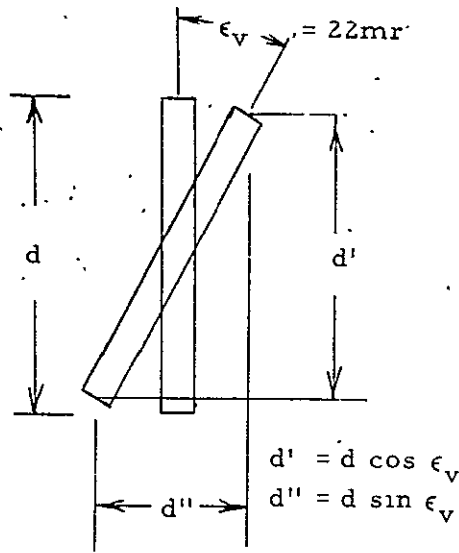
Figures 2-12 and 2-13 show distortions caused by mounting misalignment of the visible and thermal channel elements, respectively. The visible channel linear array is shown rotated about the reference axis through an angle, ϵ_v , which is estimated to be 22 mr.¹¹ The resulting distortion is 0.42 μ sec (1/6 of a dwell time) of time delay between the extreme elements of a single array. The small 0.3% underlap effect that results will tend to reduce (though only slightly) the nominal 20% overlap that exists between successive scans.

All VISSR alignment measurements will be referenced to the center of the visible channel array; therefore, no horizontal or vertical displacement errors will exist for the visible channel as such.

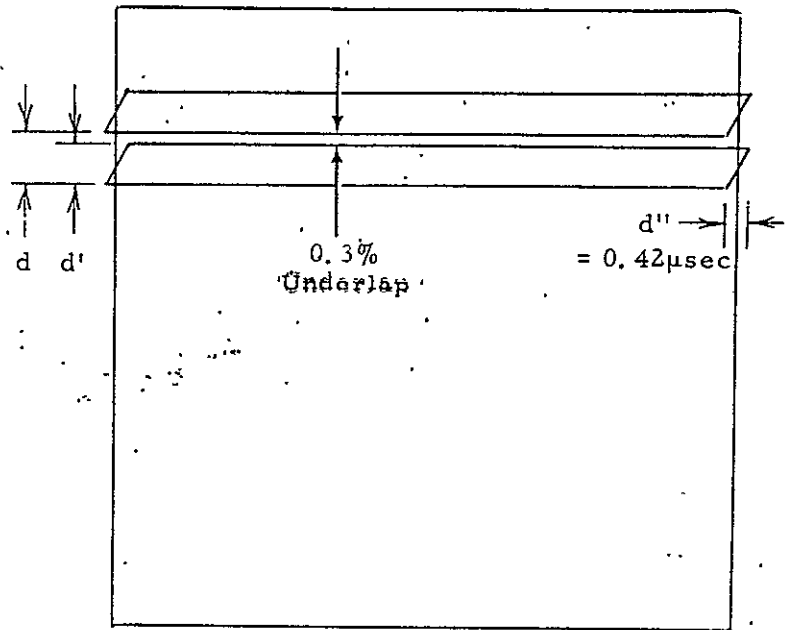
The thermal channel elements will be initially aligned with respect to the visible channel array (in the north-south direction) to within ± 0.050 mr. The subsequent shift in alignment due to environmental testing and/or the launch environment has not yet fully been determined. The relative shift in alignment measured on the engineering model VISSR following vibration and acceleration exposure was found to be approximately 0.2 mr in both the north-south and east-west alignment directions. Although the exact cause of the alignment shift was not determined, the pinning and bonding of all elements found to be possible suspects in causing the shift (during an investigation of the shift anomaly) was incorporated in the prototype VISSR design.

The diffraction effects in the thermal channel will tend to circularize the square FOV. For this reason, small rotational errors in the thermal channel detector alignment will have essentially no effect on data frame distortion.

¹¹ The value measured on the engineering model VISSR was 20 mr.

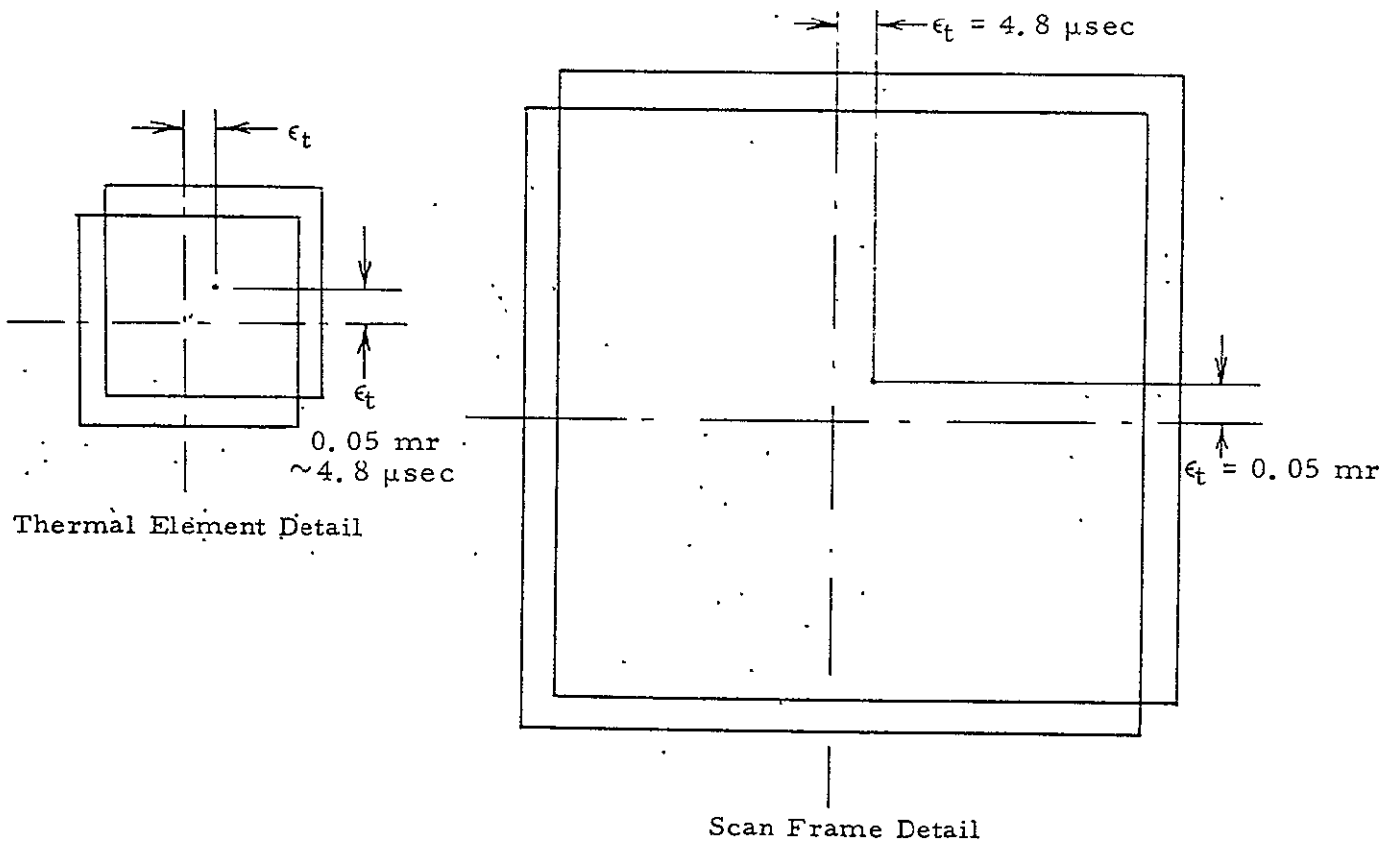


Visible Element (Array) Detail



Scan Frame Detail

Figure 2-12. Visible Channel Element Misalignment



Thermal Element Detail

Scan Frame Detail

Figure 2-13. Thermal Channel Element Misalignment

Step-Scan Axis Misalignment

Figure 2-14 depicts the distortion from angular misalignment of the scan mirror step-scan axis, ϵ_m . The resulting frame is skewed to the right or left depending on the direction of axis rotation. The value of ϵ_m is estimated to be 1.28 mr, hence the accumulated error over one complete frame is 43 μ sec or approximately two thermal dwell times out of 1821.

VISSR/SMS Misalignment

Figure 2-15 shows the type of data frame distortion that will result from a pitch - θ_p , yaw - θ_y , and a roll - θ_r misalignment between the VISSR optical axis and the SMS spin axis. The contribution to θ_p , θ_y , and θ_r due to measurement uncertainty in the VISSR alignment reference surface is expected to be 0.01 mr. The alignment uncertainty in mounting the VISSR to the SMS must be added to this value.

SMS Spin Axis Misalignment

If the SMS spin axis is misaligned in space (from the earth north-south center line) then the data frame will be distorted as shown in Figure 2-16. The effect of axis tilt about two mutually perpendicular axes, i and j, is shown in the figure. Part A shows a vertical displacement of the frame which is equal to just the angle of tilt about the j-axis. Part B shows how an angular displacement about the i-axis results in a corresponding angular rotation of the data frame. A data frame for which both angles of tilt are considered is shown in Part C.

Nutation of the SMS Spin Axis

Figure 2-17 shows the type of data frame distortion that will result when a nutation of the SMS spin axis exists and has a period which is less than the frame period.

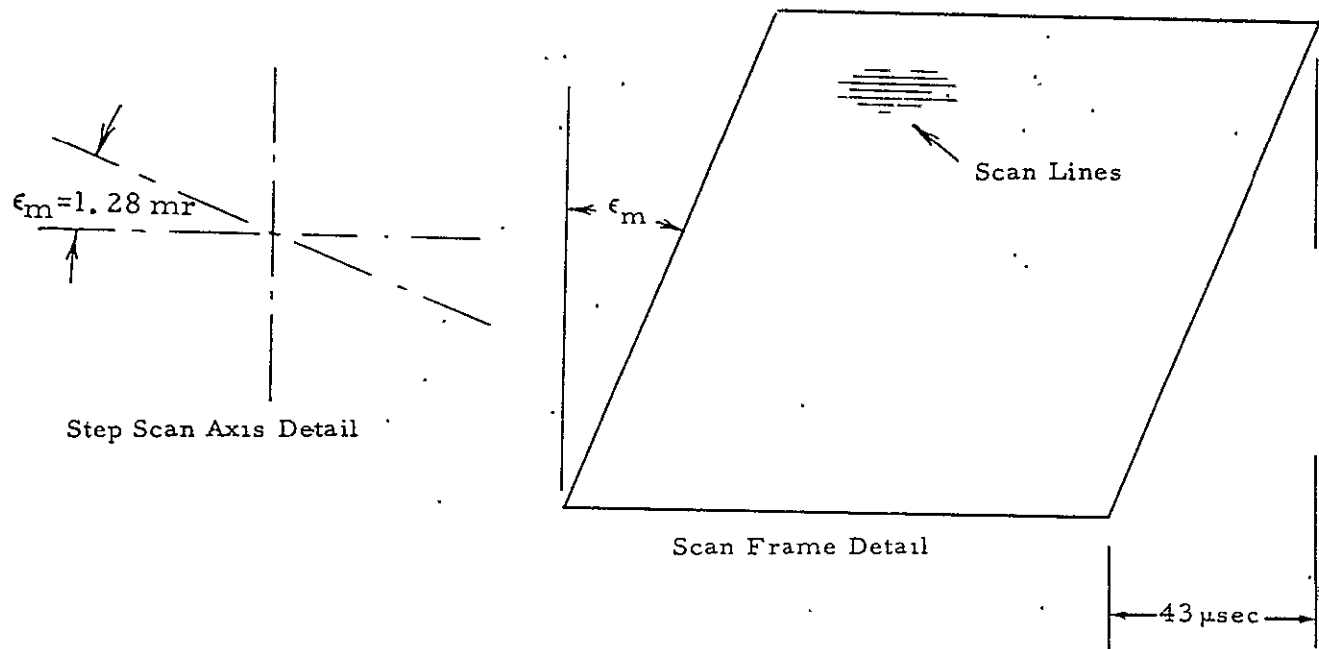
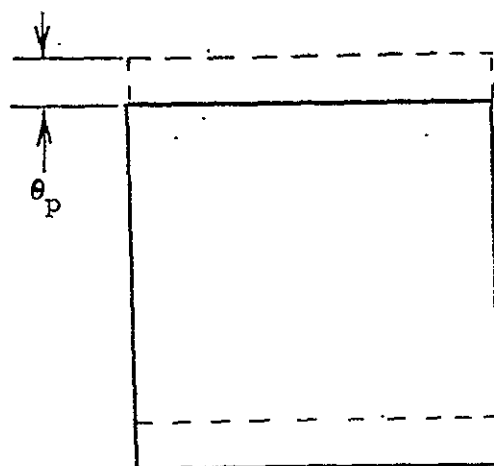
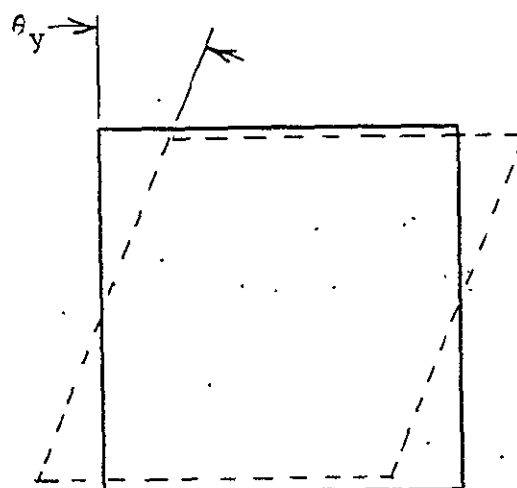


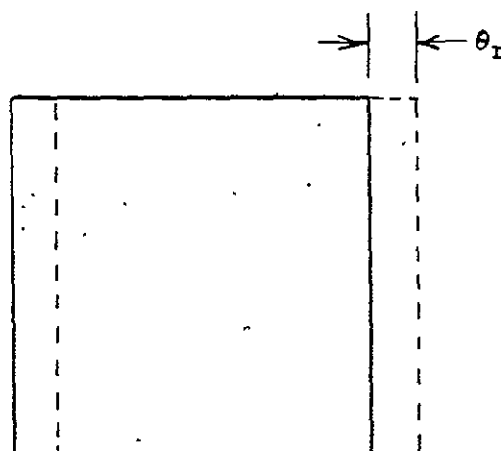
Figure 2-14. Latitude Step-Scan Axis Misalignment



Pitch Misalignment

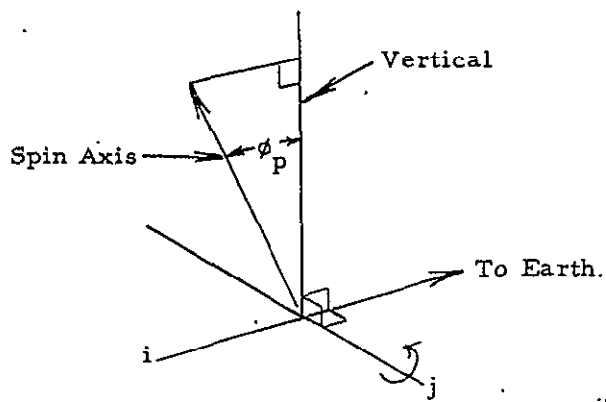


Yaw Misalignment

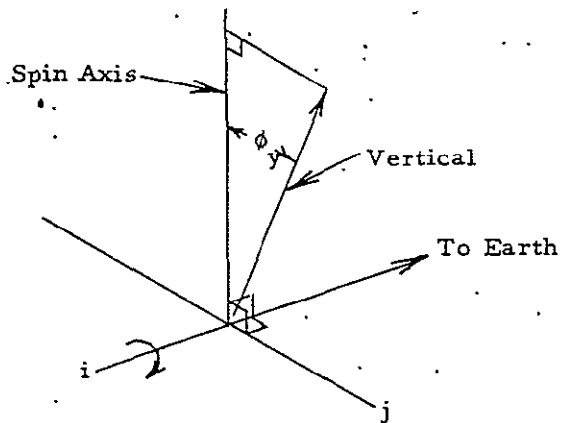
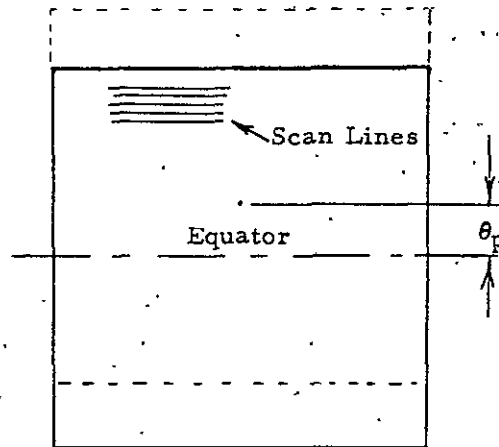


Roll Misalignment

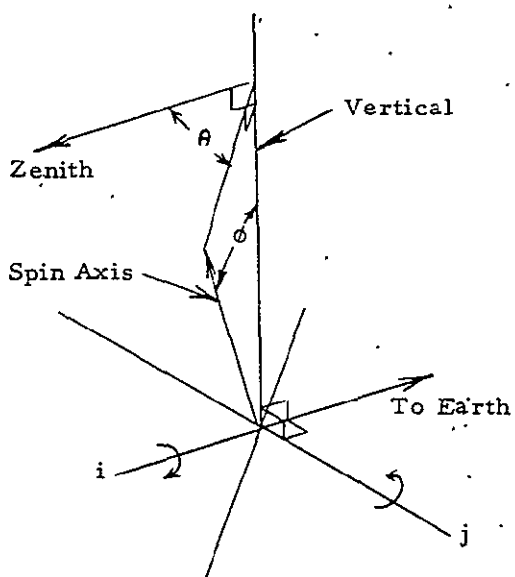
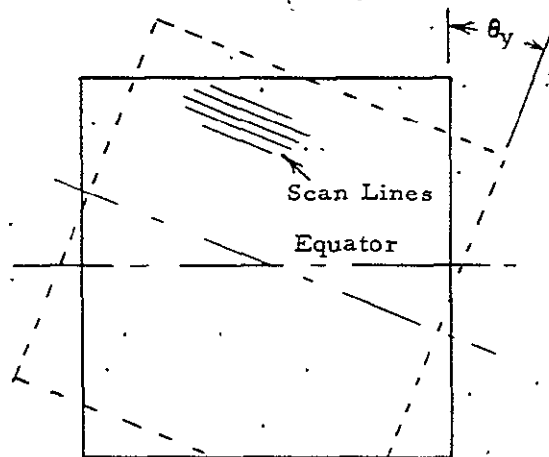
Figure 2-15. VISSR/SMS Misalignment



PART A



PART B



PART C

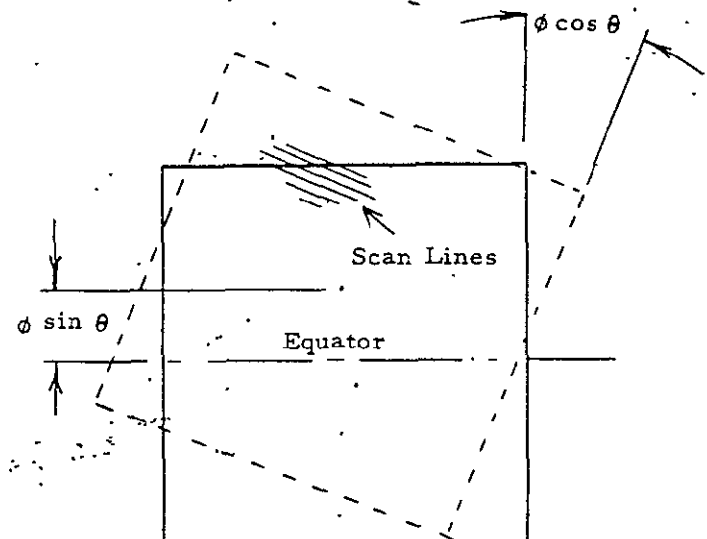


Figure 2-16. Spin Axis Misalignment

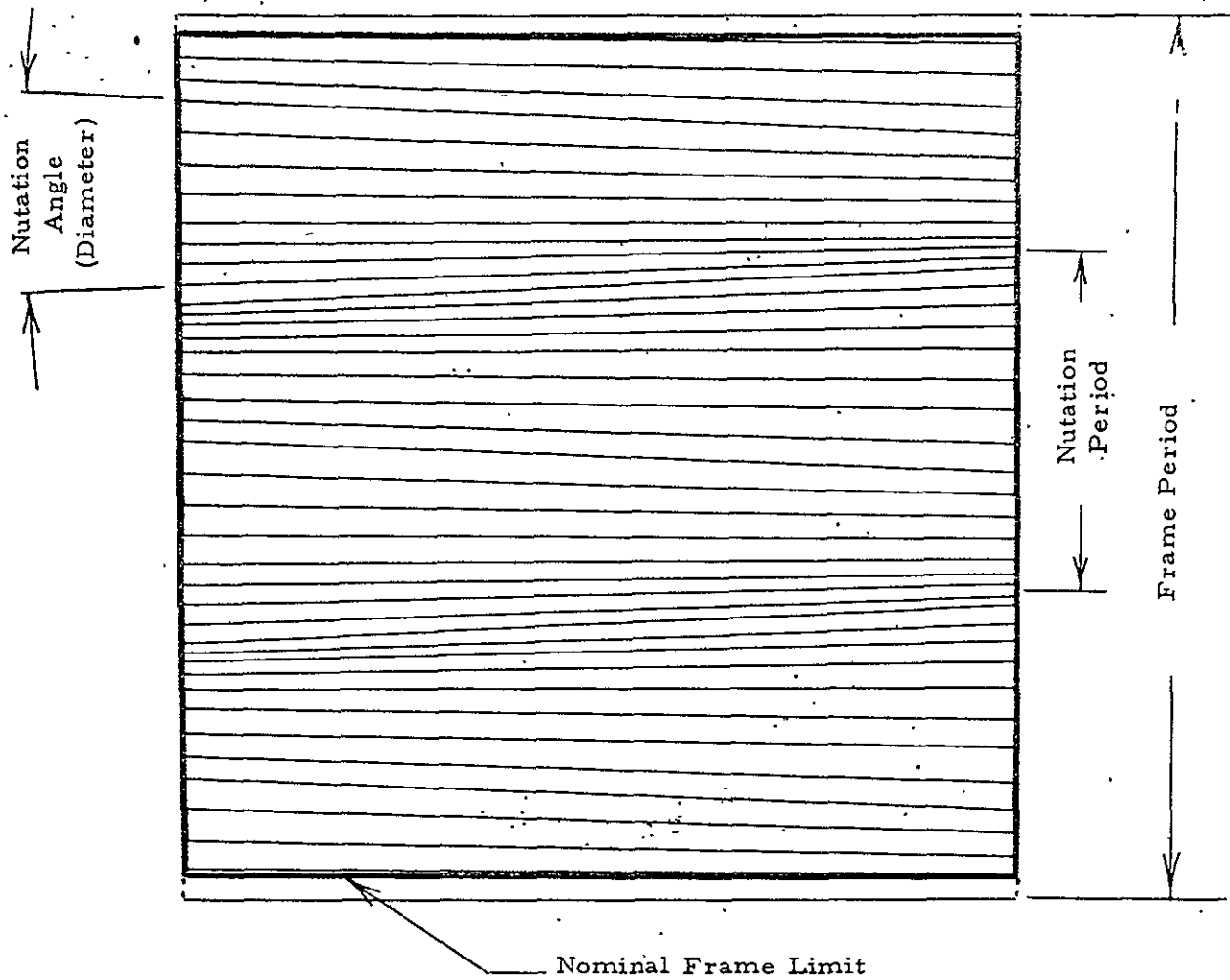


Figure 2-17. Data Frame with Nutation of the Spin Axis

VISSR/SMS ELECTRICAL INTERFACE CHARACTERISTICS

Appendix E contains information on VISSR/SMS electrical interface characteristics. All of the electrical interconnect functions between VISSR and SMS are listed. The tabulation is arranged by connector designation and includes detector type and number, and pin number assignment for each interface function. Source and load characteristics together with the appropriate ground reference designation is included for each interface function.

SCAN MIRROR STEP-SCAN OPERATION

The following is an updated description of the method of scan mirror step-scan operation used in the VISSR scanner. The description reflects the current VISSR design and includes detail descriptions of and/or requirements for the following:

1. The four modes of step-scan operation and how they are initiated.
2. Timing events and waveforms associated with the VISSR:
 - a. Scan mirror step timing signals
 - b. DC restoration timing signal
 - c. Inflight electronics and blackbody calibration.
3. Mechanical scan mirror travel limits and method of scan mirror stowage during launch.

Scan Mirror Drive - Primary Scan Drive

The purpose of the scan mirror drive is to rotate the scan mirror in steps of 0.09587 mr^{12} (19.775 arc seconds) to perform scanning and retrace motion in accordance with the VISSR step-scan mode commands. The four scan modes of operation are:

1. Single full-frame (20° , 1821 scan lines)
2. Variable frame height
3. Single-line frame height
4. Rapid forward scan stepping rate.

¹²This value is approximately 4% less than the desired nominal value of 0.1 mr; however, it permits a standard digital shaft encoder disc to be used for step-scan position control.

The scan mirror drive operates basically as a torque motor servo system. The register output of a 12-bit counter serves as the input signal to the servo loop with the output of a digital shaft angle position encoder (which is attached to the scan mirror) acting as the servo-loop feedback signal.¹³ A least significant bit of the shaft encoder output corresponds to 0.09587 mr. Therefore, each time the 12-bit counter is changed by one count, the scan mirror is rotated 0.09587 mr.¹⁴

Single Full-Frame. - In the single full-frame mode of operation of the primary scan drive (20° frame height), the 12-bit counter is advanced from -910⁽¹⁵⁾ counts to +910⁽¹⁵⁾ counts (forward scan direction), and then back to -910 counts (retrace) where the counter is stopped. In the forward scan direction, the counter register is advanced one count each spin cycle of the spacecraft. The timing signal initiating the one-count advance of the counter register is provided by the spacecraft and is timed to occur when the VISSR's IGFOV is pointing $35^\circ \pm 5^\circ$ from the north-south earth centerline and moving away from the earth (i. e., post-earth scan position). In the retrace (step-scan) operation, the counter is made to count back to -910 by a spacecraft-supplied timing signal (square wave) which has a repetition rate equal to 10.667 times the spacecraft spin rate. Therefore, the retrace time is approximately 0.1 of the forward frame time.

A block diagram of the primary scan mirror drive logic is shown in Figure 2-18. With the mirror positioned at scan line No. 1 (counter register

¹³ The encoder shaft angle position information is also supplied as a telemetry output and for use in scan line serialization by the spacecraft.

¹⁴ This results in a VISSR IGFOV rotation of 0.19174 mr (~0.2 mr) due to angle doubling.

¹⁵ -910 and +910 are the nominal encoder digital line numbers at the top and bottom of full frame. In actual practice, the top and bottom of frame encoder line numbers will be different and are selected such that the 45° position of the VISSR scan mirror will occur within one scan line of the center of the full frame.

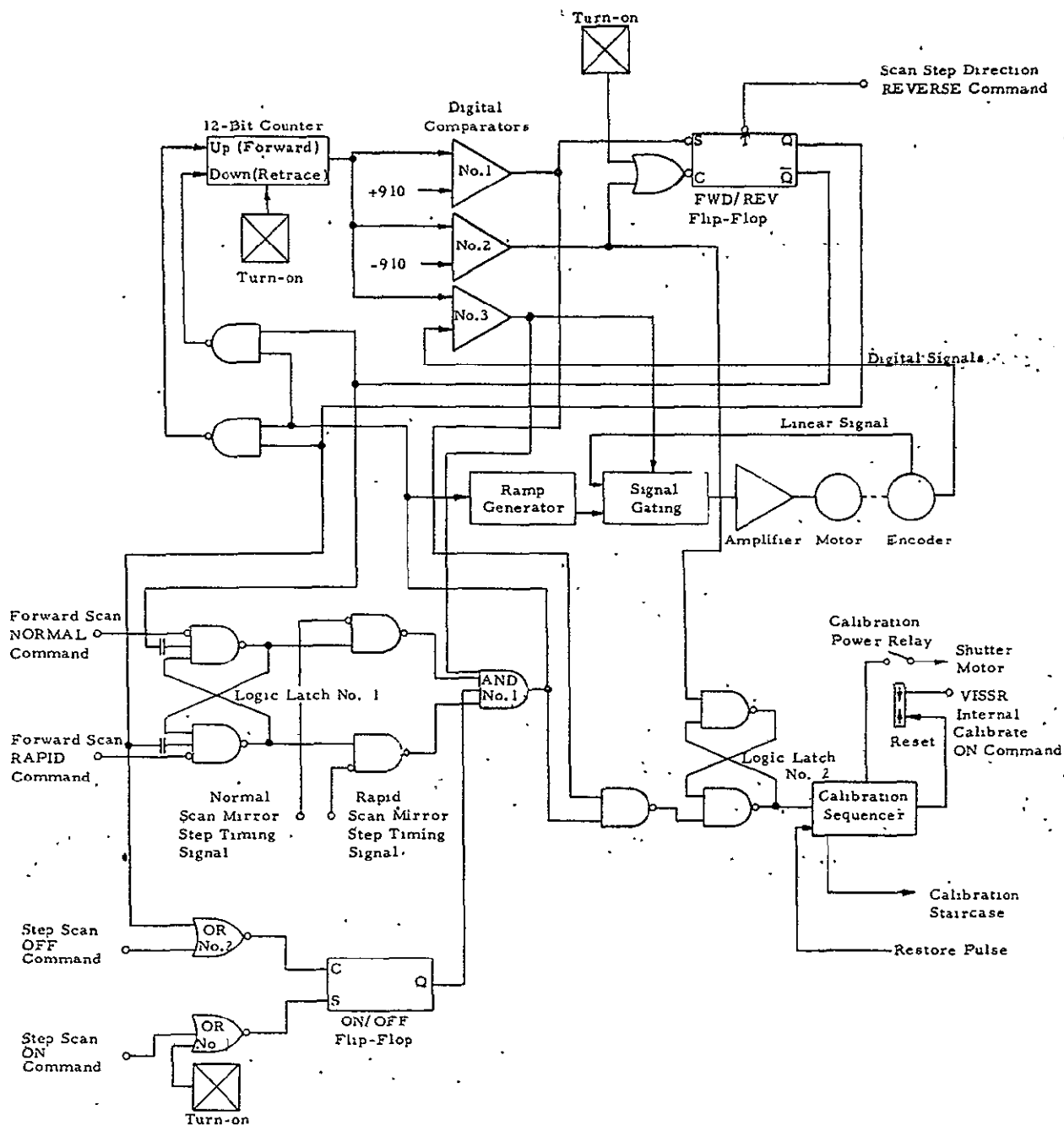


Figure 2-18. VISSR Scan Drive Logic Block Diagram

number -910), the full-frame mode of operation is initiated by setting ON/OFF Flip-Flop (OOFF) in the ON state. This is accomplished by issuing a Step-Scan ON Command to OR gate No. 1. With OOFF in the ON state, AND gate No. 1 is enabled permitting scan mirror step timing pulses to advance the 12-bit counter from -910 counts (scan line No. 1) to +910 counts (scan line No. 1821). When +910 counts is reached (or greater than +910 counts is indicated) Digital Comparator (DC) No. 1 sets the FWD/REV Flip-Flop (FRFF) so that the 12-bit counter counts back to -910 counts using the Rapid Scan Mirror Step Timing Signal. When -910 counts is reached (or less than -910 counts is indicated), DC No. 2 sets FRFF so that OOFF is set in the OFF state. With OOFF in the OFF state AND gate No. 1 is disabled and the scan mirror step timing signals are prevented from reaching the 12-bit counter, therefore leaving the counter at -910 counts (scan line No. 1).

Variable Frame Height. - In addition to the single full-frame step-scan mode of operation, the scan mirror can be operated in a variable frame height mode. At any time during the forward or retrace scan-step motion, the state of the FWD/REV Flip-Flop (see Figure 2-18) can be reversed by execution of a mirror Scan Step Direction REVERSE Command, thereby reversing the mirror step-scan direction. The scan mirror will continue stepping in the reversed direction (at the stepping frequency associated with that direction) until either another REVERSE command is received, or until the 12-bit counter reaches either -910 or +910 counts. When +910 counts (scan line No. 1821) is reached, the scan direction is reversed. When -910 counts (scan line No. 1) is reached, the stop scan motion is stopped. Therefore, by use of the REVERSE command, programming of a variable frame height can be accomplished from the ground. The size of the frame and its location (within the nominal 20° frame limits) is determined by the timing sequence established for the execution of the REVERSE commands.

At the completion of the variable height mode of operation, the remaining part of the full frame will be scanned and the scan mirror returned to scan line No. 1.

Single-Line Frame Height. - The scan mirror drive can be placed in a single-line frame-height mode by interrupting the scan mirror step timing signals from the spacecraft. This is accomplished by issuing a Step Scan OFF Command to OR gate No. 2 (see Figure 2-18) which in turn places ON/OFF Flip-Flop (OOFF) in the OFF state. With OOFF in the OFF state, AND gate No. 1 is disabled, thus preventing scan mirror step timing signals from reaching and advancing the 12-bit counter. Therefore, the same elevation line will be repeatedly scanned each spin cycle of the spacecraft. The scan mirror drive can be placed in the single-line frame-height mode when the scan mirror drive is stepping in either the forward or retrace direction.

Step scan motion is reinitiated by issuing a Step Scan ON Command to OR gate No. 1 which in turn places OOFF in the ON state. With OOFF in the ON state, AND gate No. 1 is enabled and scan mirror step timing signals are permitted to reach the 12-bit counter.

Rapid Forward Scan. - When scanning in the forward direction, the scan mirror step-scan drive can be made to advance at a rate equal to the retrace rate (10.067 times the normal stepping rate). This is accomplished by issuing a Forward Scan RAPID Command to Logic Latch No. 1 (see Figure 2-18) which in turn permits Rapid Scan Mirror Step timing signals to reach the 12-bit counter through AND gate No. 1. The forward step-scan can be returned to a normal rate by issuing a Forward Scan NORMAL Command to Logic Latch No. 1.

Turn-On Initialization. - Turn-on initialization circuits are included in the VISSR scan logic design to assure that the scan drive logic will always come on in a known state at power turn-on. At power turn-on, the VISSR scan drive circuitry will be in the following logic states.

1. The 12-bit counter will be set at 000 counts.
2. Step-scan logic will be in the ON mode.
3. The FWD/REV Flip-Flop will be set to allow rapid scan mirror step timing signals to advance the 12-bit counter in the positive direction.

Under these initializing conditions and the scan mirror position (digital encoder output) not at line 000, the scan mirror will be slewed (at approximately 20 times the normal stepping rate) to position 000. It should be noted (see Figure 2-18) that until the scan mirror arrives at position 000, no step timing signals are permitted to reach (and advance) the 12-bit counter since Digital Comparator No. 3 will not be TRUE and therefore AND gate No. 1 is disabled. When scan mirror position 000 is reached, AND gate No. 1 is enabled and rapid step timing signals are permitted to advance the 12-bit counter in the positive direction (forward direction for the primary scan drive). When the bottom of the frame is reached, the normal retrace motion (to the top of the frame) is initiated.

Scan Mirror Drive - Redundant Scan Drive

The operation of the redundant scan drive is the same as the primary scan drive described with the following exceptions:

1. All of the redundant scan drive "line number polarity" logic is reversed (from the primary scan drive) to appropriately account for the fact that the redundant encoder (nominal) digital line number at the top of a VISSR frame is +910 and the (nominal) digital line number at the bottom of the frame is -910.
2. Following slewing of the VISSR scan mirror to encoder digital line number 000 after turn-on (i. e., initialization), the scan mirror is stepped in increasing (positive) encoder digital line numbers (at 10.667 times the spacecraft spin rate) directly to the top of the full frame where the stepping motion is then stopped.

Timing Events and Waveforms

Scan Mirror Step. - As indicated in the above description of the scan mirror drive operation, the step-scan motion of the scan mirror is initiated by two scan mirror step-timing signals supplied from the spacecraft. These are the Normal Scan Mirror Step timing signal and the Rapid Scan Mirror Step timing signal. The Normal Scan Mirror Step timing signal is required to occur $35^{\circ} \pm 5^{\circ}$ after the VISSR IGFOV has passed the north-south earth centerline. The required amplitude and temporal characteristics of this signal are:

1. Amplitude 4.3 ± 0.75 vdc
2. Duration 1.7 ± 0.8 msec
3. Rise Time ≤ 0.1 msec

The Rapid Scan Mirror Step timing signal is required to be a 4.3 ± 0.75 volt square wave having a frequency equal to 10.667 times the spacecraft spin rate.

DC Restoration. - DC restoration¹⁶ of the VISSR's thermal channel(s) is timed to occur each spin cycle of the spacecraft just prior to the time the VISSR's IGFOV scans the earth. The period of dc restoration is 28.5 ± 1.5 msec.

DC restoration is initiated by the dc restore timing signal supplied by the spacecraft. The dc restore signal is required to occur once each spin cycle of the spacecraft when the VISSR's IFOV is located at the following angular positions:

1. $30^\circ \pm 1^\circ$ prior to the north-south earth centerline, except when the sun is located in an angular sector defined by lines-of-sight, as viewed from the spacecraft, which are 5° and 32° forward of the north-south earth centerline.
2. $56^\circ \pm 1^\circ$ prior to the north-south earth centerline whenever the sun is located in the 5° to 32° angular sector.

The required amplitude and temporal characteristics of the dc restore timing signal are the same as those required for the Normal Scan Mirror Step timing signal.

Inflight Electronics and Blackbody Calibration. - During the first and fourth scan lines following the start of each single full-frame scan, the channel electronics of the VISSR's visible and thermal channels are calibrated.

The electronic calibration event consists of a repetitive calibration signal. The format for each calibration signal (referenced to the channel output) is a 0- to 5-volt dc staircase increasing 1.0 ± 0.02 volt/step. The width of

¹⁶ Zeroing of the channel output when space is viewed.

each step is 1.5 msec. Therefore, a total of 16 calibration staircases occurs during the nominal 144-msec electronic calibration period.

From reliability considerations, a decision was made to provide for a disconnect capability of the VISSR staircase signal by command. This is accomplished without the addition of additional commands by utilizing the thermal channel focus Forward and Reverse Commands. A Thermal Channel Fwd Command will also disconnect the staircase circuitry from the VISSR preamplifiers and a Thermal Channel Rev Command will reconnect the staircase circuitry to the VISSR preamplifiers.

A thermal (radiation) check-of-calibration can be performed on the VISSR thermal channels by ground command. This is accomplished by placing an opaque ambient temperature blackbody shutter (whose temperature is monitored) in the optical train of the VISSR thermal channels ahead of the thermal channel relay optics. The shutter is programmed to move into the calibration position during the third scan line following the start of a single full-frame scan, provided a VISSR Internal Calibrate ON Command has been executed prior to the start of the full-frame scan. Unlike the electronic calibration which automatically occurs on the first and fourth scan lines of each full-frame scan,¹⁷ the thermal channel radiative check-of-calibration requires that a VISSR Internal Calibrate ON Command be executed each time a calibration is desired.

The start of the electronic and blackbody calibration events is programmed to occur at the end of the dc restoration period and timed to last for 144 msec. Therefore, the calibration events occur during the earth data scan period (20°) and for a minimum angle of 20° following the earth data scan period.

In the execution of the internal radiometric check-of-calibration event, the maximum time required to place the blackbody calibration shutter into the optical path of the thermal channel (following the end of dc restoration) is 30 msec.

¹⁷ Provided the last thermal channel focus command sent was a Reverse Command.

Timing and Waveform Summary. - The timing events and waveforms associated with the VISSR step-scan operation and internal calibration are diagrammatically summarized in Figure 2-19.

Mechanical Scan Limits

Mechanical scan limits are incorporated in the scan mirror drive assembly to assure that over the restricted angular travel limits of the scan mirror, one, and only one, angular position exists for every 12-bit word output from the digital shaft encoder. This arrangement permits the use of a 12-bit (rather than higher order) counter, since unambiguous angular read-out over 360° with a 19.775 arc-second resolution requires a 16-bit word.

The mechanical scan limits are set at $2-1/2^\circ \pm 1/2^\circ$ beyond the nominal 10° scan mirror travel range required to produce the 20° frame height. The mechanical scan limiting is physically accomplished by restricting the travel range of the scan mirror inertia balance arms by the use of mechanical stops.

Launch Mode Stowage. - During launch, the scan mirror is stowed against the mechanical scan limit which restricts the scan mirror in its farthest "down" direction of travel. The scan mirror is driven to this position whenever all of the following conditions are met:

1. +29 volt spacecraft power is supplied to the VISSR.
2. The VISSR primary and redundant power supplies have been commanded OFF.
3. The Scan Mirror LATCH Command has been executed.

When the VISSR primary power supply is in the OFF position and the Scan Mirror LATCH Command has been executed, a fraction of the +29 volt spacecraft power is applied directly to the coils of the primary scan drive motor causing the motor to drive the scan mirror, in an open-loop mode, in the "down" direction into the mechanical scan limit.

It is necessary that the VISSR redundant power supply be placed in the OFF position to assure that the scan mirror stow drive is not opposed by the normal scan mirror operation (which would nominally "overpower" the stow

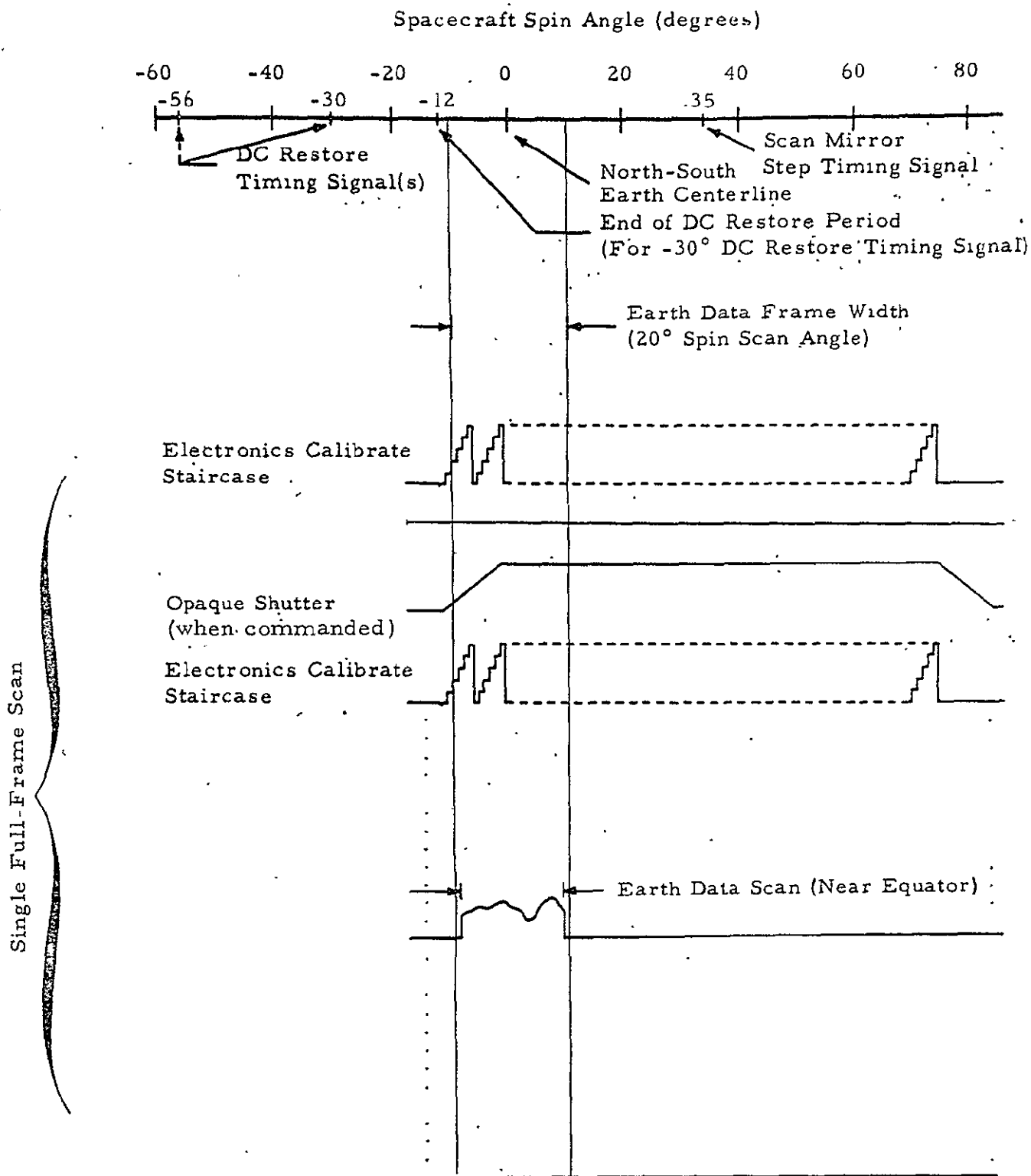


Figure 2-19. Summary of Timing Events and Waveform

drive). During the actual launch, it is assumed that both the VISSR primary and redundant power supplies will be in the OFF position.

The maximum torque available from the torque motor that could be used to hold the scan mirror against the mechanical limits is approximately 40 in.-oz. However, the torque required to hold the scan mirror against the mechanical limits under worst-case conditions during launch was calculated to be 150 in.-oz. Therefore, an additional holding force is required during launch. This is accomplished by the use of an active magnetic latch which can supply a large holding force for a small power input once the magnetic latch pole pieces are brought into close proximity. The magnetic latch pole pieces are located on the "down" mechanical stops and the scan mirror inertia balance arms. The magnetic latch is activated by placing the VISSR scan mirror Stow command relay in the LATCH position.

Torque motor power is interrupted when the scan mirror is in the stow position to minimize the power required by the radiometer during launch. A microswitch located near the end of the open-loop scan mirror travel accomplishes this purpose. The microswitch is located so that it is depressed (removing torque motor power) only after the magnetic latch pole-pieces are close enough to pull the scan mirror into its final stow position. This arrangement also assures that the scan mirror will always be returned to its stow position during launch in case a momentary interruption of the electrical power to the magnetic latch should occur simultaneously with the generation of a torque moment on the scan mirror (due to motion of the spacecraft), which moves the scan mirror from its stow position.

VISSR INFLIGHT SUN CALIBRATION PERIODS

During the normal operation of the VISSR/SMS system, VISSR video data will be limited to those signals generated during the 20° spin angle time period which is centered with respect to the north-south axis of the earth (when wide-band transmission from the spacecraft is programmed to occur). For this reason, a radiometric check-of-calibration of the VISSR's visible and thermal channels against the sun can only be accomplished during certain time periods of the day.

In addition, since the north-south limits of the relative sun position to the earth exceeds the 20° north-south full-frame of the VISSR, a check-of-calibration of the VISSR's thermal channels will, in addition, also be limited to certain times of the year.

Figure 2-20 summarizes the time periods during which a VISSR radiometric check-of-calibration against the sun can be performed.

The calibration time period limits in the "east-west" direction are in time-of-day. The time period limits in the north-south direction are in day-of-year.

For the thermal channel calibration, proper timing of the start of a frame will be required to assure that the sun is scanned when it is located in the time area shown.

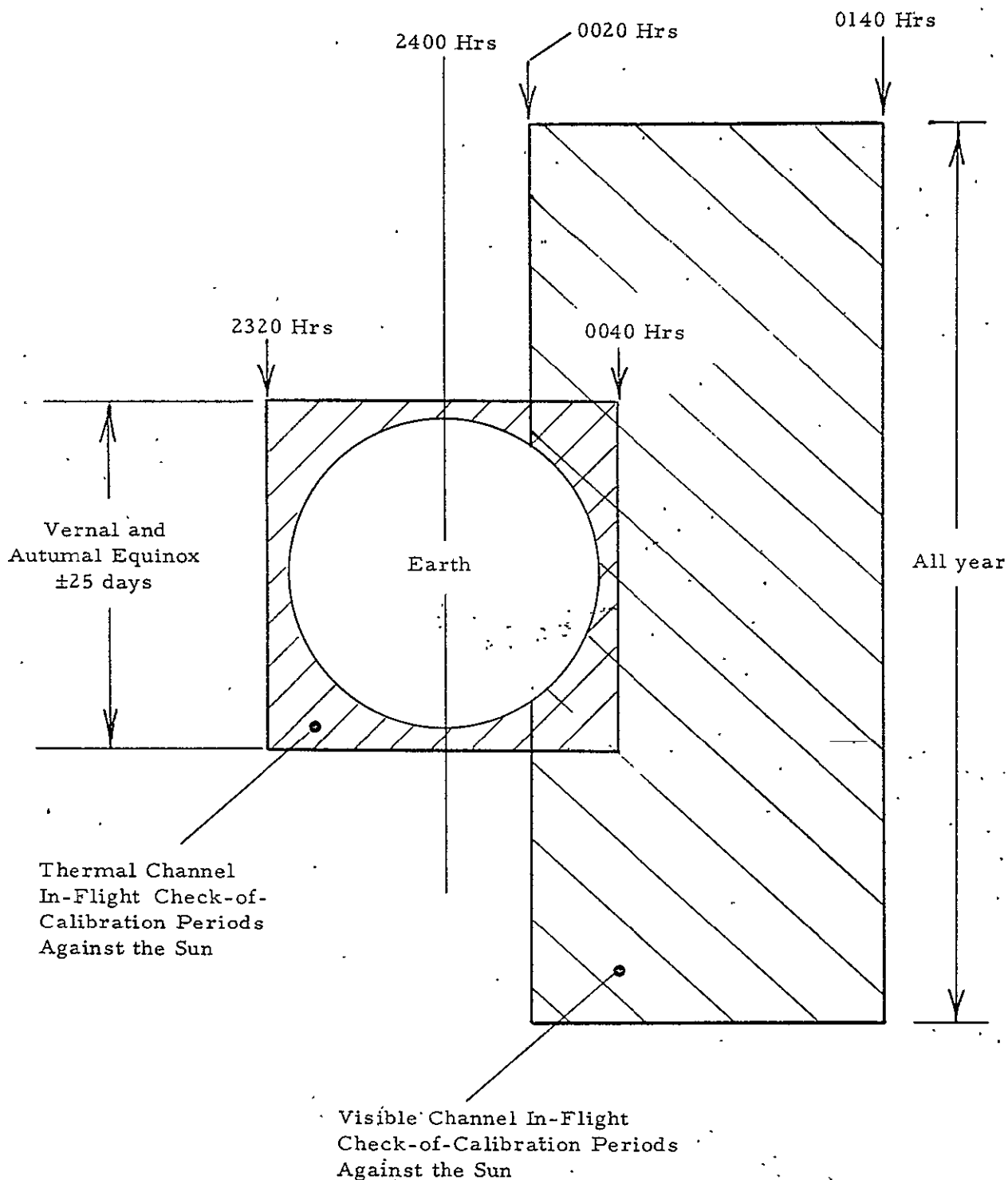


Figure 2-20. Time Periods During Which a VISSR Radiometric Check-of-Calibration Against the Sun Can Be Performed

THERMAL ANALYSIS

VISSR Scanner Thermal Model

A 72-node thermal model was formulated for the VISSR scanner and the thermal model nodal parameters sent to Philco-Ford to determine the VISSR/SMS interface coupling required to achieve acceptable VISSR operating temperatures.

The distribution of the thermal model nodes for the VISSR thermal model is shown in Figure 2-21. A description of the nodes shown is presented in Table 2-1.

The values of the VISSR scanner thermal model nodal parameters (conductive and radiative coupling plus solar and electrical power input) are presented in Appendix G.

Previous Thermal Evaluation of Isolated Scanner

An evaluation of a preliminary VISSR scanner thermal model was made during the preliminary design phase of the VISSR program (1969). For the evaluation it was assumed that the VISSR was thermally isolated from the spacecraft (radiatively and conductively) and that the primary coupling between the VISSR and the sun and space was through the VISSR optical aperture. A small amount of coupling (to the sun and space) by the inner surface of the radiation cooler sunshield was also assumed.

As might be expected under these boundary conditions¹⁸ plus electrical power being dissipated in the scanner [primarily the encoder(s) and the visible channel integrated PMTs], the average scanner temperature was found to be warmer than desired. At that time it was recommended that a heat leak to space be provided for the VISSR through the top and bottom of the spacecraft [to balance the electrical power being dissipated in the VISSR encoder(s) and integrated PMTs, respectively] to obtain the desired nominal VISSR operating temperature.

¹⁸ Basically the conditions which would result in an average scanner temperature of approximately 25°C if no additional power were supplied to the VISSR.

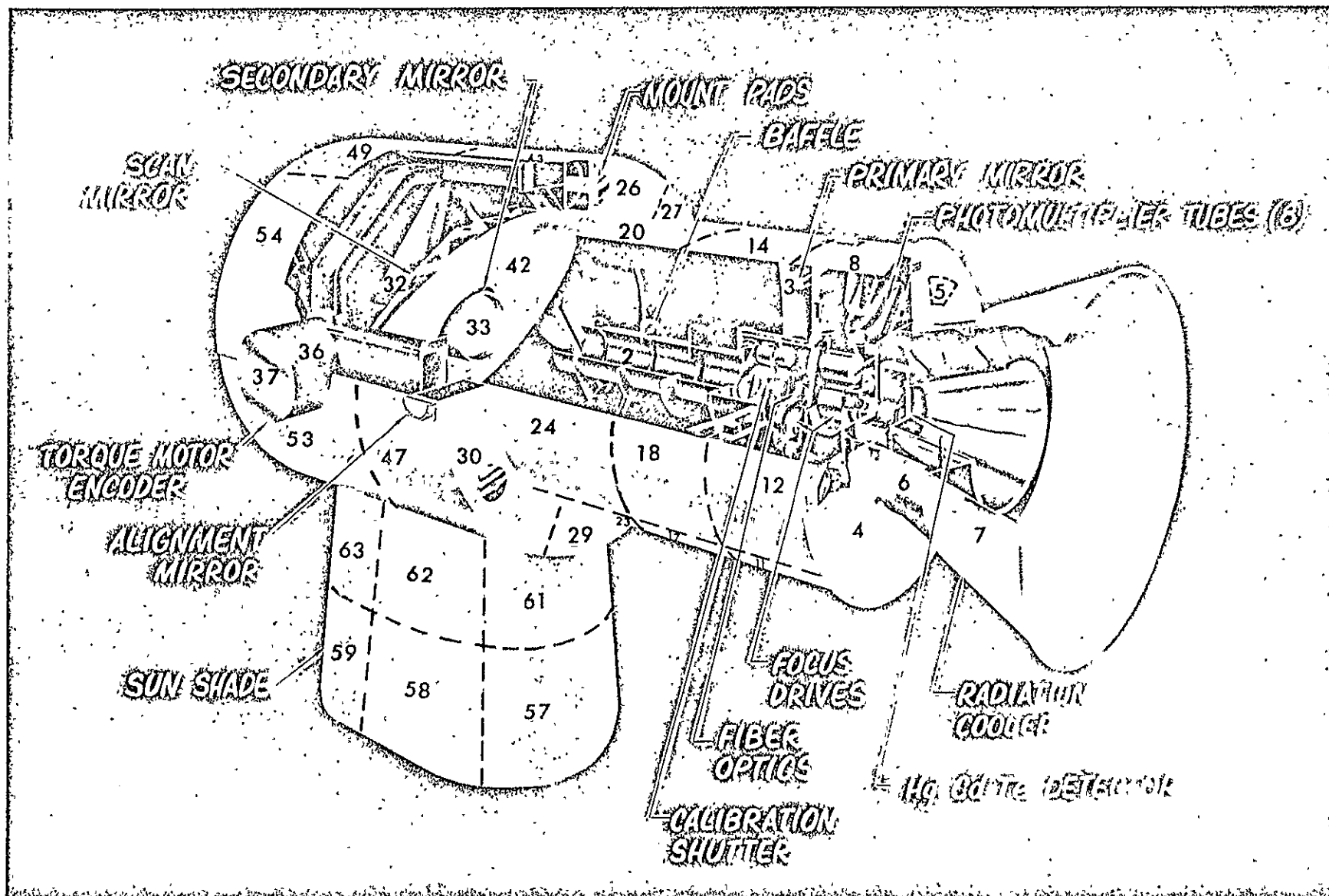


Figure 2-21. Thermal Nodal Model

Table 2-1. Thermal Model Nodal Description

Node	Description
1	The photomultiplier mounting plate. It contains the visible channel preamplifiers, the baffle mount, calibration shutter focus drives, and relay optics. The node is annular, 1/3 of the distance between the inner and outer radius.
2	The primary mirror baffle. It guards against stray radiation falling upon the image plane. The nodal point is at the half length point.
3	The primary mirror. The node is annular, half-way between the inner and outer radius.
4	The radiation cooler mounting plate. It is the annular ring with a slight bevel. This plate attaches to the Be tube and to the radiation cooler. The node is half-way between the inner and outer radius.
5	The infrared preamplifier. It is located on the plate described as node 4.
6	The housing of the radiation cooler. The node is located half-way up the housing, and has annular symmetry.
7	The sun shield of the radiation cooler. The node is located half-way up the housing. The node is annular.
8 to 13	These nodes are on the Be tube, centered between the primary mirror mount and the photomultiplier tube plate. The nodes increase in number every 60° in a CW direction as viewed from the radiation cooler end. Node 8 is on the top on the side opposite from the sunshade.
14 to 19	These nodes are analogous to 8 through 13. They are located 3/4 of the distance between the PM mounting plate and the radiometer mounting ring.
26 to 31	These nodes are on the mounting ring for the radiometer. Nodes 26, 28, and 30 coincide with the three mounting pads, and include 60 angular degrees of the ring. The intervening 60° sectors are devoted to nodes 27, 29, and 31.
32	This node is located at the junction of the four scan mirror braces. The mount for the secondary mirror is also attached at this point.
33	The secondary mirror. The shield around the mirror and the adjusting structure are defined by separate nodes.

Table 2-1 (Con't)

Node	Description
34	The rotor of the right encoder-scan motor. This encoder does not have the spacing diaphragm. It is on the right hand side when viewing into the radiometer entrance with the radiation cooler downward.
35	The stator of the same encoder-motor.
36	The side of the encoder can. It protrudes beyond the scan mirror cover forms this node.
37	The end of the encoder can. This end views the spacecraft.
38 to 41	These nodes are analogous to nodes 34 to 37, but pertain to the left encoder.
42	The scan mirror. The node has annular symmetry and is located at the mounting holes.
43 to 48	These nodes are located on the scan mirror cover in an analogous fashion to nodes 8 through 13. These nodes are located 1/4 of the distance from the mounting ring to the cover plate for the scan cavity. Node 46 is largely cut away for the entrance aperture.
49 to 54	Similar to nodes 43 to 48, but they are located 3/4 of the distance between the mounting ring and the scan cavity mounting plate.
55	The end plate of the scan mirror cavity cover. The node is annular at the half radius point.
56 to 63	These eight nodes are on the sunshade. Looking into the radiometer with the radiometer oriented such that the radiation cooler is on the bottom, node 56 is the left side flat portion of the first half of the shade, 57 is the bottom curved portion, 58 is the right flat, and 59 is the top curved portion. Similarly, nodes 60, 61, 62, and 63 are on the second (inner) half of the shade. The two halves are divided on the basis of shade length.
64	The cylindrical shield for the secondary mirror. This shield is viewed when looking into the entrance aperture, and protects the mirror from direct rays. This shield also provides a radiation shield for the mirror.
65	Circular plate. This holds the secondary mirror alignment adjusting structure. This plate connects via structure to node 32.
66	Y-shaped mount. This holds the secondary mirror.

Table 2-1 (Con't)

Node	Description
67 to 69	Nodes 26, 28, and 30 mount to the spacecraft. Nodes 67 to 69 mate with the above nodes, and thus form boundary nodes when the radiometer is considered by itself. When the radiometer is considered as part of the complete SMS system, these nodes are part of the spacecraft.
70	This is a boundary node similar to nodes 67 to 69 when the radiometer is considered by itself. In the complete system, this is the inner walls of the solar array panels.
71	This node is space, and forms a cold radiation source.
72	This node is the sun. A fixed angular view is used for the sun which necessitates using a "solar equivalent temperature."

When it subsequently became known that the spacecraft design would preclude the use of a heat leak from the VISSR encoders to space through the top (+Z axis) of the spacecraft, it was decided that the encoders should be radiatively coupled to the inner walls of the spacecraft solar panels as a means of keeping the temperature of the powered VISSR encoder within acceptable limits.

A thermal control surface (radiation patch with proper α/ϵ characteristic and size) would be used as a heat leak to space through the bottom of the spacecraft (-Z axis) to optimize the VISSR scanner temperature. The radiation patch would also serve to help the radiation cooler shield run cold which is desirable from cooler operation considerations.

Present Thermal Evaluation of "Isolated" Scanner

The present VISSR scanner nodal model was evaluated by SBRC using the following boundary conditions:

1. The scanner was isolated from the spacecraft except for radiation coupling between the VISSR encoders and the inner walls of the spacecraft solar panels which were assumed to be at a temperature of 10°C (based on discussions with Philco-Ford).

2. A thermal control surface (several sizes) was placed on the outside surface of the radiation cooler shield (a cylindrical band at the top edge of the shield having an $\alpha = 0.2$ and an $\epsilon = 0.9$).

The results of this evaluation are summarized in Figures 2-22 through 2-25 which show the steady state VISSR scanner nodal temperatures for different sun angle positions and thermal control surface sizes:

Figure 2-22 shows the nodal temperatures for summer and winter solstice when no heat leak (thermal control surface) is used:

It can be seen from Figure 2-22 that during the summer solstice, the following temperature conditions exist.

1. The radiation cooler sunshield will run significantly hotter than desired.
2. The primary mirror temperature will tend to run hot.
3. A significant temperature gradient exists between the primary and secondary mirrors.
4. Although the powered encoder runs slightly warmer than desired, the radiative coupling to the spacecraft appears to be adequate to keep the encoder within acceptable temperature limits.

Figure 2-23 shows that a significant improvement in average scanner temperature, scanner temperature gradients and summer solstice radiation cooler temperature can be achieved by using a thermal control surface having a band height of 0.6 inch.

Figure 2-24 shows the scanner nodal temperatures for the thermal control surface band height of 0.6 inch and sun angles of $\pm 10^\circ$.

The sensitivity of scanner temperature to control surface area can be seen by comparing Figure 2-25, which shows the scanner nodal temperatures at summer and winter solstice for a thermal control surface band height of 1.2 inches, with Figure 2-23.

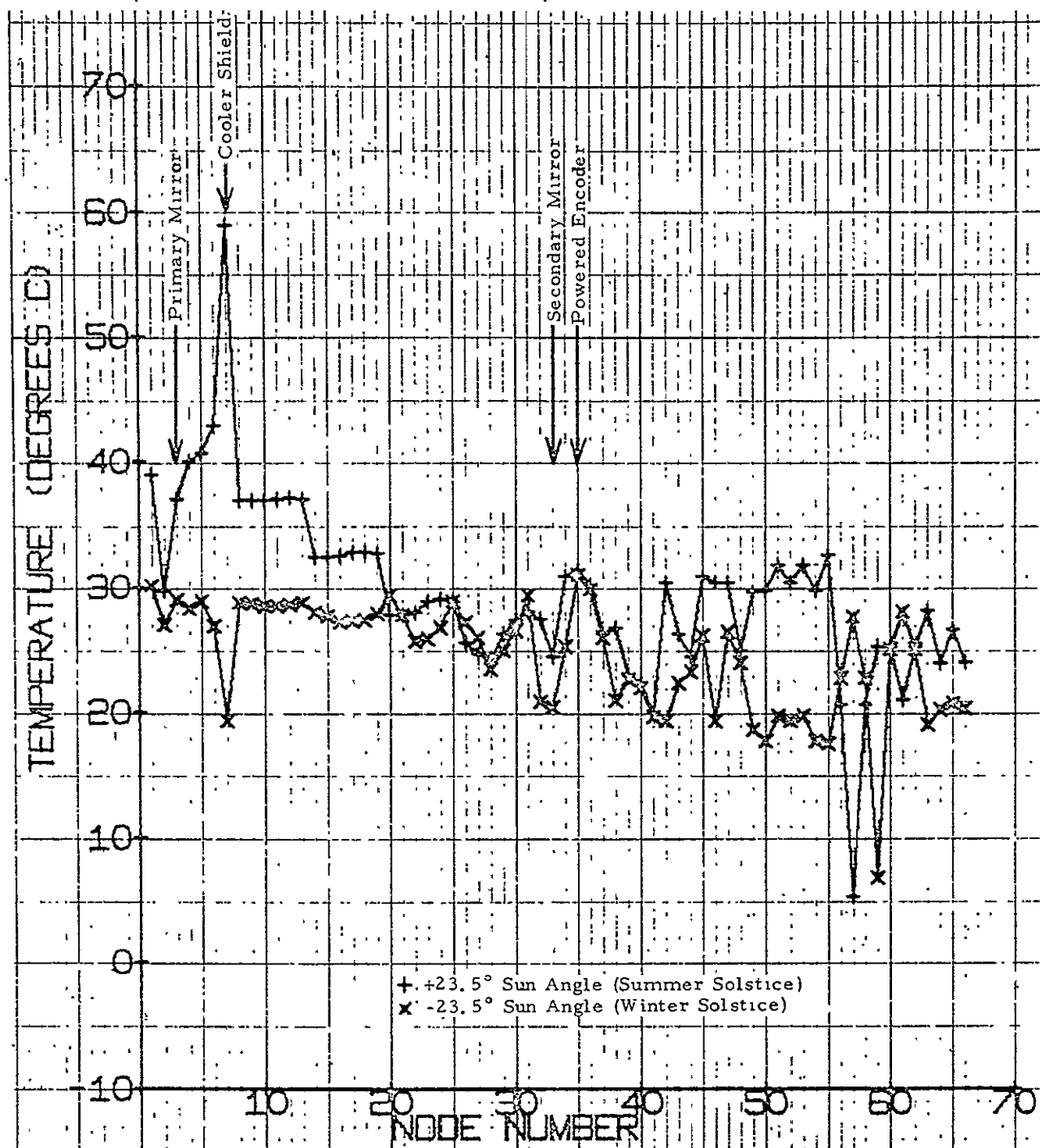


Figure 2-22. VISSR Scanner Nodel Temperatures No Thermal Control Surface, $\pm 23.5^\circ$ Sun Angle

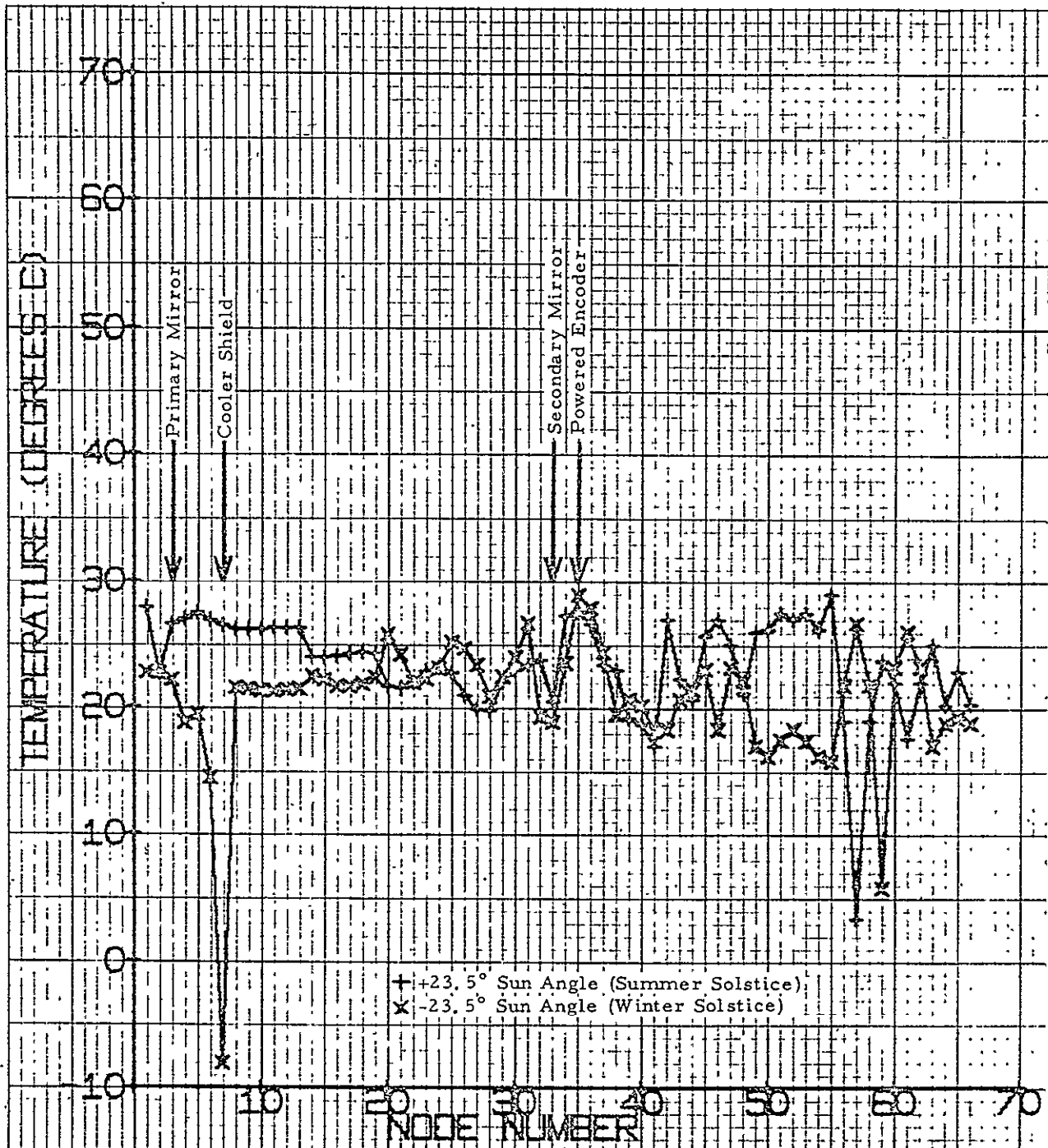


Figure 2-23, VISSR Scanner Nodel Temperatures Thermal Control Surface
Band Height = 0.6 in., $\pm 23.5^\circ$ Sun Angle.

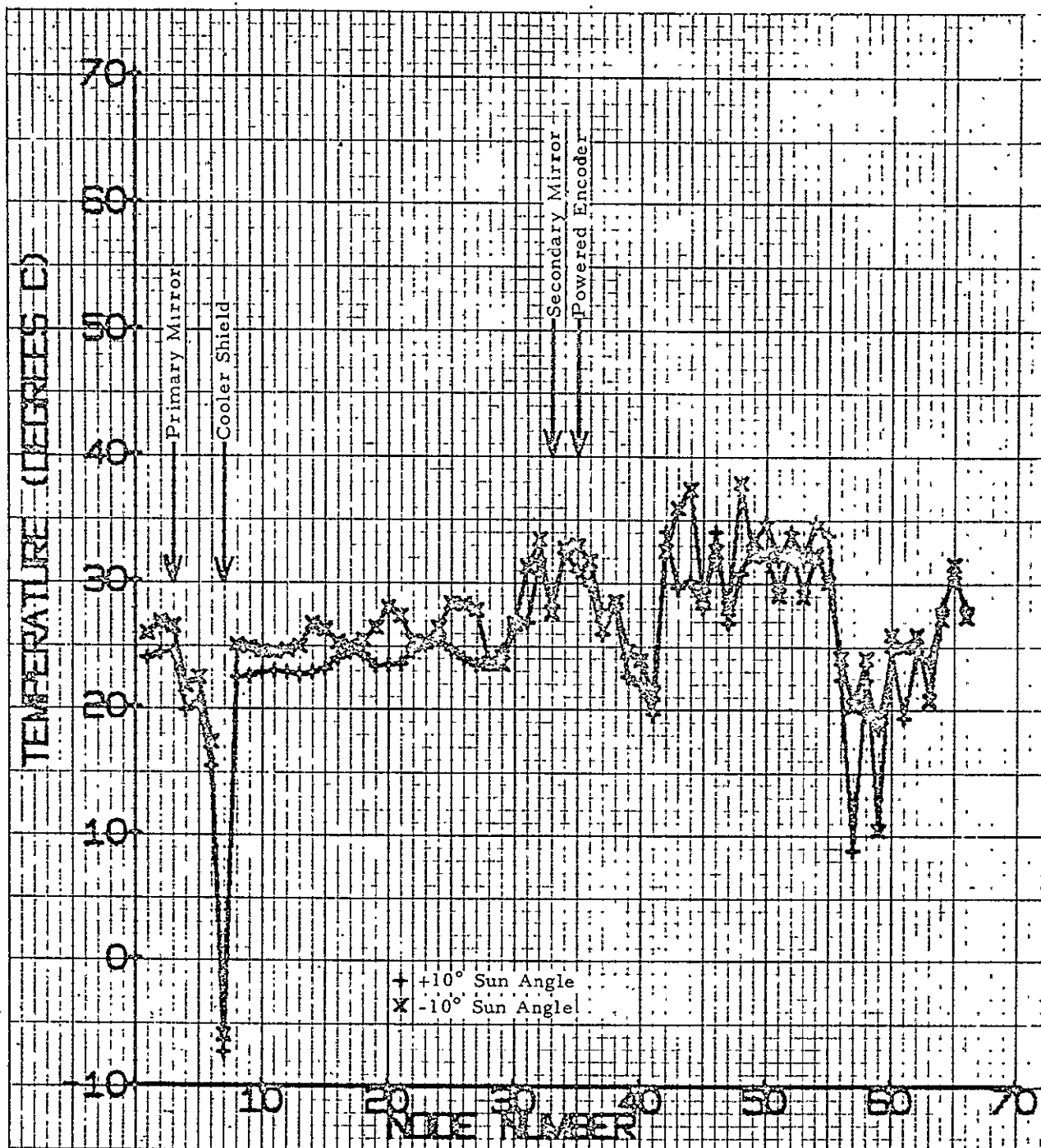


Figure 2-24. VISSR Scanner Nodal Temperatures Thermal Control Surface
Band Height = 0.6 in., $\pm 10^\circ$ Sun Angle

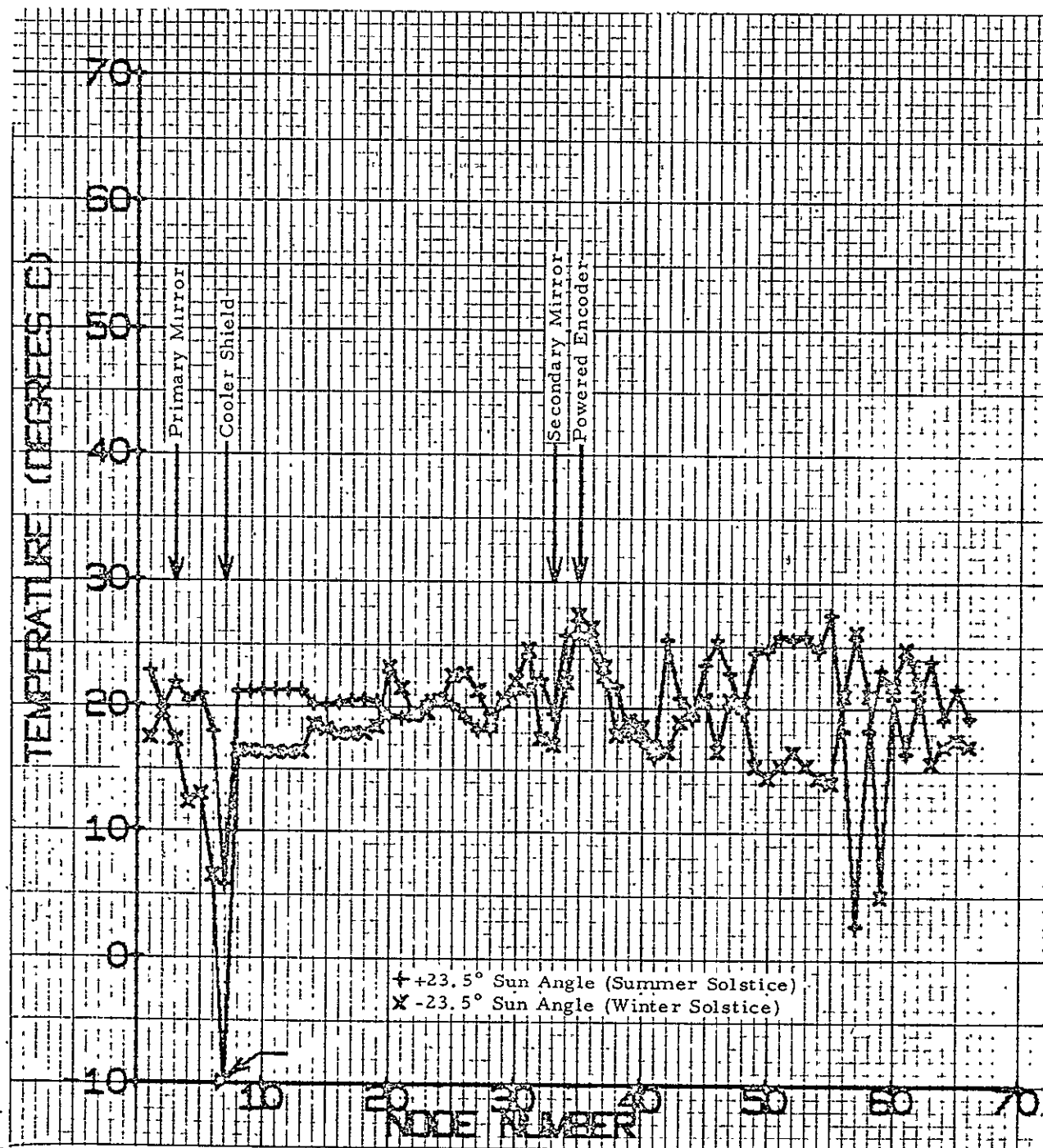


Figure 2-25. VISSR Scanner Nodal Temperatures Thermal Control
Surface Band Height = 1.2 in., $\pm 23.5^\circ$ Sun Angle

Thermal Evaluation of Integrated VISSR/SMS

The thermal model evaluation of the integrated VISSR/SMS system being conducted by Philco-Ford will include the actual conductive and radiative coupling that is expected to exist between the VISSR scanner and the spacecraft nodal parameters.

Although the conductive coupling between the VISSR scanner and the spacecraft will be minimal, radiative coupling will exist since, in general, thermal radiation shielding between the VISSR and the spacecraft is not being provided.¹⁹ For this reason, the VISSR scanner nodal temperatures are expected to be somewhat different than that shown for the "isolated" scanner condition.

Following the completion of the thermal analysis being conducted by Philco-Ford, the results of the analysis are planned to be reviewed with NASA and SBRC and a final decision made on the size of the thermal control surface to be used on the radiation cooler sunshield.

Focus Range and Blur Circle Size

Focus Range. - The focus adjustment range allocated for thermal gradients in the VISSR scanner is

$\pm 50 \times 10^{-3}$ inch for the thermal channels
and $\pm 70 \times 10^{-3}$ inch for the visible channels.

The magnitude of the focus range adjustment required for differential temperatures between VISSR optical elements can be determined from the following expressions:

Thermal Channel -

$$R_T = |-0.107\Delta T_{\text{pri-spac}} - 0.022\Delta T_{\text{pri-sec}} - 0.098\Delta T_{\text{pri-MP}}| \times 10^{-3} \text{ inch}$$

Visible Channel -

$$R_V = |-3.35\Delta T_{\text{pri-spac}} - 0.69\Delta T_{\text{pri-sec}}| \times 10^{-3} \text{ inch}$$

¹⁹ This decision was based on the results of a preliminary thermal analysis conducted by Philco-Ford which showed that no undesirable thermal effects were created when substantial radiative coupling between the VISSR and the spacecraft was assumed.

where $\Delta T_{\text{pri-spac}}$ = primary mirror temperature minus telescope spacer temperature in $^{\circ}\text{C}$

$\Delta T_{\text{pri-sec}}$ = primary mirror temperature minus secondary mirror temperature in $^{\circ}\text{C}$

$\Delta T_{\text{pri-MP}}$ = primary mirror temperature minus mounting plate temperature in $^{\circ}\text{C}$

Blur Circle Size. - Following the optimization of the VISSR thermal or visible channel focus to correct a defocused condition due to a VISSR scanner temperature gradient, the subsequent blur circle diameter change that will result due to a change in temperature gradient between VISSR optical elements can be determined from the following expressions:

Thermal Channel -

$$\text{BCD}_T = |-4.08\Delta(\Delta T_{\text{pri-spac}}) - 0.84\Delta(\Delta T_{\text{pri-sec}}) - 3.72\Delta(\Delta T_{\text{pri-MP}})| \mu\text{r}$$

Visible Channel -

$$\text{BCD}_V = |-4.08\Delta(\Delta T_{\text{pri-spac}}) - 0.84\Delta(\Delta T_{\text{pri-sec}})| \mu\text{r}$$

The above expressions used in conjunction with Figures 2-9 and 2-10 can be used to determine the change in VISSR scanner temperature gradients that can be tolerated before refocusing is required due to ground resolution (MTF) requirements.

Section 3 OPTICS

OPTICAL REQUIREMENTS

The scanner assembly contains eight identical visible channels operating in the 0.54- to 0.70-micron band and a single infrared thermal channel operating in the 10.5- to 12.6-micron band. The instantaneous geometric field of view (IGFOV) of each visible channel is 0.025×0.021 mr and the IGFOV of the thermal channel is 0.25 mr square. The eight visible channel IGFOVs are aligned in a linear array so that during the scanning process they are symmetrical with the 0.25-mr thermal channel IGFOV. A 20% underlap between channels is allowed as a practical fiber optics cladding allowance. Also, as a redundant consideration, an additional thermal channel is mounted next to the primary thermal channel and has identical characteristics.

Although the preceding requirements define the required telescope field angle, a desired system growth potential would increase this parameter. The anticipated modification includes additional thermal channels to accomplish a vertical temperature profile measurement capability. The details of this growth potential experiment have not been defined.

GENERAL DESCRIPTION

The optical system is shown schematically in Figure 3-1. It consists of the following:

1. An object-space scan mirror
2. A Ritchey-Chretien primary-secondary mirror system
3. Relay optics for the thermal channel
4. Fiber optics light-guides for the visible channels
5. Optical filters for the thermal and visible channels
6. An immersed (to PMT window) optical prism in each visible channel to achieve enhanced photocathode effective quantum efficiency.

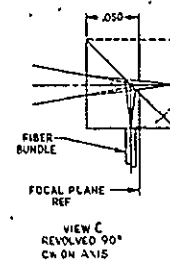


Figure 3-1. Optical Schematic, VISSR/SMS Scanner

TELESCOPE DESIGN

The selection of a specific telescope design involved the tradeoff of fabrication difficulty with the required optical performance. Several mirror systems are theoretically capable of perfect imagery at the optical axis, but they have markedly different characteristics away from the optical axis. Figure 3-2 compares three folded telescope types used by SBRC in previous spaceborne sensors. The solid lines show performance at the plane of paraxial focus, and the dashed lines the curve of best focus.

It should be noted that a parabola alone is very nearly equivalent to the Cassegrainian optical system. The blur size shown in the figure is the diameter of the maximum blur circle. The main aberration present in the Dall-Kirkham and the Cassegrain systems is coma, so one may assume that a major fraction of the energy is contained in a significantly smaller blur circle.

The Ritchey-Chretien design has been of principal interest because it provides higher resolution over a significantly wider field than the somewhat simpler Dall-Kirkham design. The wide field angle characteristics of the Ritchey-Chretien design facilitate and simplify optical alignment procedures and permit channel separation to be accomplished by angular displacement without seriously deteriorating channel spatial resolution.

Three different optical designs were explored during the preliminary design phase. They are as follows:

1. The Ritchey-Chretien design initially proposed.
2. A three-mirror design using a spherical primary mirror and aspheric second and third mirrors.
3. A Ritchey-Chretien design having slower optical characteristics as compared to the system initially proposed.

Table 3-1 summarizes some of the properties of these three systems.

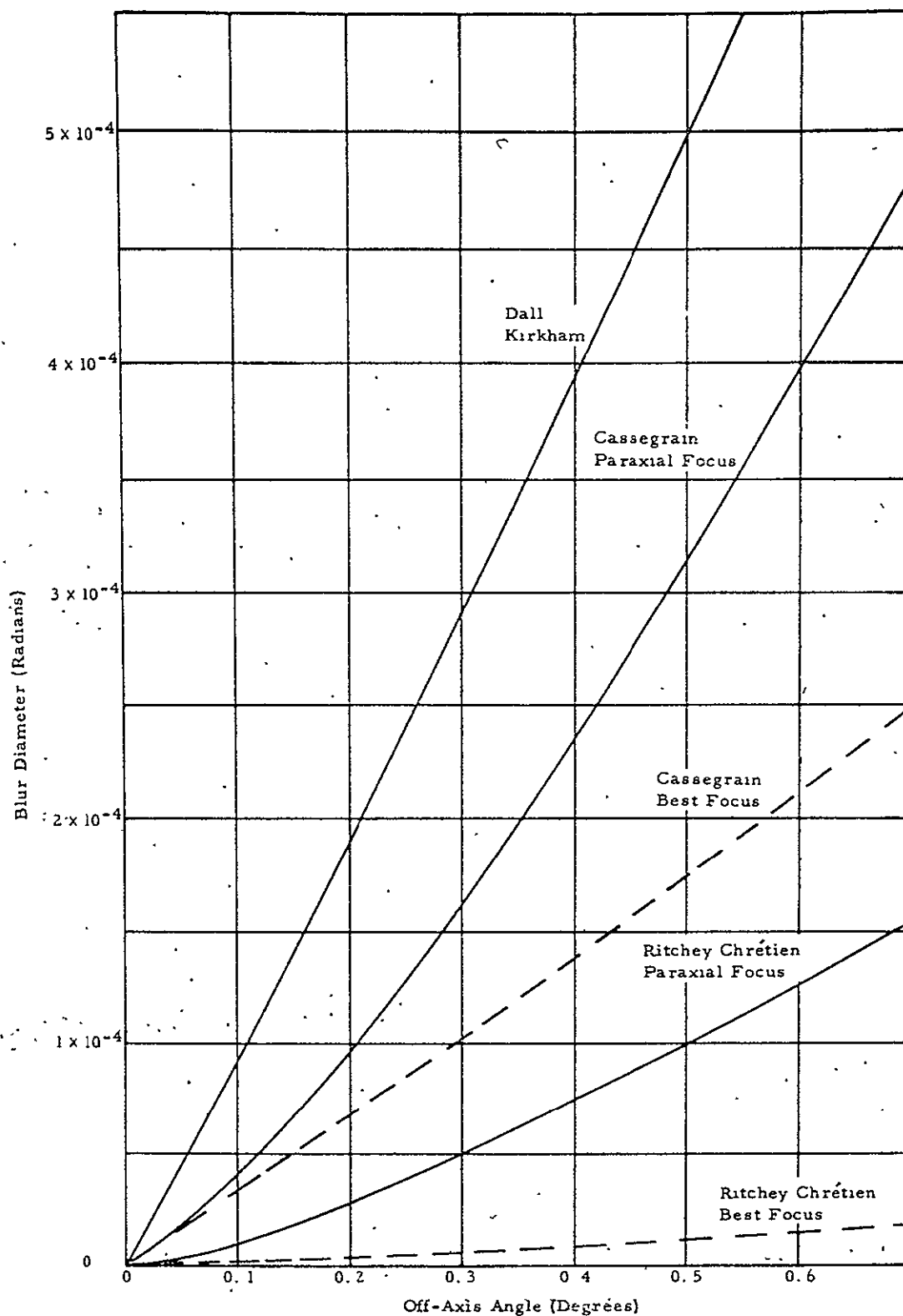


Figure 3-2. Comparison of Off-Axis Image Blur for Two-Mirror Optical Systems

Table 3-1. Summary of Three Optical Designs Characteristics

Optical Design	f/# System	f/# Primary Mirror	Optical System Configuration P S T*	Material P S T*	Image Quality	Fiber Size (In.)	Baffling	Rating
Proposed Design ¹ with Modified Back Focal Length	4	1.8	A A Ritchey Chretien	Be Be	Good	0.0016	Good	3
Three Mirror Design ²	10	2.5	Sp A A	Be SiO ₂ SiO ₂	Good	0.0045	Ext - ent	1
Revised Two Mirror Design ³	7.17	2.4	A A Ritchey Chretien	Be Be	Very Good	0.0028	Fair to Good	2

* P - Primary
S - Secondary
T - Third
A - Aspheric
Sp - Spherical

** Mirrors S & Q are identical

Designs other than No. 1 were considered because of anticipated difficulty in fabricating the relatively fast aspheric primary mirror. While this problem was difficult to define, discussions with various optical vendors proved that a slower system would increase the probability of obtaining optics meeting the requirements.

Design No. 2 would be the easiest to fabricate because of the spherical primary mirror. However, this system was not compatible with certain spacecraft configurations. Also, field angle capability is less due to the double fold, long focal length, and center hole required in the secondary mirror.

Design No. 3's only apparent disadvantage is limitations in applying radiation baffling. Using this configuration, radiant energy from outside the desired field cannot be prevented from irradiating the secondary mirror. Specularly reflected energy does no harm because it will be absorbed by the scanner baffling; however, energy diffusely scattered to the field stops cannot be shielded. Preliminary analysis has indicated that this is not a significant factor when related to reflected or radiated energy from the earth. A detailed analysis will be completed using the radiometer-sunshade configuration. It will include bidirectional (scattering) of the secondary mirror surface.

TELESCOPE AND THERMAL RELAY SYSTEM

Summary

Optical design for the VISSR 16-inch aperture telescope has been coupled with the thermal channel relay system in a continuous ray trace. The ray traces include surface printouts for determining required clear apertures as well as spot diagrams for image evaluation at the primary and relayed image planes. Effective focal length is nominally 114.7 inches.

The ray trace results indicate a blur circle of 3×10^{-5} inch on axis, and 2×10^{-4} inch at the largest field angle; at 114 inches focal length these give 3×10^{-7} and 2×10^{-6} radian, respectively. The diameter of the central diffraction maxima is about 3.7×10^{-6} radian for visual light. The geometrical aberration is less than the diffraction dimension by a factor of 10 in the field center where the visual channels are located. The diffraction maxima for the infrared channel is about 7×10^{-5} radian. At the field edge where the infrared channels are located, the geometrical aberration is about 35 times smaller than the diffraction maxima diameter.

These results assure a diffraction limited operation for the nominal telescope design.

At the relayed infrared image plane, the image blur's maximum dimensions are 1.2×10^{-4} inch for both the upper and lower field extremes. The $f/\#$ of the convergent beam at the image is $f/1.28$. For this $f/\#$ and 11.5-micron wavelength, the diffraction maximum diameter is 1.4×10^{-3} inch. The geometrical blur circle of the relayed image is about a factor of 10 smaller than the diffraction pattern. This assures diffraction limited performance for the combined nominal design of the telescope and relay system.

General Description

The primary image is formed by a 114.7-inch focal length, 16-inch diameter, Ritchey-Chretien system. This image lies 1.5 inches behind the vertex of the primary mirror to permit access for image evaluation equipment.

At the primary image surface, the infrared field consists of two segments each 0.2 mr square, or 0.023 inch per side. The segments are separated by 0.023 inch. The array lies on a radius centered at the telescope axis. The near edge of the first IR field segment is 0.100 inch from the axis. The far edge of the second detector lies 0.169 inch from the axis. This array is illustrated in Figure 3-3.

The relay axis is parallel to, but displaced from, the telescope axis by 0.156 inch. This displacement was needed because the entrance pupil of the relay is the exit pupil of the telescope and all principal rays diverge from this stop. The axial displacement dimension was selected to distribute principal ray spread equally about the relay lens aperture, thus minimizing the required aperture.

Detailed System Description

The system layout is shown in Figure 3-4. Relay lens details are outlined in expanded scale in Figure 3-5. Total length from telescope secondary vertex to detector plane is 34.556 inches.

The number of significant figures on dimensions does not necessarily indicate tolerance critically to those figures. These are rounded off in the tolerance study.

The spacing between elements B and C (Figure 3-5) must be examined to see what space is available for focal adjustment to compensate for a potential axial shift of ± 0.040 of the detector. If the detector moves 0.040 from the lens, the lens pair AB must move 0.0413 toward the filter C. This has been verified by a ray trace.

The clear aperture radius required on the concave surface of lens B is 0.312 inch. If we add 0.003 to this for tolerancing we have 0.315. Presuming the lens edge is flat and orthogonal to that axis from 0.315 outward we calculate the lens sag, or distance from flat to vertex (axial intersect) to be $R - (R^2 - 0.315^2)^{\frac{1}{2}}$ or 0.0636 inch. The spacing vertex of B to filter C is

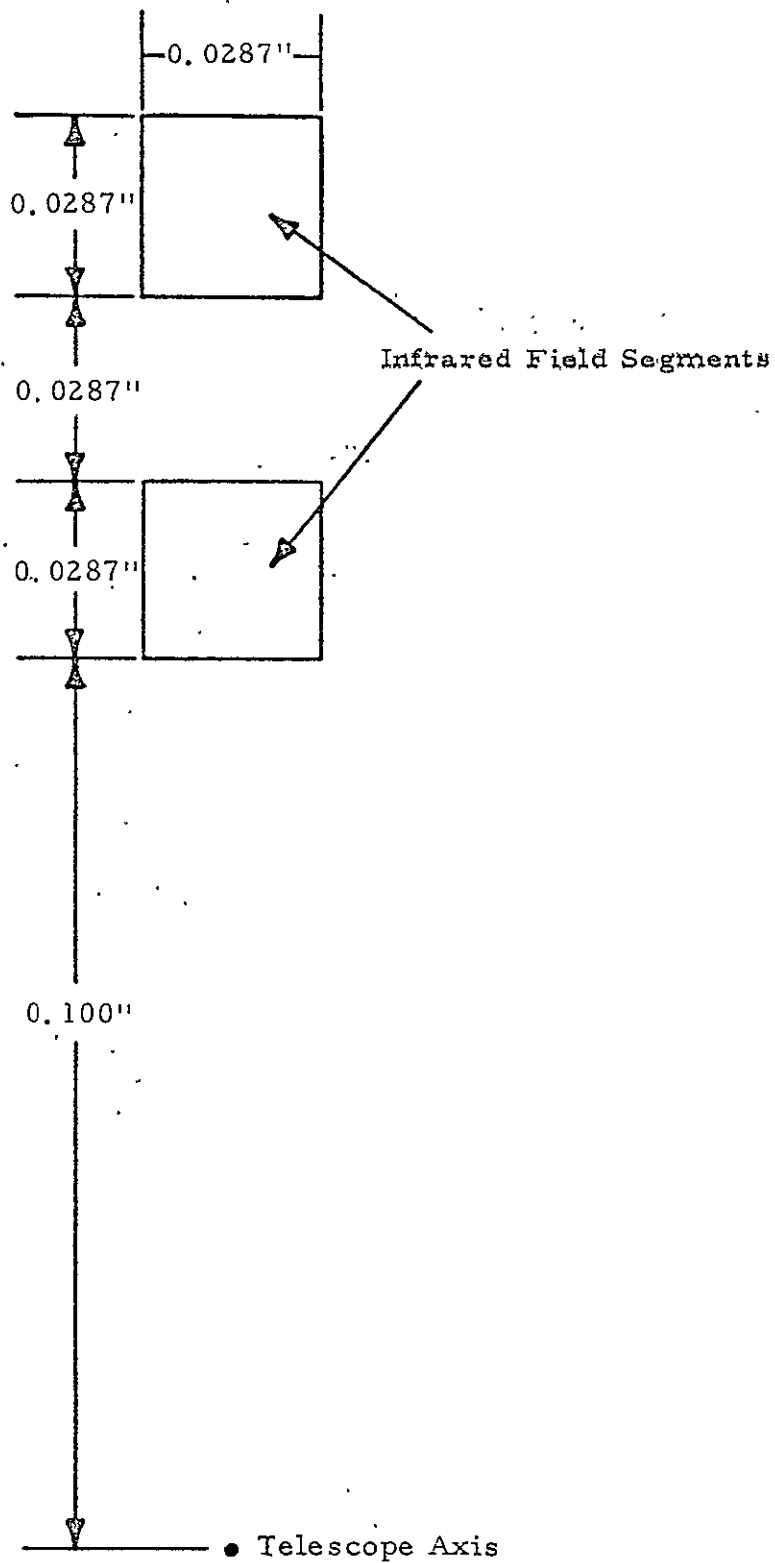


Figure 3-3. Infrared Field Segment Array

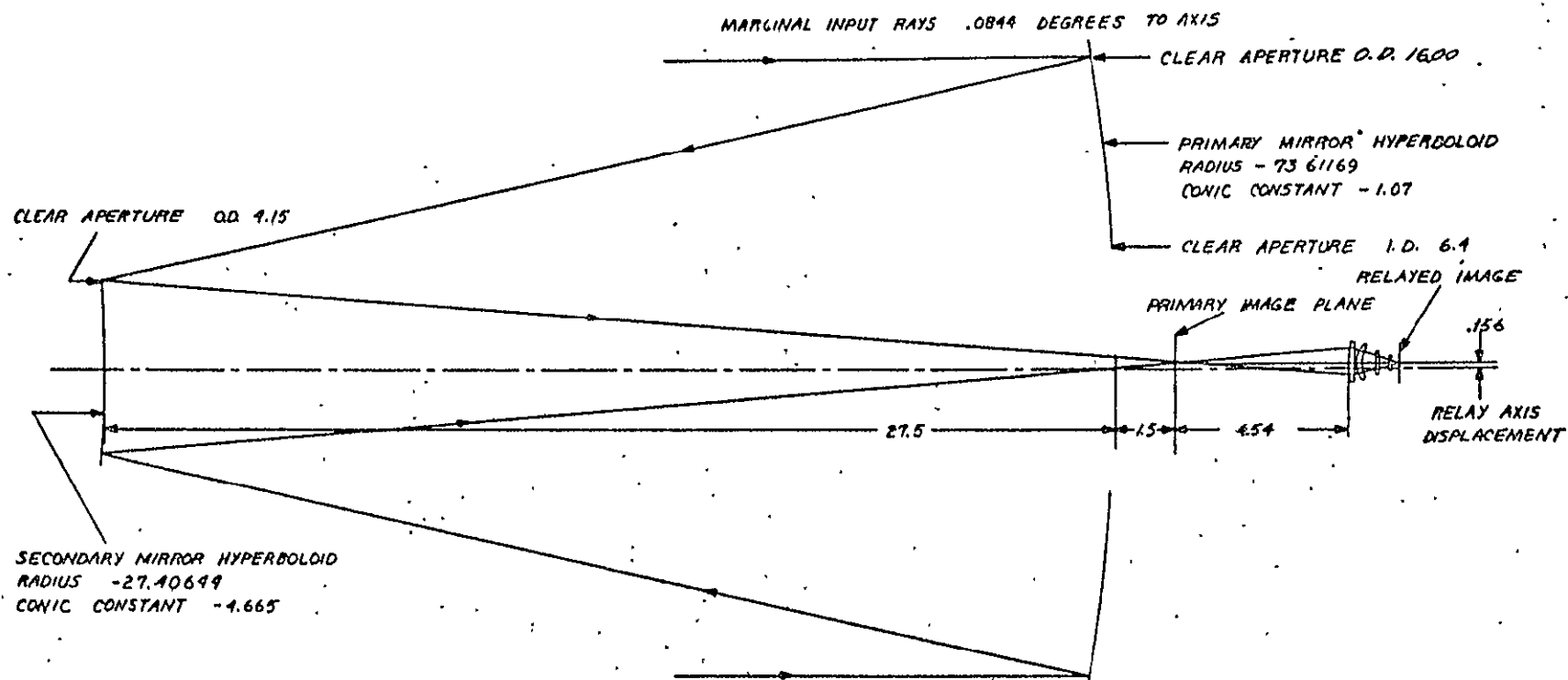


Figure 3-4. Telescope and IR Relay Schematic

LENS A $R_1 = 6.0291$
 $R_2 = \text{FLAT}$

CLEAR APERTURE RADIUS ① .359

CLEAR APERTURE RADIUS ② .356

LENS B $R_1 = .70821$

$R_2 = .81234$

CLEAR APERTURE RADIUS ③ .344

CLEAR APERTURE RADIUS ④ .312

FILTER C BOTH SIDES FLAT

CLEAR APERTURE RADIUS ⑤ .207

CLEAR APERTURE RADIUS ⑥ .198

AT MAX FOCUSED POSITION ⑤ .232

⑥ .223

WINDOW D BOTH SIDES FLAT

CLEAR APERTURE RADIUS ⑦ .063 IRTRAN 2

CLEAR APERTURE RADIUS ⑧ .055

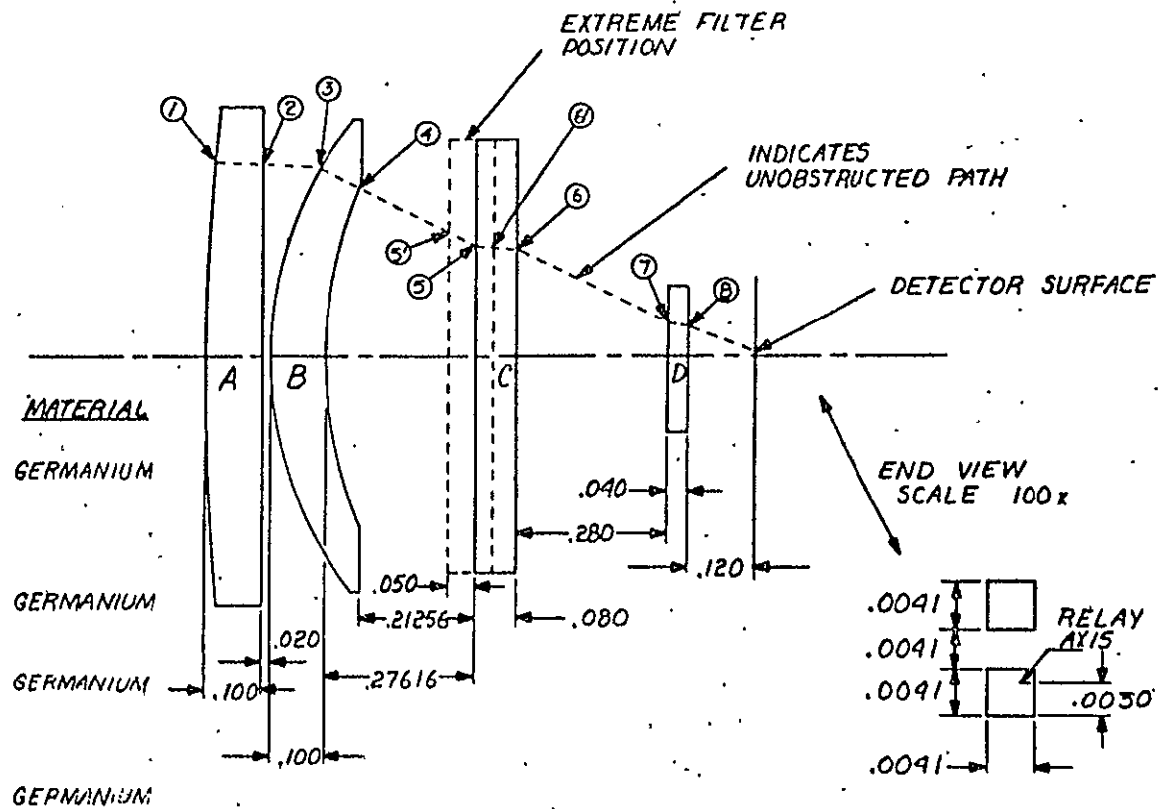


Figure 3-5. IR Channel Relay Lens Schematic

0.27616. Therefore, the distance from mounting surface of B (flat edge) to mounting surface of C is 0.21256.

The detector array is of the dimensions shown in Figure 3-5. The top detector edge is 0.0093 from the relay axis, and the bottom detector edge is 0.003 from the relay axis.

Relative to the telescope axis, the top detector edge is 0.1613 from axis and the bottom detector edge is 0.1490 from axis.

The diameter of the filter clear aperture is 0.207 on the front face for the nominal position. However, the spacing lens B to filter can shrink by 0.045 inch. To accommodate for this spacing shrinkage, the filter aperture must increase. The tangent of the steepest incidence angle on the filter is 0.4948 or about 0.5. If we presume as much as 0.050 spacing reduction we have $0.050 \times 0.5 = 0.025$ increase required in the filter diameter. This increases the required active aperture radius to 0.232 inch.

Since the overall length of relay conjugate can vary by ± 0.040 due to detector displacement, ray traces at these displacements were run. For a shortening of overall distance by 0.040, the lens to detector distance increases by 0.0013 inch. Image quality and image height deviation are less than 0.0001 inch. For an increase of 0.040, lens to detector distance is decreased by 0.0013. Image quality and image height deviation are less than 0.0002 inch.

Thus, no image deterioration or distortion of significance is introduced by required focusing. The dynamic range of motion is +0.0413 by -0.0387, or is equal to the total motion range of the detector.

Performance Summary

The computer output summarizing system performance is given in the following figures.

Figure 3-6 shows a spot diagram of the on-axis ray bundle in the primary image plane. The total ray pattern is contained within 3×10^{-5} inch.

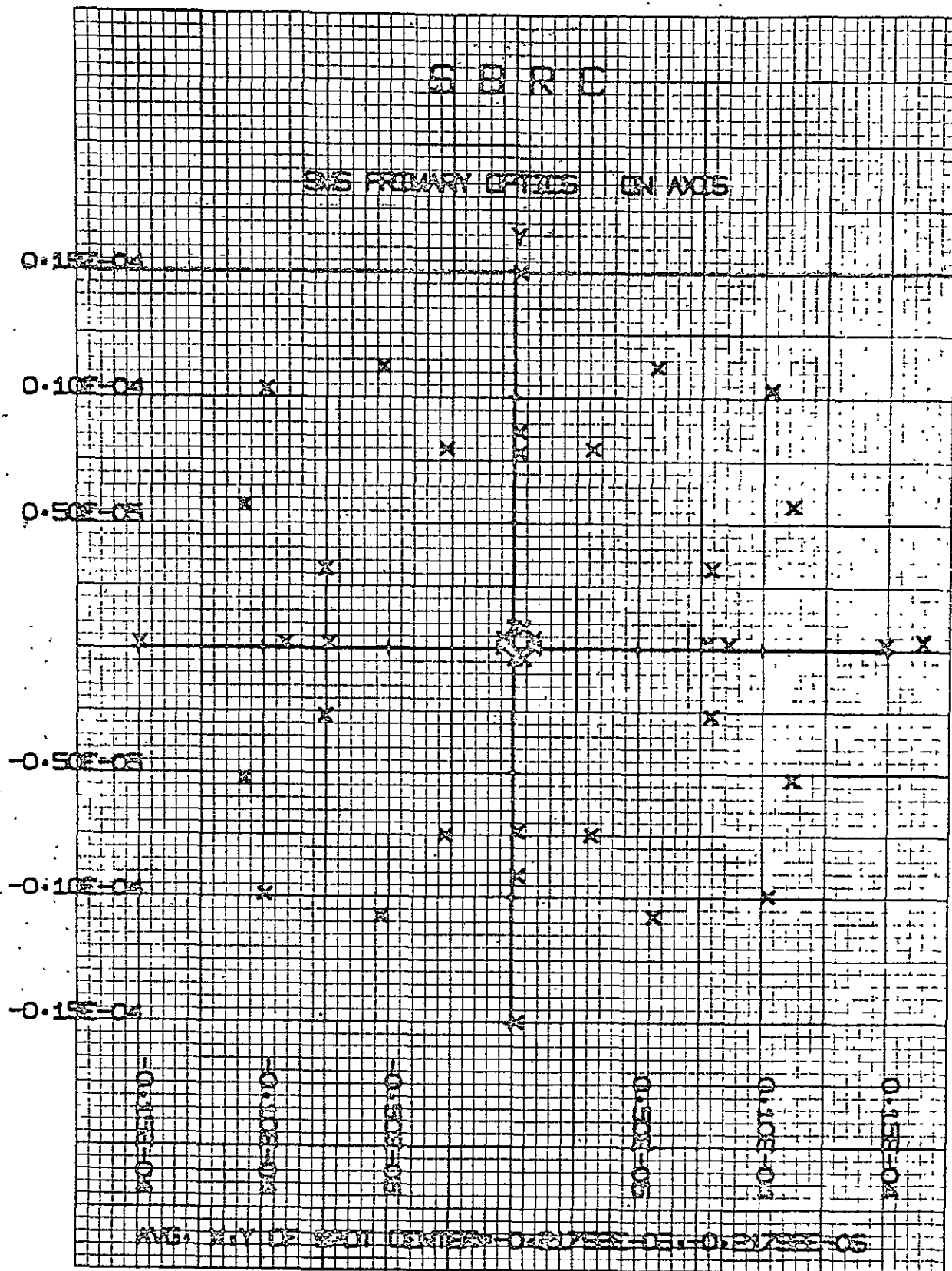


Figure 3-6. Primary Optics, On Axis

Figure 3-7 shows a spot diagram of the ray bundle in the primary image plane at 0.169 off-axis, or at the edge of the infrared field farthest from the axis. The blur pattern approximates an ellipse 1×10^{-4} inch wide by 2×10^{-4} inch high.

Table 3-2 gives a readout of the system input data to the computer.

Figure 3-8 shows a spot diagram of the image at the detector surface. This is at an entrance field angle of 0.0844° . It represents the far edge of the infrared field, but due to inversion by the relay is the detector edge closest to the axis. The maximum spot separation is 1.2×10^{-4} inch with 90% of the distribution within 0.4×10^{-4} inch.

Figure 3-9 shows a spot diagram of the near edge of the far infrared field as imaged at the detector. Its entrance angle is 0.0729° . The blur pattern maximum dimension is 1.3×10^{-4} inch, with a heavy concentration of spots in less than 0.50×10^{-4} inch.

Figure 3-10 shows a spot diagram of the far edge of the near-infrared field as imaged at the detector. The input angle is 0.0615° . Distribution is similar to the preceding cases.

Figure 3-11 shows a spot diagram of the near edge of the near-infrared field. The input angle is 0.050° . Spot distribution matches that of previous figures.

Tables 3-3 and 3-4 give surface-by-surface readouts for marginal and axial rays. Table 3-3 is for the near-infrared field limit of 0.050° while Table 3-4 is for the far-infrared field limit. The Y and Z readings are used to determine the required clear apertures and sags at each surface. All Y readings are relative to the telescope axis. The relay axis spacing of 0.156 must be considered when using these numbers to determine aperture.

Table 3-5 is the case in which overall length has been reduced by 0.040. The double underlined number on the first line $\text{BFL} = 0.121310$ is the back focal length. Since the normal BFL is 0.120 we have an increase at 0.00131.

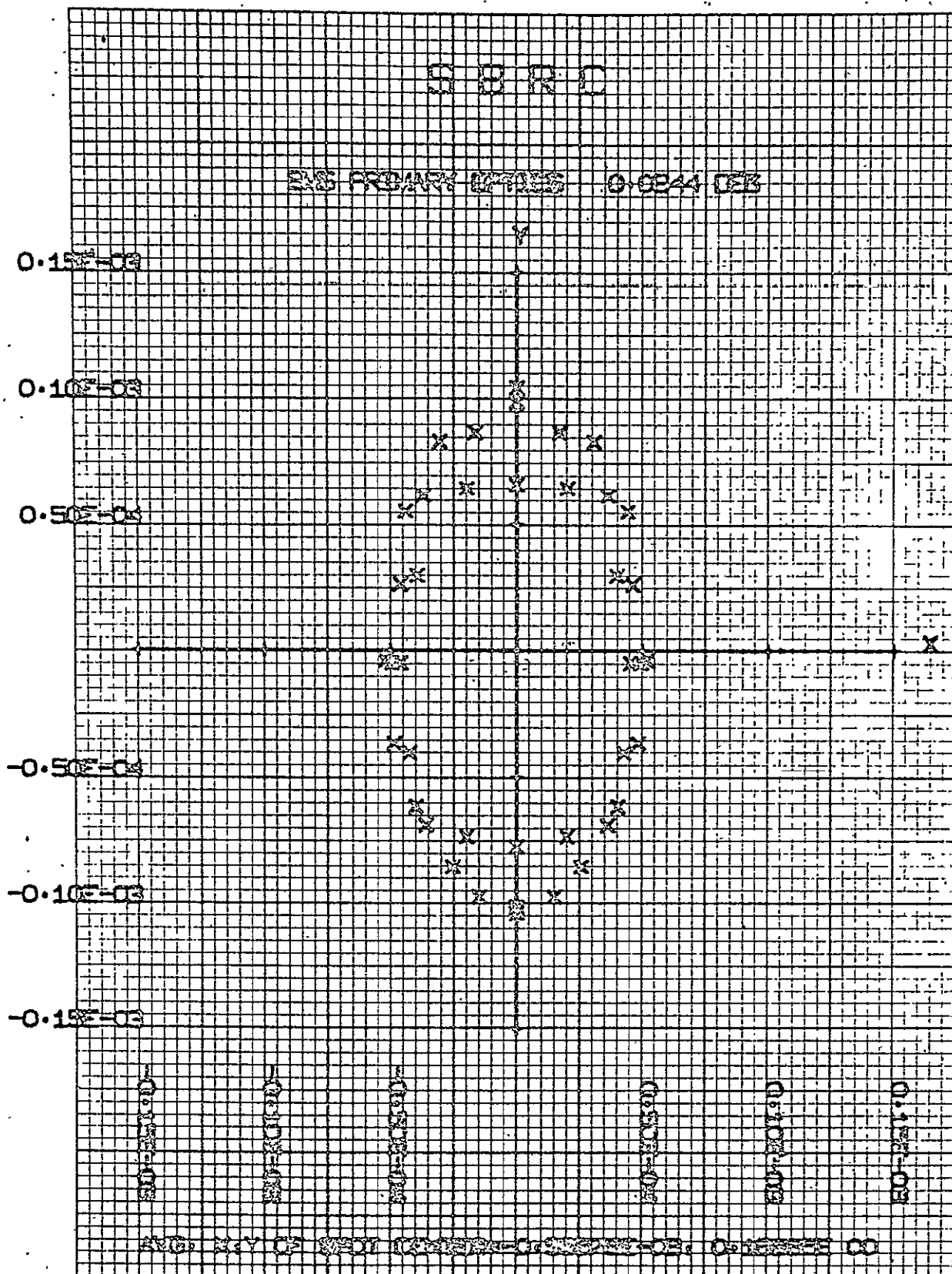


Figure 3-7. Primary Optics, Off Axis

Table 3-2. System Input Data Readout

SURF	TAG	RADIUS	T	D	F	C
1	1	-73.61169	-27.50000	-1.00000	-1.00000	-1.00000
0.000000E 00 0.000000E 00 0.000000E 00 0.000000E 00 -0.107000E 01						
2	1	-27.40644	29.00000	1.00000	1.00000	1.00000
0.000000E 00 0.000000E 00 0.000000E 00 0.000000E 00 -0.466500E 01						
3	1	*****	4.54000	1.00000	1.00000	1.00000
4	1	6.02409	0.10000	4.00000	1.00000	1.00000
DECENTERED DCX 0.00000 DCY 0.15200						
0.000000E 00 0.000000E 00 0.000000E 00 0.000000E 00 0.000000E 00						
5	1	*****	0.02000	1.00000	1.00000	1.00000
DECENTERED DCX 0.00000 DCY 0.15200						
0.000000E 00 0.000000E 00 0.000000E 00 0.000000E 00 0.000000E 00						
6	1	0.70821	0.10000	4.00000	1.00000	1.00000
DECENTERED DCX 0.00000 DCY 0.15200						
0.000000E 00 0.000000E 00 0.000000E 00 0.000000E 00 0.000000E 00						
7	1	0.81234	0.27616	1.00000	1.00000	1.00000
DECENTERED DCX 0.00000 DCY 0.15200						
0.000000E 00 0.000000E 00 0.000000E 00 0.000000E 00 0.000000E 00						
8	1	*****	0.08000	4.00000	1.00000	1.00000
9	1	*****	0.28000	1.00000	1.00000	1.00000
10	1	*****	0.04000	2.17000	1.00000	1.00000
11	1	*****	0.12000	1.00000	1.00000	1.00000

SYSTEM DATA (K=21 TO 38)

0.000000	8.010000	0.001200	0.000000	1.000000	1.000000	1.000000
11	1	1	1**33*	-0.0050	0.0000	0.0000 0.1200 -20.6051

RAY DATA (K=41 TO 49)

1	9	0.08440	8.00000	-8.00000	0.00000
			8.01000	0.00000	0.00000

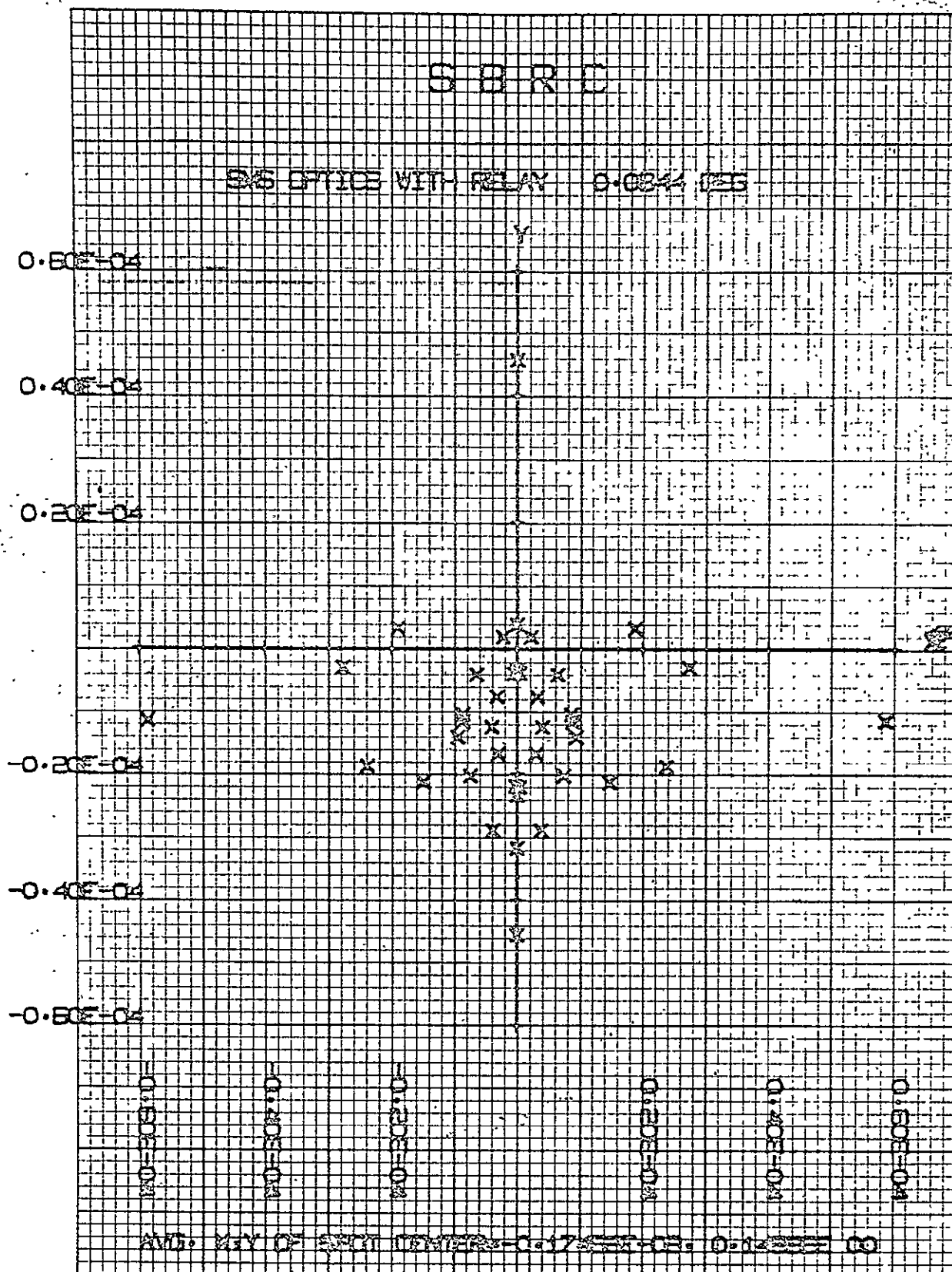


Figure 3-8. Optics with Relay

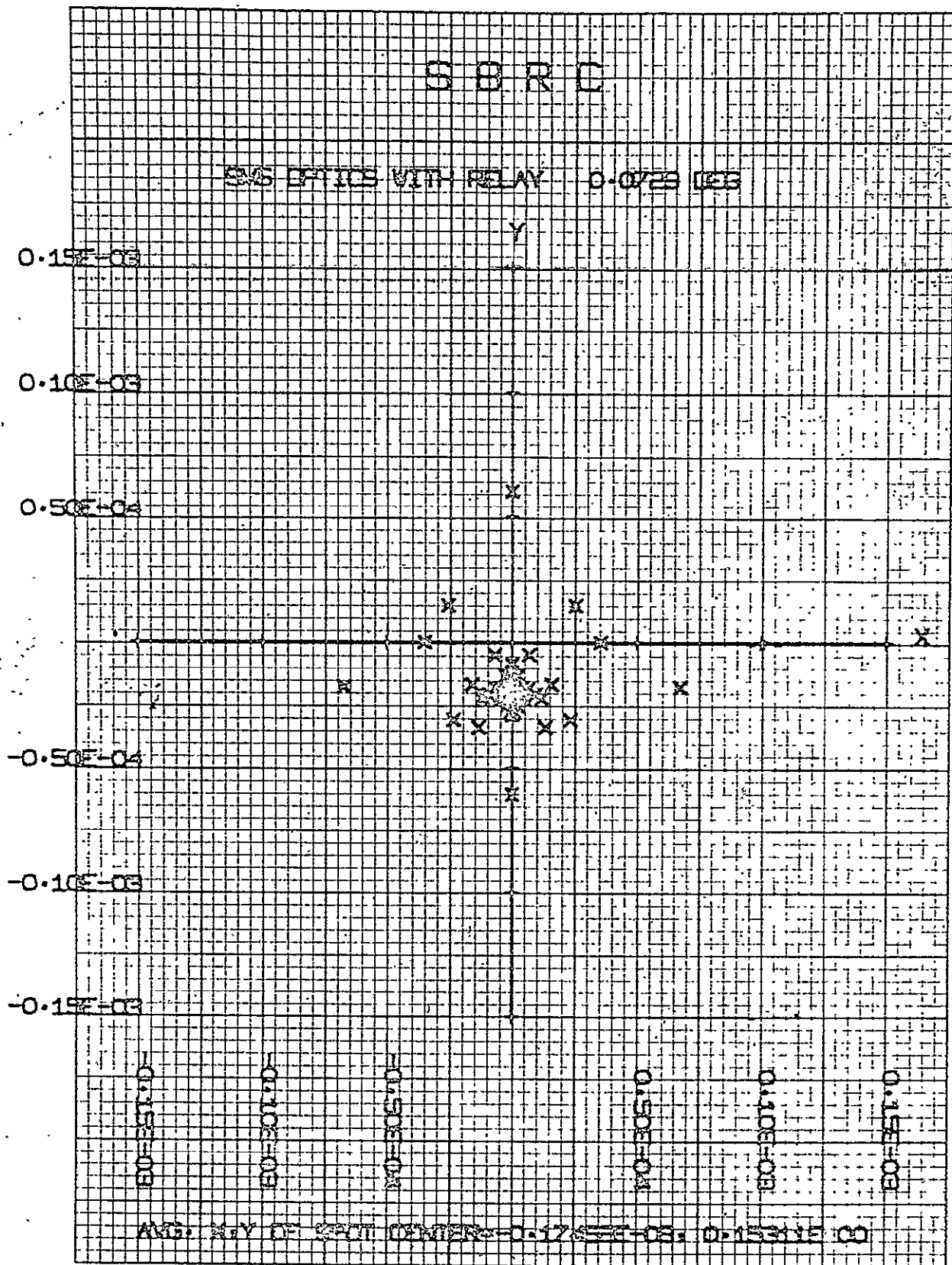


Figure 3-9. Optics with Relay

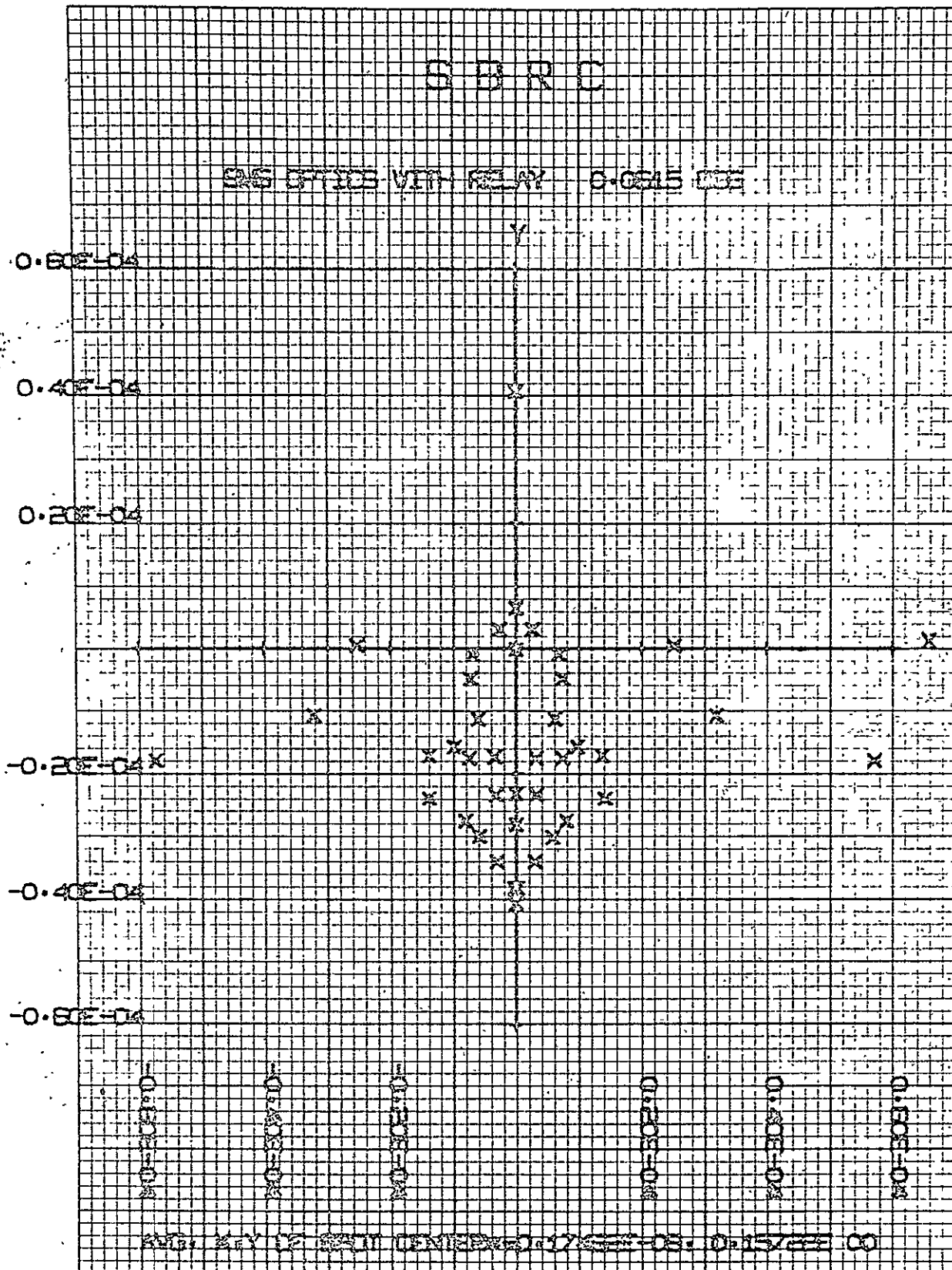


Figure 3-10. Optics with Relay

Table 3-3. Surface-by-Surface Readouts

SURF	X	Y	Z	TAN X	TAN Y	TAN XY
	THETA =	0.050000	DEG			
1	0.000000	7.999621	-0.4345	0.0000	0.2189	0.2189
2	0.000000	2.057201	-0.0768	0.0000	-0.0673	0.0673
3	0.000000	0.100027	0.0000	0.0000	-0.0673	0.0673
4	0.000000	-0.206279	0.0106	0.0000	0.0279	0.0279
5	0.000000	-0.203785	0.0000			
6	0.000000	-0.191552	0.0889			
7	0.000000	-0.159690	0.0621			
8	0.000000	-0.053799	0.0000			
9	0.000000	-0.044873	0.0000			
10	0.000000	0.093685	0.0000			
11	0.000000	0.102037	0.0000			
IM	0.000000	0.161422	0.1200	0.0000	0.4948	0.4948
1	0.000000	0.000000	0.0000	0.0000	-0.0008	0.0008
2	0.000000	0.023998	-0.0000	0.0000	0.0026	0.0026
3	0.000000	0.100093	0.0000	0.0000	0.0026	0.0026
4	0.000000	0.112006	0.0001	0.0000	0.0056	0.0056
5	0.000000	0.112568	0.0000			
6	0.000000	0.113044	0.0010			
7	0.000000	0.117722	0.0007			
8	0.000000	0.134551	0.0000			
9	0.000000	0.135771	0.0000			
10	0.000000	0.152880	0.0000			
11	0.000000	0.154004	0.0000			
IM	0.000000	0.161337	0.1200	0.0000	0.0611	0.0611
1	0.000000	-8.000379	-0.4346	0.0000	-0.2207	0.2207
2	0.000000	-2.008523	-0.0732	0.0000	0.0725	0.0725
3	0.000000	0.100174	0.0000	0.0000	0.0725	0.0725
4	0.000000	0.429928	0.0064	0.0000	-0.0165	0.0165
5	0.000000	0.428376	0.0000			
6	0.000000	0.423453	0.0540			
7	0.000000	0.396414	0.0376			
8	0.000000	0.313365	0.0000			
9	0.000000	0.306766	0.0000			
10	0.000000	0.209272	0.0000			
11	0.000000	0.203140	0.0000			
IM	0.000000	0.161356	0.1200	0.0000	-0.3481	0.3481

Table 3-4. Surface-by-Surface Readouts

SURF	X	Y	Z	TAN X	TAN Y	TAN XY
	THETA =	0.084400	DEG			
1	0.000000	7.999360	-0.4345	0.0000	0.2182	0.2182
2	0.000000	2.073935	-0.0780	0.0000	-0.0655	0.0655
3	0.000000	0.168805	0.0000	0.0000	-0.0655	0.0655
4	0.000000	-0.129075	0.0065	0.0000	0.0187	0.0187
5	0.000000	-0.127327	0.0000			
6	0.000000	-0.121698	0.0550			
7	0.000000	-0.094337	0.0382			
8	0.000000	-0.008518	0.0000			
9	0.000000	-0.001707	0.0000			
10	0.000000	0.099295	0.0000			
11	0.000000	0.105628	0.0000			
IM	0.000000	0.148917	0.1200	0.0000	0.3607	0.3607
1	0.000000	0.000000	0.0000	0.0000	-0.0014	0.0014
2	0.000000	0.040509	-0.0000	0.0000	0.0044	0.0044
3	0.000000	0.168957	0.0000	0.0000	0.0044	0.0044
4	0.000000	0.189066	0.0001	0.0000	-0.0035	0.0035
5	0.000000	0.188716	0.0000			
6	0.000000	0.188422	0.0009			
7	0.000000	0.184222	0.0006			
8	0.000000	0.170611	0.0000			
9	0.000000	0.169624	0.0000			
10	0.000000	0.155790	0.0000			
11	0.000000	0.154881	0.0000			
IM	0.000000	0.148952	0.1200	0.0000	-0.0494	0.0494
1	0.000000	-8.000640	-0.4346	0.0000	-0.2214	0.2214
2	0.000000	-1.991771	-0.0720	0.0000	0.0743	0.0743
3	0.000000	0.169122	0.0000	0.0000	0.0743	0.0743
4	0.000000	0.507355	0.0104	0.0000	-0.0258	0.0258
5	0.000000	0.505044	0.0000			
6	0.000000	0.493838	0.0879			
7	0.000000	0.462190	0.0615			
8	0.000000	0.358739	0.0000			
9	0.000000	0.350002	0.0000			
10	0.000000	0.215027	0.0000			
11	0.000000	0.206857	0.0000			
IM	0.000000	0.149008	0.1200	0.0000	-0.4820	0.4820

Table 3-5. Tangential Fan for Reduced Length

THRDR

BFL= 0.121310 EFL=-20.823223 ENT= 0.000000 EXT= 0.007947

	SPHER	COMA	ASTIG	Y-MARG	Y-PRINC	CURV	
1	-0.0206404 0.0220852	0.0002276 0.0000000	-0.0000025 0.0000000	8.010000	0.000000	-0.01358	-27.50000
2	0.0061834 -0.0076244	-0.0001034 -0.0001242	0.0000017 -0.0000020	2.025217	0.032999	-0.03648	29.00000
3	0.0000000	0.0000000	0.0000000	-0.000059	0.137637	0.00000	4.50000
4	-0.0003521 0.0000000	0.0000841 0.0000000	-0.0000201 0.0000000	-0.314327	0.153874	0.16600	0.10000
5	-0.0001907 0.0000000	0.0001606 0.0000000	-0.0001352 0.0000000	-0.312159	0.152048	0.00000	0.02000
6	-0.0000347 0.0000000	0.0000138 0.0000000	-0.0000054 0.0000000	-0.310425	0.150588	1.41200	0.10000
7	-0.0001706 0.0000000	0.0002126 0.0000000	-0.0002651 0.0000000	-0.275384	0.132815	1.23100	0.27616
8	0.0090262	-0.0051723	0.0029639	-0.169154	0.071942	0.00000	0.08000
9	-0.0086157	0.0049370	-0.0028291	-0.161461	0.067534	0.00000	0.28000
10	0.0024098	-0.0013809	0.0007913	-0.053754	0.005815	0.00000	0.04000
11	-0.0020919	0.0011987	-0.0006869	-0.046663	0.001751	0.00000	0.12131
TOTAL	B	F	C	E	P	A	XL
	-0.0000160	0.0000538	-0.0001896	0.000249	-0.306055	0.000000	0.000000

RAY	X 1	Y 1	X IM	Y IM	TAN X	TAN Y	TAN XY
	THETA = 0.084400		DEG				
1	0.0000	8.0000	0.000000	0.148912			
2	0.0000	6.0000	0.000000	0.148937			
3	0.0000	4.0000	0.000000	0.148936			
4	0.0000	2.0000	0.000000	0.148929			
5	0.0000	0.0000	0.000000	0.148920			
6	0.0000	-2.0000	0.000000	0.148908			
7	0.0000	-4.0000	0.000000	0.148892			
8	0.0000	-6.0000	0.000000	0.148885			
9	0.0000	-8.0000	0.000000	0.148927			

Since plano elements aberration introduction is independent of element location in the beam, the 0.0013 compensation can be introduced anywhere that will extend the image plane to lens B distance by 0.0013.

VISSR Image Quality versus Secondary Mirror Alignment

The VISSR image quality as a function of primary-secondary mirror alignment was determined by geometrical ray tracing. An aggregate of 40 rays distributed uniformly over the VISSR entrance aperture was used. Field angles (θ) of 0, 0.5, and -0.5 mr were used. Decentering (DCY) cases of 0.002, 0.004, and 0.006 inch were computed. Axes X and Y are two orthogonal axes perpendicular to optical axis (Z axis). Field angles are in the YZ plane and decentering is along the Y axis.

Table 3-6 is a tabulation of cases run and resultant image quality. Figure 3-12 graphically illustrates image blur (95% energy) versus decentering.

If the secondary mirror is decentered by 0.005 inch, the geometrical image degradation is equivalent to Airy's diffraction disc for 0.65 micron.

Baffle Design Parameters

A computer ray trace was run to facilitate the baffle design for the primary-secondary mirror system. Rays were introduced in a tangential fan at a field angle of $\theta = 0.0844^\circ$. This angle was used so that the beam would be focused into the infrared channel relay optics which are located at an angular displacement of 0.00147 radian from the optic axis in the horizontal plane. Ray height was adjusted so that the marginal ray would intercept the surface of the primary mirror at 8.000 inches along the positive Y-axis. This resulted in a corresponding negative Y-intercept of 7.965 inches. The inner rays in the trace were determined by the requirement for intercepts with the scan-mirror at $Y = \pm 3.200$ inches at field angle θ . In addition to the nominal ray trace, data were taken to simulate the effect of misalignment of the secondary mirror in the plane perpendicular to the optic axis. This consisted of decentering the coordinates of the secondary mirror along the Y-axis by ± 0.020 inch.

Table 3-6. Image Size vs Decentering

Case		100% Energy		95% Energy	X, Y of Center	
DCY (in.)	θ (mr)	ΔX (in.)	ΔY (in.)	Circular (in.)	X (in.)	Y (in.)
0.002	0	0.00018	0.00023	0.00019	0.00	-0.0041
	0.5	0.00018	0.00025	0.00020	0.00	0.0533
	-0.5	0.00018	0.00018	0.00017	0.00	-0.0615
0.004	0	0.00028	0.00044	0.00035	0.00	-0.0082
	0.5	0.00028	0.00045	0.00035	0.00	0.0491
	-0.5					
0.006	0	0.0004	0.00065	0.00050	0.00	-0.0123
	0.5	0.0004	0.00066	0.00050	0.00	0.0450
	-0.5	0.0004	0.00058	0.00045	0.00	-0.0697

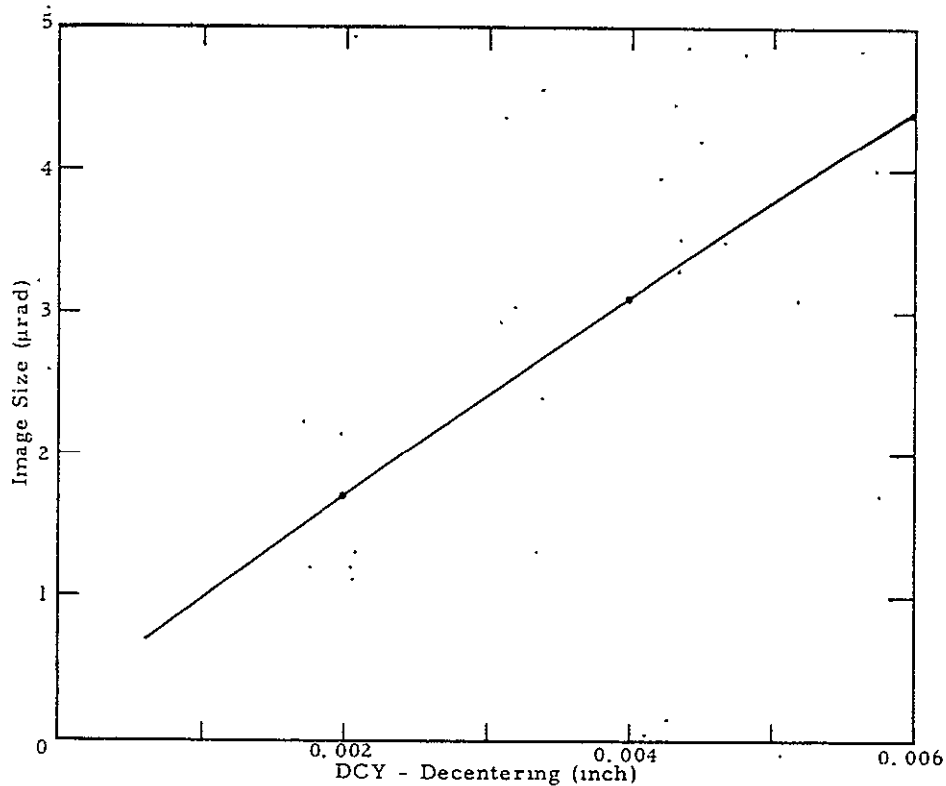


Figure 3-12. Image Blur (μr) for 95% Included Energy vs Decentering

To determine a satisfactory configuration for baffles, a set of fifteen plane surfaces was introduced between the primary and secondary mirrors. The intercepts of the rays with these surfaces along with the intercepts with the mirror surfaces themselves constituted the necessary ray trace. Aperture (stop) dimensions were chosen after an initial ray trace and were adjusted so that the definitive rays (including those for decentered data) would clear apertures nominally by 0.005 inch. The resultant data were used to design baffles.

Scan Mirror Dimensions

Requirements. - The mirror is an ellipse with an elliptical central hole. The stop of the system is the primary telescope mirror.

Maximum dimensions for clear apertures and the minimum dimensions to prevent ray obscuration or vignetting were established. The differences between these dimensions and those actually specified for the mirror represent the allowance for manufacturing and alignment tolerance as well as extra space for edge rolloff.

Summary of Hole Dimensions. -

<u>Major Semi-Axis:</u>	Cannot be larger than 4.122 inches (flat faced is used to this dimension)
	Cannot be smaller than 3.918 inches (interferes with return beam if smaller). Recommend 4.020 inches (give 0.100 inch for edge rolloff)
<u>Minor Semi-Axis:</u>	Cannot be greater than 3.158 inches (flat face is used to this dimension)
	Can be smaller by as much as 1 full inch. Recommend 3.058 inches
	Gives 0.100 inch for edge rolloff, and leaves spaces for assembling and mounting secondary mirror approaches

Outside Dimensions:

The minor semi-axis is 8.0 inches for the axial aperture plus 0.042 inch for projected aperture shift plus 0.100 inch for edge roll-off or 8.142 inches.

The major semi-axis subtends a vertical dimension of 8.00 inches for the axial aperture plus 0.003 inch for the projected aperture displacement. At the 40° inclination the major axis is $8.003/\sin 40^\circ$ or 12.466 inches. Adding 0.100 inch to this for edge runout amounts to a 12.566-inch major semi-axis.

Summary:

Major semi-axis 12.566 inches } Outer edge
Minor semi-axis 8.142 inches }

Major semi-axis 4.020 inches } Inner edge
Minor semi-axis 3.058 inches }

Tolerances of the Thermal Channel Relay Optics

To establish a tolerance basis for the relay lens, the following analysis was made. All radii were varied plus and minus 1% from nominal. All thicknesses and spacings were varied plus and minus 0.005 inch from nominal. Third order callouts were made for all cases.

The lenses were each decentered by 0.005 inch. Tangential fans were run for these two cases both off and on axis. The worst third-order case indicated a sum approximately 16 times that of the nominal. A tangential fan was also run for this case. The results indicate an image blur about 1/4 that of the diffraction pattern central diameter.

The three radius tolerances (the fourth is plane) gave about the same amount of third-order contribution. The thickness tolerance on the first element gave no significant change. The thickness tolerance on the air space between lenses gave no significant change. The thickness tolerance on element 2 introduces about 1/2 the contribution of the individual radius tolerances.

The thickness tolerance on the filter and on the window introduced about the same contribution as the radii tolerance.

Decentering elements gave no significant change in resolution. However, decentering did introduce a change in image height. For nominal, the height is 0.0096 relative to relay axis at the detector. With second element decentered, height is 0.0134 or 1.4 times larger. Since the relay magnification is $0.053/0.0096$ or 5.5 times, the infrared field edge at the primary image plane must be at:

Nominal H at primary image - magnification \times (height difference at relayed image) or 0.053×5.5 ($0.0134 - 0.0096$) or 0.032 inches.

This would make the lead edge of the infrared field 0.121 from optic axis, rather than the 0.100 in design. If this difference is to be calibrated into the system, it is not significant.

In reviewing the preceding results, we know that the individual tolerances are large relative to manufacturing capability, and they caused no significant loss in performance. If these tolerances are held to good manufacturing capability, the individual tolerance is of such a dimension that the accumulated aberration contributions do not exceed the worst case developed in our single tolerance.

Holding radius tolerance to 0.2% and the three critical spacing tolerances to ± 0.002 inch gives no more accumulated aberration than a 1.0% radius tolerance on a single surface.

For decentering, if referenced to a nominal axis location, it is possible to reference the lens mount to within 0.001 of this location, to reference the lens edge to within 0.001 of the mount and the lens center to within 0.001 of the lens edge. This guarantees a maximum of ± 0.003 decentering, which will give no measurable loss of resolution.

A worst-case accumulation was run with contributions all additive in the same direction.

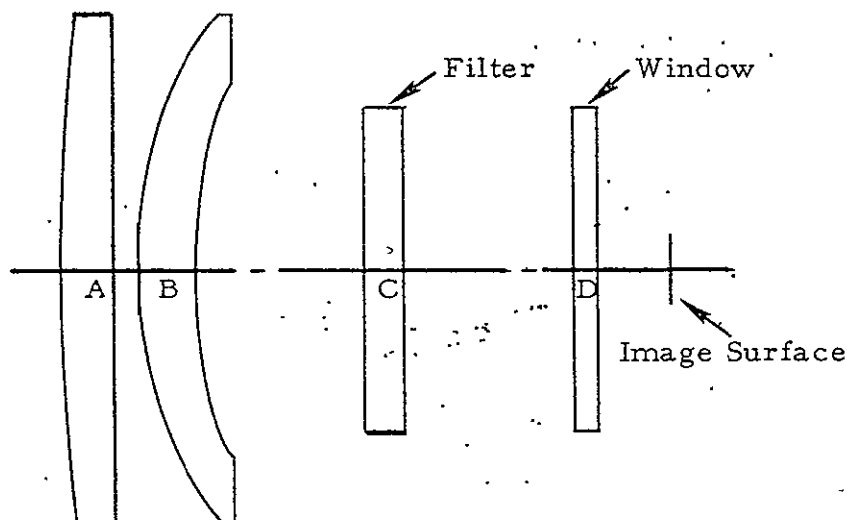
All radius tolerances were 0.2%.

Thickness tolerance on lens A was 0.005 inch.

Air space lens A-B was 0.005 inch.

Thickness lens B, filter and window was 0.002 inch.

The resultant ray trace indicated a blur circle of about 0.00024 inch which is effectively no degradation of the image. Therefore, the above tolerances, which represent reasonable manufacturing requirements, will be specified on the drawings. The system is shown in Figure 3-13. Notes summarize the tolerances.



Lens A (Part #44116)

$R_1 = 6.024$ tolerance $\pm 0.2\%$

Test plate fit 3 rings spherical,
1 ring irregularity; centered
clear aperture diameter 0.718

Thickness 0.100 tolerance ± 0.005

R_2 flat - test plate fit 2 rings spherical,
1 ring irregularity; centered
clear aperture diameter 0.712

Centering tolerance 3 minutes of arc

Spacing Lens A to Lens B 0.020
tolerance ± 0.005

Lens B (Part #44118)

$R_1 = 0.708$ tolerance $\pm 0.2\%$

Test plate fit 3 rings spherical,
1 ring irregularity; centered
clear aperture diameter 0.688

Thickness 0.100 tolerance ± 0.002

$R_2 = 0.812$ tolerance $\pm 0.2\%$

Test plate fit 3 rings spherical,
1 ring irregularity; centered
clear aperture diameter 0.624
sag to flat 0.068 ± 0.005

Centering tolerance 3 minutes of arc

Spacing Lens B to Filter (C) 0.275

The filters location has no effect
on image quality. Location toler-
ance is only determined by clear
aperture requirements. Can be
 $-0.050 + 0.200$

Filter (C)

Both sides flat to 2 rings spheri-
cal, 1 ring irregularity; thickness
0.080 tolerance ± 0.002 ; centered
clear aperture 0.464; wedge toler-
ance: surfaces parallel to 0.0005

Spacing filter (C) to window (D)

0.280. Location of window has no
effect on image quality. Location
tolerance is determined only by
aperture requirements. Can be
 $-0.010 + 0.020$.

Window (D)

Both sides flat to 2 rings spheri-
cal, 1 ring irregularity, thickness
0.040 tolerance ± 0.002 ; clear
aperture diameter 0.140
Wedge tolerance - surfaces par-
allel to 5 minutes of arc.

Distance Window to Detector 0.120

This spacing doesn't affect image
quality as long as the sum of the
three air spaces from Lens B to
the Detector are constant.

Figure 3-13. IR Relay Sketch

Thermal Channel Bandpass Filter

The thermal channel bandpass is specified as 10.5 to 12.6 microns and is determined by the optical bandpass filter, spectral effects of the AR coated germanium and Irtran 2 lenses, and second order effects of the detector spectral response. Spectral effects of these elements other than the bandpass filter are shown in Figure 3-14. The AR coatings for the germanium lenses are peaked at 12 microns due to the intrinsic absorption characteristics of germanium.

The bandpass filter response is decreased approximately 0.05 micron by the second order effects shown in Figure 3-14. The bandpass filter cut-on

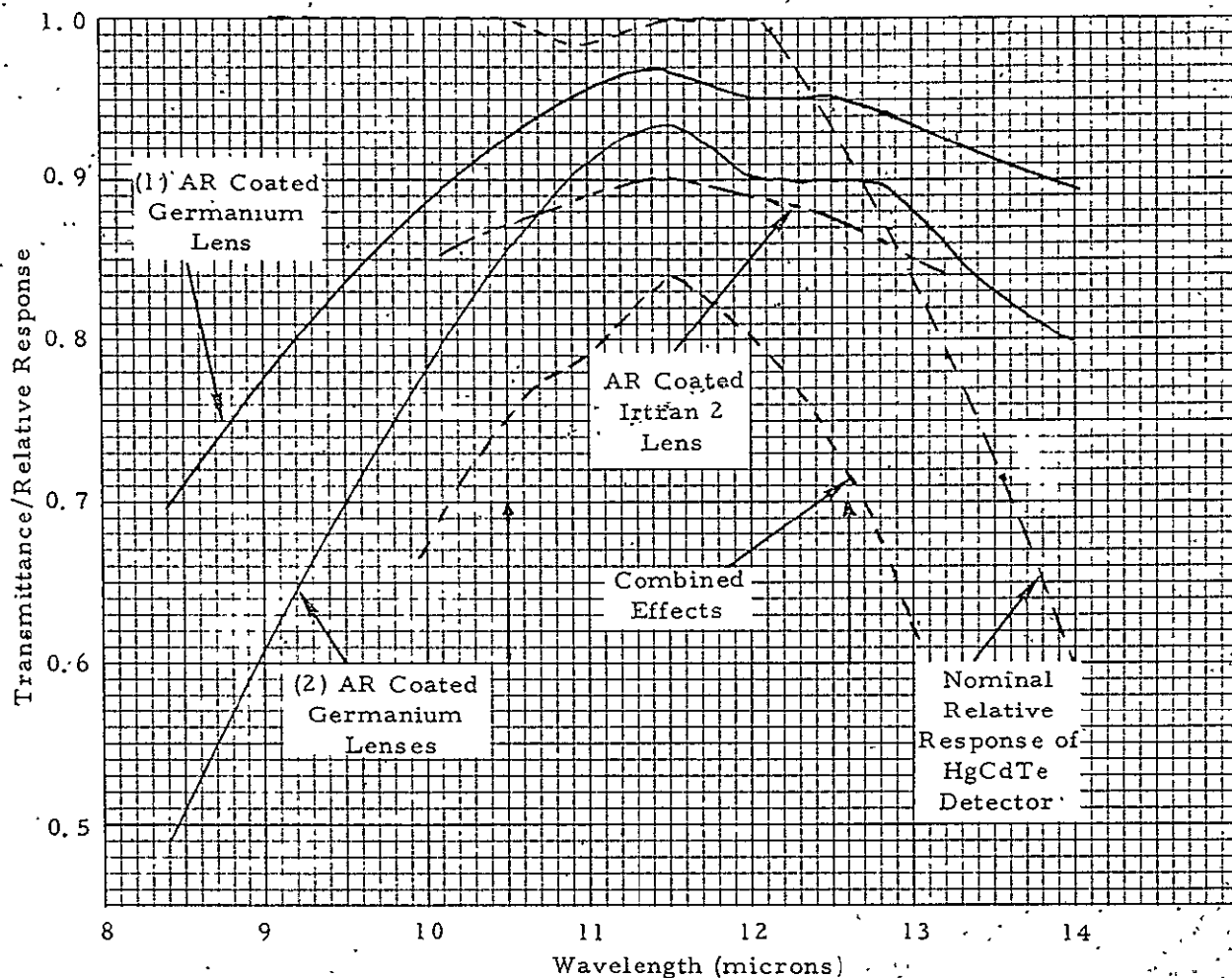


Figure 3-14. Spectral Characteristics of VISSR Optical Components (Excluding Bandpass Filter)

and cutoff wavelengths (transmittance of one-half the peak value) are specified at 10.5 ± 0.1 and 12.6 ± 0.3 microns.

Sensitivity to Thermal Gradients

Two areas are discussed:

1. The criteria for a permissible change in temperature gradient $\Delta T_{\text{pri-sec}}$ and $\Delta T_{\text{pri-spac}}$ for the thermal channel performance operation.
2. The initial temperature gradients between the primary mirror and the secondary mirror, and between the primary mirror and telescope spacer that can be compensated for by the visible and thermal channel focus adjust drives.

The thermal channel performance depends on temperature gradients in the VISSR telescope and relay optical systems. All temperature gradients will be relative to the telescope primary mirror. The image degradation, θ_{ID} , due to telescope and relay system temperature gradients is approximated by

$$\theta_{ID} = |-4.08\Delta T_{SP-S} - 0.84\Delta T_S - 0.065\Delta T_{L1} - 3.28\Delta T_R - 0.38\Delta T_{L2}| \quad (3-1)$$

where θ_{ID} = image blur (due to gradients) in microradians

ΔT_{SP-S} = primary mirror temperature minus telescope spacer temperature

ΔT_S = primary mirror temperature minus secondary mirror temperature

ΔT_{L1} = primary mirror temperature minus spacer between primary mirror and relay lens temperature

ΔT_R = primary mirror temperature minus relay lens temperature

ΔT_{L2} = primary mirror temperature minus spacer between relay lens and detector temperature

All temperature differences are expressed in °C.

The thermal channel IGFOV is 250 μ r and the image blur, excluding temperature gradients, is 210 μ r. If we assume that a total image blur of 250 μ r is permissible and the image degrading factors are independent, the image blur due to temperature gradients is given by

$$\theta_{ID} = \sqrt{250^2 - 210^2} = 136 \mu r$$

Therefore, the tolerable temperature gradients in telescope and relay optical systems can be expressed by

$$|-4.08\Delta T_{SP-S} - 0.84\Delta T_S - 0.065\Delta T_{L1} - 3.26\Delta T_R - 0.37\Delta T_{L2}| \leq 136 \quad (3-2)$$

The preceding equation gives image degradation due to temperature gradients referred to an in-focus isothermal system. However, the same equation is applicable to image degradation resulting from a change of temperature gradients; wherein, the system was initially in-focus with an initial set of temperature gradients. In this case, the ΔT is defined as the change of temperature gradients.

An example to illustrate this would be: For an initially focused system assume $\Delta T_S = -4^\circ C$. This states that the secondary mirror is $4^\circ C$ colder than the primary mirror. Now assume the system is changed, perhaps by going into an eclipse, and the result is $\Delta T_S = -20^\circ C$. The value of ΔT_S to be used in the equation is the change or $\Delta T_S = -20 - (-4) = -16^\circ$.

Thus, using the definition of temperature gradient change for ΔT 's, equation (3-2) can be used to obtain permissible change in temperature gradient and is the answer for item (1).

The relationship between image degradation, θ_{ID} , and defocusing, ΔF , is expressed as

$$\theta_{ID} = \frac{\Delta F}{(f/\#)f} \quad (3-3)$$

where $f/\#$ = system focal ratio

f = system focal length

Furthermore, the image degradation for the visible channel due to temperature gradients is given by

$$\theta_{ID} = |-4.08\Delta T_{SP-S} - 0.84\Delta T_S| \mu r \quad (3-4)$$

Thus, the focal shift drive motion, ΔF_M , required to compensate for initial temperature gradients is related by the following expressions:

Visible Channel. -

$$\Delta F_M = (-3.35\Delta T_{SP-S} - 0.69\Delta T_S) \times 10^{-3} \text{ inch} \quad (3-5)$$

Thermal Channel. -

$$\begin{aligned} \Delta F_M = & (0.017\Delta T_{SP-S} - 0.022\Delta T_S - 0.0017\Delta T_{L1} \\ & - 0.086\Delta T_R - 0.010\Delta T_{L2}) \times 10^{-3} \text{ inch} \end{aligned} \quad (3-6)$$

The total active focus drive mechanism range is

± 0.100 inch for the visible channel

± 0.080 inch for the thermal channel

A portion of this focus range is allotted for initial assembly and alignment of the VISSR optical system. The remainder may be used to correct for thermal gradients. The remainder consists of

± 0.070 inch for the visible channel

± 0.050 inch for the thermal channel

Therefore, limits can be set on equations (3-5) and (3-6) which indicate the maximum temperature gradients that can be compensated for by the active focus drive mechanism. For the visible channel, the expression is

$$|-3.35\Delta T_{SP-S} - 0.69\Delta T_S| \leq 70 \quad (3-7)$$

and the equivalent expression for the thermal channel is

$$\begin{aligned} & |-0.107\Delta T_{SP-S} - 0.022\Delta T_S - 0.0017\Delta T_{L1} \\ & - 0.086\Delta T_R - 0.010\Delta T_{L2}| \leq 50 \end{aligned} \quad (3-8)$$

Equations (3-7) and (3-8) represent the total maximum temperature gradients that can be accommodated by the active focus drive mechanism. If the range is used in the initial focusing then any subsequent change must be in the opposite direction or the drive mechanism will not be able to accommodate the change.

Reflective Coatings

As indicated in previous reports, a question exists concerning the durability of enhanced coatings when applied to the finished electroless nickel-plated beryllium optical elements. The problem is related to the limited substrate temperature that can be tolerated when applying the coatings. Temperature required to obtain reliable coatings may distort the final mirror figure. The compromise solution is to use aluminum with an oxidized silicon monoxide overcoat. These coatings are applied at substrate temperature less than 200°F. The disadvantage is that this coating has lower reflectance in the visible region; it will result in a 20% signal loss and 10% signal-to-noise loss in the VISSR visible channels. The reflectance in the thermal channels will be almost equivalent to that obtainable with the enhanced coatings.

Mr. John Osentowsky of NASA/GSFC has generated a suggested optical coating process specification for silicon monoxide (SiO) protected aluminum (Al + SiO).¹ This is shown in Table 3-7.

Based on preliminary analysis, it appears that the SiO overcoat thickness should be thicker for the scan mirror (operating at 45°) than for the primary and secondary mirrors. Using optical constants for Al from the American Institute of Physics Handbook 2nd Edition (see Table 3-8) and refractive index of reactively deposited silicon monoxide as 1.50, the reflectance for the Al-SiO was calculated and is plotted in Figure 3-15.

The optimum thickness of silicon monoxide is 0.2 micron for the primary and secondary mirrors and 0.24 micron for the scan mirror as indicated by the reflectance calculations. These values have been confirmed by test coating runs before being used on the VISSR beryllium elements.

¹ Applied Optics 9, 339 (1970).

Table 3-7. Optical Coating Specifications for VISSR Optics

1. Coating selected - Silicon oxide (SiO) protected aluminum (Al + SiO)⁽¹⁾
2. Aluminum
 - a. Deposit at a rate ≥ 300 A/sec at 10^{-5} Torr or less
 - b. Starting material 99.99% purity or better certified
 - c. Aluminum sources to be shuttered until vaporization stage reached
 - d. Thickness 800A - 1000A
3. SiO
 - a. Kemet Company selected grade or equivalent (certified)
 - b. Reactively deposit SiO at approximately 8×10^{-5} Torr oxygen at 3-5 A/sec
 - c. Thickness $\lambda/2$ at 6000A
4. Preparation of mirrors for Al + SiO coating
 - a. Mirror cleaned with GSFC supplied procedure or equivalent
 - b. Dust contamination of surface must be avoided before optics placed in vacuum chamber
 - c. DC glow discharge clean mirror just prior to deposition of optical coatings
 - d. Pre-deposit $\lambda/4$ SiO⁽²⁾ (at 5500A) on mirror. This provides an electrochemical barrier between aluminum film and metal substrate; also improves adherence
 - e. Al + SiO then deposited per items 2 and 3 above
5. UV irradiation of mirrors after coating⁽³⁾
 - a. Irradiate mirrors in air with Hanovia 7520, 435-W quartz lamp
 - b. Irradiation time required is approximately 5 hours with a lamp to mirror separation of about 20 cm
 - c. Large mirror should be illuminated as uniformly as possible
6. Thickness and reflectance uniformity
 - a. Test depositions to be made on 2 in. sq. or 2-inch diameter glass samples located to simulate large VISSR mirrors
 - b. Tests to demonstrate that coating thickness is uniform to ± 100 A/sec and reflectance uniform to $\pm 5\%$
 - c. Test samples to be retained for future reference or testing
7. Reflectance acceptance test
 - a. Acceptance will be based on the reflectance of test samples coated with each mirror
 - b. Samples, provided with mirrors, must receive same treatment; i.e., cleaning, etc.
 - c. Minimum acceptable reflectance 87%

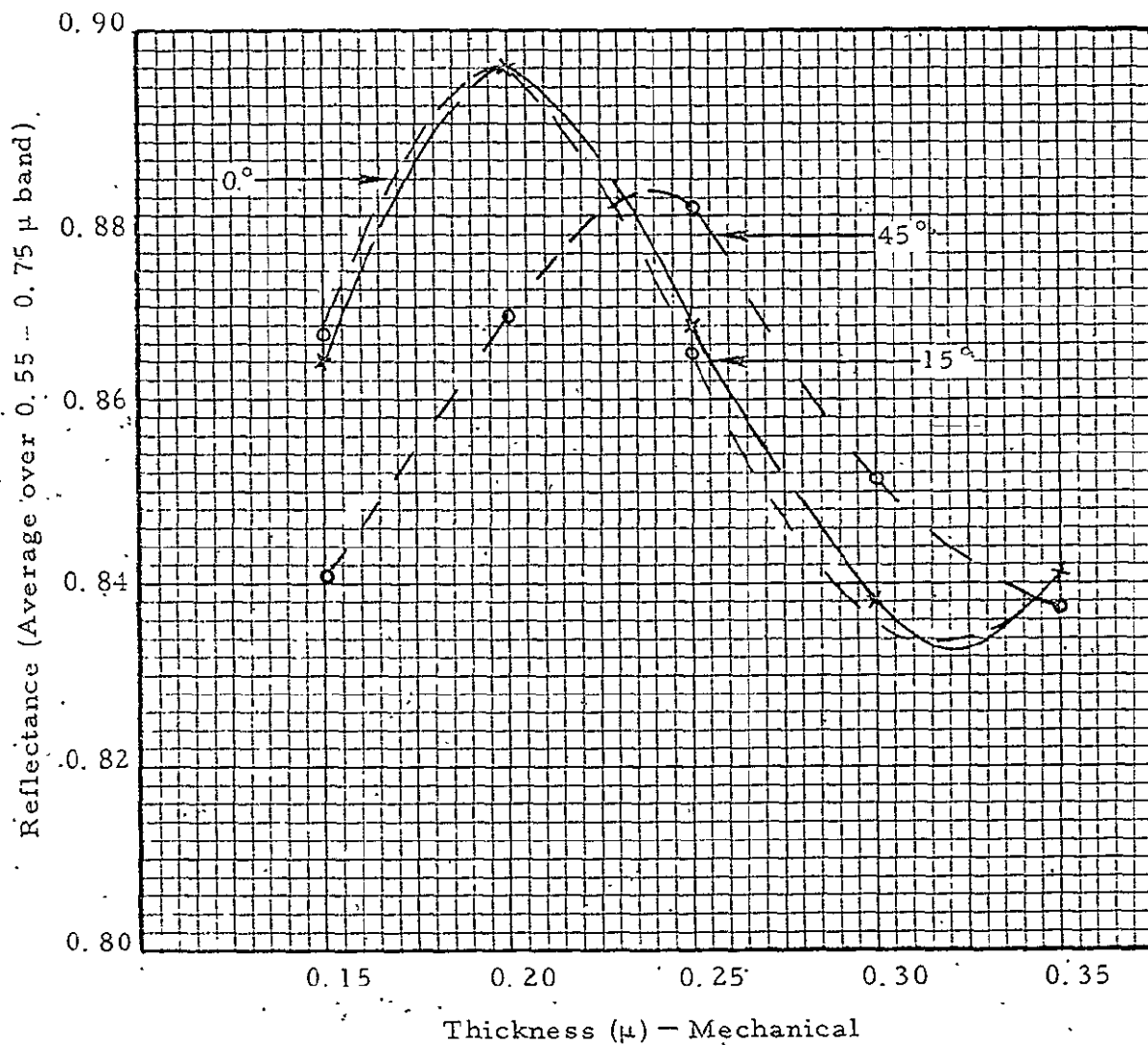
(1) Applied Optics 9, 339 (1970).

(2) This film is true SiO; i.e., deposit at low pressure and a rate of approximately 30 A/sec.

(3) J. Opt. Soc. Am. 53, 1089 (1963).

Table 3-8. Aluminum Optical Constants

$\lambda(\mu)$	η	R
0.546	0.82	5.99
0.578	0.93	6.33
0.650	1.30	7.11
0.700	1.55	7.00
0.750	1.80	7.12

Figure 3-15. Spectral Reflectance of Al-SiO
(Average Over 0.55μ-0.75μ Band)

Since the VISSR system does not require any near ultraviolet sensitivity and indeed its short-wavelength band edge is near 0.5 micron, the ultraviolet irradiation which enhances the near UV reflectance is not required.

Optical Coating Laboratory, Inc., coated the mirrors for both Tinsley Laboratories and Perkin-Elmer Corporation. SBRC has modified the optical system specifications (SBRC 18761) regarding the coating requirements. The specification is a performance specification rather than a process specification.

VISIBLE RELAY SYSTEM

General

The visible relay system detailed design uses a ten-element linear fiber array; one end cemented to the face of a $45^\circ - 45^\circ - 90^\circ$ glass prism located at the telescope prime focal plane. The prism represents a convenient way to make a sharp fold in the ray path without necessitating a short radius of curvature in the fibers. The fiber ends effectively disappear in the cemented interface because the refractive indices of fiber, cement, and prism are comparable. This minimizes the criticalness of the fiber polish and flatness. The front surface of the prism will have an anti-reflection coating and the reflecting surface will function by total internal reflection.

The two end fibers in the linear array are used for alignment purposes. They are illuminated by an auxiliary lamp and serve as a convenient means of identifying the VISSR optical system axis.

Detailed Design

The following critical optical areas required optimizing during the detailed design.

1. Transmittance
2. Decollimation effects
3. Spurious radiation
4. Fabrication limitations

Transmittance of the fiber optics assembly is optimized by 1) anti-reflection coating of the first prism surface, utilizing total internal reflection at the prism hypotenuse (material refractive index of 1.85), and 2) minimizing the surface reflections by effectively immersing the prism and fiber surfaces in EPO-TEK 301 epoxy.

The optical filtering has been combined with the fiber optics assembly by cementing a sharp cut color glass on the fiber exit end. Corning Glass No. 3484, or equivalent, is used for the fiber end block and results in a

short-wavelength cut-on point at 0.53 micron. The long-wavelength cutoff is determined by the photomultiplier spectral sensitivity.

The fiber transmittance, with end reflection losses as a function of fiber length, is illustrated in Figure 3-16. It indicates that the fiber length should be minimized for maximum transmittance. However, decollimation effects caused by bends in the fibers must be considered when routing the fibers.

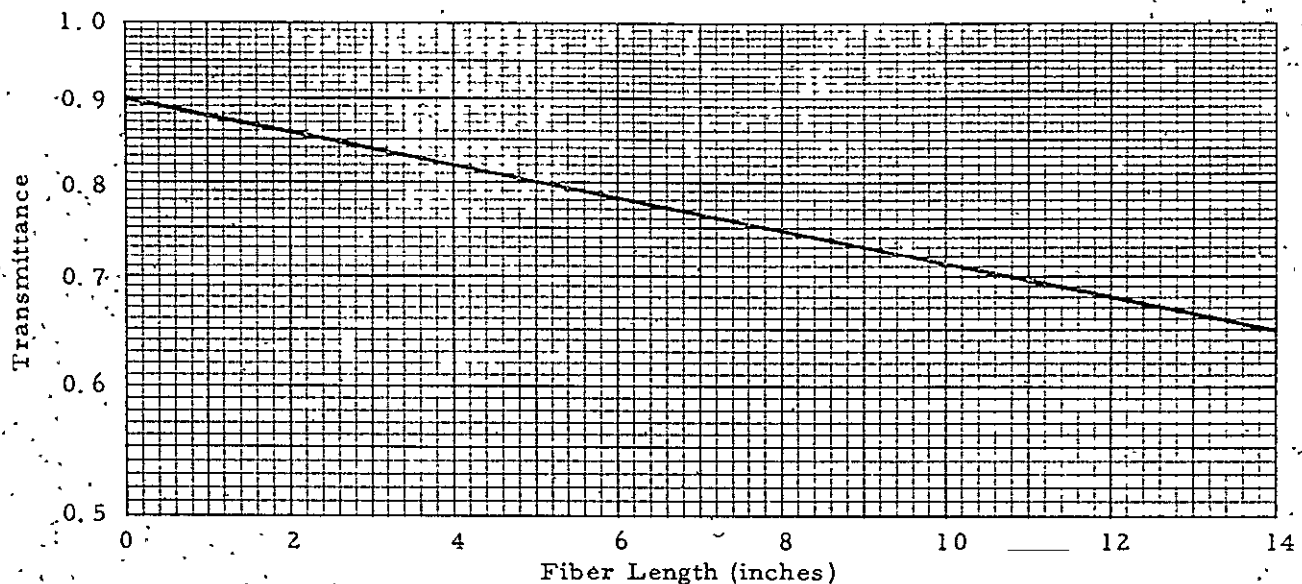


Figure 3-16. Fiber Transmittance as a Function of Fiber Length

The VISSR telescope operates at $f/7$; therefore, the incident beam at the fiber front end is $f/7$. Broadening occurs as a result of defects in the fiber, fiber bends, and surface imperfections; thus making the exiting $f/\#$ smaller.

A series of measurements was made with a square single fiber to determine the decollimation effects as a function of bend radius and length of bend arc. The results are graphically illustrated in Figure 3-17. An $f/7$ input was used throughout the measurements. Extrapolating the data in Figure 3-17 gives a relative percentage of energy contained in an $f/4$ exit solid angle for a 180° arc as a function of bend curvature. This is plotted in Figure 3-18.

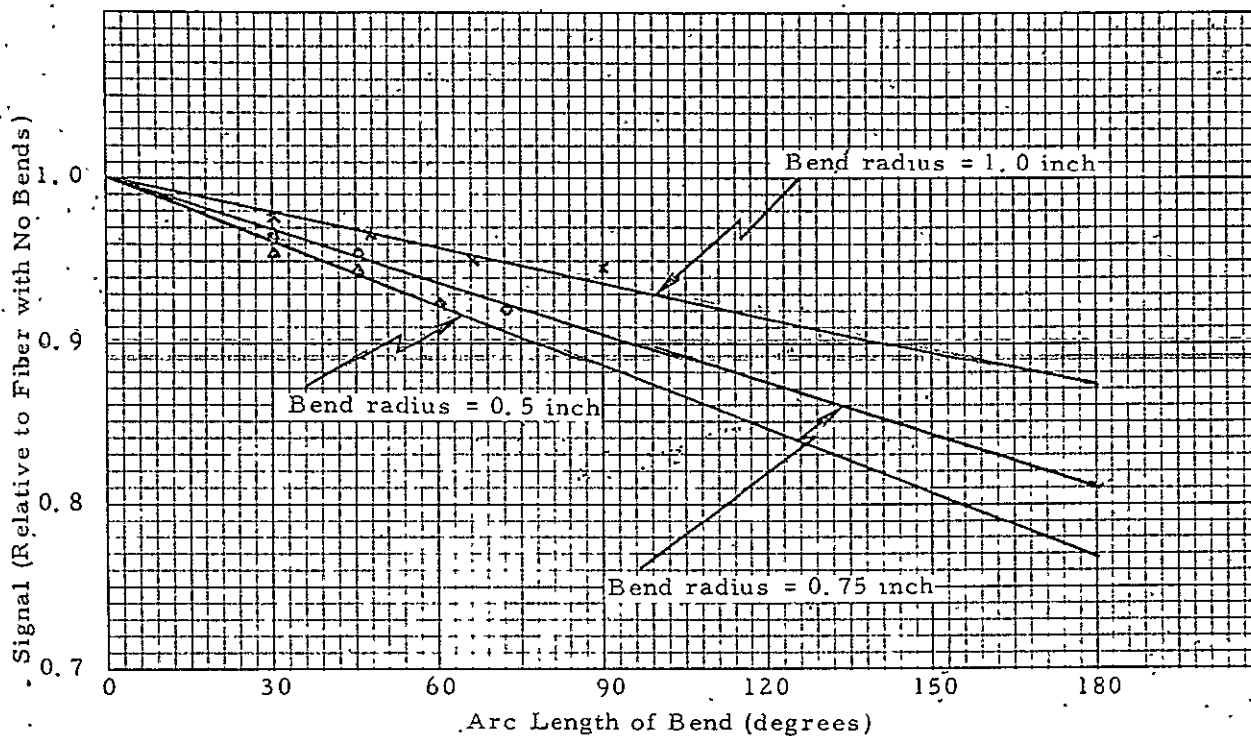


Figure 3-17. Signal vs Bend Arc Length as a Function of Fiber Bend Radii (f/7 Input with f/4 Output)

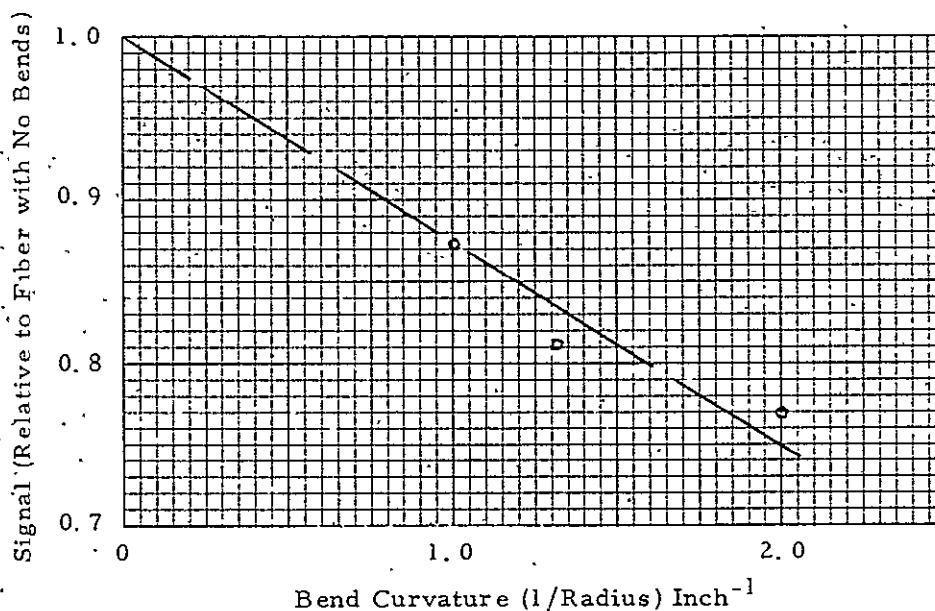


Figure 3-18. Relative Signal vs Bend Curvature for Arc Length of 180° (f/7 Input with f/4 Output)

No decollimation effects were in excess of $f/3$ exit solid angle for any of the measurements using an $f/7$ input solid angle, curvatures ($1/\text{radius}$) between 0 and 2.0 inch^{-1} and arc lengths of 0° to 75° .

The VISSR fiber optics assembly restricts the fiber curvature to less than 1.33 inch^{-1} (0.75-inch radius) and the longest fiber is 14.0 inches.

Spurious radiation or crosstalk can result from several causes. Figure 3-19 illustrates one potential source. Light rays from images formed outside the fiber face can reflect off the cement surface and enter the fiber through the cladding. At steep angles, the ray will exit through the cladding on the opposite surface. However, at lesser angles they will be conducted with the fiber-cladding unit and act as a single fiber. This is also true of imaging forming rays that are incident on the cladding area. This source of spurious energy can be minimized by placing an absorbing surface, such as potting compound, in intimate contact with the fiber bundle for some distance. The absorbing material provides an efficient sink for energy being transmitted in the cladding.

Fiber defects at the common end can result in light being scattered into other fibers. The absorbing potting compound minimizes this source of crosstalk.

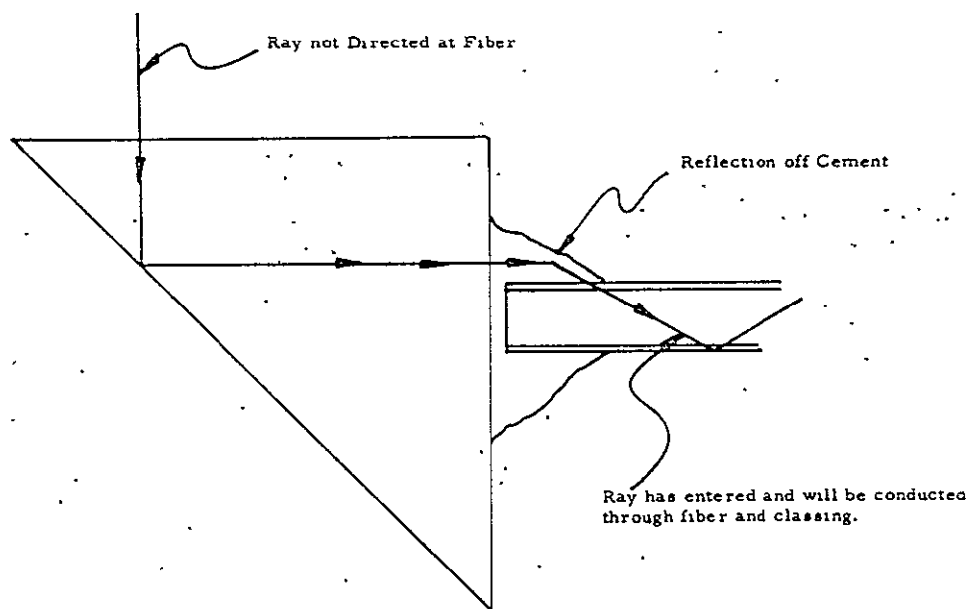


Figure 3-19. Entry of Unwanted Ray into Fiber

Since the prism is bonded to metal, the metal-prism interface could have appreciable reflectivity. Initially it was assumed that the metal surface could be chemically blackened. However, the fiber manufacturers indicated that it was necessary to polish the metal and fiber ends after the fibers are bonded into the metal. Thus, the chemically blackened surface would be polished off leaving a shiny polished metal surface.

The initial fiber optics assembly used a black Armstrong A-12 epoxy encapsulation technique. There was partial delamination of fibers-EpoTek 301-prism bonds. This was attributed in part to the black A-12 encapsulation interface. Subsequent units have polished, shiny metal-EpoTek 301-glass configurations.

The crosstalk problem noted is covered in the crosstalk specification, which is part of the fiber optics subcontract. The specification is as follows. When one fiber is illuminated (common end), the energy at the termination end for each of the other fibers (1 through 8) shall be less than 1% of the energy transmitted in the illuminated fiber. When any seven fibers 1 through 8 are equally illuminated, the energy at the termination end of the unilluminated fiber shall not be more than three times the value that occurs when any one adjacent fiber is illuminated rather than the seven. The fiber optics assemblies as built meet this crosstalk specification.

PMT Enhancement

The PMT enhancement technique has been described in Volume 1 of the Second Quarterly Report compiled for the Detailed Design Review. Due to the greater than anticipated decollimation effects of the fibers, the effective $f/\#$ incident on the PMT enhancement prism will be $f/3$ rather than $f/4$. Thus, the complete optical beam will have three encounters with the photocathode rather than four as indicated in the above referenced report although a major portion of the beam will still have four encounters or more.

The following design requirements and constraints were assumed. Damage to the photomultiplier can occur if the irradiated level is sufficiently high. To eliminate this possibility, energy exiting the fiber optics in an $f/4$

bundle will irradiate a photocathode surface area of $3 \times 10^{-2} \text{ cm}^2$, minimum.

To maximize the signal, the enhancement mechanism will accept an $f/1.5$ bundle (in air) for first impingement on the photocathode and an $f/4$ bundle (in air) will strike the photocathode at least three times.

The selection of $f/4$ and $f/1.5$ bundles was based on fiber optics beam divergence measurements illustrated in Figure 3-20, since the fiber optics are irradiated by the telescope with an $f/7$ solid angle and the beam divergence caused by the fibers, as illustrated in Figure 3-20, shows that an exit solid angle of $f/4$ contains 95% of the energy in an $f/1.5$ solid angle. Furthermore, since an $f/4$ exit angle in air converts to a 5° half-angle in glass and the enhancement literature indicates gain curves that are relatively flat for about 8° either side of the peak, it is not necessary to have any collimating optics between the fiber and the PMT enhancement prism.

The final design of the PMT enhancement used the EMR photomultiplier parameters. The dimensions are as follows:

Faceplate thickness	= 0.050 inch
Photocathode diameter	= 1.00 inch
Tube face diameter	= 1.38 inches
Angle of incidence for maximum sensitivity	= 65°

Figure 3-21 illustrates the PMT end assembly. The fiber is cemented to a glass filter block (B). The exit face of the block is brought near a 25° - 65° - 90° prism (A) cemented to the PMT faceplate.

The upper ray of the $f/2.25$ bundle will strike the prism face and be reflected to the photocathode. This gives a smaller prism base, which prevents the $f/6$ bundle from re-entering the prism.

The upper ray of the $f/6$ bundle is at $69^\circ 45'$. The space between bounces is $2t \tan \theta$ where t is tube thickness or 0.050. Since $\tan 69^\circ 45'$ is 2.710, 0.271-inch intervals occur between bounces for this ray.

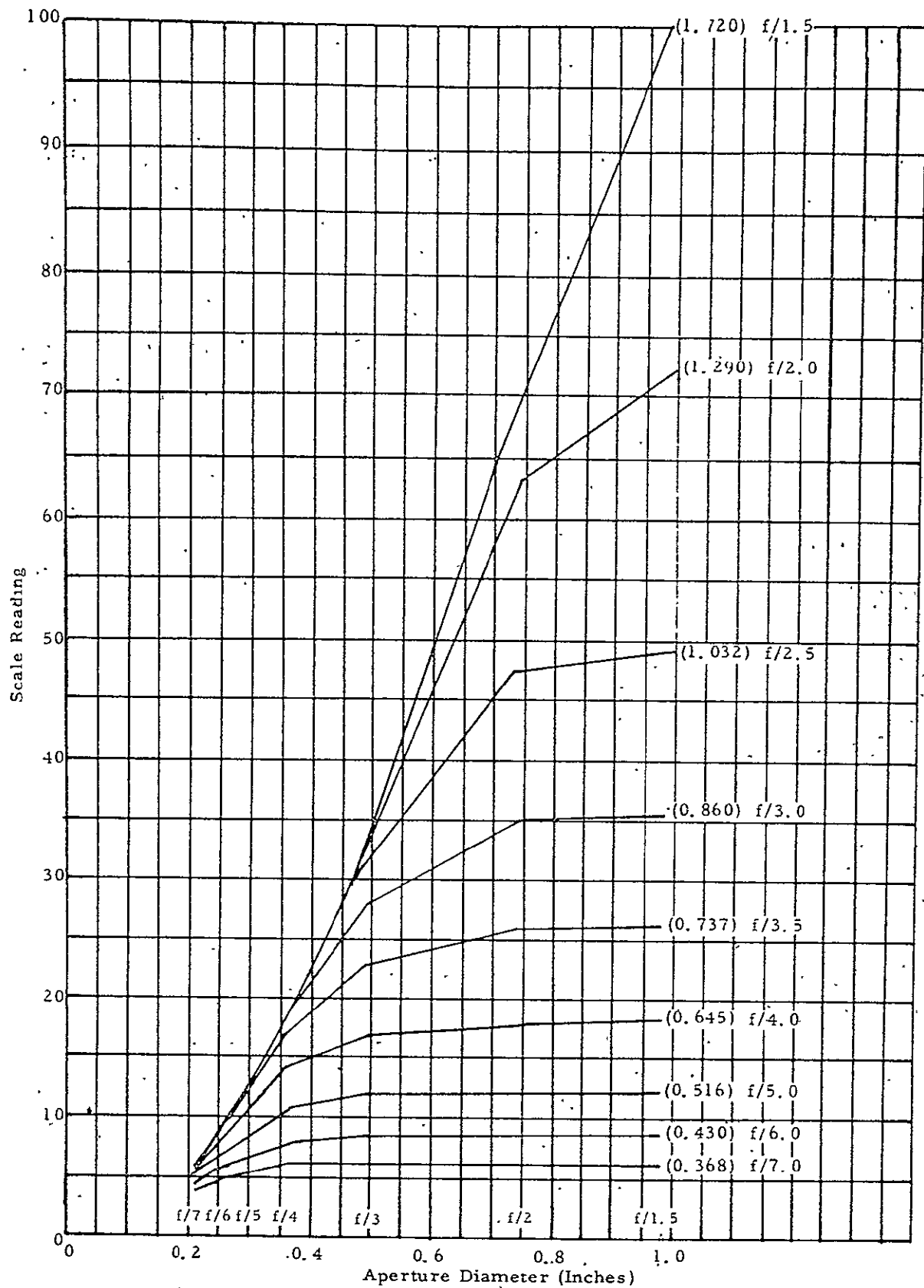


Figure 3-20. Beam Divergence

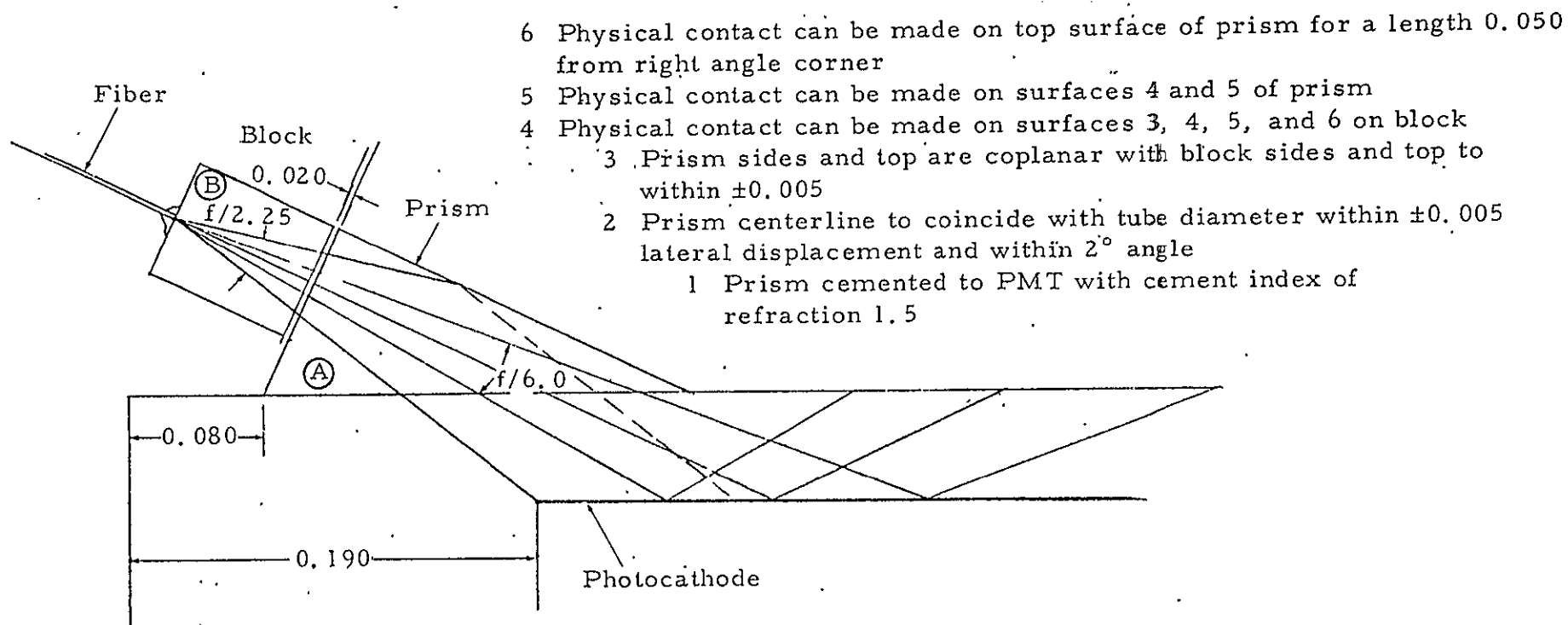


Figure 3-21. Fiber Optics - PMT Assembly, VISSR

The first bounce for this ray occurs at 0.183 inch from the photocathode edge. Three more bounces use $0.271 \times 3 = 0.813$ inch. So there are four incidences in 0.996 inch or within a cathode diameter.

For the lower f/6 ray, a $60^\circ 15'$ incidence angle and 0.175-inch interval occur between bounces. First incidence occurs at 0.060 inch from the cathode edge. The original incidence plus five bounces uses up 0.945 inch for six impingements on the photocathode.

The 25° - 65° - 90° prism was chosen to permit a ray bundle with an axis normal to the surface to pass through the faceplate and impinge on the photocathode at 65° . No loss occurs at the cemented interface because the refractive indices of the prism, cement, and PMT faceplate match.

Figures 3-22 and 3-23 give details of the PMT enhancement prism and the fiberglass block.

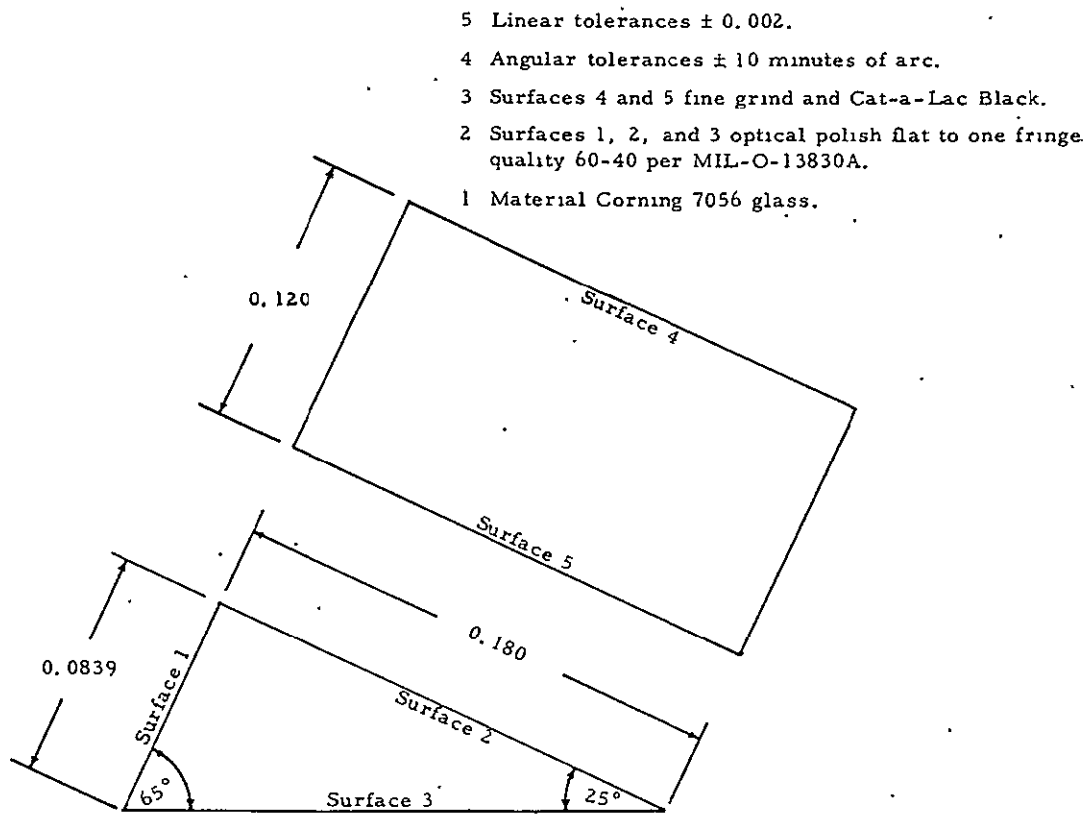


Figure 3-22. Prism for Attachment to PMT in VISSR

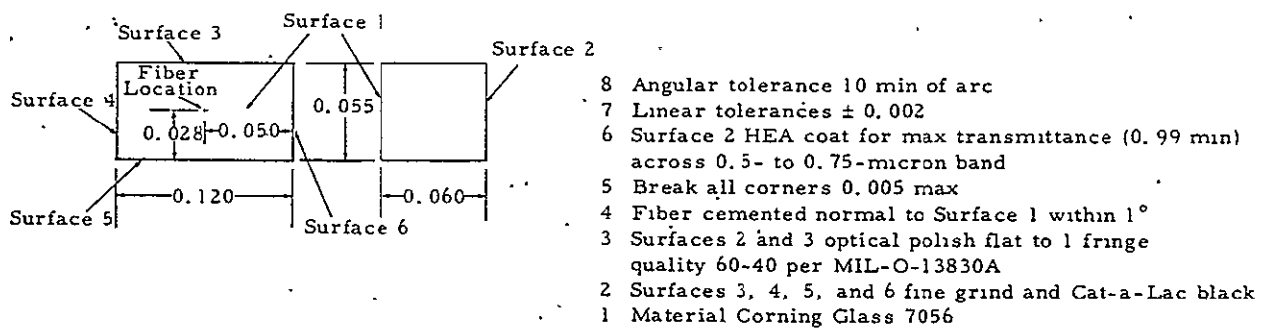


Figure 3-23. Block Details

OPTICAL RESOLUTION

The optical system considered for VISSR is moderately large and near diffraction-limited. The spatial resolution of the idealized theoretical design can be degraded by many factors. These factors have been considered and are minimized wherever possible to achieve the required optical performance.

The factors considered were:

1. Scan mirror figure
2. Primary mirror figure
3. Secondary mirror figure
4. Telescope residual geometrical aberrations
5. Primary-secondary mirror alignment
 - Axially - along optical axis
 - Laterally - perpendicular to optical axis
 - Tilt
6. Misalignment of field stops in focal plane
7. Aperture diffraction effects
8. Thermal effects
 - a. Different forms of beryllium have different thermal expansion coefficients
 - b. Thermal gradients parallel to optical axis
 - c. Beryllium anisotropy - thermal expansion coefficient is directionally dependent
 - d. Bimetallic strip effect - beryllium and Kanigen electroless nickel have different thermal expansion coefficients
 - e. Thermal channel, isothermperature and temperature gradient effects - associated with the infrared channel
 - f. Thermal gradients in VISSR optical elements with effect on optical system behavior
9. Stresses
 - a. Residual stresses - in the beryllium mirror blanks
 - b. Electroless nickel plating stresses - stress levels induced by the Kanigen electroless nickel plating
10. Spatial error resolution budget

The following summarizes considerations taken for some of these items.

1. Scan Mirror Figure

An analytic expression for image degradation, θ_{ID} , is derived. The derivation assumes that the mirror surface deviates from an idealized plane and is a spherical surface of large radius.

The focal length, F , of two mirror systems can be approximated by

$$\frac{1}{F} = \frac{1}{f_{sc}} + \frac{1}{f_o} \quad (3-9)$$

or

$$F = \frac{f_o f_{sc}}{f_o + f_{sc}}$$

Let f_o = focal length of Primary-Secondary mirror system

f_{sc} = focal length of scan mirror

By differentiation

$$\begin{aligned} \Delta F &= \frac{f_o \Delta f_{sc}}{f_o + f_{sc}} - \frac{f_o f_{sc} \Delta f_{sc}}{(f_o + f_{sc})^2} \\ &= \frac{f_o^2 \Delta f_{sc}}{(f_o + f_{sc})^2} \end{aligned} \quad (3-10)$$

Since $f_{sc} \gg f_o$

$$\Delta F \approx \frac{f_o^2 \Delta f_{sc}}{f_{sc}^2} \quad (3-11)$$

The scan mirror is oriented at an angle, ϕ , with respect to the telescope system. Thus

$$\Delta f_{sc} = \frac{f_{sc}}{\cos \phi} - f_{sc} \cos \phi \quad (3-12)$$

This corresponds to the two astigmatic images formed by a spherical mirror operated off axis. If we assume the scan mirror and telescope combination is focused, such that, the minimum blur circle is used, the angular image degradation, θ_{ID} ,

$$\theta_{ID} = \frac{\Delta F}{2} \cdot \frac{D}{f_o} \cdot \frac{1}{f_o} \quad (3-13)$$

where image degradation (linear)

$$= \frac{\Delta F}{2} \cdot \frac{D}{f_o}$$

therefore

$$\theta_{ID} = \frac{D}{2f_{sc}} \left(\frac{1}{\cos \phi} - \cos \phi \right) \quad (3-14)$$

since for a spherical surface

$$f_{sc} = \frac{R_{sc}}{2} = \frac{x^2 + y^2}{4x} \approx \frac{y^2}{4x} = \frac{D^2}{16x} = \frac{(1.414D)^2}{16x}$$

where 1.414D gives scan mirror major axis dimension. Thus

$$\theta_{ID} = \frac{2x}{D} \left(\frac{1}{\cos \phi} - \cos \phi \right) \quad (3-15)$$

where x is the scan mirror deviation from a plane and since $\phi \approx 45^\circ$ for the present system

$$\theta_{ID} = \frac{2.83x}{D} \quad (3-16)$$

If it is assumed that there is no refocusing of the telescope system, θ_{ID} would be larger by a factor of three.

2/3. Primary-Secondary Mirror Figure

The simplifying assumption made in the derivation given below is that the ideal mirror surface has superimposed on it a spherical component and that the focal plane is not adjusted to correct for it.

The system can be treated as if two mirrors are present. Thus,

$$f = \frac{f_o f_e}{f_e + f_o} \quad (3-17)$$

where f_o = focal length of ideal mirror figure

f_e = focal length of surface figure error

$$\Delta f = f_o - \frac{f_o f_e}{f_e + f_o} = \frac{f_o^2}{f_o + f_e} \approx \frac{f_o^2}{f_e} \quad (3-18)$$

where $f_o \ll f_e$

Image degradation I_D is given by

$$\frac{I_D}{\Delta f} = \frac{D}{f_o}$$

and

$$I_D = \frac{D f_o}{f_e} = \frac{D f_o}{D^2 / 16x} = \frac{16 f_o x}{D} \quad (3-19)$$

For a spherical surface

$$f_e = \frac{R_e}{2} = \frac{x^2 + y^2}{2x} \approx \frac{y^2}{4x} = \frac{D^2}{16x}$$

and the angular image degradation, θ_{I_D} , is

$$\theta_{I_D} = \frac{16x}{D} \quad (3-20)$$

4. Telescope Residual Geometrical Aberrations

The telescope residual geometrical aberrations are calculated using a computer program that traces rays through the optical system for prescribed field angles and plots X-Y image spot diagrams.

5. Primary-Secondary Mirror Alignment

The effect of axial, lateral, and tilt misalignment of the primary and secondary mirrors are calculated in an exact manner using the computer trigonometrical ray trace program mentioned above.

The axial separation misalignment effect is approximated by the use of Gaussian first order equations as shown below. The back focal length, BFL, is given by

$$BFL = \frac{f_s (S_p - f_p)}{S_p - f_p - f_s} \quad (3-21)$$

where f_s = secondary mirror focal length
 f_p = primary mirror focal length
 S_{p-s} = primary-secondary mirror spacing

Differentiating with respect to S_{p-s}

$$\frac{\partial (BFL)}{\partial S_{p-s}} = \frac{f_s}{S_{p-s} - f_p - f_s} + \frac{f_s f_p - f_s S_{p-s}}{(S_{p-s} - f_p - f_s)^2}$$

Simplifying by collecting terms

$$\frac{\partial (BFL)}{\partial S_{p-s}} = \frac{-f_s^2}{(S_{p-s} - f_p - f_s)^2} \quad (3-22)$$

and system effective focal length, EFL, is given by

$$EFL = \frac{f_s f_p}{f_p + f_s - S_{p-s}} \quad (3-23)$$

and by defining magnification, M, by

$$M = - \frac{EFL}{f_p} \quad (3-24)$$

then

$$\frac{\partial BFL}{\partial S_{p-s}} = -M^2 \quad (3-25)$$

6. Misalignment of Field Stops in Focal Plane

This effect is simple defocusing. For example, the field stops are not located in the focal plane of the telescope.

If the defocusing magnitude is denoted by ΔF_d the angular image degradation is given by

$$\theta_{ID} = \frac{\Delta F_d}{(f/\#) f_o} \quad (3-26)$$

7. Aperture Diffraction Effects

The diffraction effects have been calculated using a computer program which assumes a round aperture with a centrally located obscuration. Figure 3-24 is a graphical representation of the diffraction effects.

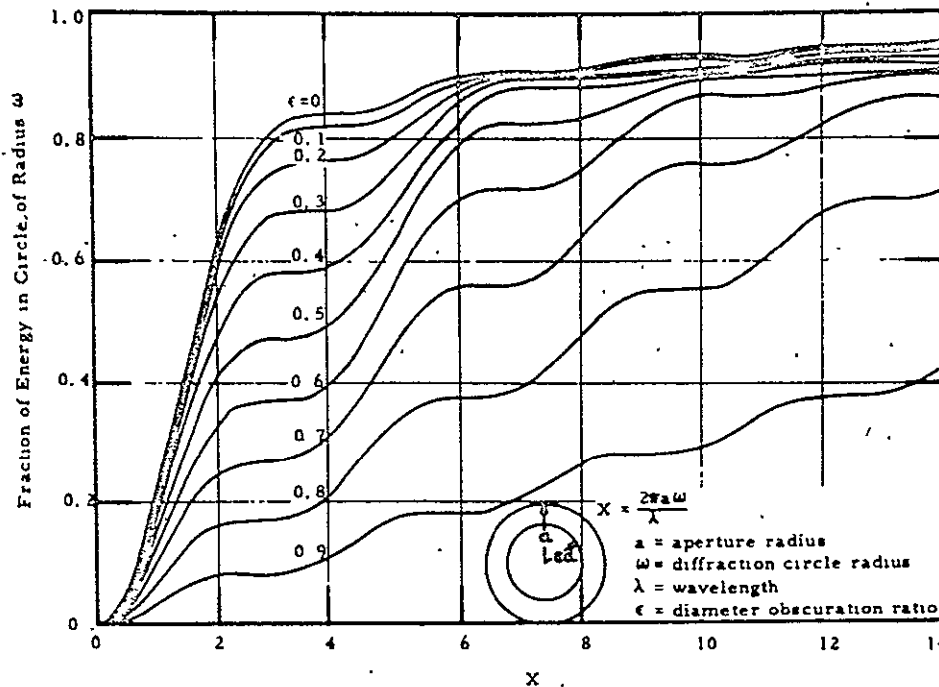


Figure 3-24. Diffracted Energy as a Function of Aperture, Obscuration, and Wavelength

8. Thermal Effects

The following thermal effects have been considered; a) isothermature system with materials having differing thermal expansion coefficients (α), and b) thermal gradients parallel to the optical axis.

During the preliminary optical design phase several alternate approaches were explored. These included the so-called two mirror and three mirror designs. Expressions based on first order (Gaussian) equations were developed for both systems to cover items a and b above.

8a/8b. Two Mirror System - This system is schematically shown in Figure 3-25. The symbols used are shown in the figure.

Defining the defocusing (F) as:

$$F = BFL - S_{s-f} \quad (3-27)$$

Differentiating

$$\frac{dF}{dT} = \frac{dBFL}{dT} - \frac{dS_{s-f}}{dT} \quad (3-28)$$

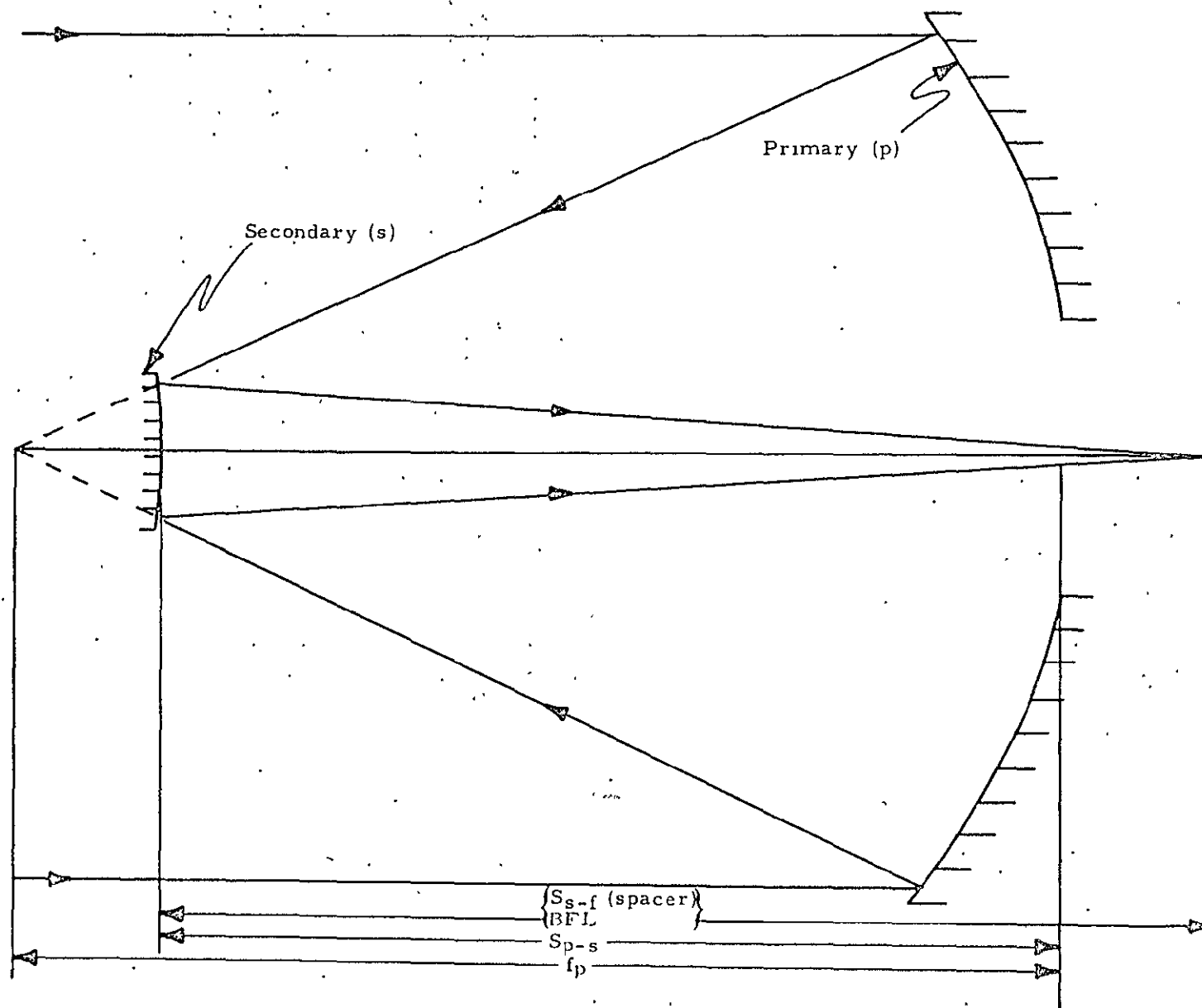


Figure 3-25. Two-Mirror Configuration

However, the back focal length (BFL) is a function of f_p , S_{p-s} and f_s . Therefore,

$$\frac{dBFL}{dT} = \frac{\partial BFL}{\partial f_p} \frac{df_p}{dT} + \frac{\partial BFL}{\partial S_{p-s}} \frac{dS_{p-s}}{dT} + \frac{\partial BFL}{\partial f_s} \frac{df_s}{dT} \quad (3-29)$$

and

$$BFL = \frac{f_s(S_{p-s} - f_p)}{S_{p-s} - f_p - f_s} \quad (3-30)$$

and it can be shown that

$$\frac{\partial BFL}{\partial f_p} = M^2 \quad (3-31)$$

$$\frac{\partial BFL}{\partial S_{p-s}} = -M^2 \quad (3-32)$$

$$\frac{\partial BFL}{\partial f_s} = (M+1)^2 \quad (3-33)$$

where

$$M = - \frac{EFL}{f_p} \quad (3-34)$$

and EFL = Effective focal length of system.

Since

$$\frac{df_p}{dT} = \alpha_p f_p \quad (3-35)$$

$$\frac{dS_{p-s}}{dT} = \alpha_{S_{p-s}} S_{p-s} \quad (3-36)$$

$$\frac{df_s}{dT} = \alpha_s f_s \quad (3-37)$$

then

$$\frac{dF}{dT} = M^2 \alpha_p f_p - M^2 \alpha_{S_{p-s}} S_{p-s} + (M+1)^2 \alpha_s f_s - \alpha_{S_{s-f}} S_{s-f} \quad (3-38)$$

An extension of the above equation gives defocusing (ΔF) caused by temperature gradients along the optical axis. It is assumed that some "average" temperature can be assigned to each element.

$$\begin{aligned} \text{Thus } \Delta F = M^2 \alpha_{p-f} \Delta T_p - M^2 \alpha_{s-p-s} S_{p-s} \Delta T_{s-p-s} + (M+1)^2 \alpha_{s-f} \Delta T_s \\ - \alpha_{s-f} S_{s-f} \Delta T_{s-f} \end{aligned} \quad (3-39)$$

8c. Beryllium Anisotropy. - Commercially hot pressed beryllium is anisotropic. The uniaxial pressing results in a nonrandom orientation of beryllium crystallites. Beryllium single crystals are hexagonal in shape with thermal expansion coefficients¹ given in Table 3-9.

Table 3-9. Thermal Expansion Coefficients per °C, Single Crystal Beryllium

Temperature	$\alpha_{ }$	α_{\perp}	$1/3(\alpha_{ } + 2\alpha_{\perp})$
250°K	7.4×10^{-6}	10.6×10^{-6}	9.5×10^{-6}
300°K	9.1	12.6	11.43
350°K	10.2	13.9	12.7

W. Goggin of Perkin Elmer Corp³ and R. Maringer of Battelle Memorial Institute³ have quoted that longitudinal and radial expansion coefficients vary as much as 7.7% for the commercially available hot pressed beryllium. Paul Winslow³ of Hughes Aircraft Company has measured 2% to 5% variation.

Due to this anisotropy, the figure of optical components will be modified as a function of temperature. An analytical approximation is given below.

Let α_R and α_L be the thermal expansion coefficients perpendicular and parallel to the mirror optical axis (which is also the pressing axis). The mirror focal length, f , is approximated by

$$f = \frac{y^2}{4x}$$

where y is the radial distance from the optical axis and

x is the surface sag at y

By partial differentiation

$$\begin{aligned} \frac{df}{dT} &= \frac{\partial f}{\partial y} \frac{dy}{dT} + \frac{\partial f}{\partial x} \frac{dx}{dT} = \frac{y}{2x} \alpha_R y - \frac{y^2}{4x^2} \alpha_L x \\ \frac{df}{dT} &= \frac{y^2}{4x} (2\alpha_R - \alpha_L) = f(2\alpha_R - \alpha_L) \end{aligned}$$

²American Institute of Physics Handbook, 2nd Edition, p 4-68.

³Private communication.

If $\alpha_R = \alpha_L$ the expression reduces to

$$\frac{df}{dT} = f\alpha$$

which is the expected result.

The quantity, $\frac{df}{dT}$, consists of two parts. One part is the focal length change due to the anisotropy, $\alpha_R \neq \alpha_L$. The other portion is due to the finite value of thermal expansion coefficient, $\alpha_R = \alpha_L \neq 0$. Since the SMS/VISSR system is all beryllium the second component, $\left(\frac{df}{dT}\right)_2$, should be subtracted out.

The beryllium housing is expected to be sheet beryllium formed in a cylinder and thus its effective thermal expansion coefficient relative to the mirror is unknown. Three cases will be considered. They consist of letting the spacer α be α_R , α_L , and $(1/3)(2\alpha_R - \alpha_L)$. An expression for (df/dT) , is given for each of three cases:

Case I using α_R

$$\left(\frac{df}{dT}\right)_1 = f(\alpha_R - \alpha_L)$$

Case II using α_L

$$\left(\frac{df}{dT}\right)_1 = 2f(\alpha_R - \alpha_L)$$

Case III using $(1/3)(2\alpha_R - \alpha_L)$

$$\left(\frac{df}{dT}\right)_1 = (4/3)f(\alpha_R - \alpha_L)$$

The image degradation, θ_{ID} , due to a temperature difference, ΔT , is given by

$$\theta_{ID} = \frac{\left(\frac{df}{dT}\right)_1 \Delta T}{(f/\#) f}$$

and the surface deformation is given by

$$\Delta X = \frac{\left(\frac{df}{dT}\right)_1 \Delta T D}{16 (f/\#) f}$$

Sample Calculation

Primary mirror is $\approx f/2.5$, $f=40$, $D=16$, let $\Delta T=15^\circ\text{C}$, $\alpha_R - \alpha_L = 0.077 \times 11.3 \times 10^{-6}$.

For Case I

$$\theta_{ID} = \frac{f(\alpha_R - \alpha_L)\Delta T}{(f/\#) f} = \frac{0.077 \times 11.3 \times 10^{-6} \times 15}{2.5} = 5.2 \times 10^{-6} \text{ rad}$$

$$\Delta X = \frac{\theta_{ID} D}{16} = \frac{5.2 \times 10^{-6} \times 16}{16} = 5.2 \times 10^{-6} = \lambda/4$$

For Case II

$$\theta_{ID} = 10.4 \times 10^{-6} \text{ radians}$$

$$\Delta X = \lambda/2$$

For Case III

$$\theta_{ID} = 6.9 \times 10^{-6} \text{ radians}$$

$$\Delta X = \lambda/3$$

8d. Bimetallic Strip Effect - The bimetallic deformation for a Kanigen nickel-plated beryllium flat plate approximating the primary mirror dimensions has been calculated. The nickel plating was assumed to be 0.005 inch thick on one side and 0.001 inch thick on the polished surface. A uniform temperature change of 10°C was assumed. Summarizing the results, the calculations indicated less than $\lambda/10$ deformation where $\lambda = 0.5$ micron. Detailed calculations were presented in the Second Quarterly Report prepared for the Detailed Design Review.

8e. Thermal Channel Isotemperature and Temperature Gradient Effects -

This consideration is principally concerned with temperature effects relative to the thermal channel relay optical system. An expression is given for the temperature dependency of the thermal channel focus. The expression assumes that the two-relay lens system is replaced with an equivalent thin lens. The following quantities are defined:

L_1 - Spacing between prime focal plane and relay lens

L_2 - Spacing between relay lens and thermal detector

d_i - Distance from relay lens to image plane

f_R - Focal length of relay lens

$\frac{dn}{dT}$ - Lens material's rate of change of refractive index with temperature

The change in L_2 is somewhat more complex to assess because it will be affected by the radiation cooler temperature in addition to the scanner temperature.

$$L_2 = L_{SC} - L_{RC}$$

where L_{SC} is the dimension associated with the scanner and L_{RC} is the dimension associated with the radiation cooler.

$$\frac{dF}{dT} = -\frac{d_i^2}{d_o^2} L_1 \alpha_{L_1} + \frac{d_i^2}{f_R^2} \left[f_R \alpha_R - \frac{f_R}{n-1} \frac{dn}{dT} \right] - (L_{SC} \alpha_{L_{SC}} - L_{RC} \alpha_{L_{RC}})$$

As before, an "average" temperature can be assigned to each of the elements giving:

$$\Delta F = -\frac{d_i^2}{d_o^2} L_1 \alpha_{L_1} \Delta T_{L_1} + \frac{d_i^2}{f_R^2} \left[f_R \alpha_R - \frac{f_R}{n-1} \frac{dn}{dT} \right] \Delta T_R - (L_{SC} \alpha_{L_{SC}} \Delta T_{L_{SC}} - L_{RC} \alpha_{L_{RC}} \Delta T_{L_{RC}})$$

8f. Thermal Gradients in VISSR Optical Elements with Effect on Optical

System Behavior - A first-order worst-case analysis has been made of thermal gradients in the VISSR scan mirror, primary mirror, and secondary mirror. Thickness and facial gradients have been considered.

Geometric blur circles have been examined, as have focal plane shifts for the locations of minimum blur circles.

In order to assure worst-case conditions, all pertinent data have been used at the most unfavorable value in the range of uncertainty. Wherever such ranges could not be established, unfavorably exaggerated values were assumed which fell well beyond the anticipated most probable value.

To further assure worst-case conditions in the study of facial gradients, it was found necessary to consider two models for each of the optical elements. In the simpler first model, each optical element is assumed to be attached, without thermal resistance, to an infinite heat sink located behind the element. In the second and more realistic model, each optical element is coupled to an infinite heat sink behind the element by means of thermally resistive elements. While such resistive elements cannot be ascertained with better than moderate accuracy, it is found that in some cases the accuracy is not necessary, and in cases where it is, the most unfavorable value for such resistive elements is used.

The models are discussed in detail in Appendix A.

Analyses Results

Table 3-10 presents a summary of the results of the analyses described above.

For thickness gradients, the extrema occur at equinoctial periods and at winter solstice.

For facial gradients, worst cases occur at different points of time and for different modes of operation. Such gradients arise from area-selective insolation.

In the table:

A positive thermal gradient indicates the optical surface is at a higher temperature than the back surface.

A positive focal shift is in the direction of longer focal lengths.

Blur circles refer to the earth-referenced diameter in nautical miles which includes all the geometrically blurred energy.

A zero blur circle implies that, to a first order, refocusing removes the geometrical blur.

A zero focal shift or temperature difference implies a value less than 0.0001.

Wherever refocusing is used to arrive at minimum blur, the refocusing is assumed to have occurred in the normal seasonal progression - for example, at six to eight week intervals. Special cases of area-selective insolation with locked scan mirror are not assumed to be refocused, except in cases where the mode is used to replace the scan mode in order to create a worst-case condition.

Table 3-10. Thermal Gradients and Optical Effects in VISSR Fore-Optics Elements

Declination and Operating Mode	Optical Element	Type of Gradient	Temperature Difference (°C)	Focal Shift (in.)	Blur Circle Diameter (nmi)	Refocus
Equinox, Any Mode	Scan Mirror	Thickness	0.0317	0.0047	0.036	Yes
Winter Solstice (-23.5°), Any Mode	Scan Mirror	Thickness	-0.0149	-0.0022	0.017	Yes
+10°, Any Mode	Scan Mirror	Facial	---	0.006	0.118	Yes
First Model			---	0.00002	0.068	
Second Model						
Equinox, Scan Mirror Fixed at 45° (Worst-Case)	Primary	Thickness	0.0073	0.0027	0	Yes
Winter Solstice (-23.5°), Scan Mode	Primary	Thickness	-0.0018	-0.0007	0	Yes
+3°, Scan Mirror Fixed at 40° (Worst-Case)	Primary	Facial	0.0035	0.0013	0.060	No
First Model			0.0515	0.0001	0.006	
Second Model						
Equinox, Scan Mirror Fixed at 45° (Worst-Case)	Secondary	Thickness	0.008	0.0003	0	Yes
Solstices (Scan Mode)	Secondary	Thickness	"0"	0	0	--
-6.5°, Scan Mirror Fixed at 40° (Worst-Case)	Secondary	Facial	0.0065	0.0002	0.012	No
First Model			0.064	-0.00002	0.001	
Second Model						

Analyses Conclusions

The behavior of the optical elements with respect to thermal gradients is summarized in Table 3-10, preceding.

The detailed analyses for the individual optical elements are presented in the subsequent text and appendices.

The greatest thickness "gradient" (more correctly, temperature difference) encountered in any element is 0.032°C .

The greatest geometric blur circle encountered is 0.12 nmi (first model) with a more likely maximum blur circle (second model) of 0.07 nmi. These compare with the 90% diffraction-limited blur circle, for the obscuration ratio of 0.4, of 0.197 nmi, and the IGFOV of 0.48 nmi. No optical degradation in system performance is expected to arise from thermal gradients in the optical elements, except for possible transient conditions. But such transient behavior, due to eclipses, will be dominated by inter-element and spacer temperature differences, and not by gradients within the elements.

Facial gradients arising from selective insolation produce the greatest blur circles. No mechanisms of comparable magnitude could be envisioned for other facial gradients, such as "radial gradients," and none other were analyzed.

Focal plane shifts arising from gradients are moderate, compared with the active focal adjustment of ± 0.080 inch. The extreme range, from equinox to solstice, required to compensate for gradients within all elements is approximately 0.011 inch (from $+0.008$ to -0.003 inch), combining the effects in the three elements.

Optical effects arising from variations in the overall temperatures of elements, as distinct from gradients within elements, were not investigated in this study.

9. Stress-Strain

Dimensional instability of Kanigen plated beryllium mirrors is caused by:

- a. Metallurgical instability
- b. Relaxation of residual stresses.

The residual stresses may be due to machining, heat treatment, anisotropy of thermal expansion of the composite.

9a. Residual Stresses. - Dimensional instability of beryllium mirrors can be caused by metallurgical instability, relaxation of residual stresses, and plastic deformation. These possible conditions are usually interrelated and difficult to define in the actual part.

Metallurgical instability can be described as residual stresses caused by thermal expansion anisotropy of the composite or material irregularities peculiar to a particular material pressing. While some evidence of metallurgical instability has appeared, it is not presently clear whether or not the noted effects have been isolated from the normal causes of residual stresses.

The common types of residual stresses are minimized by elaborate machining, heat treatments, and chemical etching processes in the beryllium mirror blanks prior to electroless nickel plating. These processes are detailed in SBRC Specification No. 18842, entitled "Machining and Stress Relief of Beryllium, Process for."

Plastic deformation is the result of applied stresses exceeding the precision elastic limit (PEL). PEL is defined as the stress at which 1 micro-inch/inch of plastic strain occurs and should be used in designing optical components rather than the usual yield strength used in structural applications.

9b. Electroless Nickel Plating Stresses. - Appreciable stress levels have been observed in electroless nickel-plated beryllium thin strips. Stress levels as high as 33,000 psi have been reported by Battelle Memorial Institute. Stress levels of 10,000 to 15,000 psi may be common after the standard temperature annealing cycle.

General American Transportation, under contract to Hughes Aircraft Company, has developed a "low stress" Kanigen plating on beryllium. The phosphorous content of this "low stress" Kanigen plating is approximately 12% compared with 8% for the normal Kanigen plating. Using this method the stress levels in plated, thin beryllium strips have been reduced to less than 2000 psi.

There is not complete agreement on the most appropriate method of calculating the stress levels within the electroless nickel nor the most appropriate selection of beryllium strip thickness.

The initial work by General American Transportation (GAT-X) and Hughes Aircraft Company used strips which were 0.010 inch thick and about 3 inches long. The work by Battelle Memorial Institute and Perkin Elmer was also on very thin strips. Speedring Corporation said they thought that it was impossible to process 0.010 inch thick strips of a hot pressed block beryllium material in a manner that would make them suitable for the stress measurements. It appears that the material used for the General American Transportation experiments was sheet beryllium. The difference in anisotropy of sheet and hot pressed block makes the data questionable at best.

The following are comments concerning various means of calculating stress levels due to interaction between the beryllium and electroless plating.

Comparison was made between GAT-X, Stoney, Shemenski, and Brenner equations for calculating stress in the nickel plating.

Shemenski and Brenner equations were numerically compared. The calculated stress values agreed within 3%. It is possible to derive Stoney's formula from Brenner's transcendental stress equation and Shemenski equations by making appropriate approximations. Due to these approximations, Stoney's formula was not used in the calculations. The GAT-X equations were not used because of some errors in the derivation.

The Shemenski equations given in the following have been used in the SBRC process specification for the optical system (Specification 18761).

Calculation of Maximum Stress:

Fixed Quantities:

$E_1 = 30.0 \times 10^6$ psi elastic modulus for Ni

$E_2 = 44.0 \times 10^6$ psi elastic modulus for Be

Measured Dimensions: (inches)

W = width of strip (0.30 ± 0.04)

C = length of strip (3.00 ± 0.04)

t_1 = thickness of Ni coating (0.004 ± 0.0003)

t_2 = thickness of Be substrate (0.010 ± 0.0003)

l = bow-out at the center (sagitta of the arc)

(Requirement: $S_{\max} < 2.00 \times 10^3$ psi)

The absolute value of the maximum stress (psi) in the Ni coating is to be calculated from the following formula⁴ using measured dimensions and the above values for fixed quantities:

$$S_{\max} = \text{abs} \left[\frac{P}{A_1} - \frac{E_1 (t_2 - \bar{y})}{R} \right]$$

where

abs = absolute value

$A_1 = Wt_1$ cross-sectional area of Ni coating

$R = \frac{C^2 + 4l^2}{8l}$ radius of curvature

$$\bar{y} = \frac{\frac{t_2^2}{2} + \left(\frac{E_1}{E_2}\right) \frac{t_1^2}{2} + \left(\frac{E_1}{E_2}\right) t_1 t_2}{t_2 + \left(\frac{E_1}{E_2}\right) t_1}$$

⁴R. M. Shemenski, J. G. Beach, and R. E. Maringer, "Plating Stresses from Electroless Nickel Deposition on Beryllium," J. Electrochem. Soc. 116, 402 (1969).

$$P = \frac{E_2 W}{2R (t_1 + t_2)} \left\{ \frac{t_2^3 + \left(\frac{E_1}{E_2}\right) t_1^3}{3} + \left[\frac{\left(\frac{E_1}{E_2}\right) t_1 t_2 \left\{ \left(\frac{E_1}{E_2}\right) t_1^3 + t_1^2 t_2 \left(2 \left(\frac{E_1}{E_2}\right) + 1 \right) + t_1 t_2^2 \left[2 + \left(\frac{E_1}{t_2}\right) \right] + t_2^3 \right\}}{t_2^2 + 2 \left(\frac{E_1}{E_2}\right) t_1 t_2 + \left(\frac{E_1}{E_2}\right)^2 t_1^2} \right] \right\}$$

Companies that have worked on the low stress electroless nickel plating for VISSR include Grunwald and GAT in Chicago, Illinois; ElectroCoating, Inc. (ECI) in Houston, Texas; and Magnacomp (ECI) in Mountain View, California. The work by these companies was completed under subcontract with either Perkin-Elmer Corporation or Tinsley Laboratories. The latter two companies are under contract with SBRC for the fabrication of the VISSR beryllium optical elements.

Stress levels as monitored with 0.040-inch thick and 4.00-inch long beryllium test strips have been consistently higher than the specified 2000-psi stress levels. The plating by GAT has had the lowest stress levels; these have been in the 4000- to 6500-psi range. The preceding equations were used in stress calculations.

As indicated above, the basis of the specification feasibility was based on previous GAT/HAC work. Cross-rolled beryllium test strips of 0.010-inch thickness were used to monitor deformation caused by the electroless nickel plating. It is only partially understood why VISSR stress levels as monitored by hot pressed beryllium block machined to a thickness of 0.040 inch results in significantly different calculated stress levels.

Part of the discrepancy can be explained by the greater anisotropy of cross-rolled beryllium. The electroless nickel plating bath is maintained at 100°C; thus, stresses are introduced due to a bimetallic strip action

since nickel and beryllium have different thermal expansion coefficients. If the thermal expansion coefficients of cross-rolled beryllium differ from hot pressed block, the calculated stress levels are expected to be different.

Quantitatively, this can be approximated by using Timoshenko's equation for a bimetallic strip:

$$\frac{1}{R} = \frac{6(\alpha_2 - \alpha_1)(T_1 - T_0) \left(1 + \frac{t_1}{t_2}\right)^2}{\left\{ (t_1 + t_2) \left[3 \left(1 + \frac{t_1}{t_2}\right)^2 + \left(1 + \frac{t_1 E_1}{t_2 E_2}\right) \left(\frac{t_1^2}{t_2^2} + \frac{t_2 E_2}{t_1 E_1} \right) \right] \right\}}$$

where E_1 = elastic modulus of nickel
 E_2 = elastic modulus for beryllium
 t_1 = thickness of nickel plating
 t_2 = thickness of beryllium substrate
 R = radius of curvature of deformed strip
 T_1 = plating temperature
 T_0 = room temperature
 α_2 = thermal expansion coefficient of beryllium
 α_1 = thermal expansion coefficient of nickel plating

This can be rewritten as

$$\frac{1}{R} = K(\alpha_2 - \alpha_1)(T_1 - T_0)$$

The radius of curvature, R , is related to deformation bow, x , and strip length, $2y$, by the equation for a circle

$$R = \frac{x^2 + y^2}{2x} \approx \frac{y^2}{2x}$$

Thus, the strip bow is given by

$$x = \frac{y^2}{2} K(\alpha_2 - \alpha_1)(T_1 - T_0)$$

By differentiation we have the rate of change of bow with respect to beryllium thermal expansion coefficient.

$$\frac{dx}{d\alpha_2} = \frac{y^2}{2} K(T_1 - T_0)$$

For the case where $y = 2.0$ inches, $t_1 = 0.004$ inch, $t_2 = 0.040$ inch, $T = 100^\circ\text{C}$, $T_0 = 23^\circ\text{C}$, $E_2 = 40 \times 10^6$ psi, $E_1 = 20 \times 10^6$ psi, which results in $K = 9.2$.

For cross-rolled beryllium sheet $\alpha_2 = 12.5 \times 10^{-6}/^\circ\text{C}$

For VISSR hot pressed beryllium block $\alpha_2 = 11.5 \times 10^{-6}/^\circ\text{C}$

Thus $\Delta x = 1330 \times 10^{-6}$ inch.

Therefore, the differential stress explainable due to difference in beryllium material is 1200 psi. However, this explains only about 25% of the stress levels being observed on VISSR platings compared to previous GAT/HAC platings. The mechanism for the remainder is not understood.

Figures 3-26 and 3-27 have been useful in evaluation of the electroless nickel plating. Figure 3-26 relates stress levels to strip deformation for three thicknesses of beryllium substrate. Figure 3-27 relates stress levels to strip deformation for five thicknesses of nickel plating.

Based on data from GAT experimentation⁵ two mechanisms would result in lower stress levels for VISSR optical elements.

1. Increase the phosphorus content in the electroless nickel plating.
2. Reduce the post-plating bake temperature.

It appears that a developmental program would be required to significantly increase the phosphorus levels. Side effects of an increased phosphorus content are unknown.

⁵K. Parker and H. Shah, "The Stress of Electroless Nickel Deposits on Beryllium," J. Electrochem. Soc. 117, 1091 (1970).

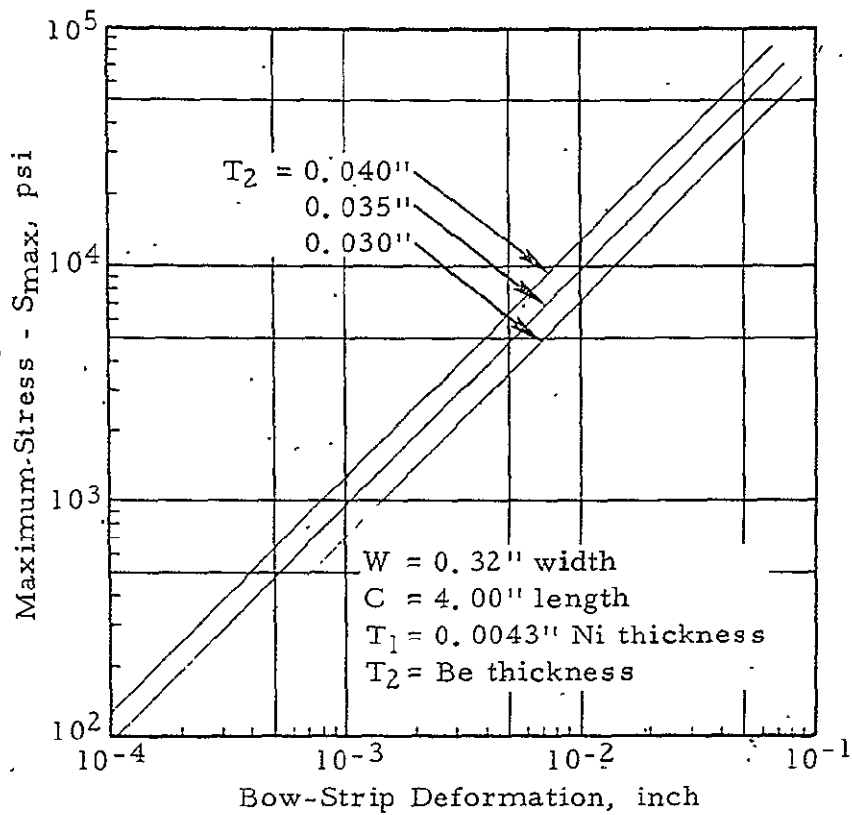


Figure 3-26. Maximum Stress versus Bow-Strip Deformation as a Function of Beryllium Strip Thickness, T_2

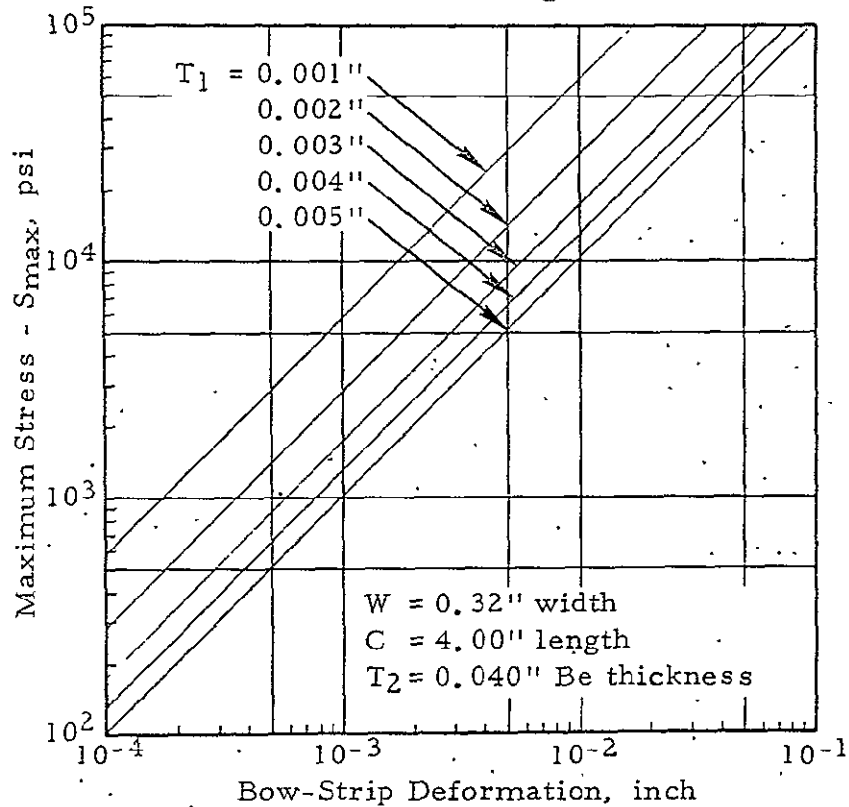


Figure 3-27. Maximum Stress versus Bow-Strip Deformation as a Function of Nickel Plating Thickness, T_1

The recommended post-bake temperature is 375°F (190°C) for four hours. This post-bake increases the nickel-beryllium adhesion bond. Reduction of the post-bake temperature may adversely affect the Be-Ni bond.

In conclusion, the allowable stress levels in the VISSR electroless nickel plating as monitored by 0.040-inch thick beryllium strips will be relaxed from 2000 to 6500 psi. The reason for this is that to achieve stress levels less than 2000 psi, a development program would be required. It should be noted that the 6500-psi relaxed level is significantly lower than would be achieved if standard electroless nickel plating techniques are used.

10. Spatial Resolution Error Budget

A spatial resolution error budget has been developed and is summarized in Table 3-11.

Table 3-11. Tabulation of Factors Affecting Spatial Resolution, θ_{ID} , Image Size (mr)

	θ_{ID}	
	Visible Channel	IR Channel
Diffraction Effects, 90% of energy contained within, ($\epsilon = 0.4$)	0.01	0.192
Scan Mirror, $\lambda/2$	0.005	0.005
Primary Mirror, $\lambda/3$	0.007	0.007
Secondary Mirror, $\lambda/4$	0.010	0.010
Primary-Secondary misalignment to optical axis, 0.002 in.	0.002	0.002
Focal Plane misalignment	Active Focus	Active Focus
Thermal Gradient " to optical axis		
Spacer $\Delta T = 2^\circ\text{C}$		
Secondary mirror $\Delta T = 4^\circ\text{C}$	0.012	0.012
Isotemperature Change $\Delta T = 10^\circ\text{C}$		
Beryllium anisotropy	0.007	0.007
IR relay system		0.081
Mounting - mirror	0.01	0.01
Summation of Effects		
$\left[\sum_1 (\theta_{ID})_i^2 \right]^{1/2}$	0.024	0.21

OPTICAL VENDORS

Only those optical vendors who have successfully demonstrated a capability in fabricating fast aspheric optics from metal in moderate sizes were considered.

Vendor survey trips were made to the potential suppliers. Several optical suppliers commented on the optical design, mechanical structure, beryllium composition, and reflective coatings. These comments are summarized in Table 3-12.

The VISSR design and fabrication philosophy was modified in several areas where it appeared appropriate, based on the optical vendor comments.

The following companies were solicited for proposals on fabrication of the VISSR telescope system.

- Diffraction Limited
- Owens-Illinois (Fecker Systems)
- Perkin-Elmer Corporation (Norwalk, Connecticut, and Costa Mesa, California)
- Speedring Corporation (Schiller)
- Tinsley Laboratories

Each of these companies were solicited to give a quotation for fabricating the VISSR telescope using polished bare beryllium and/or electroless nickel polished beryllium substrates. Diffraction Limited and Perkin-Elmer Corporation (Costa Mesa) limited their response to electroless nickel-plated beryllium. Owens-Illinois (Fecker Systems) and Perkin-Elmer (Norwalk) response was limited to polishing bare beryllium. Speedring Corporation and Tinsley Laboratories were responsive to both methods.

Firm fixed priced contracts were let with Tinsley Laboratories and Perkin-Elmer (Costa Mesa). Tinsley Laboratories' contract is for one bare beryllium polished system and two electroless nickel-plated beryllium systems. Perkin-Elmer Corporation (Costa Mesa) contract is for two electroless nickel-plated beryllium systems.

Table 3-12. Optical Vendors

	Vendors			
	Diffraction Limited	Perkin-Elmer Corp. (Norwalk)	Owens Illinois Fecker Systems	Tinsley Laboratories
1. Recommended beryllium material	HP40 (1400) OK	HP50	HP40 (1400) OK	HP50
2. Willingness to polish Kanigen nickel plated beryllium	Yes	Yes	Yes	Yes
3. Willingness to polish beryllium directly	No	Yes	Yes	Yes
4. Recommended route Kanigen versus bare Be	Kanigen	Bare Be Use HP50 or HP20 (S200)	Kanigen	Bare Be Use HP50 or HP20 (S200)
5. Mirror structures	OK	OK - Suggested looking at 3-point scan mirror mounting again.	OK - Suggested rib at scan mirror ID	OK - alternate scan mirror approach use closed back with EDM central structure
6. Rough and medium machining cuts and heat treatment as given on initial preliminary specification	OK	OK	OK	OK; but would recommend a simplified machining schedule and heat treatment Heat treat at temperature > 1450°F.
7. Fine machining	OK	OK	OK	OK
8. Chemical etch 0.002-0.004 inch	OK	Should be 0.010 in.	Acceptable but felt it should be greater.	Should be 0.010 in
9. Cyclic stabilization	OK	Delete	Probably can delete	Delete
10. Kanigen nickel plating low stress type	OK	OK	OK	OK
11. Heat treatment - Kanigen	OK	OK	OK	OK
12. Optical finish - scattering spec - 1%	Would prepare samples for measurements	No adverse comment	No adverse comment	No adverse comment
13. Image quality as spelled out in spec	OK	OK	OK	Essentially asking for diffraction limited operation.
14. 600°F heat cycle after polishing	Concerned	Concerned	Concerned	Reduce to 400 F at least.
15. Enhanced silver reflective coatings	OK	OK - PE can apply at temperatures less than 375°F.	OK	OK
16. Testing of mirrors	Interferometric and blur circle OK	Interferometric and blur circle OK	Interferometric and blur circle OK	Interferometric and blur circle OK
17. Fabrication problem associated with f/1.8 versus f/2.4 primary	1.2x	1.5x	10x	3x
18. Desirability of using Irtan 1 secondary from fabrication standpoint	Do not use	Would certainly be easier.	Toss-up	Would not recommend.
19. Recommended Kanigen nickel plater	Grunwald	Grunwald	Grunwald	Grunwald
20. Willingness to be responsible for total mirror fabrication (from material to reflective coatings)	Yes	Yes	Yes	Yes - Desire incremental funding.
21. Machine Shop - recommendations	Pioneer Tool (Boston Area)	Speedring Warren, Mich.	Speedring, Mich. Pioneer Astro Chicago, Ill	American Beryllium Company Sarasota, Fla

BERYLLIUM MATERIAL

The selection of the beryllium composition was based on beryllium oxide, precision elastic limit (PEL), and cost considerations. A low beryllium oxide content was required if polishing beryllium directly was to be an option. A high PEL is highly desirable to achieve mirror stability as a function of time. Table 3-13 compares several different beryllium compositions.

The material per SBRC Specification 18834 appears to represent a good compromise between the various performance parameters and cost.

Table 3-13. Beryllium Material Factors

Material	PEL (psi)	Yield Strength 0.2% Offset (psi)	Ultimate Tensile Strength (psi)	BeO Content (%)	Relative Cost
HP20 S200	2,000	30,000	40,000	2 Max	1.0
HP40 I400	8,000	40,000	50,000	4 Min	1.4
HP50	20,000		85,000	3 Nom	1.7
SBRC Spec 18834	5,000	30,000	40,000	2 Max	1.1

The low beryllium oxide content composition (2% or less) is desirable if polishing beryllium directly is to be an option. Table 3-14 compares polished electroless nickel-plated beryllium and bare beryllium. Information in the table indicates reasons why the polished bare beryllium would be a better mirror choice for VISSR, provided the required low scatter surface polish can be obtained within the current state of the art. Two optical suppliers have indicated they can polish bare beryllium mirrors to the 1% VISSR optical surface scatter specification. However, the SBRC evaluation indicated that a conclusive decision could not be made because of restricted experience and inconsistent data. Therefore, it was concluded to use

electroless nickel-plated (low stress) mirrors as the principal process, in addition to a backup order using the bare beryllium polishing technique.

Firm fixed priced contracts were processed for four VISSR optical systems using electroless nickel-plated beryllium, and one system using bare beryllium.

Table 3-14. Polished Kanigen Nickel-Plated Beryllium
versus Bare Beryllium

Kanigen-Plated Beryllium	Bare Beryllium	Preferred Method	
		Kanigen	Bare Be
Bimetallic Strip Effect			X
Kanigen Nickel Stress Levels			X
Delamination			X
Kanigen Thickness Nonuniformities			X
Kanigen Metallurgical Unstable			X
Weight			X
Kanigen Nickel Pits	Be Voids (Pits)		
Kanigen Nickel Hardness Nonuniformities	?	?	?
Be Anisotropy	Be Anisotropy		
Be Residual Stress	Be Residual Stress		
Surface Scatter (Low)	Surface Scatter (?)	X	
	Reflective Coating Compatibility (?)	X	
	Cost	X	
	Schedule	X	

TELESCOPE PERFORMANCE SPECIFICATION

The optical system specification is covered by SBRC Specification 18761, "Process Specification for Optical System VISSR/SMS." The image quality, effective focal length, and back focal length are only specified regarding the assembled system. The optical system composed of scan mirror, primary mirror, and secondary mirror is tested as an assembly. Surface scatter and mirror reflectance are specified and measured on a component basis.

Two classes of measurements are specified with Class II measurements made with the optical system (scan mirror, primary mirror and secondary mirror) assembled in a laboratory setup. The secondary mirror is adjusted ± 0.020 inch perpendicular to optical system axis and ± 0.125 inch parallel to optical system axis to facilitate optimum performance. Class I measurements are made with the optical system assembled in VISSR/SMS hardware.

The performance specifications were written to be consistent with any of the following test methods.

1. Interferometric Methods. - These are commonly used methods that are relatively simple to set up. A large volume of data and information can be obtained in a short time span. They are not sensitive to surface microstructure, i. e., surface scatter.
2. Image Energy Distribution Measurements. - This is a standard test method where several different distributions can be measured. For example, the image can be scanned with a knife edge, a slit aperture, or an opaque wire. Radial distribution can be obtained by using varying circular pinhole apertures symmetrically aligned with the image.
3. Modulation Transfer Function Measurements (MTF). - This is an effective but relatively new technique. Few optical manufacturers have the required equipment.

An analysis was made to determine the relationship of wavefront distortion to image quality in the sense of radial energy distribution or MTF complex. The conversion depends on the wavefront distortion contour. The analysis used a simple parabolic wavefront distortion as the model. Under these conditions, it can be shown using first order equations that the angular image blur θ_{ID} is approximated by $\theta_{ID} = \frac{16X}{D}$ where X is the surface deviation from

the ideal surface figure and D is the diameter of the optical element. Rather than a parabolic wavefront deformation, let distortion be related to

$$X = A \sin \frac{4\pi y}{D}$$

where X = surface departure from ideal configuration

A = amplitude of surface distortion

y = radial distance on mirror

D = mirror diameter

This results in the equivalent equation for angular image blur of

$$\theta_{ID} = \frac{25X}{D}$$

As a rule of thumb, a diffraction limited system has classically been figured to $\lambda/8$ wave. Substituting this into the equation for θ_{ID} , we have,

$$\theta_{ID} = \frac{2\lambda}{D}$$

the Airy disc diameter is given by

$$\theta_{\text{Airy}} = \frac{2.44\lambda}{D}$$

Thus, this lends some credibility to the validity of the simple model assumed.

The radial energy distribution was approached from the standpoint of having several independent contributors to the image size. The addition of image degradation factors was done in a root sum square (rss) manner. The image degradation factors considered included

- Diffraction effects
- Residual design aberrations
- Fabrication tolerances
- Mounting tolerances

Because computer ray trace data indicated that the residual design aberrations were negligible compared with diffraction effects, no degradation function was included for them.

Figure 3-28 illustrates the predicted energy distribution as a function of angular dimension at the image plane. Curve 1 shows the distribution due to diffraction from a 0.4 central obscuration. Curve 2 shows an e^{ax} intensity curve. Curve 3 shows the % energy within the given angular dimensions due to the e^{ax} degradation factors. Curve 4 shows the root sum square of Curve 1 and 3. Curve 5 shows the root sum square of Curve 1, Curve 3, and Curve 3 taken a second time.

Thus if the distortions are of the form e^{ax} that Curve 4 represents, the predicted distribution of one distorting source is present. Curve 5 represents the predicted distribution if two distorting sources are present.

The radial energy distributions described in these figures have been used as a basis for MTF calculations. The distortions due to diffraction, fabrication, and mounting are therefore inherent in the MTF results.

For the Class II case; the line spread functions based on the radial intensity distribution of the diffraction and fabrication distortion were convolved to obtain the combined line spread intensity distribution. A bar pattern with sinusoidal transmission is used to obtain the modulation.

$$M = \frac{I_{\max} - I_{\min}}{I_{\max} + I_{\min}}$$

as the energy pattern is scanned over the bar pattern. The bar pattern is effectively infinite in one direction and by varying the width of the bars a spectrum of spatial frequencies is attained.

In an analogous manner a square bar pattern can be used. Square bar is defined as having a transmission of 1.00 or 0.00.

A tabulation of modulation using square bar pattern is given in Table 3-15.

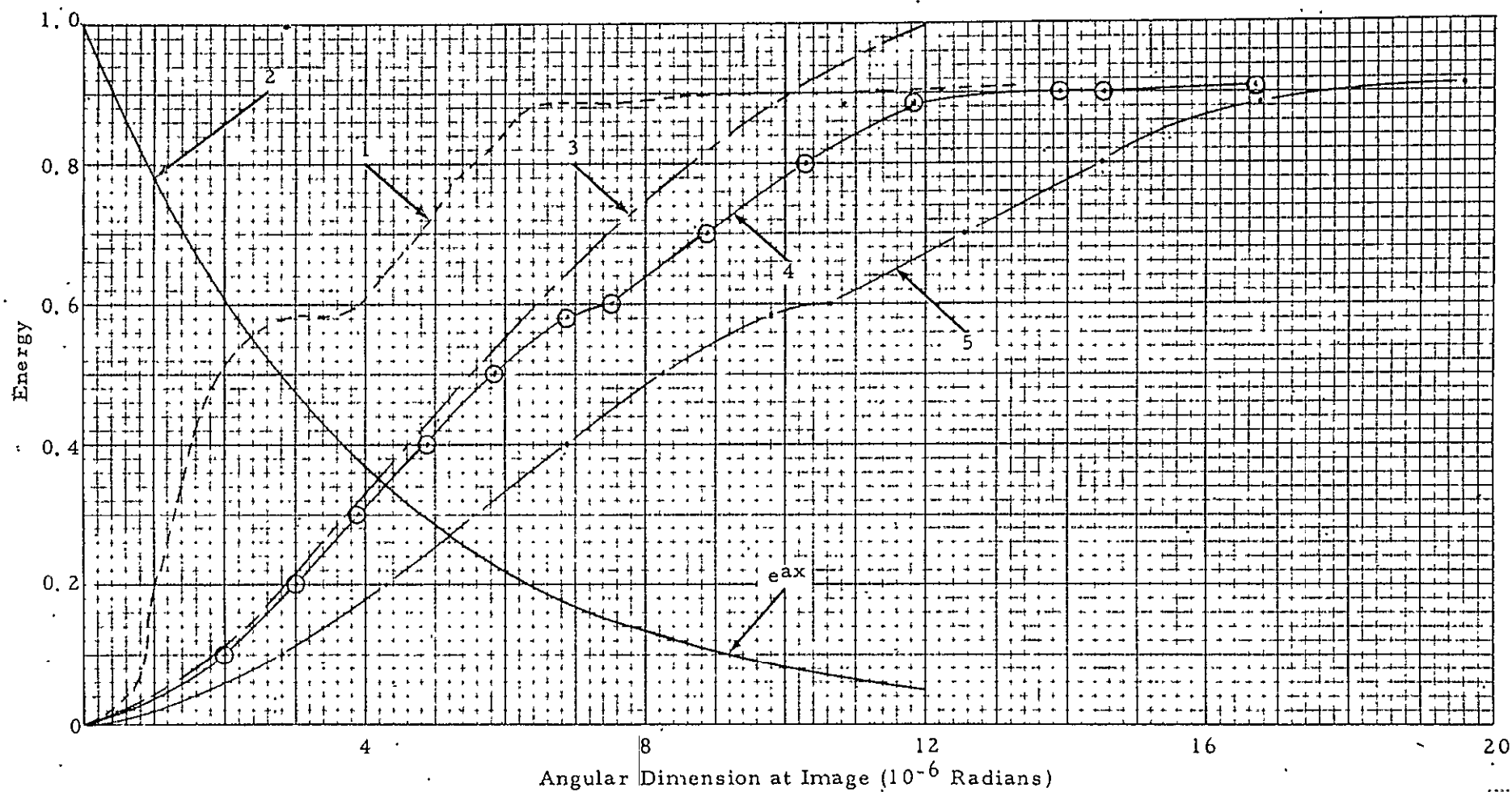
Figure 3-28. Energy Distribution for e^{ax} Distortion Function .

Table 3-15. Square Bar Modulation Transfer

Spatial Frequency (cycles/radian)	Modulation	
	Class II	Class I
1, 000	1.00	1.00
5, 000	1.00	1.00
10, 000	0.98	0.96
15, 000	0.96	0.92
20, 000	0.94	0.88
25, 000	0.93	0.83
30, 000	0.92	0.78

Inflight Solar Calibrator

The final inflight solar calibrator is briefly described below. The detailed design was covered in the Fifth Quarterly Report.

The requirements of the inflight solar calibrator include the following factors:

1. The solar calibrator provides three optical channels at different angles.
2. The channel spacing (angular) is such that one channel angle will be 16° greater than, one channel 16° less than, and one channel parallel to the line-of-sight as determined by scan mirror position.
3. All channels lead by 15° the aim point of the telescope as determined by telescope rotation.
4. The active aperture of each channel is sufficient to simulate an effective albedo of 0.50. Tolerance of about 5% effective aperture from channel to channel is anticipated.
5. The solar calibrator and mount should obscure a minimum of energy directed into the principal aperture of the telescope.

System Description. - A cartesian coordinate system is used. The X-axis is the telescope axis, the Y-axis is the axis of tilt for the tilt mirror and the Z-axis is the central aim point of the tilt mirror. The origin is the center of the tilt mirror, which is the intersection of the telescope axis and the tilting axis.

The General Concept

The deflection system consists of three prisms. These are shown in three views in Figure 3-29. The left illustration in Figure 3-29 is a view with the observer sighting from the -Y direction. The central illustration is viewed from + or -X. The right illustration is viewed from a direction of 15° from the X-Z plane as measured in the Y-Z plane.

The top surface of the top prism is in an X-Y plane. The two top corners of this prism have direction X.

Incident on this surface will be beams of light which in the X-Z plane vary from normal to $+10^\circ$ and -10° . The X-Z plane is perpendicular to this surface and parallel to its edges.

This top prism has two internal reflecting surfaces which tilt the incident fans from the X-Z plane to a plane at 15° to the X-Z plane with the line of intersection of the planes having direction X. The incident (top) and emergent (bottom) surfaces are both perpendicular to the central ray so that

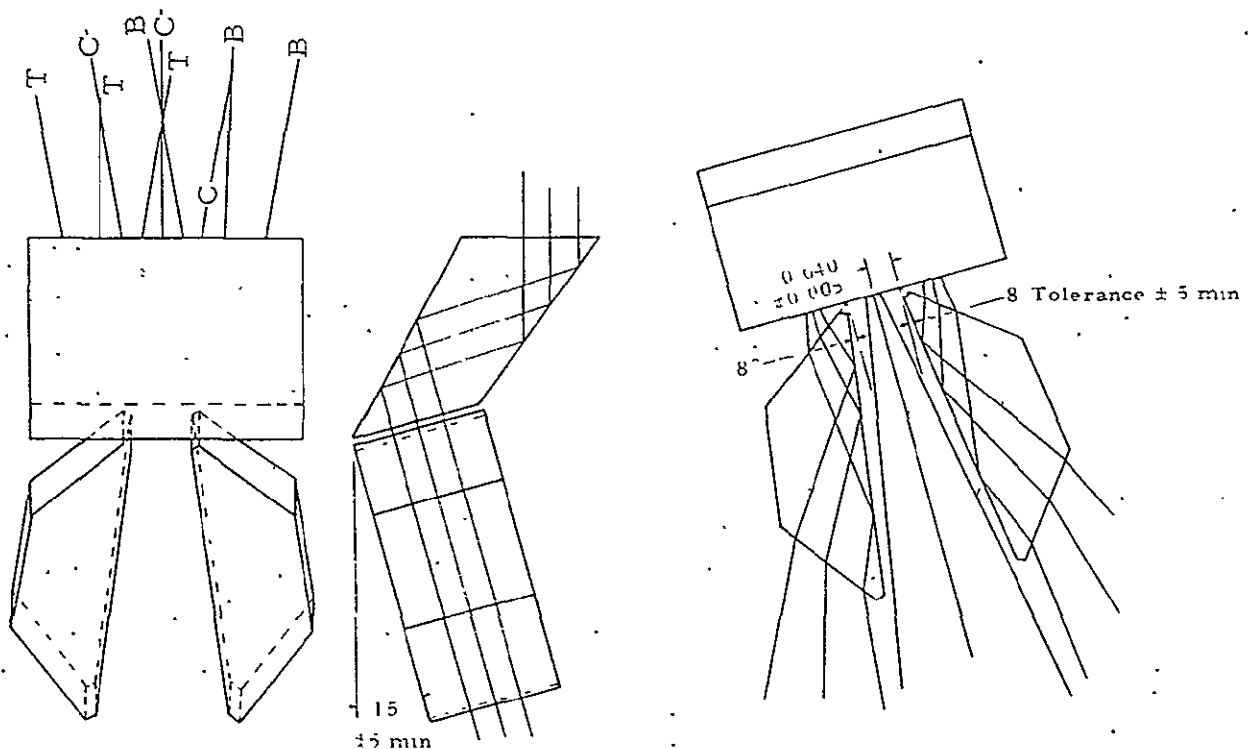


Figure 3-29. Solar Calibrator Prism Assembly

refractively the prism behaves as a plane parallel sheet of glass, and no dispersion or angular difference occurs between rays within the fan prior to and after their path through the prism, Figure 3-30. Three stops are located on the bottom of this prism. One controls the dimension of the central fan, the other two control the two side fans.

The central fan needs only to be tilted at the 15° provided by the top prism and requires no further deviation.

The two side fans must be tilted at $+16^\circ$ and -16° . This is accomplished by placing right angle prisms in front of the two side apertures with bases at

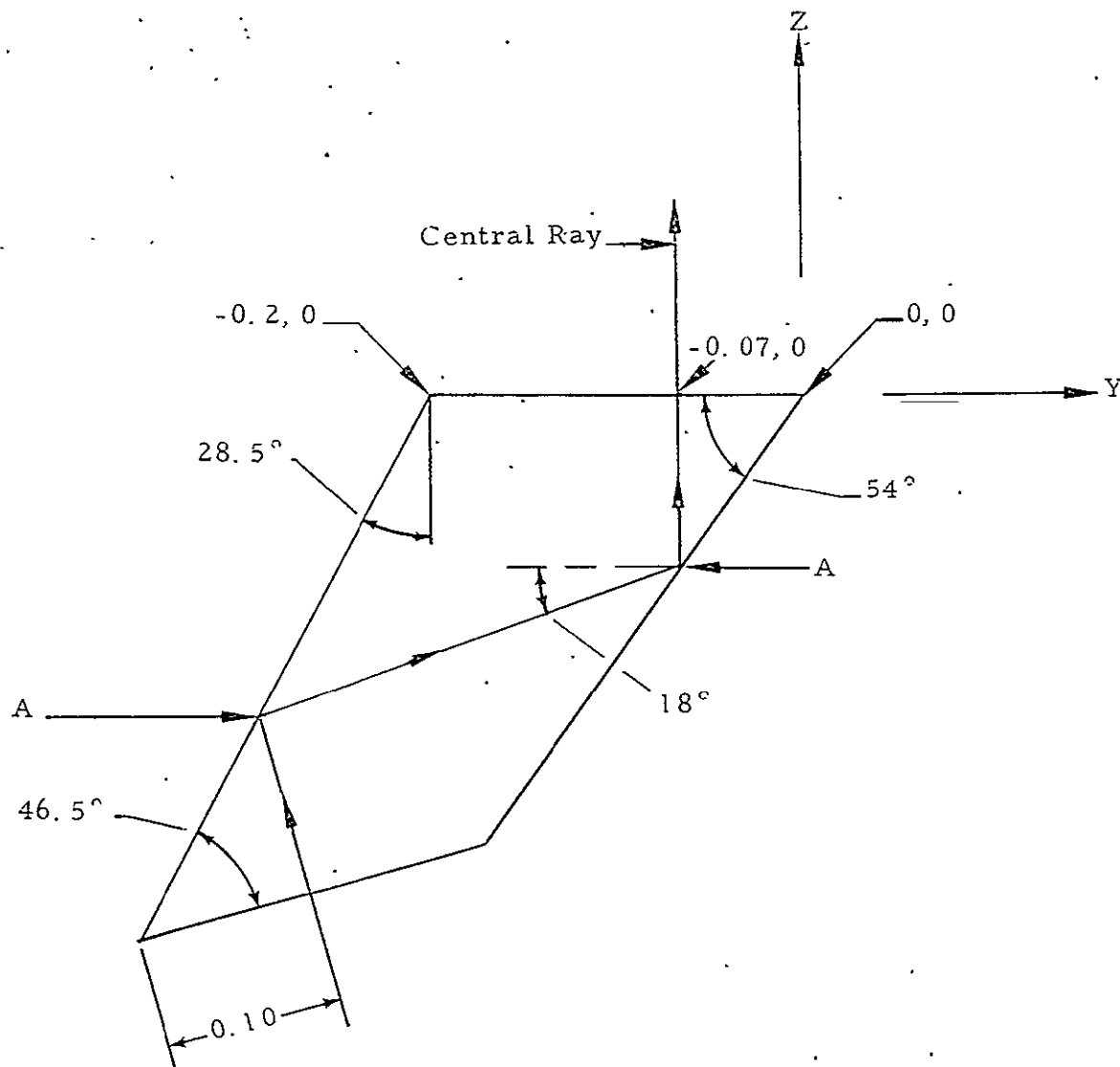


Figure 3-30. Ray Path Through Top Prism

$+8^\circ$ and -8° to the normal to the bottom of the top prism. The prism sides are in the 15° lead plane in roll angle. The separation between prisms is such that they will not vignette the fans from the central calibration bundle.

The result is that a plane has been established which has an angle of 15° to the tilt plane of normal telescope viewing. The intersection of the two planes will lie in the X direction. In this established plane will be three calibrator fans. One will sweep from $+10^\circ$ to -10° as the tilt mirror travels. The other two will sweep from $+6^\circ$ to $+26^\circ$ and from -6° to -26° . These angular sweeps are measured in the 15° plane from a center line which would project onto the Z axis.

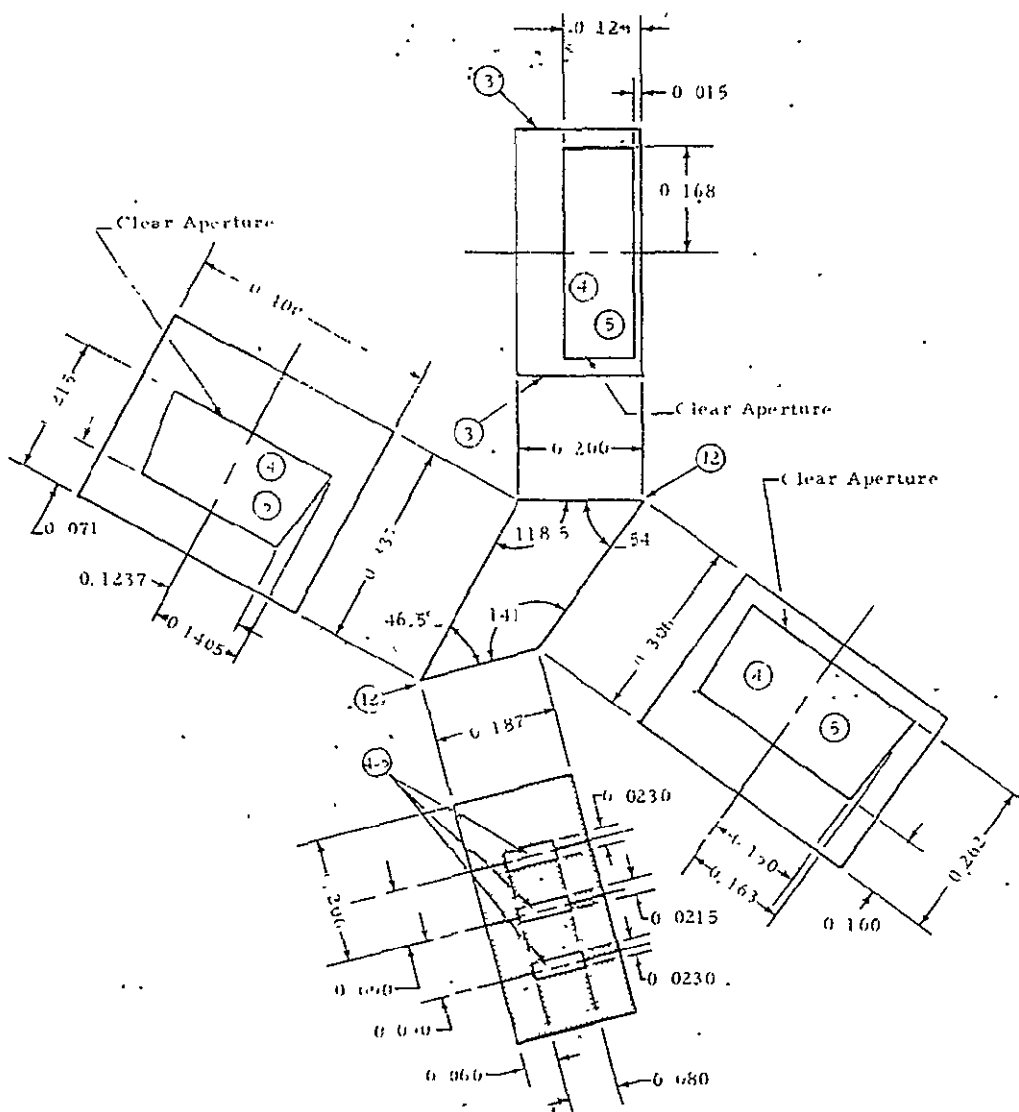
Component Details and Basis for Determination

1. Top Prism. - Figure 3-31 is a detail of the top prism.

- a. Angular Deviation: - A ray incident on the top surface and normal to the top is to emerge from the bottom surface normal to it. Since the bottom surface is at 15° to the top surface, the emergent ray will be at 15° to the top ray. The incident ray strikes the top surface undeviated and is incident on the right surface at 54° to the normal. After reflection, the ray will be at 108° to its original direction or 18° from the top surface (this ray direction is best illustrated in Figure 3-29 which has superimposed rays).

The normal to left surface is at $118.5^\circ - 90^\circ$ or 28.5° to the top surface. Therefore, the ray is incident at $28.5^\circ + 18^\circ$ or 46.5° . The introduced deviation is twice this angle or 93° . The ray direction is now $93^\circ - 18^\circ$ or 75° to the top surface. This places the ray at $90^\circ - 75^\circ$ or 15° to the top surface normal or 15° to its incident direction. Since the bottom surface normal is 15° to the top surface normal, the deflected ray will be coincident with a bottom surface normal.

Therefore, the prism angles result in the required angular deviation. Since Total Internal Reflection (TIR) occurs at $43^\circ 18'$ and the steepest incidence is $46^\circ 30'$, we are $3^\circ 12''$ beyond TIR.



12. Break between 0.005 and 0.010 inch.
11. Linear tolerances on mask apertures ± 0.0005 . All other linear tolerances ± 0.005 .
10. Mask on bottom surface to be opaque; adherence and humidity durability per Mil-M-13508.
9. All angular tolerances ± 5 minutes of arc.
8. All dimensions are to sharp corners.
7. Edge chips shall not be within clear aperture or not greater than 0.015.
6. Break all edges 0.005 max (except Note 12)
5. Surface finish 40-10 per Mil-0-13830
4. Optical polish flat to $1/2$ fringe within clear aperture ($\lambda = 589 \mu\text{m}$).
3. Fine grind finish.
2. Bubbles and inclusions shall be 10 per Mil-0-13830 within view of clear apertures.
1. Material: Fused Silica may be:
 - a. Dynasil: fused silica UV No. 1000
 - b. Corning: fused silica 7940 UV
 - c. Amersil: fused silica Suprasil 1.

Figure 3-31. Solar Calibrator - Top Prism

- b. Clear Apertures. - The effective stop areas are to be 1.0 mm squared or 0.0016 square inch.

No loss in efficiency will occur at the reflective surfaces since total internal reflection is essentially perfectly efficient. Absorption losses through the short glass path will be negligible. The only significant losses will be due to reflection at the refractive surfaces.

The transmittance at each of these surfaces is $1 - \left(\frac{1.458-1}{1.458+1} \right)^2 = 0.9653$. The transmittance for the system is $(0.9653)^n$ where n is the number of refractive surfaces encountered. For the central channel, $n = 2$ and efficiency is 0.9318. For the side channels, $n = 4$ and efficiency is 0.8682.

To compensate for this light loss, the area used will be equal to area desired/efficiency, giving effective area equal to area desired.

For the central channel area used = $\frac{0.0016}{0.9318} = 0.001717$.

For the side channel area used = $\frac{0.0016}{0.8682} = 0.001843$.

The stops located on the bottom of the prism will be 0.080 in length.

The central channel will be $\frac{0.001717}{0.080} = 0.0215$ wide.

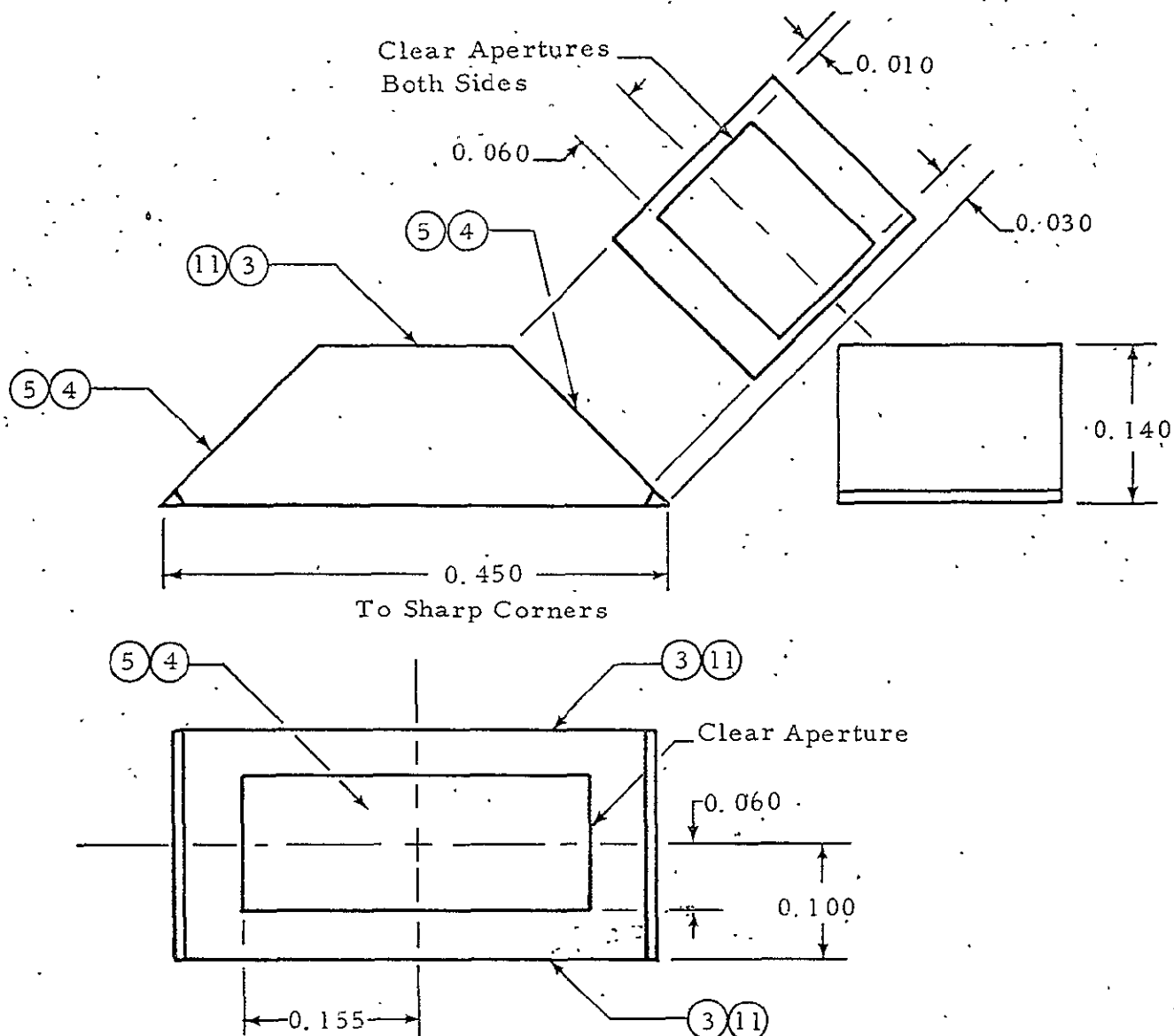
The side channel will be $\frac{0.001843}{0.080} = 0.0230$ wide.

The three stops will be spaced 0.090 between center lines.

The surface outside the stops will be opaque.

2. Bottom Prism. - The two bottom prisms are identical. Their location is such that they will be symmetrical about a Y-Z center-plane of the system. See Figure 3-32.

The prism is a truncated 45° - 45° - 90° with the truncated side being parallel to the prism base.



11. Paint per SBRC Spec. 18863 using 463-3-8 Cat-a-Lac black paint (Finch Paint and Chemical, Torrance, California).
10. Break between 0.015 and 0.020 at $60^\circ \pm 10^\circ$ to base.
9. Linear tolerances ± 0.005 .
8. All dimensions are to sharp corners.
7. Edge chips shall not be within clear aperture nor greater than 0.015.
6. Break all edges 0.005 max (except Note 10).
5. Surface finish 40-10 per Mil-0-13830.
4. Optical polish flat to within 1/2 fringe within clear aperture ($\lambda 5894$).
3. Fine grind finish.
2. Bubbles and inclusions shall be 10 per Mil-0-13830 within view of clear apertures.
1. Material fused silica may be:
 - a. Dynasil: fused silica UV No. 1000
 - b. Corning: fused silica 7440 UV
 - c. Amersil: fused silica Suprasil 1.

Figure 3-32. Solar Calibrator Prism Bottom

Assembly Requirements

Figure 3-29 shows three views of the assembled system. The two lower prisms are in a plane normal to the bottom face of the top prism. Their bottom sides will lie on that plane which intersects the lower left corner (center view, Figure 3-30) and is normal to the bottom face of the top prism.

The two lower prisms are located so that their top corners if left sharp would intersect the bottom face of the top prism in a line 0.040 from the center of the top prism (see right view, Figure 3-29).

The bottom prism faces are at 8° to a plane bisecting the top prism. The 8° is measured in a plane containing the bottom prism sides (see right view, Figure 3-29).

Location in System

To define the prism location, refer back to the coordinate system mentioned under "The General Concept"; that is, telescope axis is X, tilt axis is Y, and Z axis is central look angle. The origin is at the center of the tilt axis.

The top surface of the top prism is at $Z = -8.25$; the two edges of the top prism are parallel to the X axis. By the selection $Z = -8.25$, double blockage of the incoming light by the prism assembly is prevented, viz., it is placed below the active telescope aperture.

The maximum possible y location is necessary. The prism assembly should be as close to the outside edge of the telescope as possible. This is for two reasons: 1) to give a minimum of light blockage, and 2) to give a maximum possible path across the sunshade volume to prevent vignetting at the sunshade aperture.

The following is the derivation for the selection of the y location. Figure 3-33 is used for illustrating the terms of the derivation.

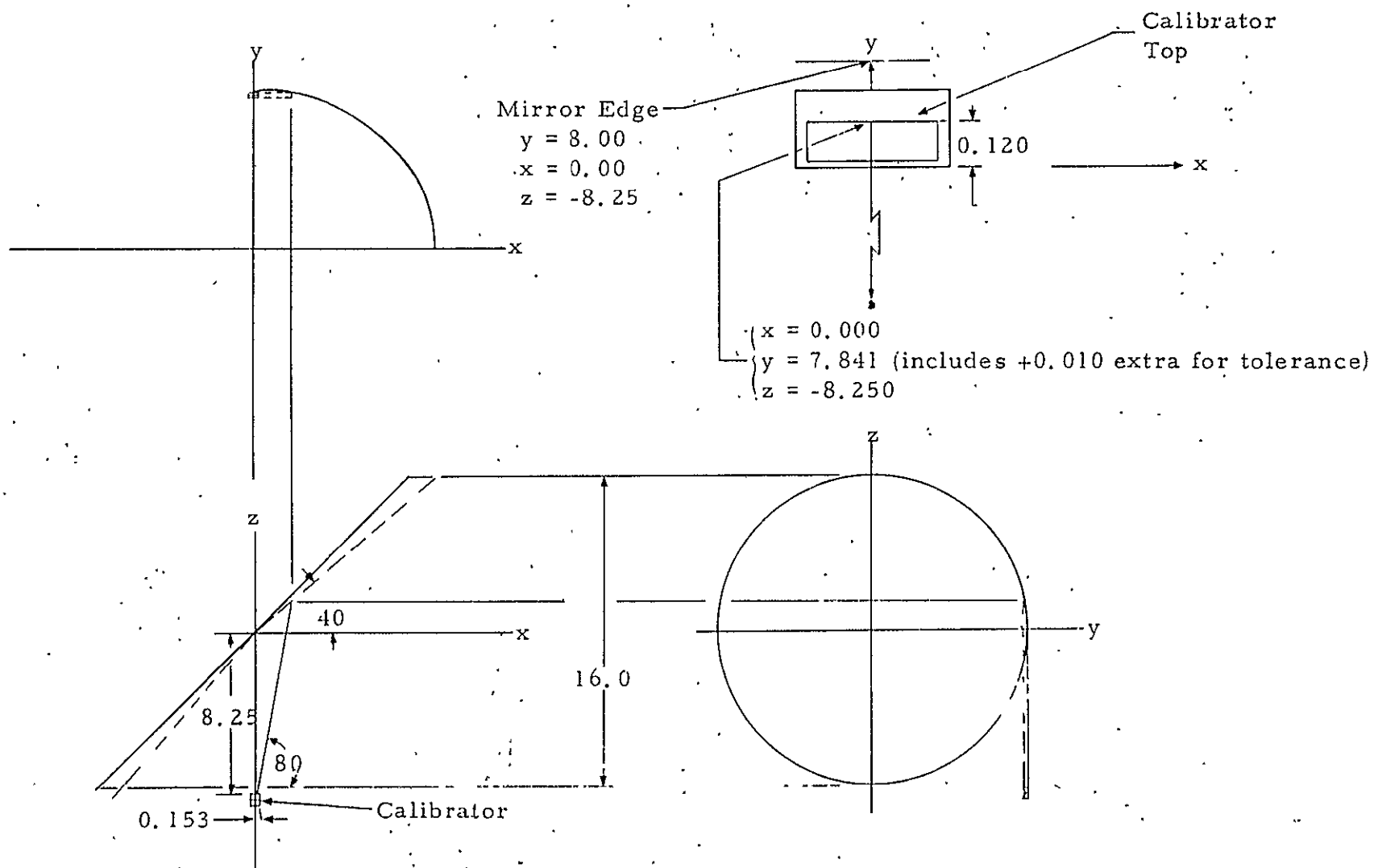


Figure 3-33. Basis for Calculations of Calibrator Location Relative to Telescope Coordinate

The extreme ray leaves the calibrator top surface at an angle of 10° from a point at $X = 0.153$, $Z = -8.25$ (see lower left illustration, Figure 3-33). This ray will strike the tilt mirror when it is at an angle of 40° from the X axis.

The equation for the line before incidence on the mirror is $Z = X \tan 80^\circ + b$. Inserting the origin points values to establish b results in

$$-8.25 - 0.153 (5.6713) = B = -9.1177$$

$$Z = 5.673X - 9.1177$$

The equation for the mirror is $Z = X \tan 40^\circ = 0.83910X$. Solving simultaneously results in $0.83910X = 5.6713X - 9.1177$.

$$X = \frac{-9.1177}{0.8391 - 5.6713} = \frac{-9.1177}{-4.8322} = 1.8869 \text{ inches}$$

and

$$Z = 1.8869 \times 0.83910 = 1.5832$$

To establish the Y value, transfer to a Y-Z plane after reflection off the mirror. The Z value has been established above at 1.5832. The Y value, since it will represent the back edge of the calibrator aperture, can lie on the mirror periphery at radius = 8 inches.

$$\begin{aligned} \text{The equation of the circle is } Y^2 + Z^2 &= 8^2 \text{ and } Y = (64 - Z^2)^{\frac{1}{2}} = \\ (64 - 2.5065)^{\frac{1}{2}} &= (61.4935)^{\frac{1}{2}} = 7.841 \end{aligned}$$

The upper right sketch of Figure 3-33 shows the top of the calibrator relative to the mirror edge. It includes a 0.010-inch safety factor for tolerancing.

Now examine the penetration points in the sunshade aperture for origin points at the calibrator.

Since all the fans are in a plane at 15° to the tilt plane of the telescope the slope of any ray in the Y direction is $\tan 15^\circ = 0.26795$.

The Z distance to the sunshade is $37.5 - 8.25 = 29.25$. (Actually the effective origin is slightly greater than $Z = -8.25$, but since using -8.25 is a conservative step, it will be used.)

All fans will intersect the sunshade in a line. This line is the intersection of the 15° plane starting at the calibrator mechanism and the X-Y plane of the sunshade at $Z = -37.5$.

The Y value of this line is the Y value of the calibrator plus ΔZ calibrator to sunshade times $\tan 15^\circ$, or $Y = -7.841 + (29.25 \times 0.26795) = -7.841 + 7.837 = -0.004$ or the calibration fans exits within 0.004 of the sunshade center line in the X direction.

For the X value consider only the extreme ray; that is, the one at 26° from center in the tilted fan.

The length of a central ray from calibrator to sunshade is $\Delta Z \secant 15^\circ = 29.25 \times 1.0353 = 30.283$ inches.

The X distance from this ray's intersection with the sunshade plane to the extreme ray's intersection with the sunshade plane is its length times $\tan 26^\circ$ or $30.283 \times 0.48773 = 14.770$ inches.

The length of the sunshade from center to end along the X center line is 14.872. Therefore, the ray is within the sunshade aperture by 0.102 inch.

Aperture Blocking

The maximum width of the calibrator optics is 0.43 inch. The maximum penetration into the beam is 0.28 inch.

The blocked area is 0.1204 square inch. This is about 0.75 of a square centimeter, or less than 0.06% blocking.

The previously designed calibrator had blocked off 0.0964 square inch, so an increase in blocking of about 30% is realized in this system.

Tolerance Basis

The angular tolerance on the top prism has been set at ± 5 minutes of arc. With two reflections the total error could be 10 minutes which would give a deviation of ± 20 minutes possible. This would set the roll angle lead at $15^\circ \pm 20$ minutes.

All required clear apertures have been overdimensioned by at least 0.010 inch. This permits 0.005 on the part and 0.005 in assembly without exceeding clear aperture limits.

The aperture stops have been toleranced ± 0.0005 . This will permit a 2.5% change in area if the maximum occurs on both dimensions.

On the bottom prism, angular tolerances are ± 10 minutes of arc. This would represent introduction of 20 minutes of prism if a maximum occurred. The deviation introduced would be $(n-1) \Delta\theta = 0.458 \times 20$ minutes or about 9 minutes. The angular orientation of the base on assembly should be ± 5 minutes since this is the reflecting surface and the tolerance would give double the deviation or ± 10 minutes possible.

Accumulative maximum angular error from all sources on this would be ± 19 minutes. This would set the extreme lead angle at $26^\circ \pm 19'$ which would still permit sun viewing.

Linear tolerances are again $\pm 0.005''$ manufacture and $\pm 0.005''$ assembly with all clear apertures overdimensioned to compensate.

OPTICAL DATA

Thermal Channel Inflight Calibrator

The following considers the relationship of the thermal channel inflight shutter surface finish to its emissivity. During the design review in November 1970, a roughened or grooved surface was proposed as a method to enhance the shutter's emissivity. However, such a configuration is not realistic due to the shutter's thin structure. Furthermore, when the VISSR cavity effect is considered, a relatively smooth shutter finish is quite adequate. The shutter will be painted with Cat-a-Lac (463-3-8) black paint. Its intrinsic emissivity in the 10- to 13-micrometer range is 0.90 to 0.93. The reflected component from a Cat-a-Lac painted surface even when applied on a smooth surface will be partially diffused. When the VISSR optical-detector system is considered, the detector will see principally the ambient VISSR housing temperature. The relationship of shutter effective emissivity (ϵ_{eff}) as a function of the difference of shutter and VISSR housing temperature is expressed by

$$\epsilon_{eff} = 1 + \frac{(1 - \epsilon_{SH}) \frac{dN}{dT} \Delta T}{N_{T_0}}$$

- where ϵ_{eff} = shutter effective emissivity within VISSR spectral band
 ϵ_{SH} = painted shutter intrinsic emissivity within VISSR spectral band
 N_{T_0} = blackbody radiance (within VISSR spectral band) at temperature T_0 , where T_0 is shutter temperature
 $\frac{dN}{dT}$ = radiance derivative with respect to temperature at shutter temperature within VISSR spectral band
 ΔT = temperature difference between shutter and VISSR housing temperature.

Assuming $\Delta T = 5^\circ\text{C}$, $\epsilon_{SH} = 0.9$, $T_0 = 300^\circ\text{K}$, $\epsilon_{eff} = 1 \pm 0.003$.

The effective emissivity will be somewhat lower because a part of the shutter reflected energy will originate from the cooled detector window and vicinity; however, it is believed that the diffuse properties of the Cat-a-Lac

painted shutter will make this effect small. Therefore, it can be concluded that the effective shutter emissivity will approach unity without special roughening or groove contouring of the shutter blade.

SCATTERING

The relationship of VISSR mirror scattering and radiometric uncertainty is described as follows. The hemispherical scatter specification per the initial release of Specification No. 18761, Process Specification for Optical System, VISSR/SMS, was 1% for each VISSR optical element. Based on scattering measurements, made at SBRC, this specification is stringent for Ritchey Chretien optical systems using metal optics such as used in the VISSR. The simultaneous attainment of both surface figure and low scattering is within the state of the art but difficult.

The effect of "near field" scattering on the VISSR radiometric accuracy has been approximated by numerical integration techniques. "Near field" is defined as scattering within 7° of the specular reflection direction. The numerical integration technique accounted for vignetting due to the VISSR sunshade and secondary mirror structure in relation to scan and primary mirrors. The secondary mirror scattering analysis is considerably more complex, and thus a worst-case analysis was made to give an upper bound for the secondary mirror scattering component.

The scattering components for each mirror are given in terms of fractional effective scattering. For example, if the whole mirror were uniformly irradiated by the earth through a solid angle having a half angle of 7° , its fractional effective scattering would be 1.0.

Scan Mirror	0.97
Primary Mirror	0.72
Secondary Mirror	<0.20

The near field scattering for measured VISSR mirrors has been 0.2 to 0.4 of the total hemispherical scatter. Assuming a nominal fraction of $1/3$

for near field scattering, the near field scattering will be 1/3 and 2/3% for total hemispherical scatter of 1% and 2%, respectively. The total near field scattering, $\rho_{sc}(\text{total})$, is given by summing individual mirror contribution.

$$\rho_{sc}(\text{total}) = \rho_{sc}(\text{scan}) + \rho_{sc}(\text{primary}) + \rho_{sc}(\text{secondary})$$

For Case I where hemispherical scatter is 1%

$$\begin{aligned}\rho_{sc}(\text{total}) &= (0.97)(0.33)(0.01) + (0.72)(0.33)(0.01) + 0.20(0.33)(0.01) \\ &= 0.0062\end{aligned}$$

For Case II where hemispherical scatter is 2%

$$\rho_{sc}(\text{total}) = 0.0124$$

The VISSR signal (SVISSR) will be a function of earth albedo (α_o) within the instantaneous field of view (IFOV) and the average earth albedo (α_{sc}) within the near field scattering solid angle. The relationship can be expressed by

$$SVISSR = K(\alpha_o + \rho_{sc} \alpha_{sc})$$

where K = sensitivity constant

The fractional quantity (F)

$$F = \frac{K\alpha_o}{K(\alpha_o + \rho_{sc} \alpha_{sc})} = \frac{\alpha_o}{\alpha_o + \rho_{sc} \alpha_{sc}}$$

is an indication of the effect of the scattering component on the accuracy of the radiometric measurement.

Figure 3-34 is a plot of F versus α_o for two cases of average earth (α_{sc}), $\alpha_{sc} = 0.4$ and 0.8. VISSR mirror hemispherical scattering of 1% is assumed. Figure 3-35 gives equivalent data for VISSR mirror hemispherical scattering of 2%.

In each of these figures, the upper curve represents a fairly typical case since it assumes an earth albedo of 0.40. The lower curve is a worst-case since the earth would have to be covered with high reflectivity clouds.

Based on Figures 3-34 and 3-35, the SBRC Specification No. 18761 regarding scattering has been changed from 1% to 1.5%. This could result in a radiometric measurement uncertainty of 0.9% due to scattering for a "nominal" earth scene; nominal earth scene being defined as $\alpha_o = 0.4$ and $\alpha_{sc} = 0.4$. The corresponding uncertainty for worst-case earth scene is 3.6%. Worst-case earth scene is defined as $\alpha_o = 0.2$ and $\alpha_{sc} = 0.8$.

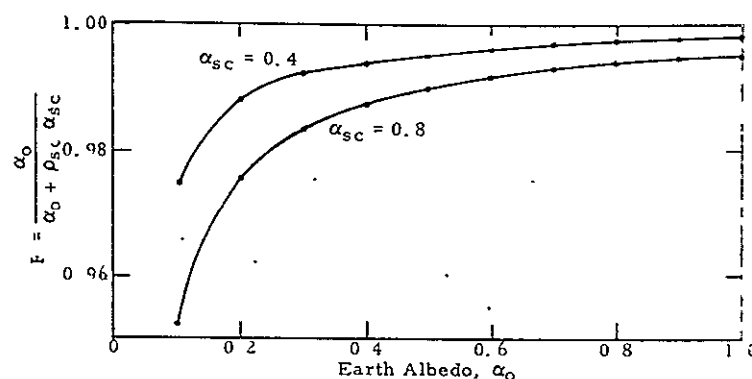


Figure 3-34. Functional Quantity (F) vs Earth Albedo (α_o), Hemispherical Scatter of 1% for VISSR Mirrors

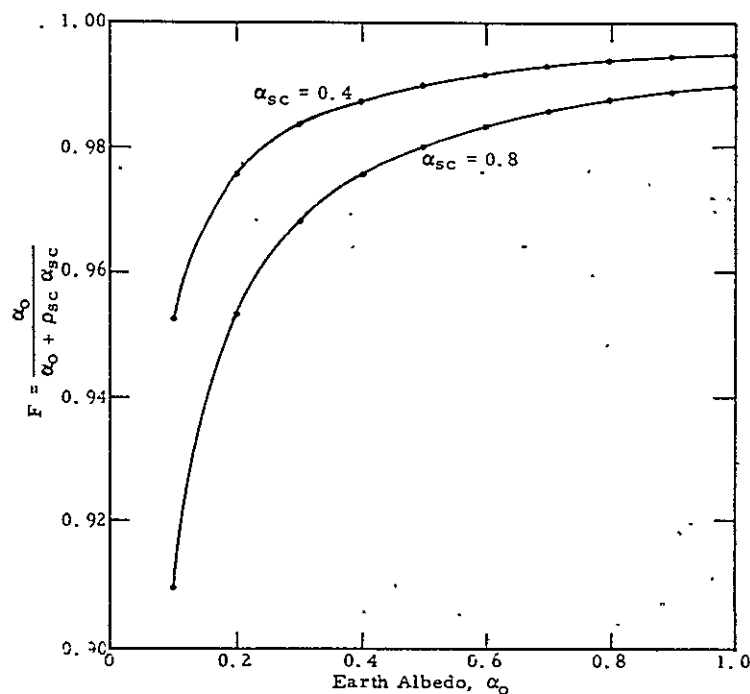


Figure 3-35. Functional Quantity (F) vs Earth Albedo (α_o), Hemispherical Scatter of 2% for VISSR Mirrors

VISSR/SMS CALIBRATOR

Optical Design

Design Considerations - Collimator. - The VISSR calibrator philosophy has dictated that the optical system have ± 3 mr field coverage for the visible channel 0.11-microradian (μ r) image quality. The IR channel requires a field coverage of ± 4 mr with roughly 50 μ r. The ± 3 mr visible-channel field coverage dictated the use of a Ritchey-Chretien system.

Design Details - Collimator. - The calibrator optical system uses a Ritchey-Chretien system. The optical schematic is shown in Figure 3-36.

The primary mirror operates at $f/2.4$ with a focal length of 43.4 inches. The mirror diameter is 20.00 inches with a clear aperture in excess of 18.00 inches. The ID is 4.995 inches with a usable ID of 5.40 inches. The primary-secondary spacing is 32.15 inches. The secondary mirror has a focal length of -15.12 inches. Its diameter is 5.100 inches with a clear aperture of 4.90 inches. The back focal length (BFL) is 43.992 inches. The effective focal length (EFL) is 169.7 inches. The magnification of the secondary mirror is $169.7/43.40 = -3.91$. Thus the focal plane shift with change in primary-secondary mirror spacing is $(-3.91)^2 = 15.3$. This value is greater than is considered optimum, but the desired ± 4 mr field angles make it a necessity if vignetting is to be minimal for the 45° scan mirror position.

Optical ray trace analyses have been completed using the IBM 1130 computer. The computer ray trace program uses a surface-defining equation of the type

$$Z = \frac{CS^2}{1 + \sqrt{1 - (K + 1)C^2S^2}} + DS^4 + ES^6 + FS^8 + GS^{10}$$

where Z = surface sag

C = curvature

S = radial position on mirror

K = conic constant

D = 4th order deformation coefficient

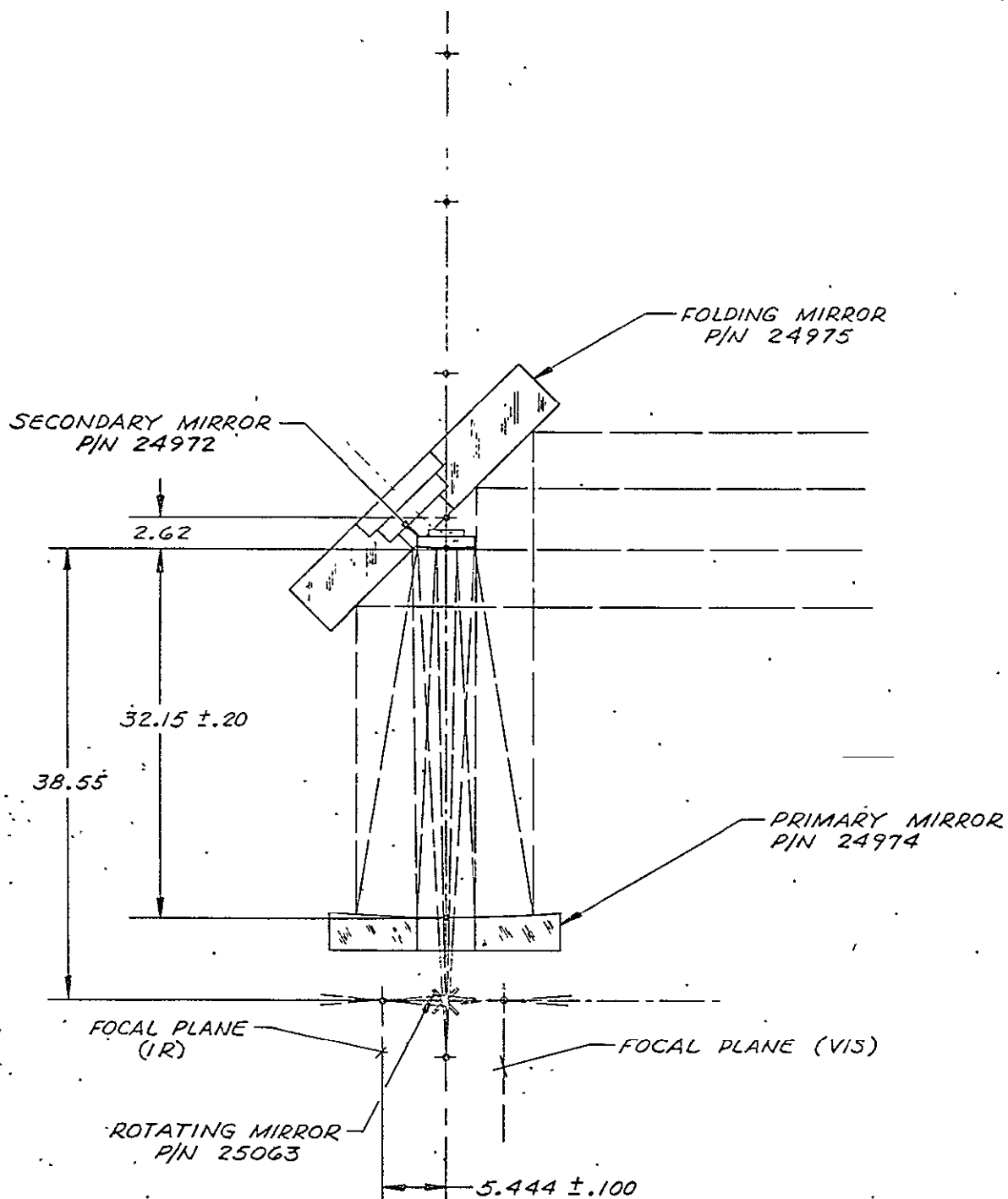


Figure 3-36. VISSR/SMS Calibrator Optical Schematic

E = 6th order deformation coefficient

F = 8th order deformation coefficient

G = 10th order deformation coefficient

The optical system parameters are given in Table 3-16.

Table 3-16. Optical System Parameters

Description	Surface Configuration	Parameters	Comments
Mirror, Folding P/N 24975	Plane	$R = 1/C = \infty$	Mirror oriented at 45° to optical axis
Spacing from Mirror, Folding to Mirror, Primary		34.77	
Mirror, Primary P/N 24974	Concave Hyperbolic	$R = -86.80534$ $K = -1.0459$	
Spacing from Mirror, Primary to Mirror, Secondary		-32:15	
Mirror, Secondary P/N 24972	Convex Hyperbolic	$R = -30.24$ $K = -3.275$	
Spacing from Mirror, Secondary to Mirror, Rotating		38.55	Mirror oriented at 45° to optical axis
Mirror, Rotating P/N 25063	Plane	$R = \infty$	
Spacing from Mirror, Rotating to Focal Plane		5:442	

Figures 3-37 through 3-40 are spot diagrams for field angles 0, 2, 3, and 4 mr, respectively. The compromise image plane is 43.992 inches from the secondary mirror. The principal residual aberrations are field curvature and astigmatism. The magnitude of field curvature and astigmatism is illustrated in Figures 3-41 and 3-42. The field angle is 4 mr and the plotting planes are 43.978 and 43.972 inches, respectively.

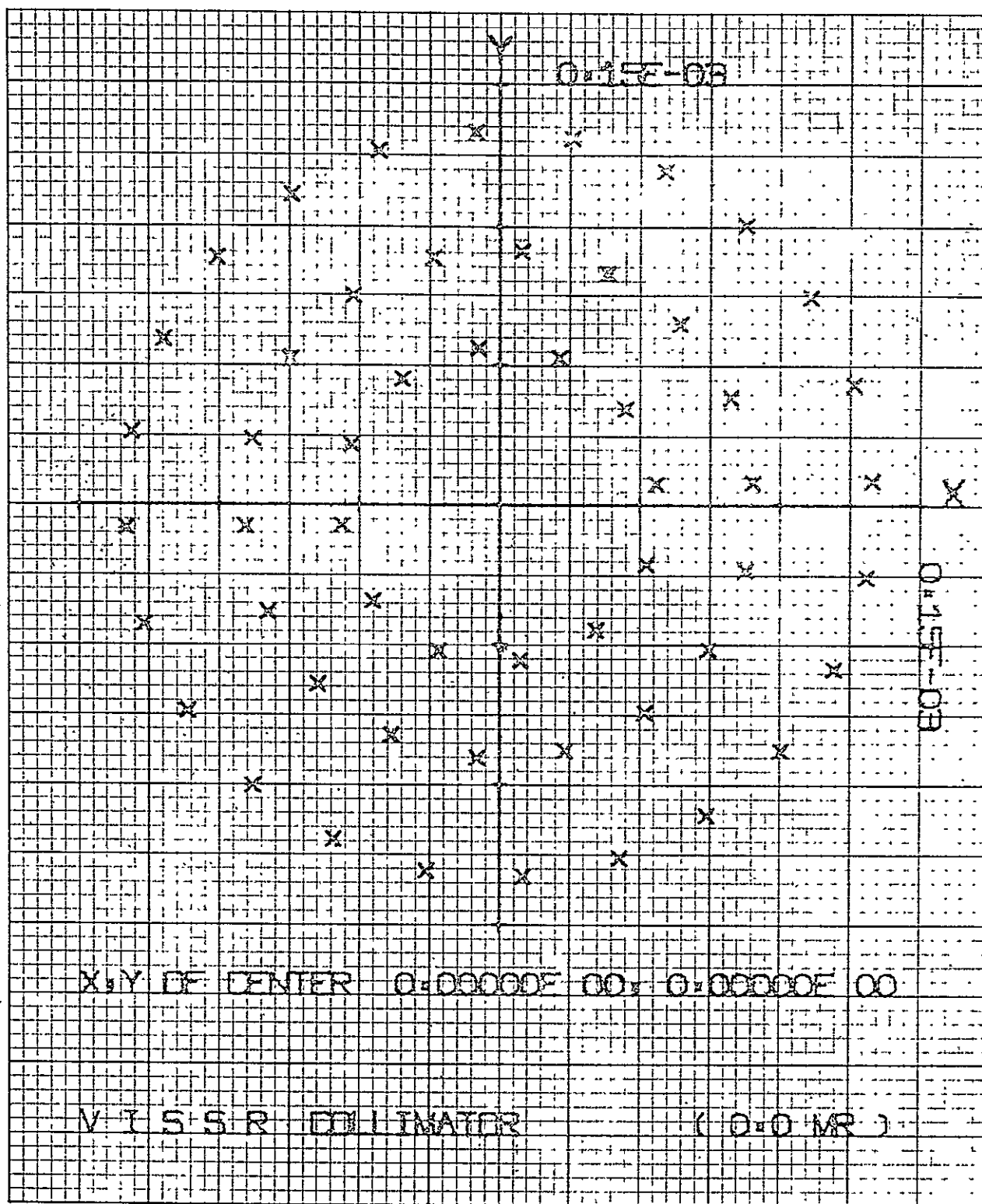


Figure 3-37. Spot Diagram 0.0 mr

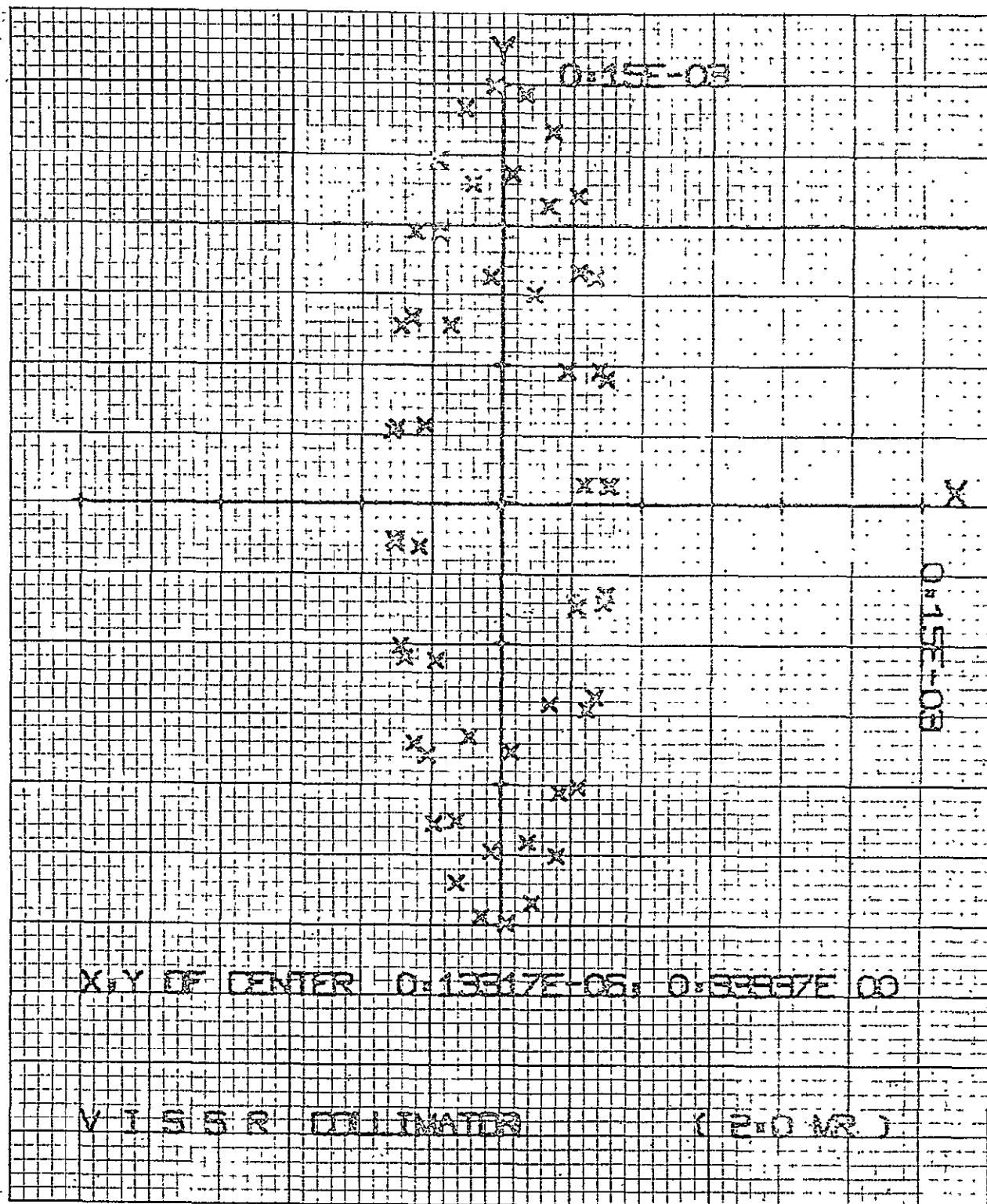


Figure 3-38. Spot Diagram 2.0 mr

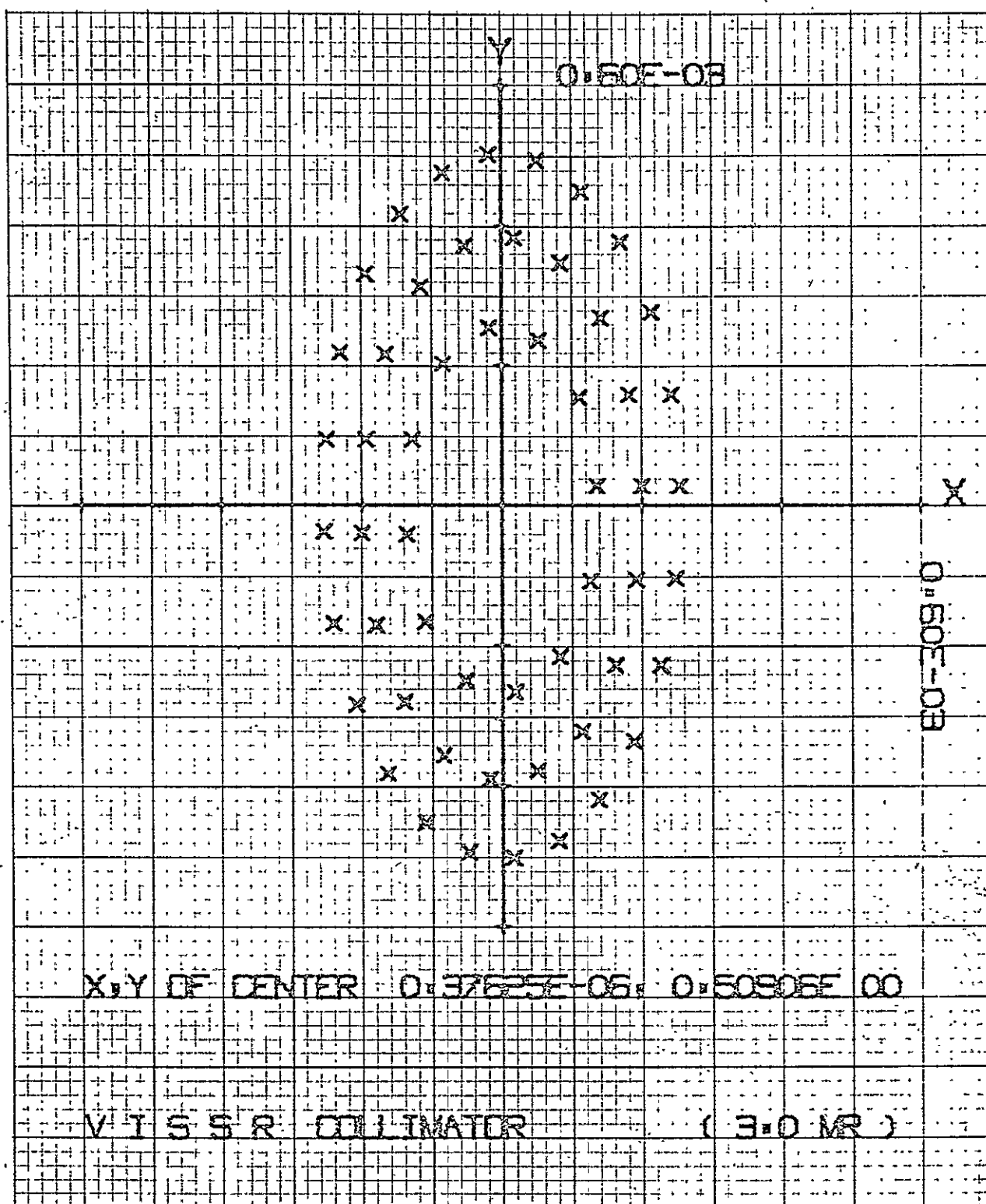


Figure 3-39. Spot Diagram 3.0 mr

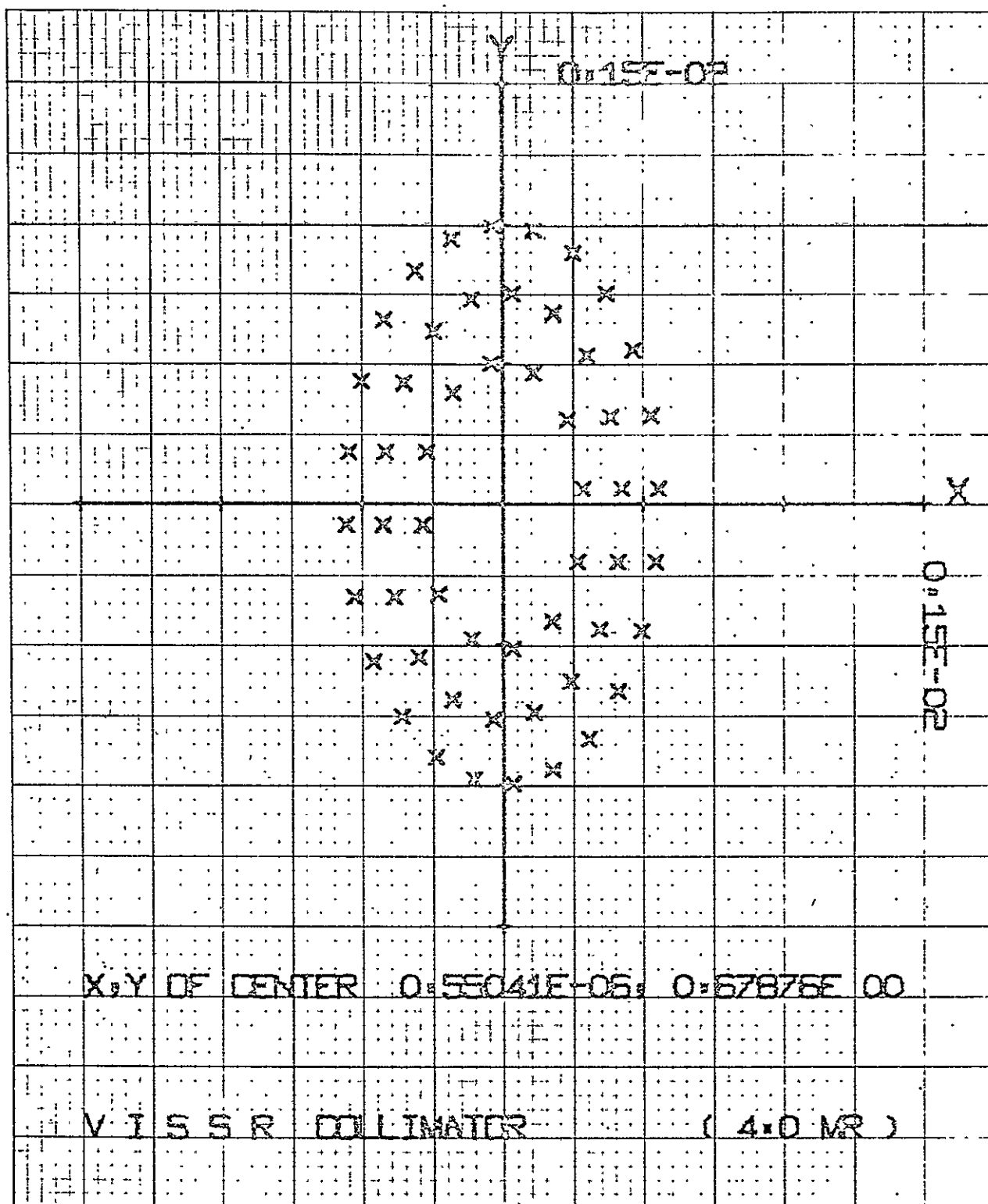


Figure 3-40. Spot Diagram 4.0 mr

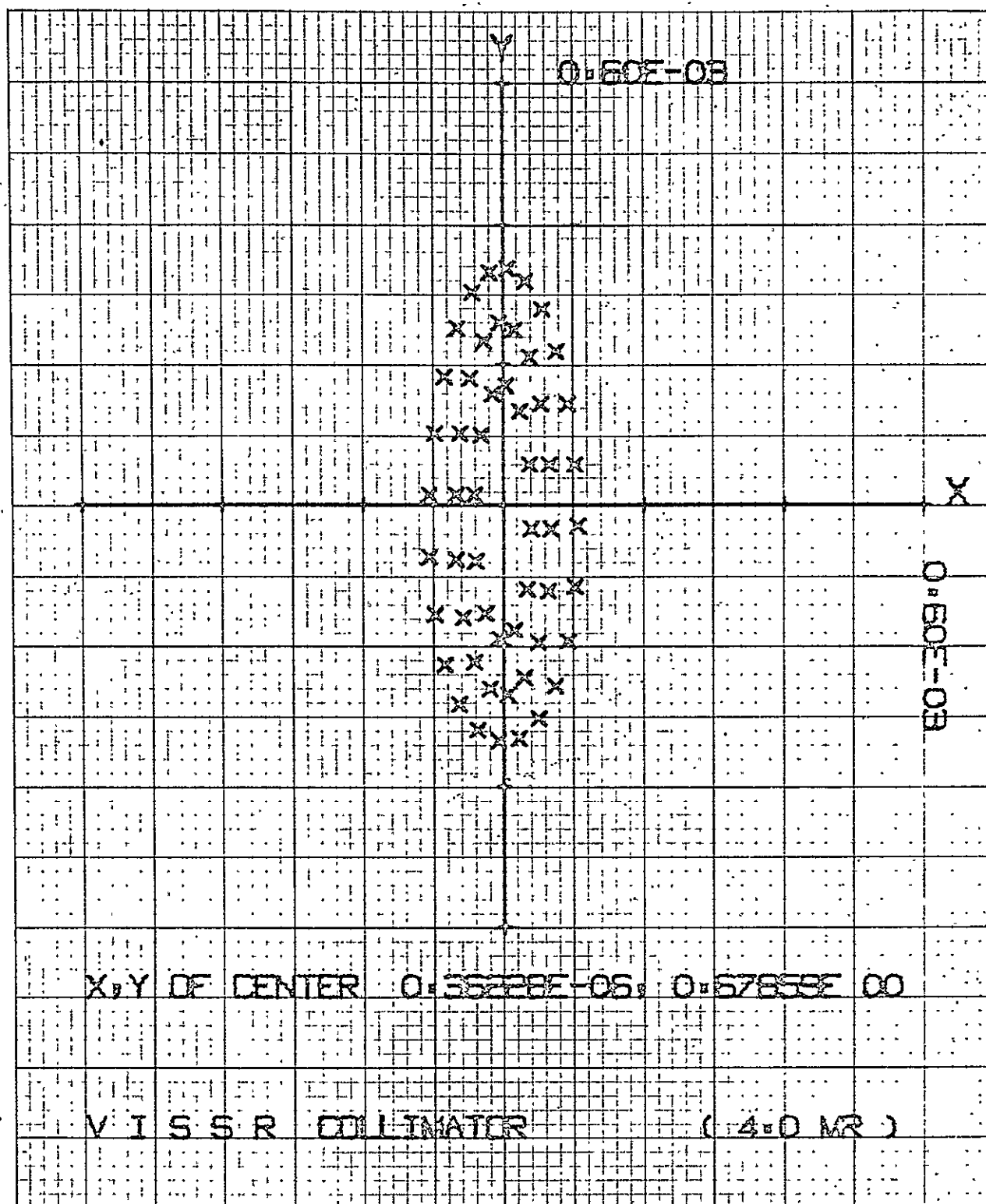


Figure 3-41. Field Curvature and Astigmatism (43.978 in.)

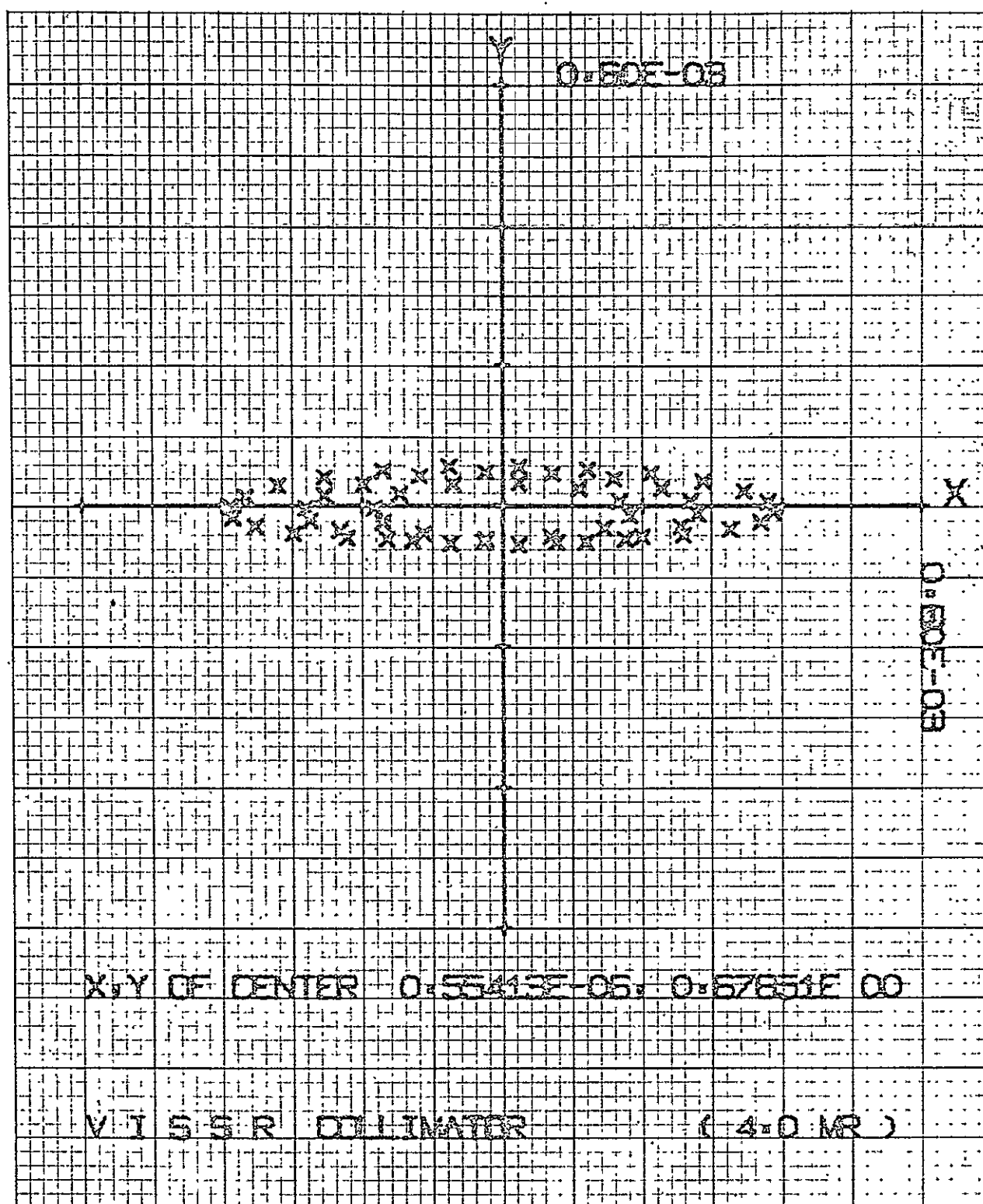


Figure 3-42. Field Curvature and Astigmatism (43.972 in.)

Table 3-17 gives the geometrical blur circle including 95% energy based on the image spot diagrams.

Table 3-17. Image Blur

Field Angle (mr)	Geometrical Blur Circle Including 95% Energy (μ r)
0	1.4
± 2	1.5×0.6
± 3	5.0×3.0
± 4	10.6×7.1

Radial energy distributions for various fixed angles are tabulated in Table 3-18. These energy distributions were obtained by root-sum-square (rss) of the following:

Residual geometrical aberrations

Diffraction effects ($\lambda = 0.6 \mu\text{m}$)

Fabrication tolerances

Table 3-18. Energy Distribution, Optical System (Class I and II)

Angular Dimension of Measuring Aperture (rad)	Fractional Energy Contained within Specified Aperture			
	0 mr	± 2.0 mr	± 3.0 mr	± 4.0 mr
2×10^{-6}	0.13	0.13	0.07	0.00
4×10^{-6}	0.44	0.44	0.27	0.05
6×10^{-6}	0.62	0.62	0.58	0.26
8×10^{-6}	0.82	0.82	0.74	0.52
10×10^{-6}	0.89	0.89	0.88	0.66
12×10^{-6}	0.91	0.91	0.90	0.82
14×10^{-6}	0.92	0.92	0.91	0.90
16×10^{-6}	0.93	0.93	0.92	0.91
18×10^{-6}	0.94	0.94	0.93	0.92
20×10^{-6}	0.95	0.95	0.94	0.93

The estimated equivalent wavefront deformation is given in Table 3-19.

Table 3-19. Wavefront Deformation (Class I and II).

Field Angle (mr)	Wavefront Deformation $\lambda = 0.6\mu$
0	0.4λ
± 2	0.4λ
± 3	0.5λ
± 4	0.6λ

The equivalent modulation is given in Table 3-20.

Table 3-20. Modulation Transfer

Spatial Frequency (cycles/radian)	MTF	
	Sine Wave	Square Wave
1,000	1.00	1.00
5,000	0.97	0.99
10,000	0.94	0.96
15,000	0.91	0.93
20,000	0.88	0.91
25,000	0.86	0.91
30,000	0.83	0.91
35,000	0.80	0.90
40,000	0.78	0.88
50,000	0.72	0.85
60,000	0.67	0.81
70,000	0.61	0.76

Tolerance Analysis. - Image quality is being specified relative to the assembled optical train. No specific tolerances have been imposed on the flat mirrors or on the primary and secondary mirrors.

Several degrees of freedom are necessary to optimize a near diffraction-limited optical system. These include tilt of one mirror, lateral motion (perpendicular to optical axis), and axial motion (parallel to optical axis). These

adjustments are accommodated by motions built into the primary-secondary mirror system as follows:

1. Tilting the primary mirror $\pm 2.25^\circ$ about its vertex
2. Lateral adjustment of the secondary mirror ± 0.040 inch
3. Axial adjustment of the primary mirror ± 0.26 inch.

The lateral and tilt adjustments are used to compensate for misalignment between the mirror surfaces and the mechanical axis. The axial adjustment is required to adjust the system back focal length (BFL). The BFL must be adjusted to ± 0.100 inch.

The optical design equations (equivalent to those contained in the VISSR/SMS Second Quarterly Report) indicate that if no change in primary-secondary mirror spacing were permitted, the aspheric primary mirror basic radius would be required to be within 0.015% of its nominal design. This is clearly unreasonable. However, the magnitude of $\frac{\partial \text{BFL}}{\partial f_p}$ and $\frac{\partial \text{BFL}}{\partial S_{p-s}}$ are equal and opposite in sign. Therefore, with a $\Delta S_{p-s} = \pm 0.2$ adjustment, the primary mirror basic curve tolerance can be relaxed to approximately 1/4%. This is a reasonable tolerance for a system of this type.

Vignetting. - The VISSR entrance aperture (16-inch OD, 6.4-inch ID) ideally would be the only aperture stop in the VISSR-calibrator setup for field angles of ± 4.0 mr. Because of multiple constraints in the optical-mechanical design, this design goal was not realizable. The maximum vignetting, with the folding mirror in the 45° position, for the visible and thermal channels is 1/2 and 3/4%, respectively. After the calibrator is assembled, aligned, and calibrated, the uncertainty in the vignetting levels is expected to be less than 1/3 and 1/2% for the visible and thermal channels, respectively.

Structural-Mounting Analysis. - The optical component structures and mounting configurations were considered critical elements in the overall design. It has been assumed that the collimator will always be operated in a single spatial orientation; vertical with the folding mirror in the UP position.

Deflections of the primary mirror structure were calculated. As an approximation, a flat plate was used with the following dimensions: OD, 20 inches; ID, 4.0 inches; and thickness, 3.334 inches. Calculations were made to determine the mounting zone where the inner and outer edge deflections are comparable in amplitude. Figure 3-43 indicates the results. It indicates the mirror should be supported at a zone with a 7.6-inch radius and that the edge deflections for this case are 1.7×10^{-6} inch (less than $\lambda/10$). The mirror will be supported from this zone by a Pro-Seal annulus serving as a bonding agent between the primary mirror and the Invar mounting plate. Additional data are contained in this report in the section entitled Test and Calibration Equipment.

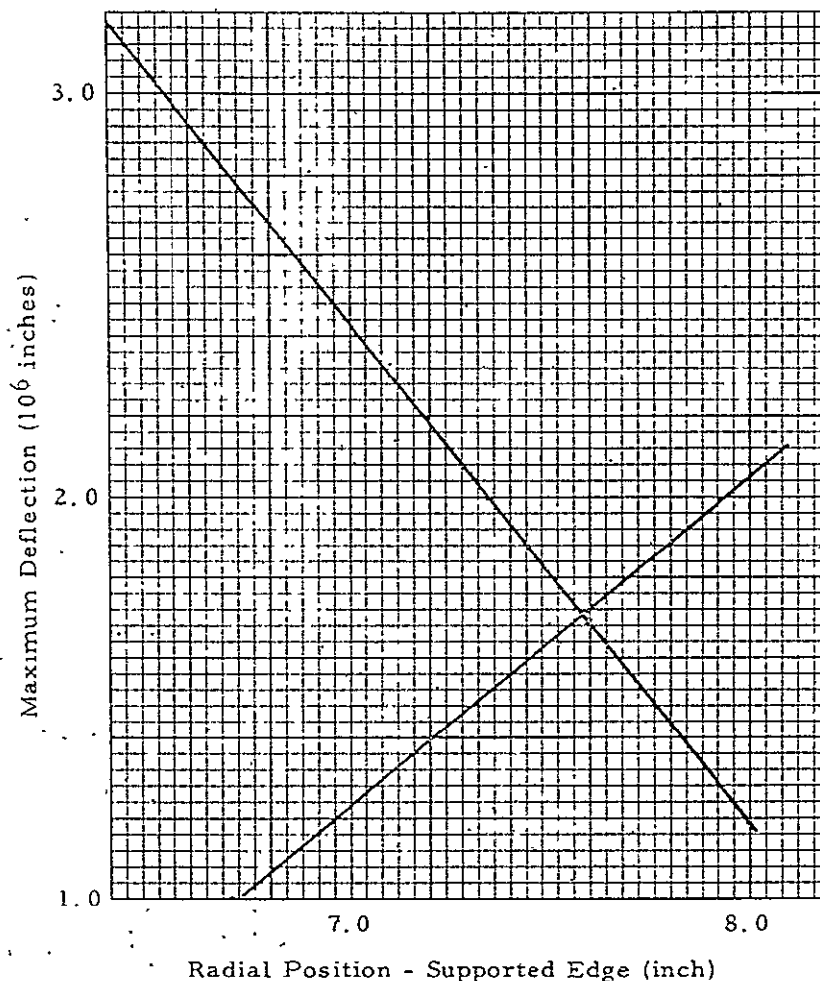


Figure 3-43. Primary Mirror Deflection vs Radial Position

Calibrator-Collimator Optical System Image Quality

In the final figuring stages of the calibrator optical elements, it was apparent that relaxation of the specification image quality might be necessary to enable Perkin-Elmer to have the mirror coatings applied by OCLI in a timely manner. Thus, it was important to determine energy distribution trade-off and possible relaxation in the optical specification.

In addition to the possible specification relaxation, Perkin-Elmer indicated it was desirable to measure the image energy distribution in a double-pass mode. Visualize a point source placed at the calibrator optical system prime focal plane. Energy traverses the optical system (backwards) and is retro-reflected by an auxiliary plane mirror such that the energy traverses the optical system (forward) a second time. The measuring pin hole detector is located at the prime focal plane.

Double-pass measurement mode necessitated modifying the single-pass image energy distribution, thus raising the question of what was the appropriate method to use. Computer ray tracing showed that image diameter due to residual aberrations for double-pass was twice single-pass image diameter. Thus, it was assumed that image size due to fabrication would also be doubled in the double-pass mode. On the other hand, diffraction effects were assumed to be the same for either measurement mode.

Thus, the image energy distribution was calculated in the following manner:

Single pass (SP)

$$\theta_{ID_{Total}}^{(SP)} = [\theta_{ID_I}^2 + \theta_{ID_{II}}^2 + \theta_{ID_{III}}^2]^{\frac{1}{2}} \quad (3-40)$$

where $\theta_{ID_{Total}}^{(SP)}$ = Total angular image diameter

θ_{ID_I} = Angular image diameter due to residual aberration

θ_{IDII} = Angular image diameter due to fabrication

θ_{IDIII} = Angular image diameter due to diffraction

Double pass (DP)

$$\theta_{ID_{Total}}^{(DP)} = \left[(2\theta_{IDI})^2 + (2\theta_{IDII})^2 + \theta_{IDIII}^2 \right]^{\frac{1}{2}} \quad (3-41)$$

In like manner, double-pass measurements are extrapolated to single-pass by

$$\theta_{ID_{Total}}^{(SP)} = \left\{ \left[2 \left[\left(\theta_{ID_{Total}}^{(DP)} \right)^2 - \left(\theta_{IDIII} \right)^2 \right]^{\frac{1}{2}} \right]^2 + \theta_{IDIII}^2 \right\}^{\frac{1}{2}} \quad (3-42)$$

Figures 3-44 and 3-45 illustrate the specification image energy distribution for three field angles for single-pass and double-pass, respectively.

Due to uncertainties in interpretation of the double-pass data, the decision was made to run single-pass energy distribution measurements. The results are given in Figure 3-46. Experimental data (Class II) is plotted for single-pass and double-pass. The double-pass experimental data is extrapolated to single-pass. It appears that the RSS calculation methods as given above fit the experimental data well. Although it is seen that the experimental data does not meet the optical specification, it is close. The system was considered acceptable.

The collimator mirrors were mounted and lined in the VISSR calibrator structure. The Class I interferograms are shown in Figure 3-47. The measuring technique uses a scatter plate interferometer operating at 0.6328μ . The calibrator optical system is autocollimated with a 22-inch diameter test flat. The scatter plate is located at the focus. Since the system uses a double pass configuration, each fringe in the interferogram represents $\lambda/4$ deformation. If all fringes are straight and parallel, the system is perfect; any deviation from straightness or parallelism represents optical error. Photographs were taken with calibrator axis vertical. The folding mirror was at 45° . Temperature was room ambient at 73°F .

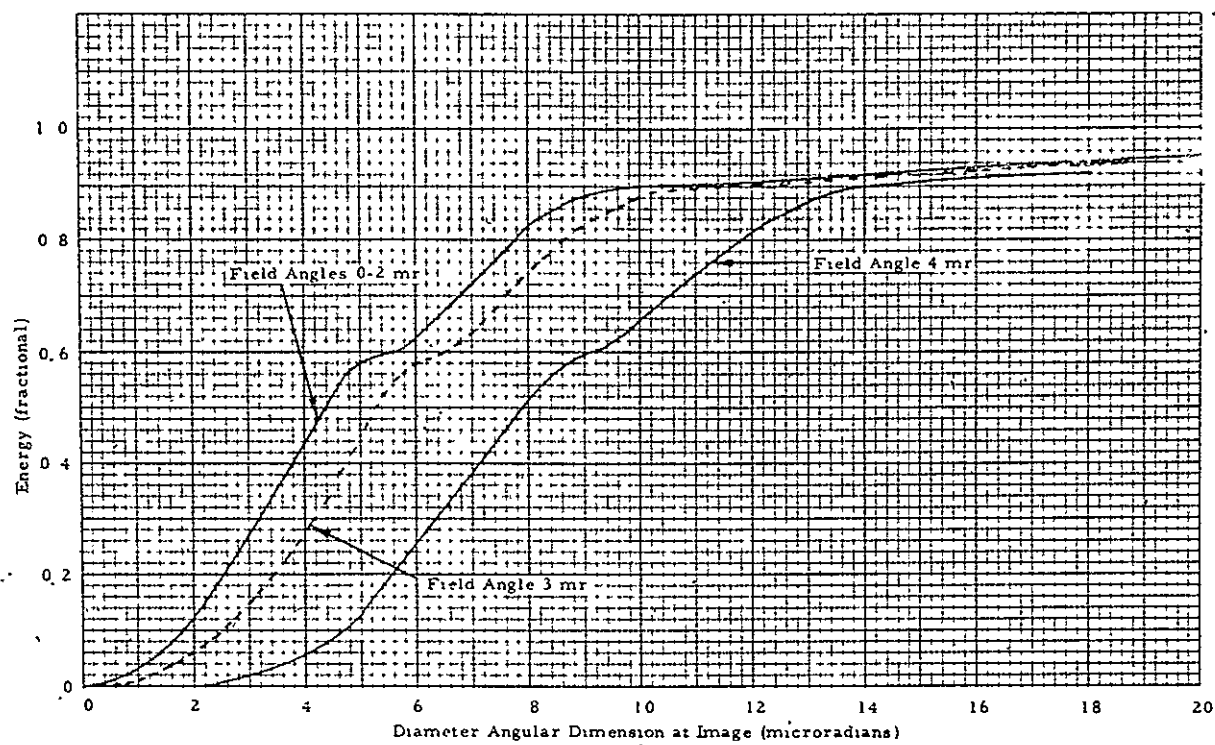


Figure 3-44 Energy Distribution Combined Effects
(Single Pass)

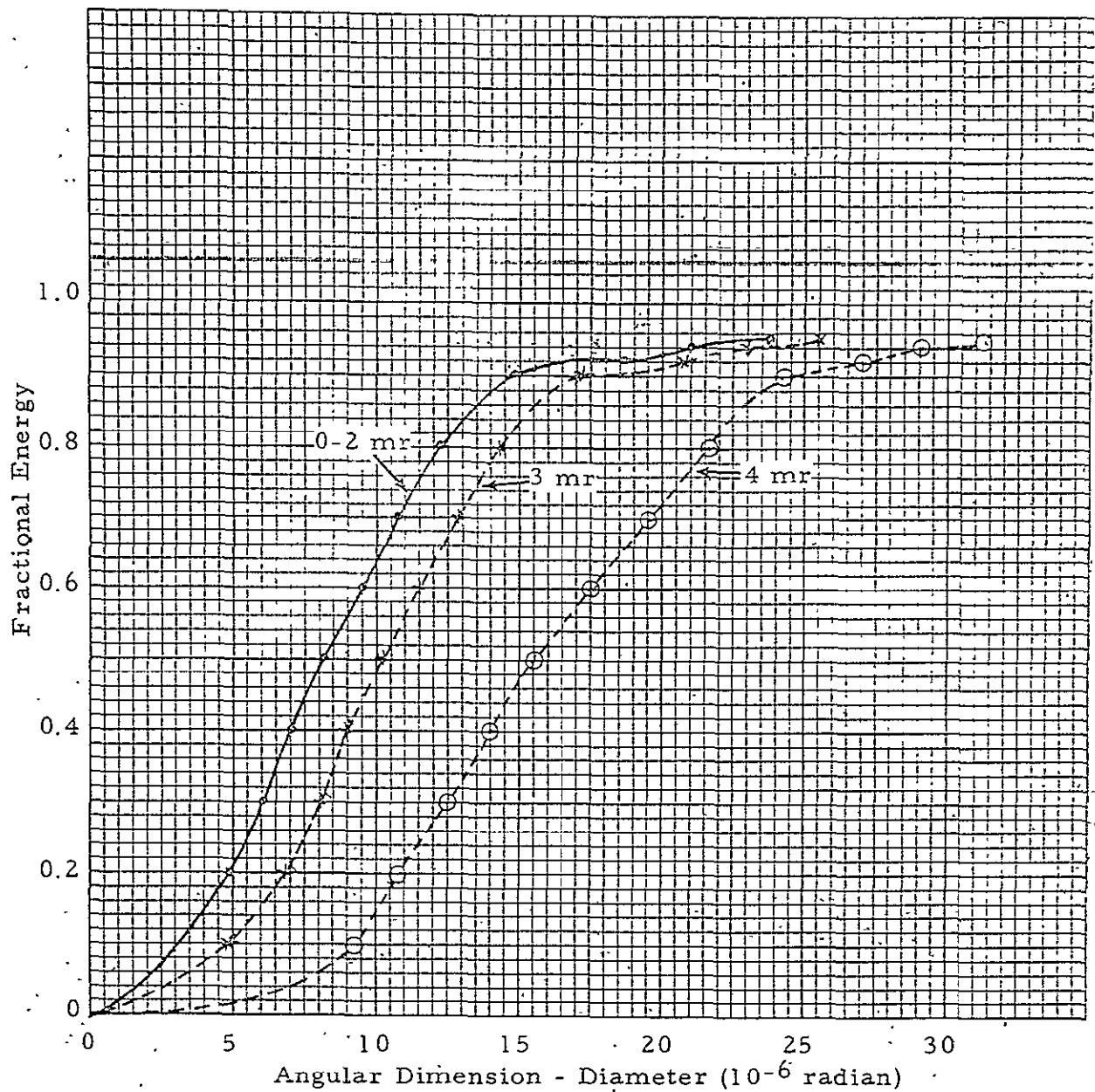
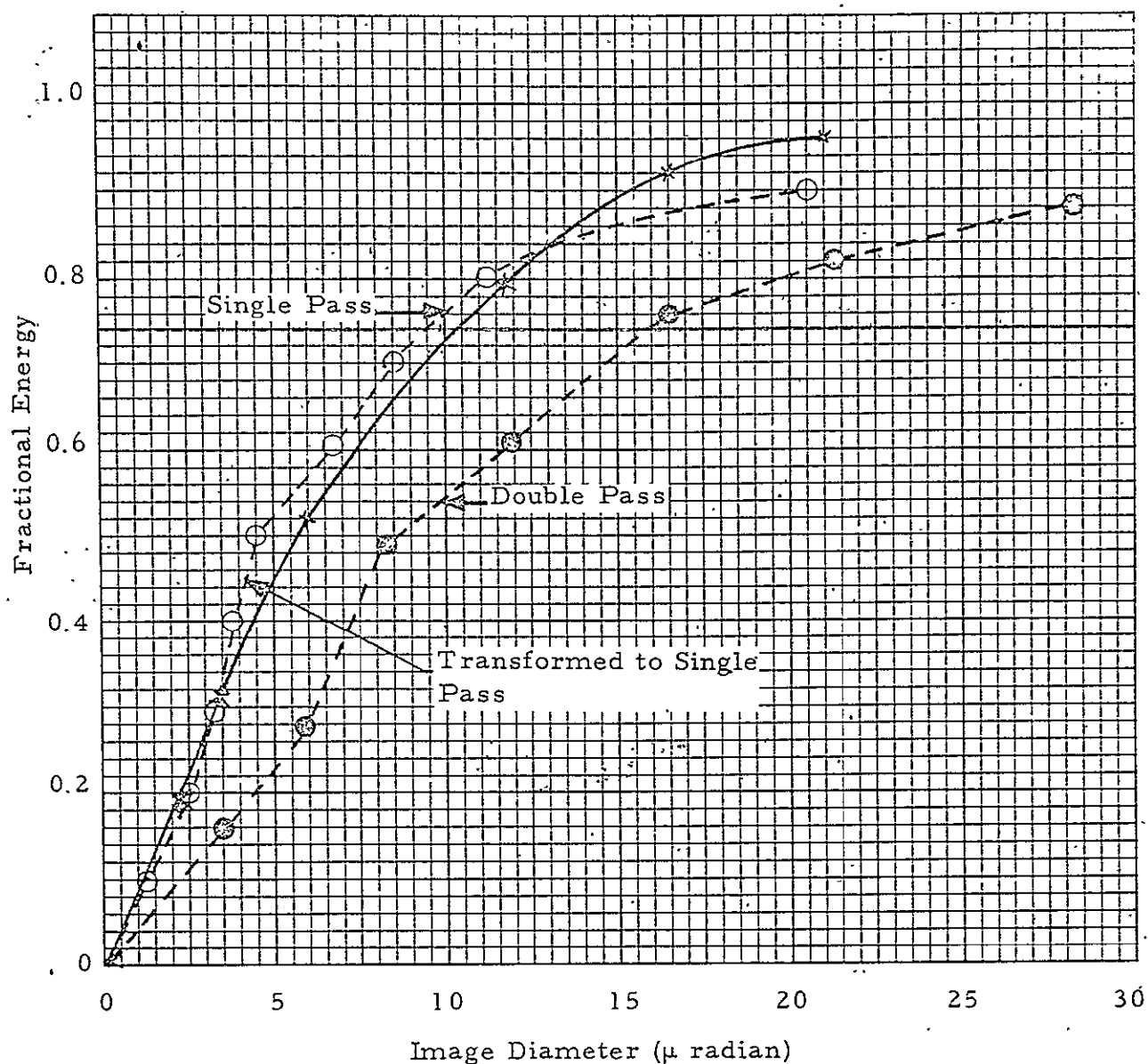
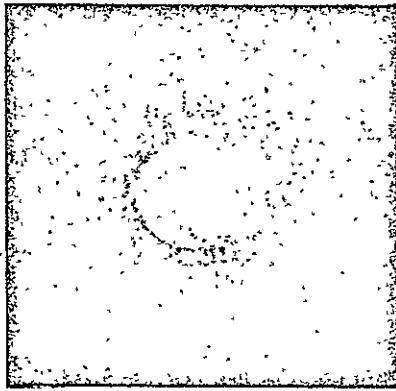


Figure 3-45. Calibrator Optical System Double Pass Energy Distribution

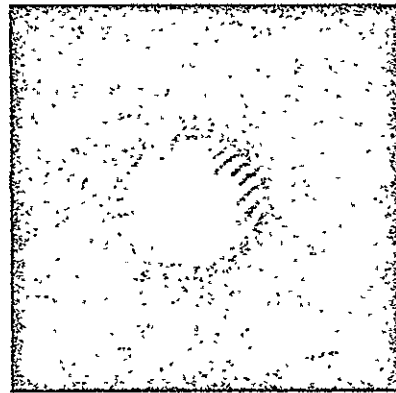


- Data in Double Pass Energy Distribution Measurements Which Has Been Converted to Single Pass Measurement Mode.
- × × Single Pass Measurement Data.

Figure 3-46. Energy Distribution Measurement



View A



View B

Figure 3-47. Interferograms - VISSR Calibrator No. 1 - Class I

Subsequently, square bar MTF was measured. The results are shown in Figure 3-48. The decreased modulation at higher spatial frequencies is probably associated with:

1. Image quality slightly less than specification
2. Measurement configuration
 - a. 7-micron wide slit
 - b. SiPD/electronics frequency response
3. SBRC collimator.

The MTF measurements confirm that the VISSR calibrator image quality is sufficient, such that the calibrator can be used to measure VISSR.

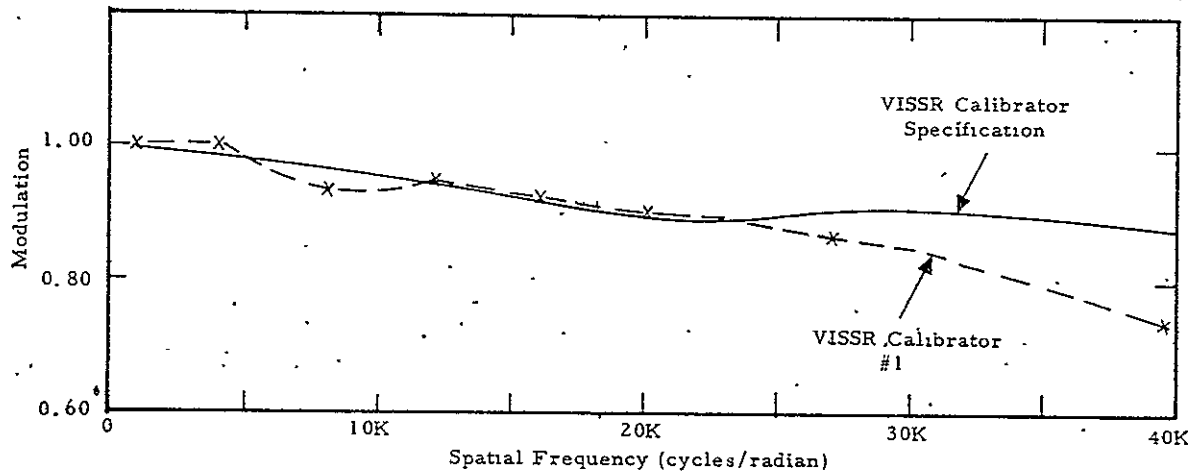


Figure 3-48. Square-Wave Modulation, VISSR Calibrator No. 1

Relation Between EFL, BFL, f_p , S_{p-s} , and f_s

The following analysis is useful in determining appropriate methods to measure calibrator-collimator effective focal length (EFL).

The following gives the mathematical relationship between the quantities.

$$EFL = \frac{f_s f_p}{f_p + f_s - S_{p-s}}$$

$$BFL = \frac{f_s (S_{p-s} - f_p)}{S_{p-s} - f_p - f_s}$$

where EFL = effective system focal length

BFL = back focal length, distance from secondary mirror to focal plane

f_p = primary mirror focal length

f_s = secondary mirror focal length

S_{p-s} = spacing between primary and secondary mirrors

By differentiation and collection of terms

$$\frac{\partial \text{EFL}}{\partial f_p} = M^2 \frac{(f_s - S_{p-s})}{f_s}$$

$$\frac{\partial \text{EFL}}{\partial S_{p-s}} = M^2 \frac{f_p}{f_s}$$

$$\frac{\partial \text{EFL}}{\partial f_s} = M^2 \frac{f_p}{f_s^2} (f_p - S_{p-s})$$

where $M = -\frac{\text{EFL}}{f_p}$

For the VISSR calibrator system

$$\text{EFL} = 169.7$$

$$M = -3.91$$

where $f_p = 43.4$ inches, $f_s = -15.12$ inches, and $S_{p-s} = 32.15$ inches.

Therefore,

$$\frac{\partial \text{EFL}}{\partial f_p} = (3.91)^2 \frac{(-15.12 - 32.15)}{-15.12} = 47.8$$

$$\frac{\partial \text{EFL}}{\partial S_{p-s}} = (3.91)^2 \frac{43.4}{-15.12} = -43.9$$

$$\frac{\partial \text{EFL}}{\partial f_s} = (3.91)^2 \frac{43.4}{(-15.12)^2} (43.4 - 32.15) = 32.6$$

The change of focal plane location (ΔF) as a function of change of f_p , f_s , and S_{p-s} is given by

$$\Delta F = M^2 \Delta f_p - M^2 \Delta S_{p-s} + (M^2 - 1) \Delta f_s + \Delta S_{s-f}$$

where S_{s-f} is the structure's distance from secondary mirror to prime focal plane

The calibrator specifications include EFL = 169.7 ± 3 inches and the focal plane occurs at the nominal design value ± 0.100 inch.

Assuming the optical vendor can hold the focal length of aspheric surfaces within 0.25% of the design values,

$$\text{if } \Delta f_p = 0.0025 f_p = 0.109 \text{ inch}$$

$$\Delta f_s = -0.0025 f_s = 0.038 \text{ inch}$$

$$\begin{aligned} \text{then } \Delta \text{EFL} &= (47.8)(0.109) + (32.6)(0.038) \\ &= 5.2 + 1.24 = 6.44 \end{aligned}$$

To correct for this, a change in S_{p-s} is required:

$$\Delta S_{p-s} = \frac{\Delta \text{EFL}}{43.9} = -\frac{6.44}{43.9} = -0.147$$

The change of focal plane, ΔF , for this condition is

$$\begin{aligned} \Delta F &= (3.91)^2 (0.109) - (3.91)^2 (0.147) \\ &\quad + (3.91^2 - 1)(0.038) + 0.147 \\ &= 1.67 - 2.25 + 0.54 + 0.147 = 0.11 \end{aligned}$$

Thus, both EFL and focal position are not compensated for simultaneously by a change of S_{p-s} . Thus, a compromise may be necessary.

For the case given above, assume residual $\Delta F = 0.050$. Then

$$\Delta S_{p-s} = \frac{-0.050 + 1.67 + 0.54 + 0.147}{3.91^2} = \frac{2.307}{15.3} = 0.151$$

This results in ΔEFL of

$$\begin{aligned} \Delta \text{EFL} &= (47.8)(0.109) - (43.9)(0.151) + (932.6)(0.038) \\ &= 5.2 - 6.64 + 1.24 = -0.20 \end{aligned}$$

Thus, if the aspheric surfaces can be figured such that their focal lengths are within 1/4% of the design values, the calibrator specifications for EFL and image plane location can be met with the adjustment capability built into the VISSR calibrator hardware.

One of the potential optical vendors has asked how the EFL of an optical system can be measured to the accuracy being requested for the VISSR calibrator. Since the EFL has been specified as 169.7 ± 3 inches, the measurement technique should be good to 1.5 inches.

The image motion, D , (perpendicular to optical axis) as a function of input collimator beam angle (θ) is given by

$$D = (\text{EFL}) \theta$$

By differentiation

$$\frac{\partial(\text{EFL})}{\partial D} = \frac{1}{\theta}, \quad \frac{\partial(\text{EFL})}{\partial \theta} = -\frac{D}{\theta^2}$$

The total error in measurement of EFL, $(\Delta \text{EFL})_T$, due to errors in linear dimension, D , and angle, θ , is given by

$$(\Delta \text{EFL})_T \leq \left| \frac{\Delta D}{\theta} \right| + \left| \frac{D \Delta \theta}{\theta^2} \right| = \frac{\theta \Delta D + D \Delta \theta}{\theta^2}$$

If measurement accuracy of $D = 0.003$ inch and $\theta = 3 \text{ sec} = 15 \times 10^{-6}$ radian is assumed, and a nominal change of collimator beam angle of $\theta = 0.003$ radian

$$\begin{aligned} (\Delta \text{EFL})_T &= \frac{(0.003)(0.003) + (0.509)(15 \times 10^{-6})}{(0.003)(0.003)} \\ &= 1.8 \text{ inches} \end{aligned}$$

Thus, it is apparent that a careful measurement setup is required if accuracy of EFL measurement is to be achieved to ± 1.5 inches, although it does appear feasible to accomplish it.

Visible Source

Design Goals. - The design goals for the VISSR calibrator visible source included:

1. Field coverage - 4 mr
2. Earth albedo radiance levels - 0.15 to 1.0 in eight steps achieved by NDF elements
3. Uniformity
 - a. Field $\pm 2\%$
 - b. Aperture $\pm 10\%$
4. Simulation of solar spectral distribution
5. Radiometric calibration - 10%

The task of achieving the above requirements simultaneously was a formidable one. However, the reasons for achieving them appeared valid. For example, the field coverage was necessary to reduce thermal vacuum alignment problems, especially at Philco-Ford. VISSR had to be calibrated over the 0 to 1.0 earth albedo range. Field uniformity has a direct relationship to calibration accuracy. There is some evidence that PMTs have spectral sensitivity changes as a function of temperature. The effect on VISSR radiometric calibration of the above, or any other cause of VISSR spectral sensitivity change, will be minimized by having the VISSR calibrator spectral radiance distribution simulate solar spectral distribution.

Detailed Design. - The final design concept is schematically illustrated in Figure 3-49. The radiant energy source is a Sylvania Halogen lamp Model FAV. The lamp filament is imaged at the calibrator "entrance pupil image plane" via the first field lenses and relay lens. It is then imaged onto the calibrator entrance pupil via the second field lens. The plane labeled "image of calibrator focal plane" is imaged at the MTF reticle plane/calibrator focal plane via the relay lens.

A ground fused silica diffuser is placed near the FAV lamp envelope to diffuse the lamp filament at the calibrator entrance pupil and to enhance

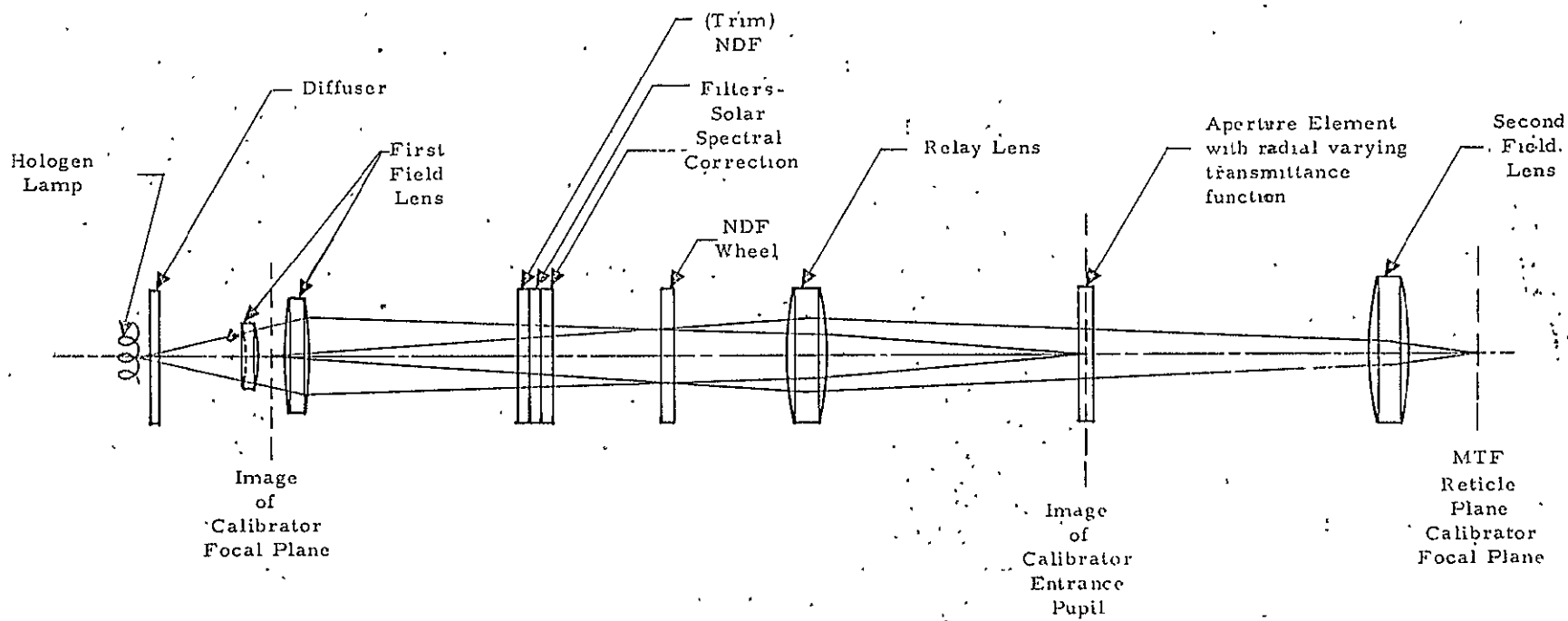


Figure 3-49. Calibrator Visible Source Optical Schematic

uniformity at the calibrator focal plane. This diffuser causes large non-uniformity of radiance level across the calibrator entrance pupil. The element with radial-varying transmittance function is introduced at the plane labeled image of calibrator entrance pupil to compensate for the diffuser effect.

The trim NDF element is used to reduce visible source/collimator maximum radiance level to unity effective albedo. The filters-solar spectral correction converts the visible source/collimator spectral radiance to a distribution approximating solar spectral distribution.

Initial design efforts used computer ray tracing techniques. The uniformity aspects of the optical system could not be handled with existing programs and knowledge of diffusing element characteristics.

The optical system was set up breadboard fashion in the laboratory. Solid angle-area (ΩA) calculations were used to obtain appropriate spacings and lens focal lengths. The solid angle-area product required by the design goals was 0.0038 sr in.² The solid angle-area products throughout the optical system were verified. Table 3-21 summarizes the visible source optical system parameters.

The element with radial varying transmittance function serves two purposes. First, there is a photoetched mask which simulates the calibrator entrance pupil. This permits more realistic laboratory uniformity measurements without the necessity of having the massive calibrator-collimator optics. The second function is to improve uniformity across the calibrator entrance pupil. Figure 3-50 illustrates the radial transmittance function. The transmittance function as illustrated was obtained by vacuum-depositing techniques. The photoetched titanium-gold mask was fabricated first. The part was then coated with Nichrome. The Nichrome was deposited through a 0.020-inch wide evaporation slit. During the depositing, the glass element was rotated about an axis perpendicular to the surface being coated. The result is a film thickness that varies in the radial direction.

Table 3-21. Visible Source Optical System Parameters

Description	Dimensions (inches)	Configuration	Comments
Quartz Iodine Lamp - FAV	0.10×0.11	Helical	Sylvania
Ground Fused Silica to Field Lens 1A	0.485	Spacing	
Fused Silica			
Thickness	0.067	Plane parallel	
OD	0.70		
Filament to Field Lens 1A	0.725	Spacing	
Field Lens 1A			Fused silica
R ₁	-1.351	Spherical	
Thickness	0.20		
R ₂	-0.65		
Field Lens 1A to 1B	0.10	Spacing	
Field Lens 1B			
Focal length	1.97	Spherical	
Thickness	0.146		
OD	1.18		
Field Lens 1B to Relay Lens	4.00	Spacing	
Relay Lens			
Focal length	2.50		
Thickness	0.138		
OD	0.985		
Relay Lens to Aperture Element			
Element	2.07	Spacing	
Aperture Element		Plane parallel	
Thickness	0.10		
OD	1.15		
Aperture Element to Field Lens 2	2.53	Spacing	
Field Lens 2			
Focal length	2.48		
Thickness	0.198		
OD	1.18		
Field Lens 2 to MTF Wheel	1.075		

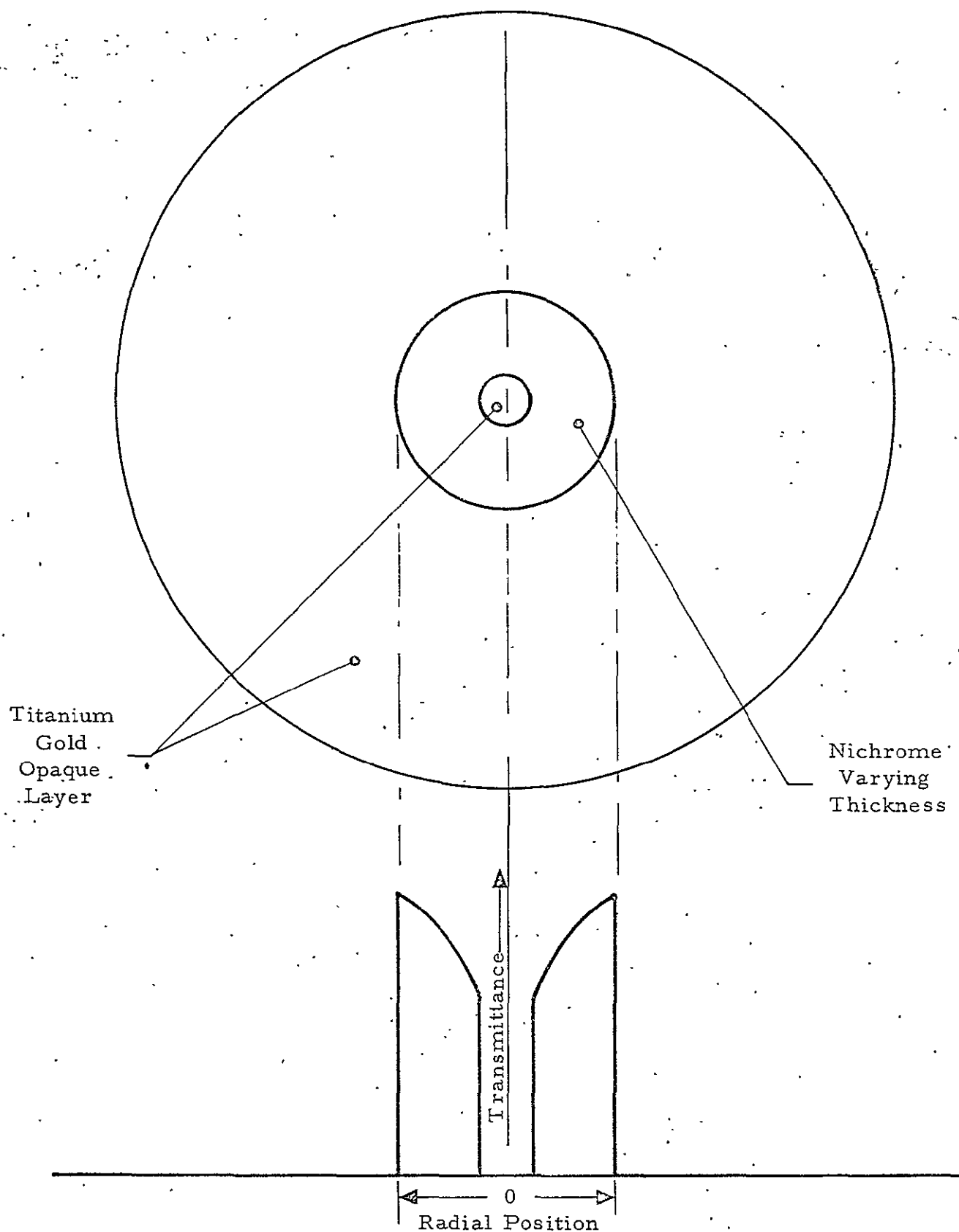


Figure 3-50. Aperture Element - With Radial Varying Transmittance Function

The evaporation slit with uniform slit width was used for VISSR calibrator No. 1. Figure 3-51 illustrates the anticipated corrected relative radiance function across the calibrator entrance pupil. If an evaporation slit with variable width were used, the relative radiance (corrected) curve could be made flat within the bounds of the visible source radial symmetry. Due to schedule and cost considerations, this was not done.

The ground fused silica scatterer is fabricated in the following manner. American Optical grinding compound No. 302 $\frac{1}{2}$ is mixed with water and spread thinly on a thick glass plate. The fused silica substrate is pressed firmly against the plate and slowly moved in a figure 8 pattern for a few minutes until the surface is ground.

The neutral density filter wheel provides filters for eight albedo levels. The nominal transmittance of the NDF wheel elements is listed in Table 3-22.

Table 3-22. NDF Wheel Elements, Nominal Transmittance

Position	Transmittance
1	1.00
2	0.91
3	0.84
4	0.75
5	0.65
6	0.51
7	0.32
8	0.15

Uniformity Measurements. - Preliminary uniformity measurements have been made on the revised design breadboard visible source system. The aperture uniformity is shown in Figure 3-52. The inner and outer diameters correspond to the VISSR calibrator entrance pupil. The average value across the aperture is 3.40. The variation is +15%, -20% for 95% of the aperture. Figure 3-53 illustrates field uniformity. The total field diameter is 4 mr. Average value across the field is 3.54 with a variation of $\pm 5\%$.

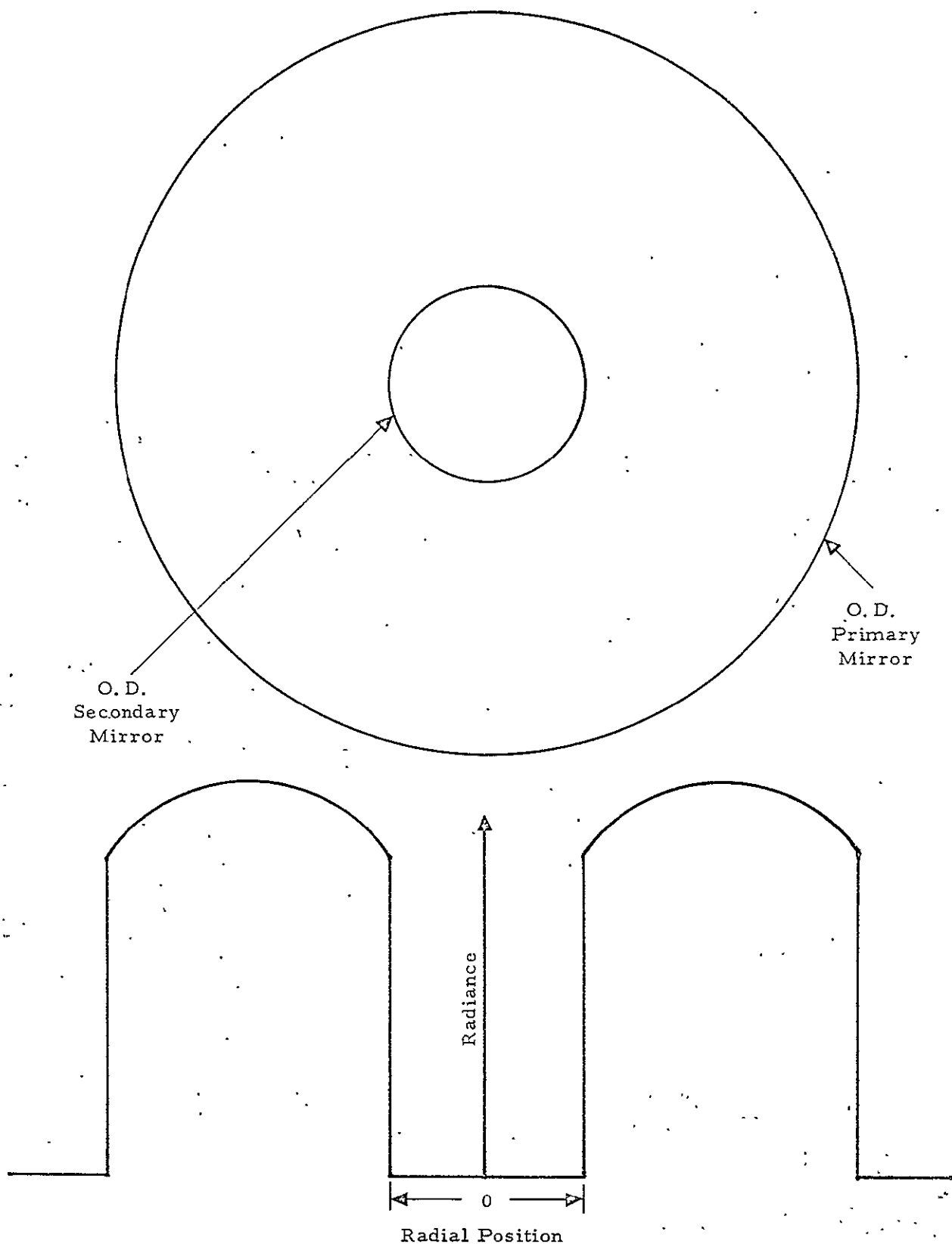


Figure 3-51. Radiance Profile Across VISSR Calibrator Entrance (Exit) Pupil

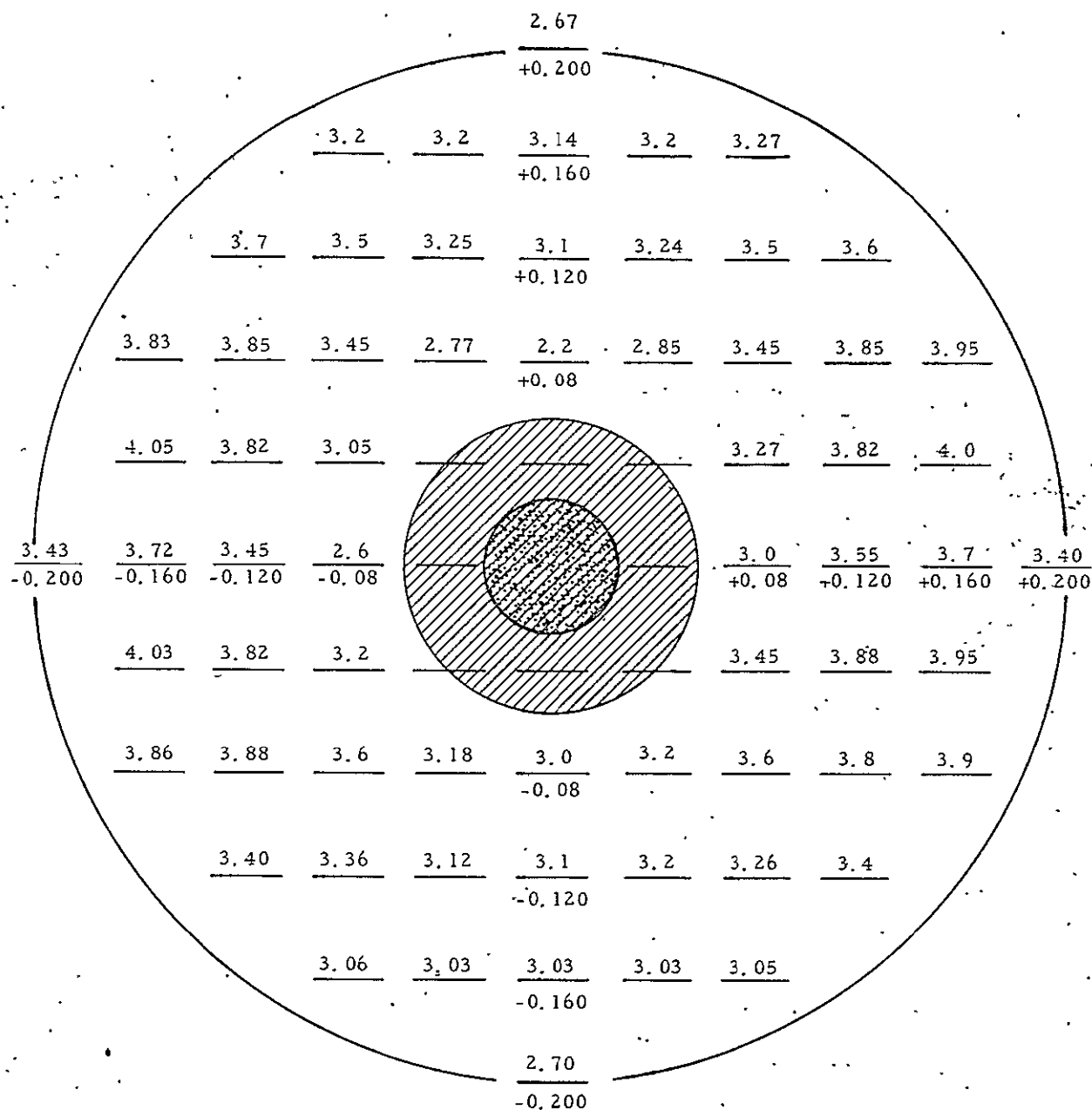


Figure 3-52, Aperture Uniformity - Breadboard Visible Source - Revised Design

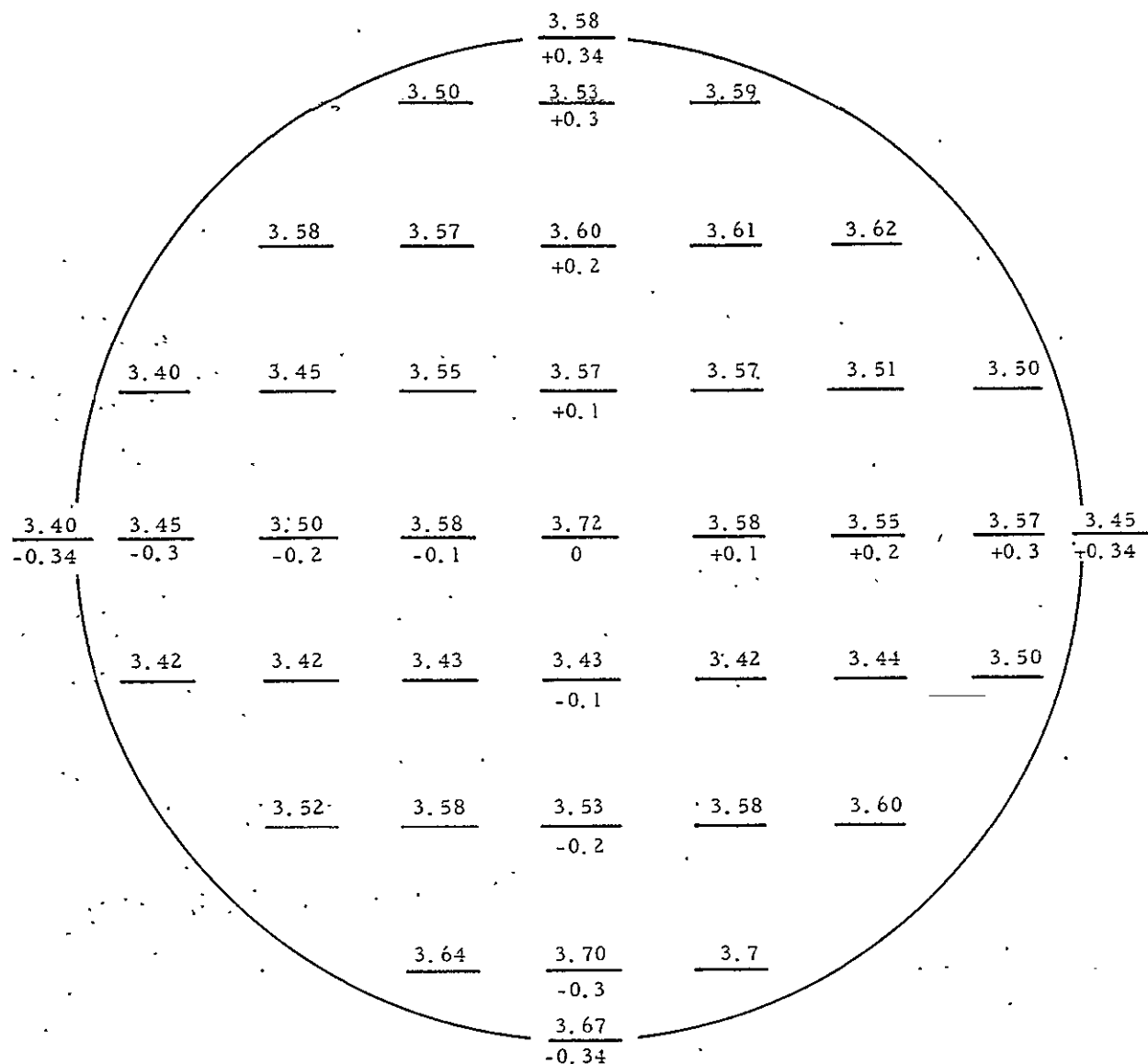


Figure 3-53, Field Uniformity - Breadboard Visible
Source - Revised Design

Spectral Radiance Distribution Matching. - The VISSR calibration accuracy will be enhanced if the VISSR calibrator spectral distribution matches solar spectral distribution. Schott glass filters FG6 (4 mm) and BG34 (1.0 mm) modified the quartz iodine lamp and collimator spectral characteristics. Table 3-23 lists measured transmittance for Schott glass.

Table 3-23. Schott Glass Transmittance

λ (μm)	FG6 (4.0 mm)	BG34 (1.0 mm)
0.50	0.70	0.59
0.55	0.60	0.49
0.60	0.51	0.40
0.65	0.44	0.31
0.70	0.48	0.32
0.75	0.45	0.29

Figure 3-54 compares earth spectral radiance with relative calibrator spectral distribution and a quartz iodine lamp (GE/FDT) operated at 60 watts giving a filament temperature of 2850°K.

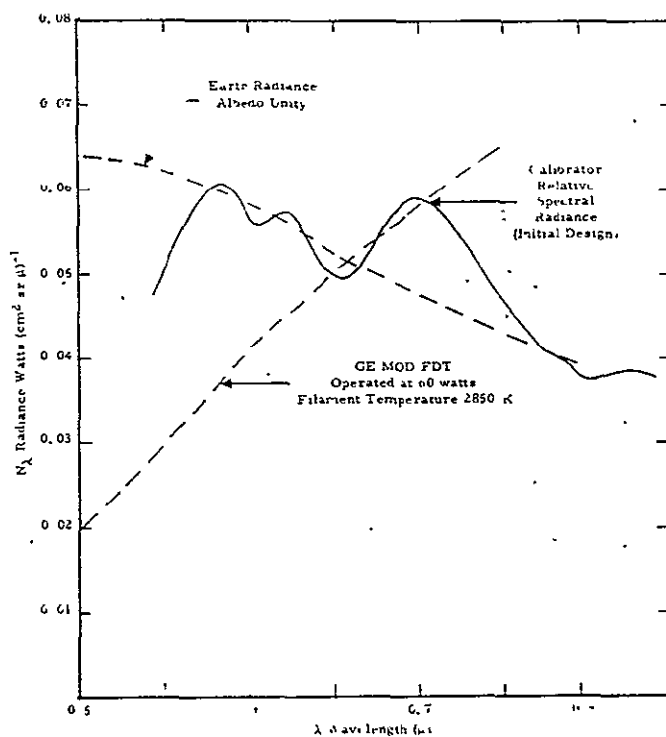


Figure 3-54. Spectral Radiance Distribution Matching

Lamp Parameters

The lamp filament temperature versus current was measured for three quartz-iodine lamps, Sylvania Model FAV. An optical pyrometer was used for the color temperature measurements. The current was regulated using an EG&G Model 590 ac power supply. The pyrometer readings were converted to true temperature using:

$$T_{\text{true}} = \frac{T_{\text{pyrometer}}}{1 + T_{\text{pyrometer}} \frac{\lambda}{C_2} \ln(\epsilon_w T_{\text{envelope}})}$$

Table 3-24 is a tabulation of the results.

Table 3-24. FAV Quartz Iodine Lamp Filament Temperature vs Current

Current (amps)	Filament Temperature (°K)		
	Lamp No. A	Lamp No. H	Lamp No. I
5.0	2280	2288	2284
5.2	2313	2343	2346
5.4	2385	2420	2398
5.6	2466	2489	2480
5.8	2530	2534	2529
6.0	2592	2597	2588
6.2	2648	2658	2637
6.4	2702	2699	2712
6.6	2780	2762	2759
6.8	2832	2852	2850
7.0	2900	2882	2892
7.2	2964	2944	2932
7.4	2998	2992	3005
7.6	3060	3050	3040

The strip filament lamp used as a secondary standard of radiance was measured at two current levels to develop a relationship between current regulation and radiance level. Figure 3-55 illustrates the results, where N is the spectral radiance, I is the lamp current, and E is the exponent derived from the measurements.

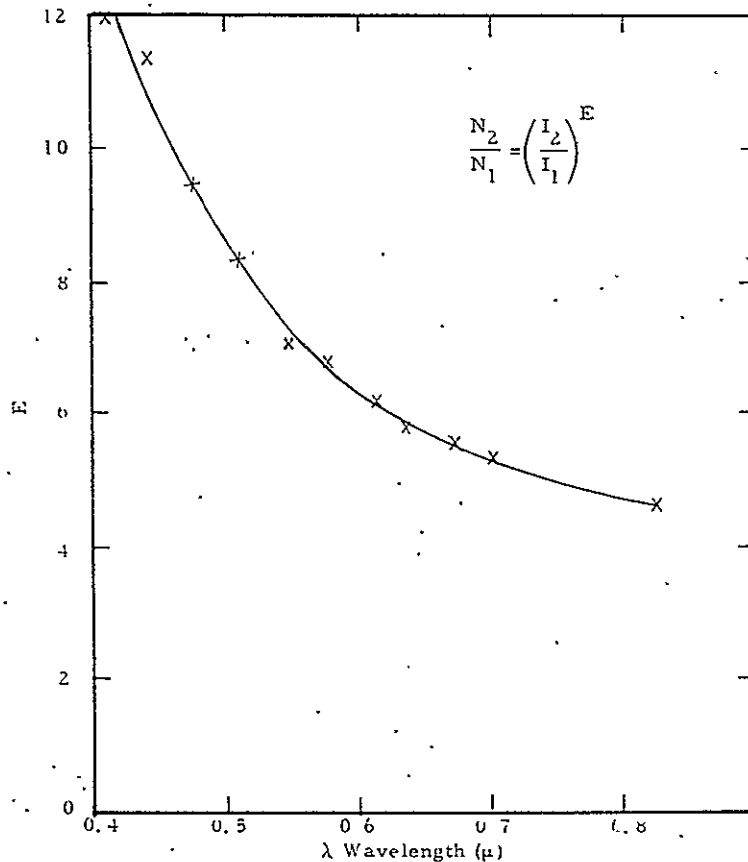


Figure 3-55. Spectral Radiance vs Current,
Strip Filament - Secondary
Standard of Radiance

Calibration

Visible Source. - The VISSR calibrator's visible source calibration shall include the following:

1. Measurement of aperture uniformity
2. Measurement of field uniformity
3. Adjust radiance level to approximate a maximum of unity albedo
4. Calibration of calibrator radiance levels for all positions of filter wheel
5. Confirm quartz iodine lamp assembly replaceability

The calibrator aperture uniformity will be measured by sampling the output beam. Areas (1 through 12) to be measured are illustrated in Figure 3-56. The field uniformity will be measured by scanning a point detector

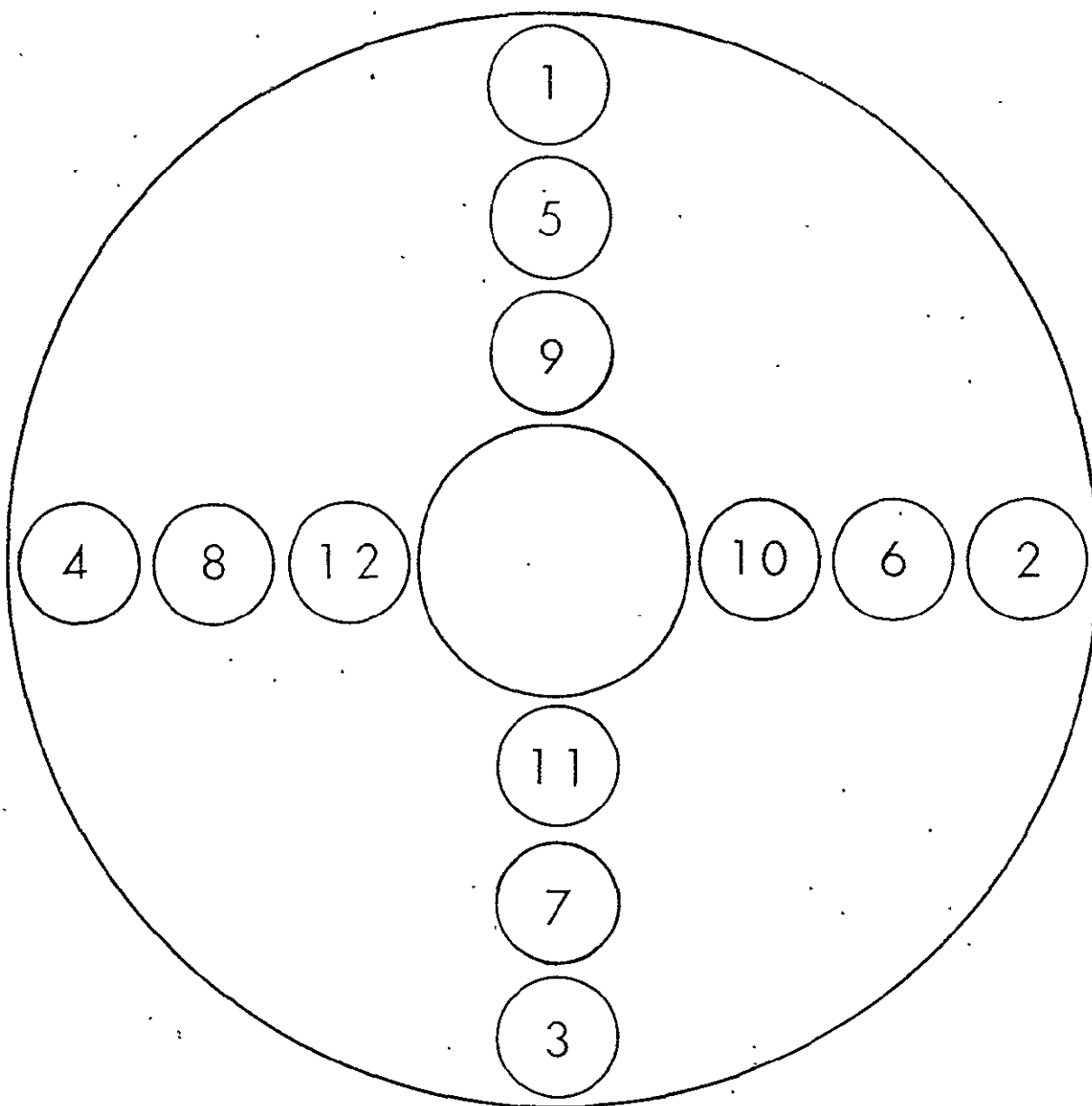


Figure 3-56. VISSR Calibrator Exit Pupil -
Uniformity Sampling

across the field. Point detector is defined as having an IFCV of approximately 25 μ r. A total field of 4 mr will be sampled at intervals of 0.25 mr.

The spectral radiance calibration of the calibrator shall be determined by comparison with a strip filament secondary standard of radiance. The calibration block diagram is given in Figure 3-57.

The SBRC collimator enables complete sampling of the VISSR calibrator exit pupil. The fused silica lens L_1 collimates radiation coming through the SBRC collimator. Lens L_2 collimates radiation from a secondary reference standard lamp. Neutral density filter (NDF_c) reduces the secondary standard radiance, N_{SS} , such that $N_{SS} \approx N_{VC}$. The reflecting chopper enables the SiPD detector to see the VISSR calibrator and secondary standard twice per chopper wheel revolution. Lens L_3 images the standard lamp filament and VISSR calibrator focal plane onto the entrance slit of the Perkin-Elmer Model 16U filter grating spectrophotometer. The aperture mask, SBRC collimator, and VISSR calibrator are aligned so that the VISSR calibrator exit pupil is imaged on the aperture mask symmetrically. The aperture mask must be the only aperture limiting stop.

The spectrophotometer slit width will be 2 mm (0.080 inch) and the slit length will be masked to 0.216 inch (nominal). Thus, the spectrophotometer will sample an instantaneous field of 0.8 mr by 2 mr. The spectral slit width for this condition is 0.0044 micron. Lens, L_4 , will image the exit slit onto the SiPD.

SiPD detector signals for the following conditions will be used.

- S_{VC-SS} - SiPD alternately sees VISSR calibrator visible source (VC) and radiance standard (SS).
- S_{VC_0-SS} - SiPD alternately sees VISSR visible reference (VC_0) and SS. Calibrator five-position mirror is actuated.
- S_{VC} - SS arm is blocked off. Block between chopper and lens L_2 .
- S_{SS} - VC arm is blocked off. Block between chopper and lens L_1 .
- S_0 - Block at PE 16U entrance slits.

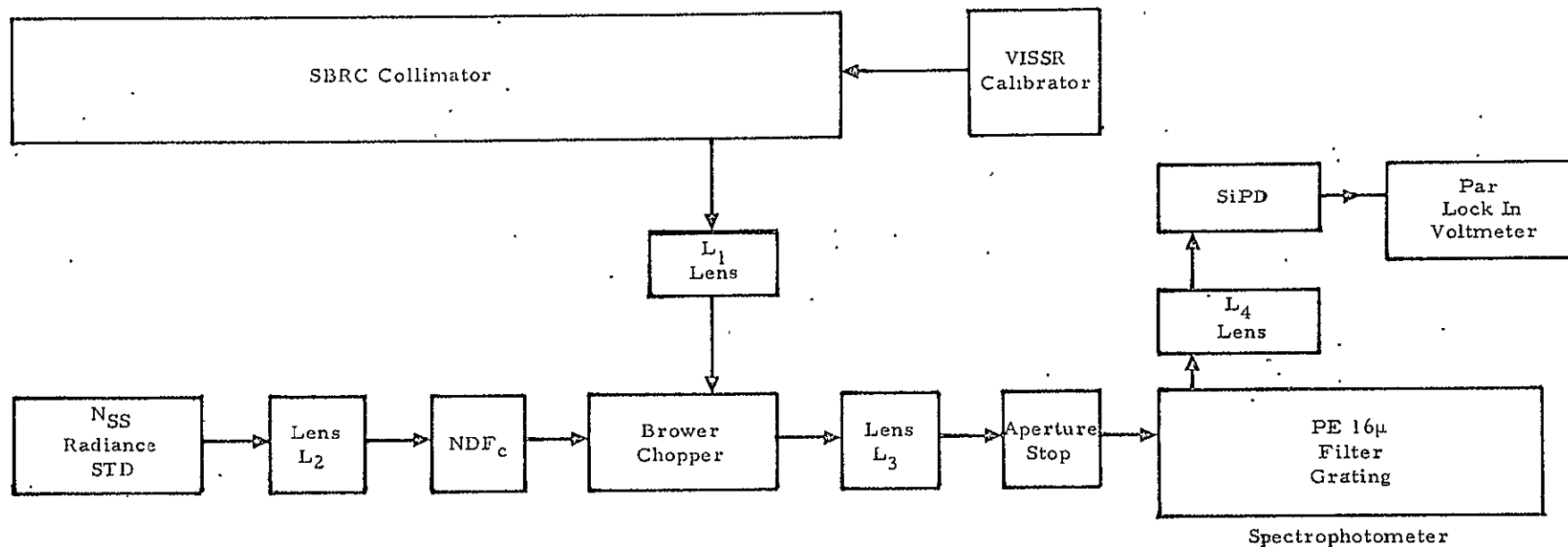


Figure 3-57. Calibration Block Diagram

Note: S_{VC_0-SS} and S_{SS} should be the same for all wavelengths.

If this is the case, only one sample needs to be taken.

S_0 should be zero for all wavelengths. If this is shown to be the case, only occasional checks are required.

With blocks between chopper L_1 and chopper L_2 , the signal must be equivalent to S_0 .

Record SiPD signals for the spectral range of $0.5 \leq \lambda \leq 1.0 \mu$ in steps of $\Delta\lambda = 0.02 \mu$. Recorded signals shall include:

$$S_{VC-SS}, S_{VC}, S_0, S_{SS}$$

Data will be examined for internal consistency in the following manner.

$$(S_{VC-SS}) - (S_0) - (S_{VC} - S_{SS}) = \Delta$$

where Δ should have the relationship $\Delta \leq 0.03 S_{VC-SS}$. This is a calibration design goal.

The spectral radiance of the VISSR calibrator is calculated using the following equations:

$$N_{VC}(\lambda) = \frac{K(\lambda) S_{VC-SS} - N_{SS}(\lambda) \tau_{L_2}(\lambda) \tau_{NDF}(\lambda)}{\rho_{COLL}(\lambda) \tau_{L_1}(\lambda) \rho_{CH}(\lambda)}$$

where
$$K(\lambda) = \frac{N_{SS}(\lambda) \tau_{L_2}(\lambda) \tau_{NDF}(\lambda)}{S_{SS} - S_0}$$

The VISSR calibrator effective albedo level is calculated using

$$\alpha_{EFF} = \frac{\int_{\lambda} N_{VC}(\lambda) R_{VISSR}(\lambda) d\lambda}{\int_{\lambda} N_{earth}(\lambda) R_{VISSR}(\lambda) d\lambda}$$

where α_{EFF} = effective albedo level

$R_{VISSR}(\lambda)$ = VISSR relative spectral response

$N_{earth}(\lambda)$ = earth radiance, a perfect diffuse scatterer is assumed.

The required transmittance for the trim NDF element for a given lamp assembly (A)/VISSR model is calculated by

$$T_{\text{NDFA}} = \frac{1}{\left[\frac{8}{\sum_{i=1}^8 (\alpha_{\text{EFF}})_i} \right] / 8}$$

The various VISSR visible channels are represented by i values.

The detailed calibration procedure for the VISSR calibrator visible source calibration is covered by SBRC Specification No. 19474.

Polarization Effects. - Polarization is a potential source of radiometric calibration uncertainty. There are three principal sources of polarization:

1. Scene
2. Calibrator
3. Instrumental polarization

The scene polarization is unknown. However, since VISSR may view the earth (near the edges at least) at highly oblique angles, the anticipated polarization is not expected to be negligible.

The calibrator uses a quartz iodine lamp. Measurements made at SBRC on several lamps indicate polarization levels of 5 to 14%. In addition, the calibrator will have folding mirrors operating at 45° incidence angle which will increase the calibrator's polarization.

The VISSR scan mirror ($\approx 45^\circ$) will introduce additional polarization. The fiber optic will serve as a depolarizing element; this is probably very fortunate since the photomultiplier tube being used with an enhancement prism will be a major polarization sensitive element.

Equations are given such that radiometric accuracy can be calculated for various scene, calibrator, and VISSR polarization models.

Degree of polarization (P) is defined by

$$P = \frac{N_{\perp} - N_{\parallel}}{N_{\perp} + N_{\parallel}} \quad (3-43)$$

This expression is useful both for scene and calibrator radiance (N). The calibrator radiance can be further broken down to lamp radiance modified by various calibrator elements.

A method is required to handle the VISSR fiber optics depolarization effects. It is assumed that the depolarizer function is such that

$$P_f = DP_i \quad (3-44)$$

where D = a constant, $0 \leq D \leq 1.0$ and subscripts "f" and "i" mean final and initial.

$$P_i = \frac{N_{\perp i} - N_{\parallel i}}{N_{\perp i} + N_{\parallel i}} \quad (3-45)$$

The fiber is assumed to be a lossless element relative to polarization effects. Thus

$$N_{\perp f} + N_{\parallel f} = N_{\perp i} + N_{\parallel i} \quad (3-46)$$

Furthermore,

$$N_{\perp f} - N_{\parallel f} = D(N_{\perp i} - N_{\parallel i}) \quad (3-47)$$

From equations (3-46) and (3-47) we obtain

$$N_{\perp f} = \frac{1}{2} [(1+D)N_{\perp i} + (1-D)N_{\parallel i}] \quad (3-48)$$

and

$$N_{\parallel f} = \frac{1}{2} [(1-D)N_{\perp i} + (1+D)N_{\parallel i}] \quad (3-49)$$

Equations (3-48) and (3-49) describe the effects of the depolarizer element (fiber) where $N_{\perp i}$ and $N_{\parallel i}$ are radiance levels going into fiber and subscript "f" designates values at exit end of fiber.

The expression for VISSR signal level (S) can be written as

$$S = \tau_o \Omega A \left[\frac{1}{2} K_{\perp} \{ (1+D)N_{\perp} \rho_{\perp v} + (1-D)N_{\parallel} \rho_{\parallel v} \} + \frac{1}{2} K_{\parallel} \{ (1-D)N_{\perp} \rho_{\perp v} + (1+D)N_{\parallel} \rho_{\parallel v} \} \right] \quad (3-50)$$

where S = VISSR signal
 τ_o = VISSR optical system transmission
 Ω = VISSR FOV, sr
A = VISSR entrance aperture, cm²
 K_{\perp} = PMT and electronics sensitivity to \perp component, volts/watt
 K_{\parallel} = PMT and electronics sensitivity to \parallel component, volts/watt
D = Depolarizing fiber element constant
 N_{\perp}, N_{\parallel} = Radiance levels, watts (cm² sr)⁻¹
 $\rho_{\perp}, \rho_{\parallel}$ = Scan mirror reflectivity

Equation (3-50) can be used to numerically determine the polarization effect on radiometric accuracy in the following manner:

$$\frac{S_1}{S_2} = \frac{[K_{\perp}\{(1+D)N_{\perp}\rho_{\perp V} + (1-D)N_{\parallel}\rho_{\parallel V}\} + K_{\parallel}\{(1-D)N_{\perp}\rho_{\perp V} + (1+D)N_{\parallel}\rho_{\parallel V}\}]_1}{[K_{\perp}\{(1+D)N_{\perp}\rho_{\perp V} + (1-D)N_{\parallel}\rho_{\parallel V}\} + K_{\parallel}\{(1-D)N_{\perp}\rho_{\perp V} + (1+D)N_{\parallel}\rho_{\parallel V}\}]_2} \quad (3-51)$$

The base line condition will assume the following parameters:

1. Nonpolarized incident radiation, $N_{\perp} = N_{\parallel}$
2. Fiber depolarizer, $D = 0.02, 0.06, 0.10$
3. VISSR scan mirror, $\rho_{\perp V} = 0.99$
 $\rho_{\parallel V} = 0.93$
4. PMT sensitivity, $K_{\perp} = 2.5$
 $K_{\parallel} = 1.7$

Note: PMT sensitivity is patterned after published data from Applied Optics.

Holding items 2, 3, 4 constant, the base line conditions should be compared with the following conditions for item 1.

- a. $P = 1.0$
- b. $P = 0.4$
- c. $P = 0.1$
- d. $P = 0.05$

For all cases

$$\left(\frac{N_{\perp} + N_{\parallel}}{2}\right)_{\text{baseline}} = \left(\frac{N_{\perp} + N_{\parallel}}{2}\right)_{a, b, c, d}$$

The results of these comparisons are graphically illustrated in Figures 3-58, 3-59, and 3-60. Values for the fiber optics depolarization, D , used to calculate data for plotting of the figures are 0.02, 0.06, and 0.10, respectively.

It is to be noted that the ratio of S_1/S_2 is not a strong function of D . The proper interpretation of this is that the interaction of the incident partially polarized radiation and the 45° scan mirror are the principal causes of the ratio S_1/S_2 to deviate from unity.

Thermal Blackbodies. - No radiometric calibration is made on the thermal blackbodies. The source cavity is designed such that the emissivity is greater than 0.99 based upon theoretical arguments. Thus the blackbody radiance is calculated assuming an emittance of 1.00 using the measured cavity temperature.

The VISSR calibrator mirrors will modify the calibrator IR radiance levels by their reflectances. There are four such mirrors.

A means of monitoring the combined mirror reflectance as a function of time has been considered. NASA/GSFC has indicated this is not to be implemented at this time.

It should be noted that the initial spectral reflectance measurements of VISSR calibrator mirrors have an uncertainty of 1/2 to 1% per mirror.

Alignment

Alignment Functions. - The VISSR calibrator has several alignment functions. These are:

1. Folding mirror - electronic autocollimation
2. Vernier pattern on visible MTF wheel
3. Alignment microscope
4. Accessory alignment telescope/prism assembly

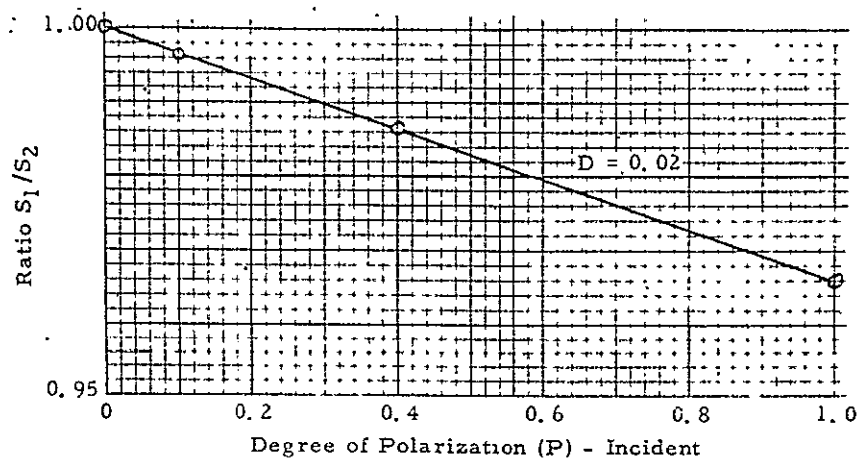


Figure 3-58. Radiometric Calibration Accuracy versus Degree of Polarization for Incident Light

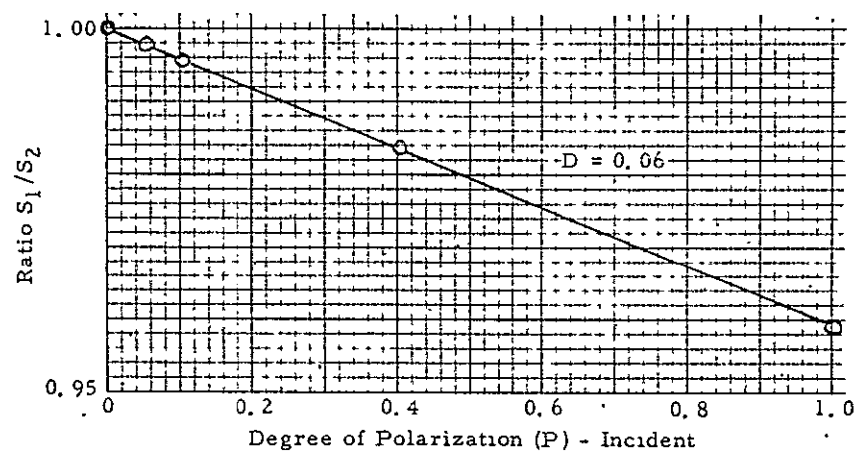


Figure 3-59. Radiometric Calibration Accuracy versus Degree of Polarization for Incident Light

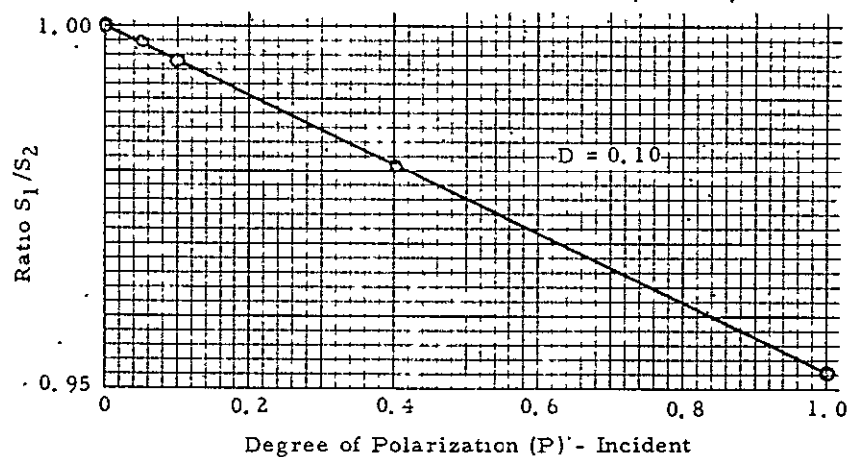


Figure 3-60. Radiometric Calibration Accuracy versus Degree of Polarization for Incident Light

Detailed Discussion. - The VISSR system testing required that the scan mirror drive system be tested in thermal vacuum environments. Items 1 and 2 are used to accomplish the measurements.

The large folding mirror can be set at any of three angles remotely. The angles are 41° , 45° , and 49° . This is accomplished by mounting a three-faceted mirror monitor onto the folding mirror. Adjacent facets have an included angle of 176° . The angles are known with an accuracy of better than 1 arc sec. An electronic autocollimator is aligned with respect to the mirror monitor center facet such that a null signal is obtained when the folding mirror is at 45° . Null signals from the autocollimator are obtained when the folding mirror is rotated by $\pm 4^\circ$. Thus, for any given temperature, the folding mirror can be rotated to three positions for which the relative angular relationship is known with precision.

Each time the VISSR calibrator is used to test the VISSR system, the two systems must be optically aligned. There is an alignment microscope on the VISSR calibrator instrument plate that is aligned to the VISSR calibrator optical axis and is focused on the calibrator focal plane.

The VISSR and VISSR calibrator optical axes can be aligned parallel to each other by aligning the VISSR illuminated fibers symmetrically to the alignment microscope cross hairs. The VISSR optical system axis is defined by the center of the fiber optics array.

The accessory alignment telescope/prism assembly provides the means to assure superposition of the optical axes via measuring lateral (perpendicular to optical axis) alignment. The accessory assembly consists of a prism and alignment telescope with supporting structure. The assembly is aligned to the VISSR calibrator so that the alignment telescope line of sight is coincident with the VISSR calibrator optical/mechanical axis as it is projected away from the calibrator folding mirror toward the VISSR. The VISSR has an alignment target on the secondary mirror which is located on the projected VISSR optical/mechanical axis.

The VISSR and VISSR calibrator are aligned when the VISSR projected illuminated fibers are aligned to the alignment microscope and the alignment telescope line of sight pierces the VISSR secondary mirror alignment target simultaneously.

Optical Effects Related to VISSR to VISSR-Calibrator Alignment. - There are several effects associated with misalignment of the VISSR/SMS to VISSR/SMS calibrator.

The separation between the VISSR/SMS and VISSR/SMS calibration instruments will affect the VISSR/SMS radiometric calibration accuracy and the measurement of scan drive step accuracy. Both effects are related to illumination vignetting of the VISSR optical systems.

Visualize a configuration where VISSR and VISSR calibration optical axes are "nominally" parallel with angular and lateral misalignments resulting in the VISSR calibrator clear aperture and/or field not filling the VISSR entrance aperture and/or field. The vignetted VISSR aperture or field will result in a pseudo-decrease in VISSR sensitivity.

Figure 3-61 illustrates the vignetting for a pure lateral misalignment (perpendicular to instrument line of sight). The distance from the VISSR/SMS calibrator centerline to VISSR/SMS centerline is assumed to be 90 inches.

Figure 3-62 illustrates the vignetting for angular misalignment. The vignetting discontinuity at 2 mr for the visible channel is due to the calibrator visible source angular diameter of 4 mr.

It is assumed that the radiometric calibration will be limited to the case where the VISSR scan mirror and VISSR calibrator folding mirror are at 45° with respect to the optical axes.

The vignetting present in the scan drive step measurements is much larger since the VISSR scan mirror and VISSR calibrator folding mirror are rotated from the 45° angular position. However, it is assumed that scan drive step measurement accuracy is not a function of aperture vignetting

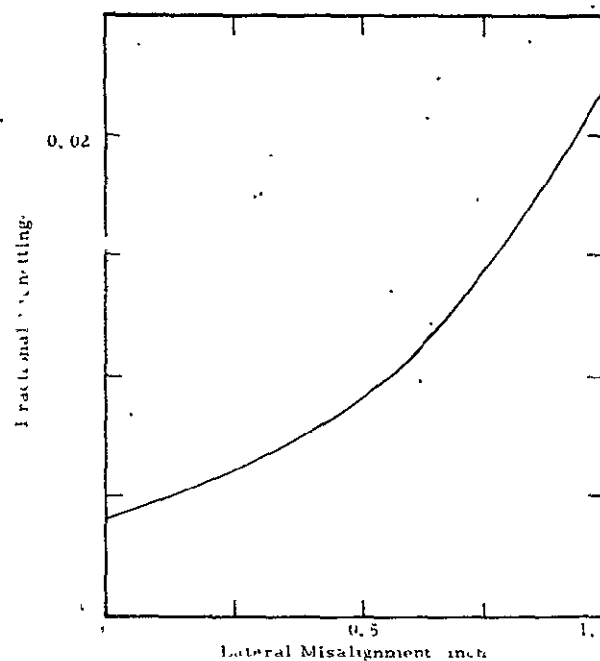


Figure 3-61. VISSR Fractional Vignetting vs Lateral Misalignment

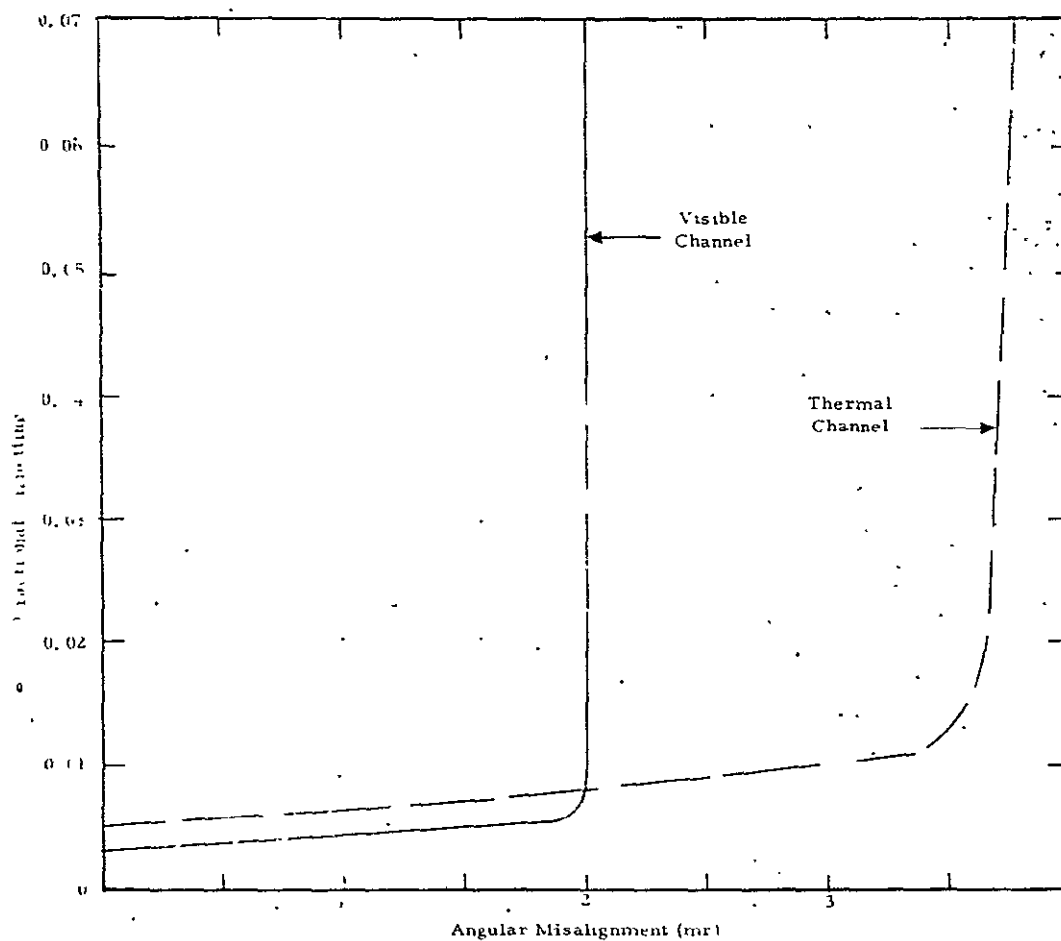


Figure 3-62. VISSR Fractional Vignetting vs Angular Misalignment

providing sufficient illumination is present to give an adequate signal-to-noise ratio. The vignetted case signal-to-noise ratio, SNR_{VIG} , can be approximated by

$$SNR_{VIG} = SNR_0 \sqrt{F}$$

where SNR_0 = signal to noise with VISSR entrance aperture filled;
 $SNR_0 \approx 35$

F = fraction of VISSR aperture being illuminated

Figure 3-63 illustrates the fractional VISSR illuminated aperture as a function of separation between the center lines of VISSR and VISSR calibrator. The curve assumes scan mirror angles of 41° and 49° .

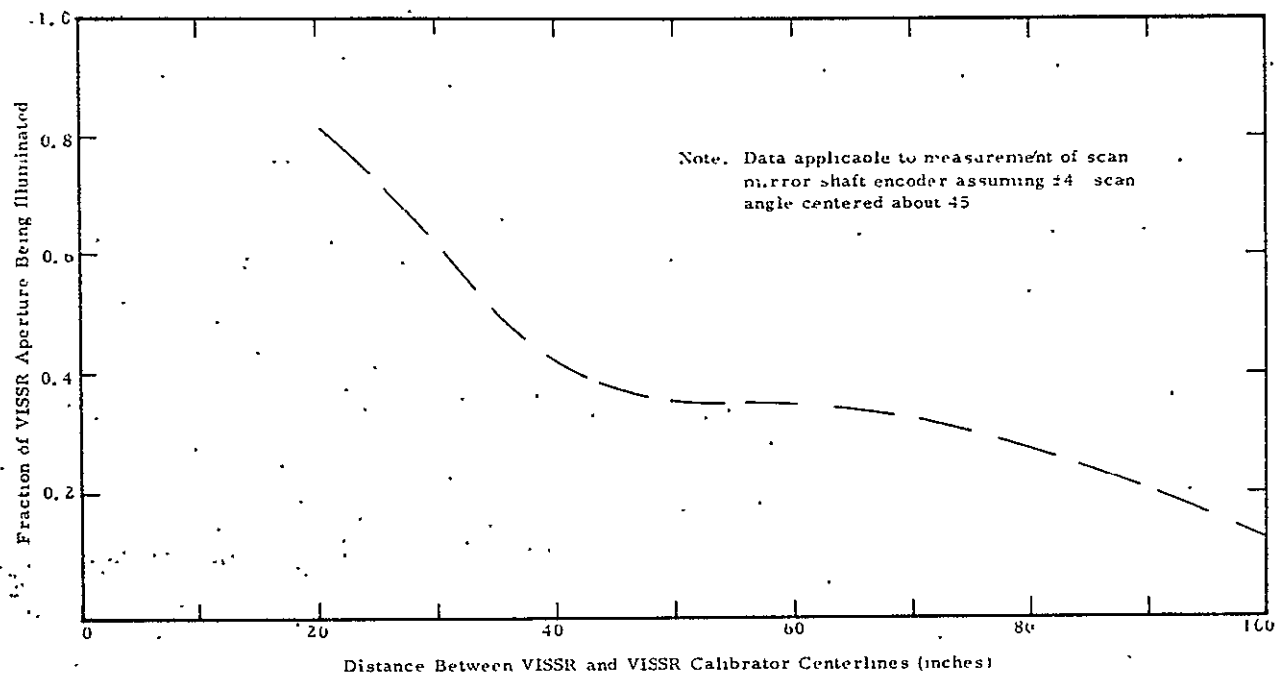


Figure 3-63. Fraction of VISSR Aperture Being Illuminated as a Function of Distance between Center Lines of VISSR and VISSR Calibrator

Calibrator No. 1 Uniformity Measurements

Major difficulties have been encountered with respect to VISSR calibrator uniformity. During the January 1972 radiometric calibration, measurements were made of VISSR calibrator No. 1 field and aperture uniformity. Field uniformity is that measured at the calibration focal plane. Aperture uniformity is that measured in the collimated beam. The measurements were made using a small optical system consisting of a 2-inch diameter fused silica lens with a pinhole at its focal plane. An SiPD detector was positioned behind the pinhole. The calibrator's aperture was sampled with 1.0-inch diameter apertures. The field uniformity was sampled with a pinhole of 0.004 inch. The measured results were:

- a. Field Uniformity $\pm 10\%$
- b. Aperture Uniformity 25%

Subsequent to these measurements, VISSR calibrator No. 1 was taken to El Segundo in preparation for VISSR thermal vacuum testing. Prior to VISSR testing, it was necessary to replace field lens 1A, P/N 25331, and the quartz iodine FDT lamp. Due to schedule commitments, no measurements were made at this time to ensure optimum alignment.

Limited measurements were made on calibrator No. 1 field uniformity using engineering model VISSR. VISSR scan mirror was used to scan calibrator focal plane. These data are summarized in Table 3-25.

Table 3-25. VISSR Calibrator No. 1 Field Uniformity

Scan Mirror Encoder Readout	VISSR Channel 1* Output (volts)	
	Initial	Repeat
-3	3.44	3.40
-2	3.52	3.50
-1	3.48	3.46
0	3.45	3.44
+1	3.72	3.74
+2	3.81	3.81
+3	3.20	3.20

*NDF wheel position No. 6 was used in the above measurements.

VISSR output changed by a factor of 2 at encoder line +6. These data were verified in a dummy bench test at SBRC on 22 May 1972.

Detailed VISSR calibrator No. 1 field and aperture uniformity were made 12 June 1972. The calibrator was aligned to the SBRC collimator. A 0.0025-inch diameter fiber was located in the SBRC collimator focal plane. The energy transmitted by the fiber was collected by an SiPD detector. Thus the calibrator field was sampled with a 23- μ m probe. The aperture was sampled with 2-inch diameter masks located between the calibrator and collimator. The same fiber - SiPD was used as the detecting system.

The aperture sampled areas are illustrated in Figure 3-64. SiPD output voltages associated with each sampled area are listed in Figure 3-64 also.

The field uniformity was measured in 0.050-inch increments at the SBRC collimator focal plane. This corresponds to angular increments of 0.46 mr. The results are tabulated in Table 3-26.

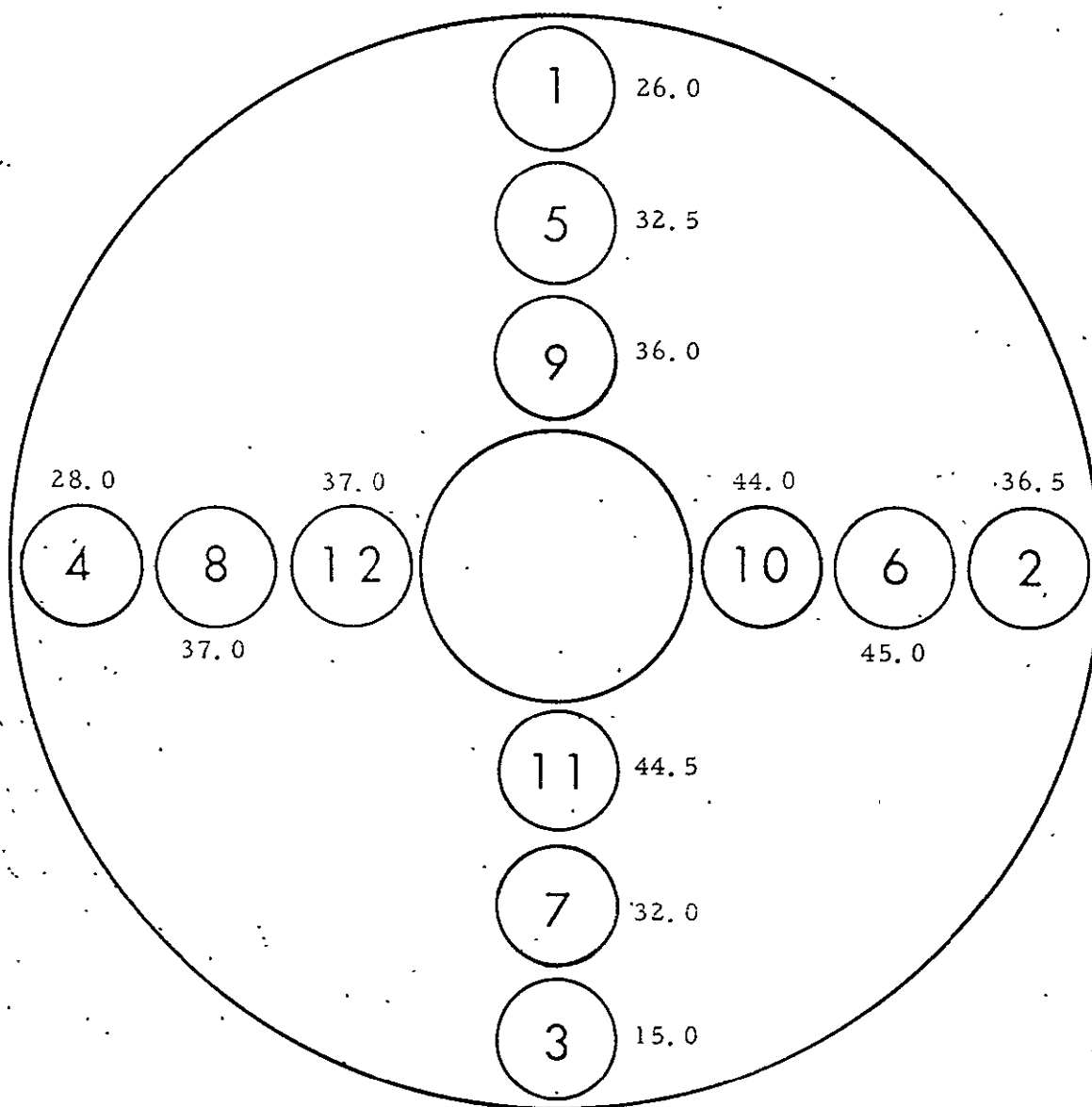
Table 3-26. VISSR Calibrator No. 1 Field Uniformity Data (6/12/72)

	0.20	0.30	1.20	1.70	2.10	2.60	2.30	1.95	1.10	0.20
	0.15	1.45	2.00	2.60	2.80	3.60	3.30	2.90	2.30	1.10
	0.10	2.10	2.50	3.20	3.10	2.10	2.66	4.10	2.80	2.00
	0.05	2.65	3.00	3.60	2.60	3.00	2.80	3.00	2.95	2.20
	0	2.90	3.10	3.05	2.70	2.80	3.00	3.15	2.90	2.40
	-0.05	2.65	2.60	2.70	2.60	1.95	2.70	2.75	2.60	2.15
	-0.10	2.50	2.50	2.40	1.90	2.10	2.05	2.30	2.15	1.70
	-0.15	1.65	2.10	2.10	1.90	1.75	1.65	1.65	1.71	1.10
	-0.20	0.17	1.50	1.80	1.70	1.60	1.50	1.35	1.00	0.10
		-0.20		-0.10		0		+0.10		+0.20
Y Axis (inch)										
				X Axis (inch)						

Based upon the above data, aperture uniformity varies by a factor of three. However, if one point is discounted, the uniformity is $\pm 30\%$ and $\pm 25\%$ from the average. The field nonuniformity varied by more than a factor of two.

In addition, calibrator No. 1 visible source does not appear uniform (qualitative) when viewed visually. It appears much less uniform visually and radiometrically now than before it was taken to El Segundo (initially). The differences may be associated with the replacement of the FDT lamp, field lens 1A, and changes in visible source optical alignment.

With the revised visible source to be retrofitted into VISSR calibrator No. 1, the uniformity should be improved greatly.



(SiPD Output is Listed Along Side Each Sampled Area)

Figure 3-64. Sampling - VISSR Calibrator No. 1 Aperture

OPTICAL COMPONENT MEASUREMENTS

Reflectance - Coated Mirrors (Protoflight)

Spectral reflectance for silicon oxide overcoated aluminum mirror surfaces is shown in Figures 3-65 and 3-66 for the visible and IR regions, respectively.

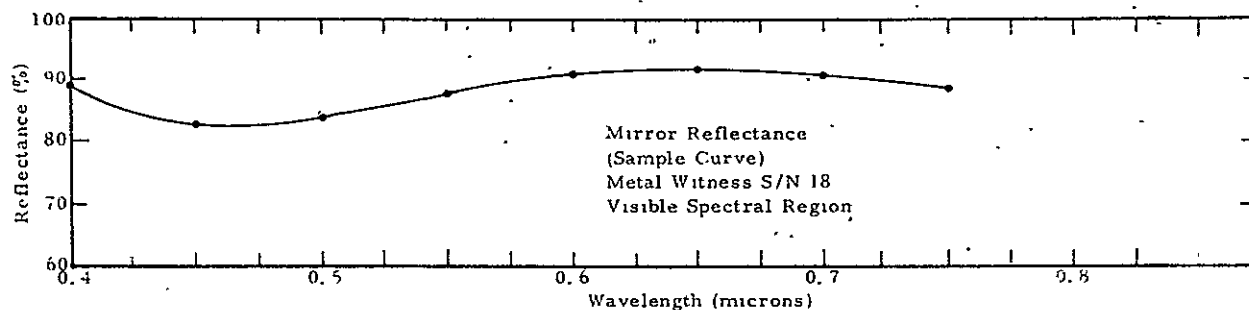


Figure 3-65. Coated Mirror Reflectance, Visible Region

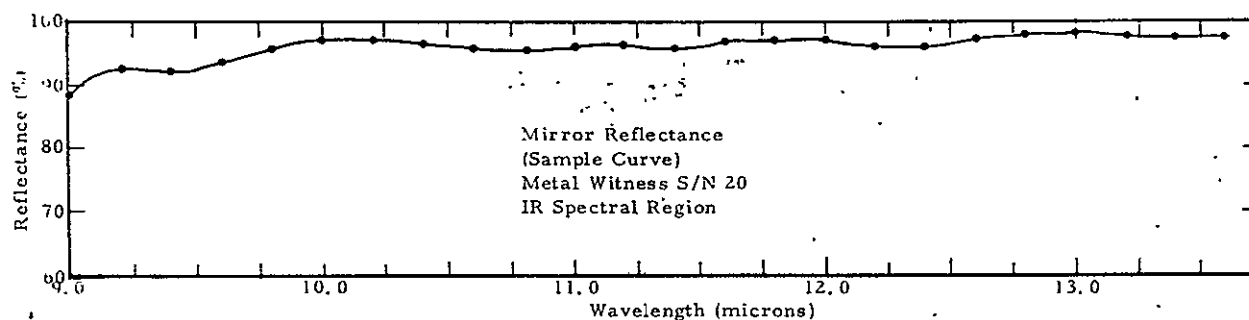


Figure 3-66. Coated Mirror Reflectance, IR Region

Reflectance - Polished Electroless Nickel

The reflectance of one of the VISSR polished electroless nickel test specimens is plotted in Figure 3-67.

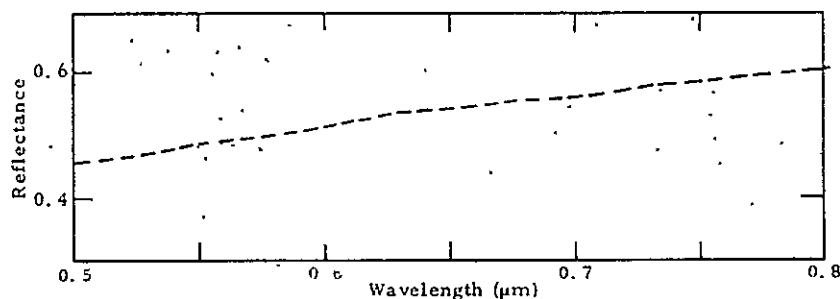


Figure 3-67. Spectral Reflectance of Polished Electroless Nickel

Transmittance and Crosstalk - Fiber Optics

Transmittance (absolute) and crosstalk measurements are made by the vendor (Bendix Mosaic) for each fiber of the fiber optics assembly prior to delivery to SBRC. Both measurements are made with the same test setup. The beam from a He/Ne laser source (0.6328 micron) is focused down to a 0.000175-inch spot (radius) and directed into an integrating sphere where the total amount of light is collected and measured by an El Dorado Model 20F photometer. The input beam is then directed onto the common end of the initial fiber in the array. The integrating sphere is placed just below the surface of the filter block located at the other end of the fiber and a measurement is made. The transmittance measurement for the fiber is the ratio of the photometer reading obtained through the illuminated fiber to that for the direct laser input to the photometer. Data for crosstalk is obtained by positioning the integrating sphere under each of the remaining seven unilluminated fiber filter blocks and recording the photometer reading in each of the seven cases. Crosstalk value for the illuminated fiber is the sum of the photometer readings for the seven unilluminated fibers normalized to the input beam. Transmittance and crosstalk measurements are made for each of the eight fibers. Table 3-27 indicates the values obtained on fiber optics assembly, serial No. 102. Transmittance values are given for hemispherical pickup (collecting sphere placed just below the surface of the filter block; i.e., $f/0.5$ solid angle) and for a slightly decollimated beam (collecting sphere withdrawn a distance of 0.746 inch from the output fibers; i.e., $f/3$ solid angle).

Relative Spectral Transmittance - Fiber Optics

Relative spectral transmittance measurements are made on each fiber optics assembly when received at SBRC. Relative spectral transmittance for a representative fiber optics assembly is illustrated in Figure 3-68. Measurements are over the visible wavelength region.

Table 3-27. Fiber Optics Assembly Transmittance and Crosstalk

		Light Output from Fiber No.									
		0	1	2	3	4	5	6	7	8	9
Incident Light On	No. 1		X	0.25	0.05	0.02	0.02	0.02	0.02	0.02	
	No. 2		0.15	X	0.40	0.03	0.03	0.02	0.02	0.03	
	No. 3		0.02	0.20	X	0.30	0.03	0.02	0.02	0.02	
	No. 4		0.02	0.03	0.20	X	0.19	0.03	0.03	0.02	
	No. 5		0.02	0.03	0.02	0.15	X	0.20	0.02	0.02	
	No. 6		0.02	0.02	0.02	0.02	0.23	X	0.21	0.03	
	No. 7		0.03	0.02	0.02	0.02	0.02	0.19	X	0.15	
	No. 8		0.07	0.03	0.02	0.02	0.02	0.03	0.12	X	
		Crosstalk from Other 7 Fibers									
			0.33	0.58	0.73	0.56	0.54	0.51	0.45	0.29	
		Transmittance with Hemispherical Pickup									
		77	80	81	80	79	78	78	87	77	75
		Transmittance with f/3 Pickup									
			78	77	75	72	74	71	85	71	

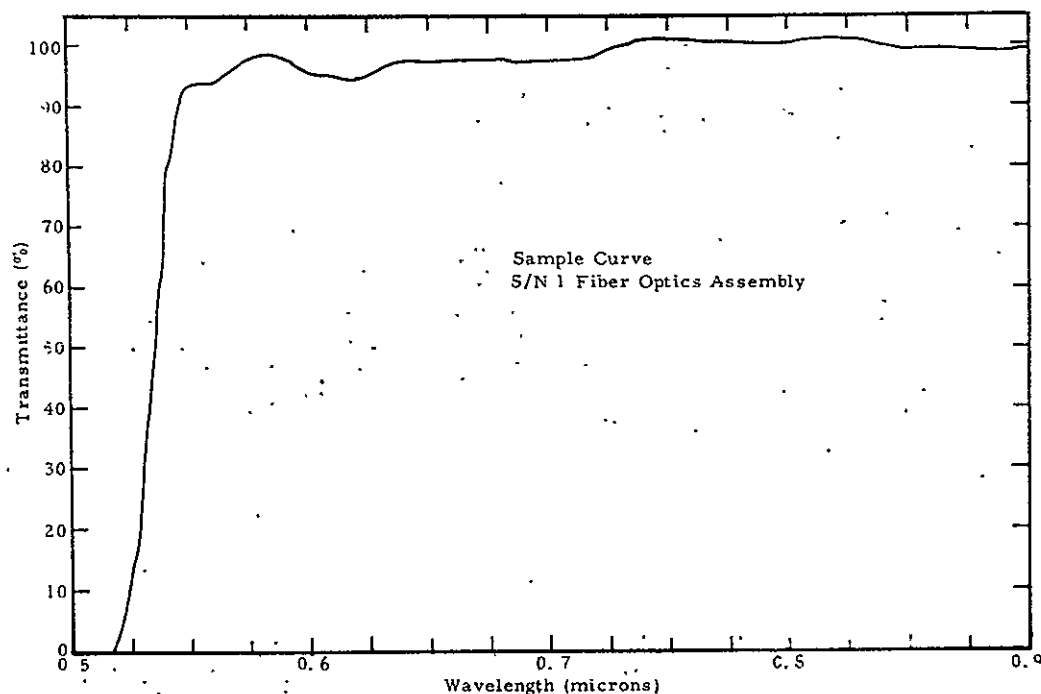


Figure 3-68. Relative Spectral Transmittance - Fiber Optics

Transmittance - IR Channels Optical Elements

Spectral transmittance curves for the optical elements of the IR channels are shown in Figures 3-69 through 3-72. Figures 3-69 and 3-70 illustrate the spectral transmittance for 0° incident light for the IR relay lenses and for the IR bandpass filter, respectively. Figure 3-71 illustrates spectral transmittance at 0° incident light for the Irtran 2 window on the radiation cooler. Additional plots for the Irtran 2 window over an extended IR spectral region are shown in Figure 3-72. In addition to spectral transmittance measurements over the extended IR spectral region, calculated absorption and reflectance measured at 45° incidence are plotted for the extended spectral region.

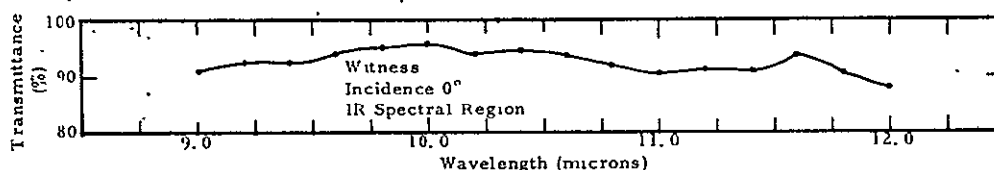


Figure 3-69. Spectral Transmittance - Relay Lens

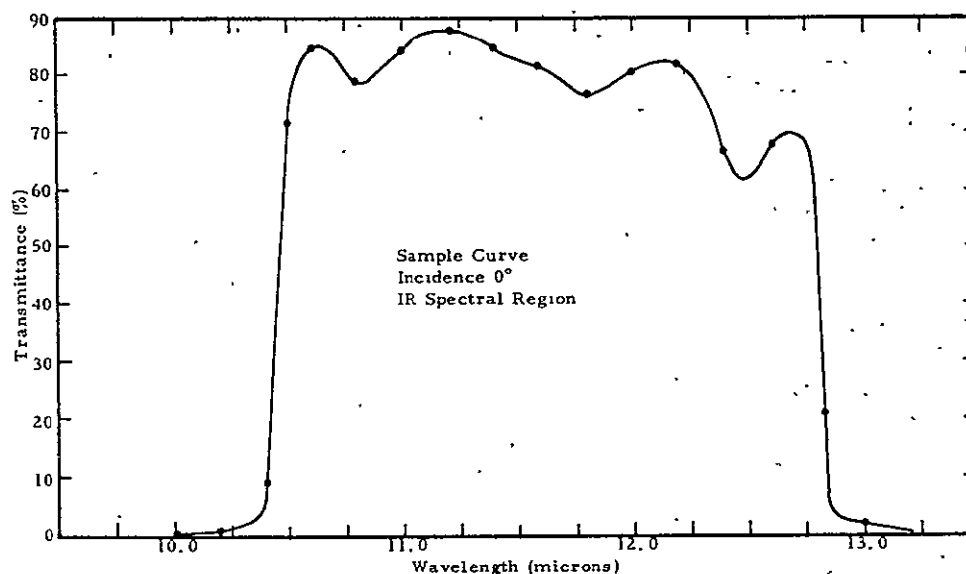


Figure 3-70. Spectral Transmittance - Bandpass Filter

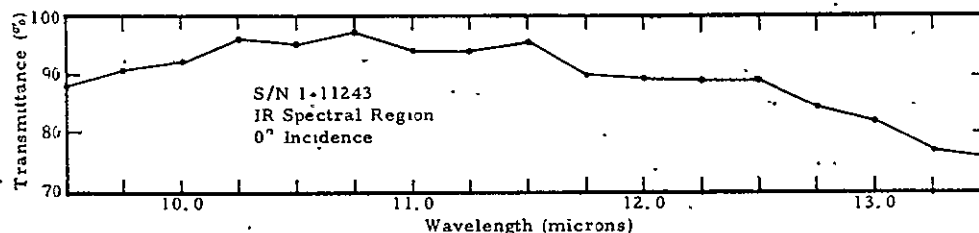


Figure 3-71. Spectral Transmittance - Irtran 2 Window

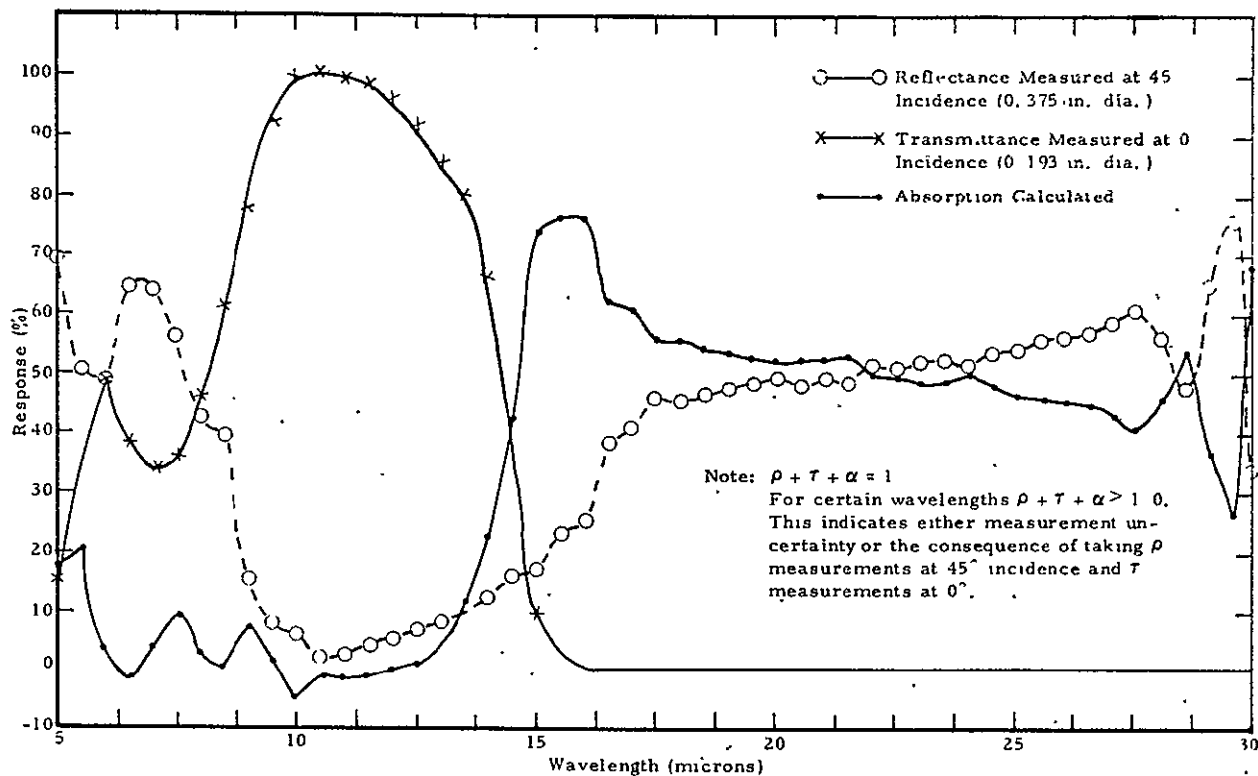


Figure 3-72. Spectral Transmittance - Irtran 2 Window -
Extended IR Spectral Region

INTEGRATED MULTIPLIER PHOTOSENSOR (IMP) MEASUREMENTS

Extensive tests on the IMP units were to be made by the vendor (EMR) prior to delivery. A limited number of optical performance tests were performed at SBRC after receipt of the IMP units to verify results of vendor tests. Tests were made on a representative sample after a 1-hour run-in and comprised: 1) dc photocurrent from a single intensity, known dc source, at one wavelength - 6250Å, 2) noise-in-signal at that light level, and 3) confirm output stability by repeating photocurrent measurement periodically over several months.

Limited Measurements of Specification Performance

Measurements to be Made. -

1. DC Photocurrent. A single measurement of the photocurrent was to be made at a known light level near, but less than 1.94×10^{-9} watt. This measurement was to confirm paragraph 3.1.2.5 of

SBRC Specification 18858 for anode radiant sensitivity. A value of 700 amps/watt at 0.625 micron was required.

2. Noise Level. A single measurement of the noise-in-signal was to be taken, and when combined with the dc photocurrent value, the requirements of paragraph 3.1.2.1 of SBRC Specification 18858 were to be met. A value of $S/N \geq 3.68 \times 10^8 (W/\Delta B)^{1/2}$ is required.
3. Stability. Periodic photocurrent measurements were to be made over a span of several months. Paragraph 3.1.2.3 of SBRC Specification 18858 requires a variation in anode radiant sensitivity of less than $\pm 3\%$ after a 1-hour warmup from any value taken within the previous twelve months.

Test Setup. - An IMP test set was designed and built using a calibrated irradiance lamp to irradiate a white, diffuse reflector painted with barium sulfate reflectance standard paint. The size and distance of this reflector from the IMP was selected so that the light into the IMP was coming from an f/4 cone. Thus, the incident radiation more closely simulated in-use conditions for the IMP than if it came from a more nearly point source. A calibrated interference filter was interposed in the light path, which peaked at 0.6250 micron, and had a bandwidth of approximately 0.0150 micron. (See Figure 3-73.) A calibrated pinhole aperture of 0.040-inch diameter was provided to limit the input aperture of the IMP.

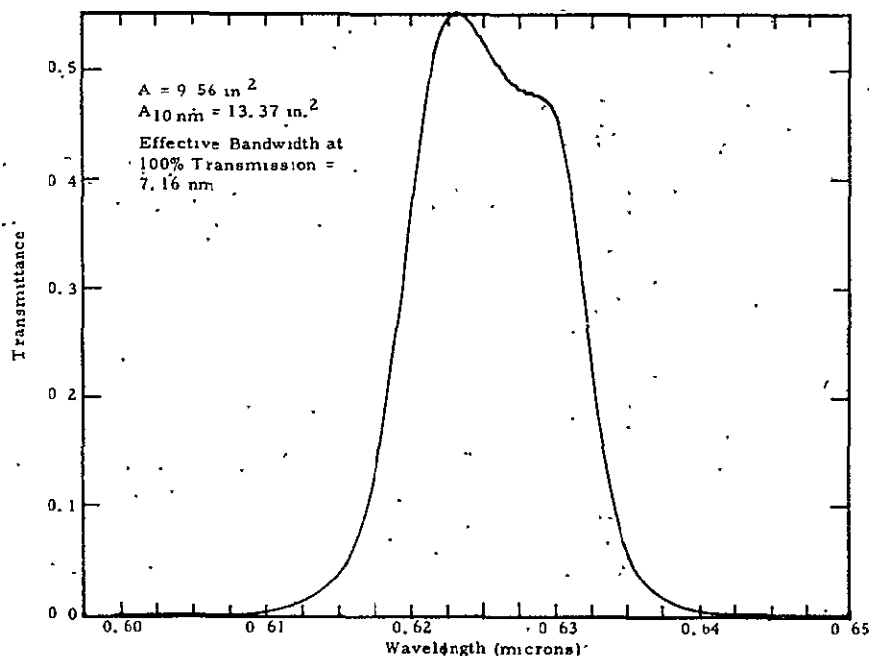


Figure 3-73. Spectral Response of Bandpass Filter in IMP Test Set

Figure 3-74 shows the optical configuration and the measured parameters. The value for $\Delta\lambda_{\text{eff}} = 7.16 \text{ nm}$ was arrived at by two means: 1) by computer integration of the spectral irradiance times the spectral transmission, and 2) by measuring the normalized area under the filter spectral curve with a polar planimeter. The difference in these two cases was less than 1%. The significance of $\Delta\lambda_{\text{eff}}$ is that it is the bandwidth of an equivalent square pass filter of 100% peak transmission which passes the same total power as the one actually used. The value of $\rho = 0.94$ was measured with a 625-nm filter relative to a pressed-powder sample of Ba_2SO_4 at a 30° angle of incidence. The reflectivity of the Ba_2SO_4 pressed-powder reference sample is greater than 99%. The test set target reflector was a 1.750-inch diameter button coated with a Ba_2SO_4 spray paint. Baffles were used to control stray light and to avoid vignetting or shadowing on either leg of the test set. The insides of the IMP test set were painted matte black.

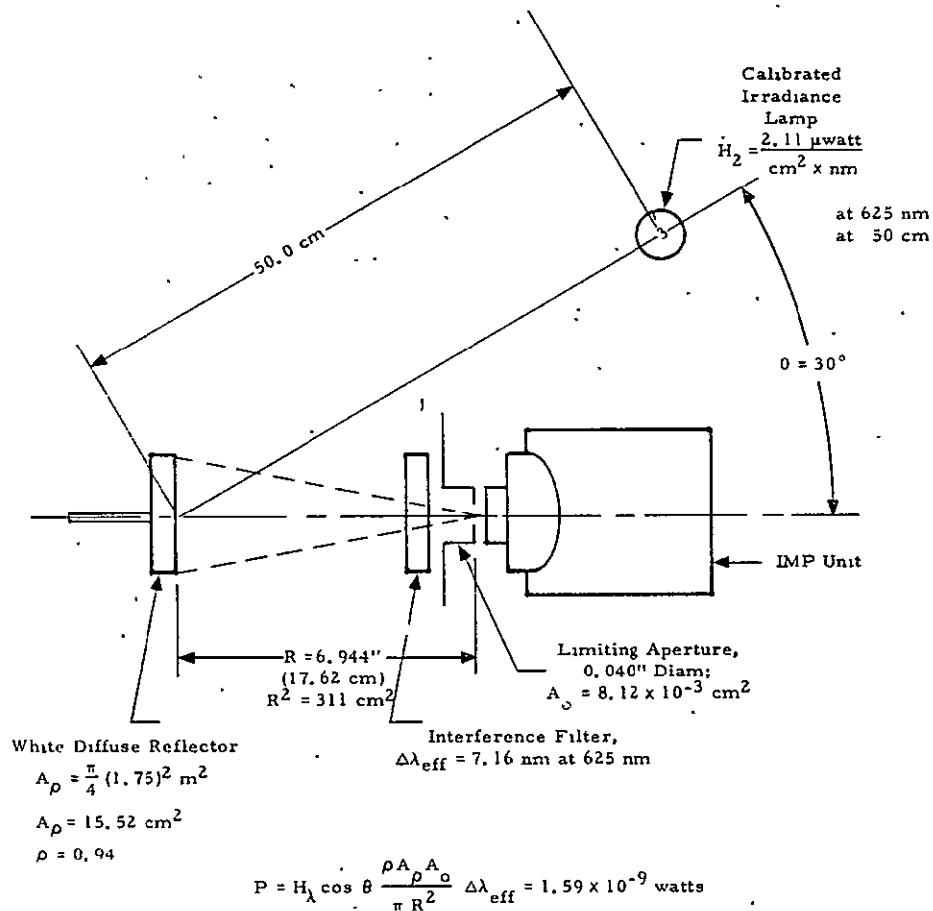


Figure 3-74. Optical Configuration and Calibration of IMP Test Set

The measured values used in the basic equation in Figure 3-74 result in a value for the power arriving at the phototube prism input as $P = 1.59 \times 10^{-9}$ watt. The only other factor required to assure accuracy of this test set is to ascertain that the proper current is flowing in the lamp to produce the calibrated irradiance.

The output of the IMP was close-coupled to a transimpedance preamplifier which was the breadboard preamplifier for flight hardware design. Preamplifier effective input impedance was 2.20×10^5 ohms. Effective bandwidth for noise determinations was 250 kHz ($\pm 10\%$). Preamplifier output characteristics were 1000 ohms and 0.001 μ f to minimize effect of loading by the measuring instruments.

To keep the source in calibration, use of the calibrated lamp was minimized. This was facilitated by the introduction of a secondary, or keeper, lamp internal to the test set. During warmup periods and periods between measurements, the IMP photocurrent was maintained at approximately the same level as during actual measurements.

To assure accurate and reproducible positioning of the IMP input aperture with respect to the test set pinhole aperture, a special mount was made for the IMP unit. Fixed reference surfaces were used on the mount that corresponded to the three primary reference surfaces of the IMP unit as called out on SBRC Drawing 44284. These surfaces were initially adjusted to assure proper mating of the input/output apertures and then locked in place. Spring tension for each axis was used to assure proper and repeatable contact of the reference surface.

The PMT test set was enclosed so stray light would not affect the measurement accuracy. An electrical interlock was provided as a protection backup to remove power to the IMP unit whenever the PMT compartment door was unlatched.

Measurement Results. - Initial measurements showed that a 1-hour warmup was not adequate to achieve reasonable initial stability. The same was true when a keeper lamp was used during the warmup. A 4-hour warmup regime with keeper lamp was started, but still no point of stability was reached. Figure 3-75 shows the output over a period of 3-1/2 days (89 hours) for IMP serial No. 8. During the entire time, the IMP was kept on and exposed to the same light input. Neglecting the first 5 minutes of operation, IMP response dropped 6.2% in the first hour, 3.0% in the next 6 hours, 4.1% in the next 22 hours, and 4.2% in the next 61 hours. In 89 hours, the IMP output response dropped 16.4%, and was continuing to drop further without positive signs of leveling off. A similar case was observed with IMP serial No. 4. Over a period of 1 week (168 hours) IMP serial No. 4 dropped in output response by 22%, and as seen in Figure 3-76, it had not yet reached a minimum value. The apparent rate of decrease in response was still about 1% per day.

The engineering model IMP units (Nos. 1 through 8) were tested for a minimum of 4 hours each in sequence. The measurements on the IMPs were repeated 3 times in 3 different runs, and runs were repeated a fourth time on units No. 4 and No. 8. These measurements occurred over a one-month interval. A summary of these measurements is shown in Figure 3-77. This figure shows that the anode radiant sensitivity among units varies between 411 amps/watt to 538 amps/watt. Thus the IMPs are between 23% and 41% too low. The factor of greater concern, however, is the variation of sensitivity with time, e. g., IMP No. 8 dropped 16.4% and IMP No. 4 dropped 22%. All tubes indicated a drop in sensitivity with time, greater than the 3% maximum called for in the specification, and all showed evidence of continuing decrease.

The ratio of the dc signal to the ac (rms) noise-in-signal is to be equal to or greater than:

$$S/N \geq 3.68 \times 10^8 (W/\Delta B)^{\frac{1}{2}}$$

for $W = 1.4 \times 10^{-9}$ watt

$\Delta B = 2.5 \times 10^5$ Hz

$S/N \geq 29$ required.

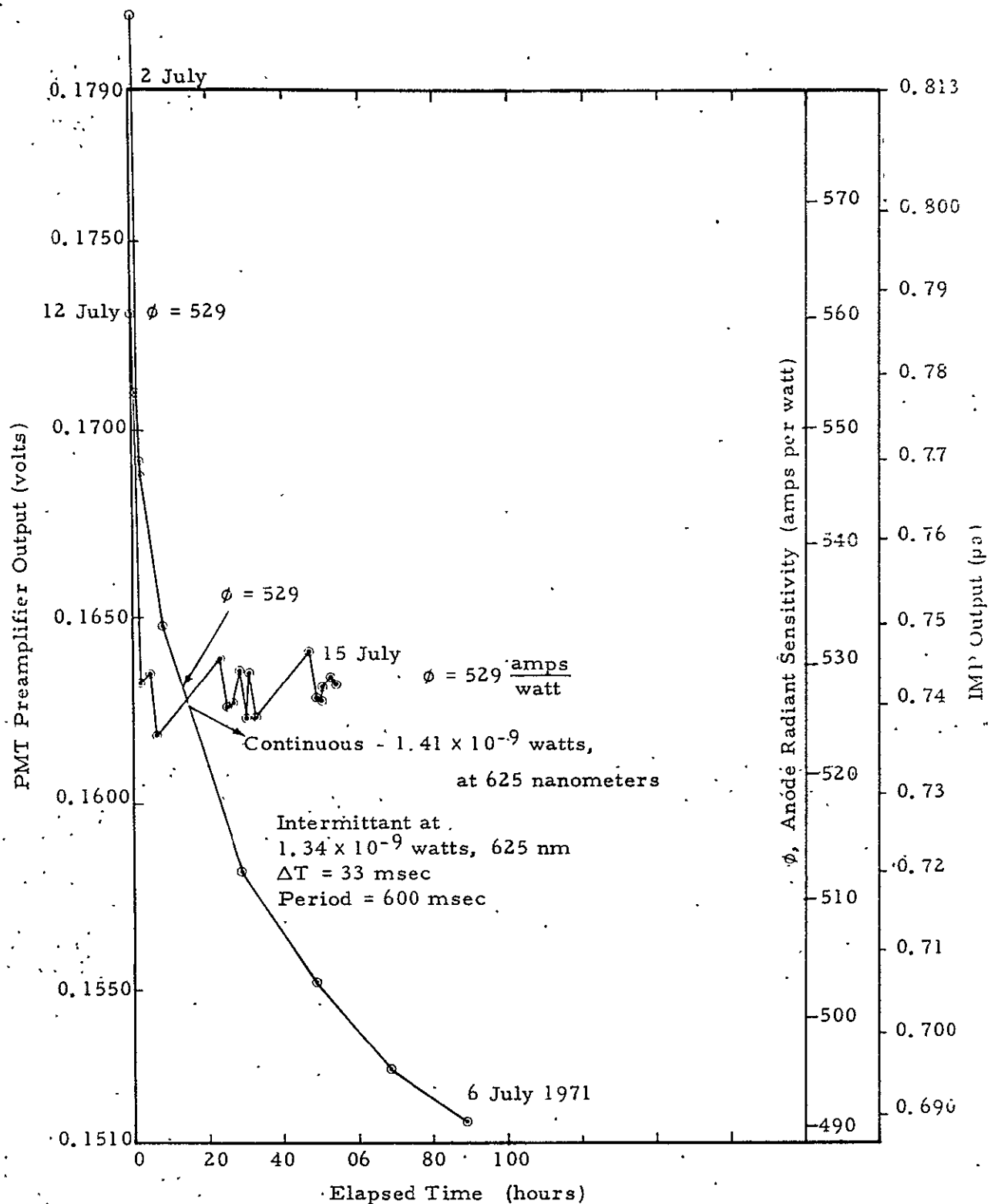


Figure 3-75. IMP Serial No. 8 Stability Test

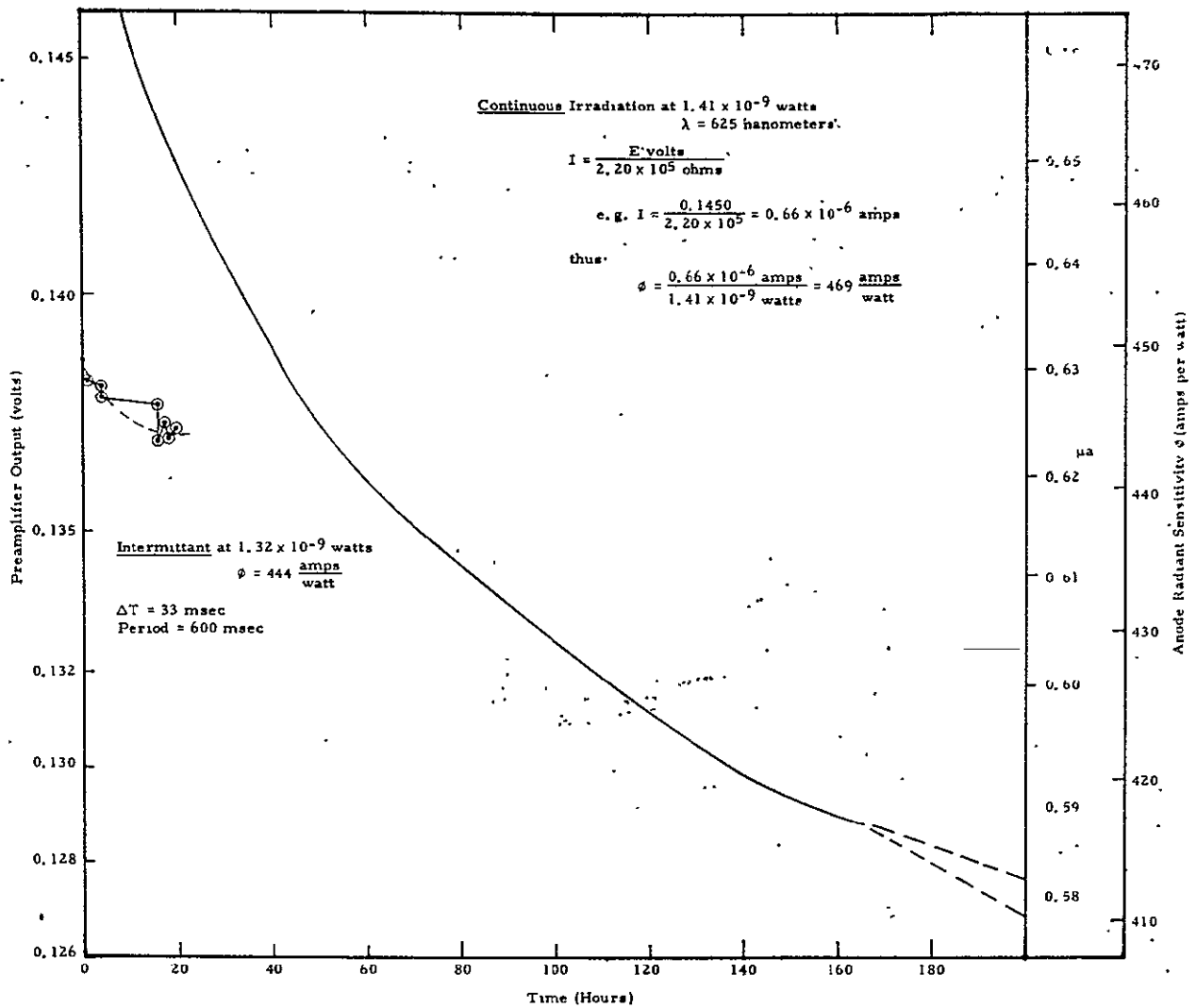


Figure 3-76. IMP Serial No. 4 Stability Test

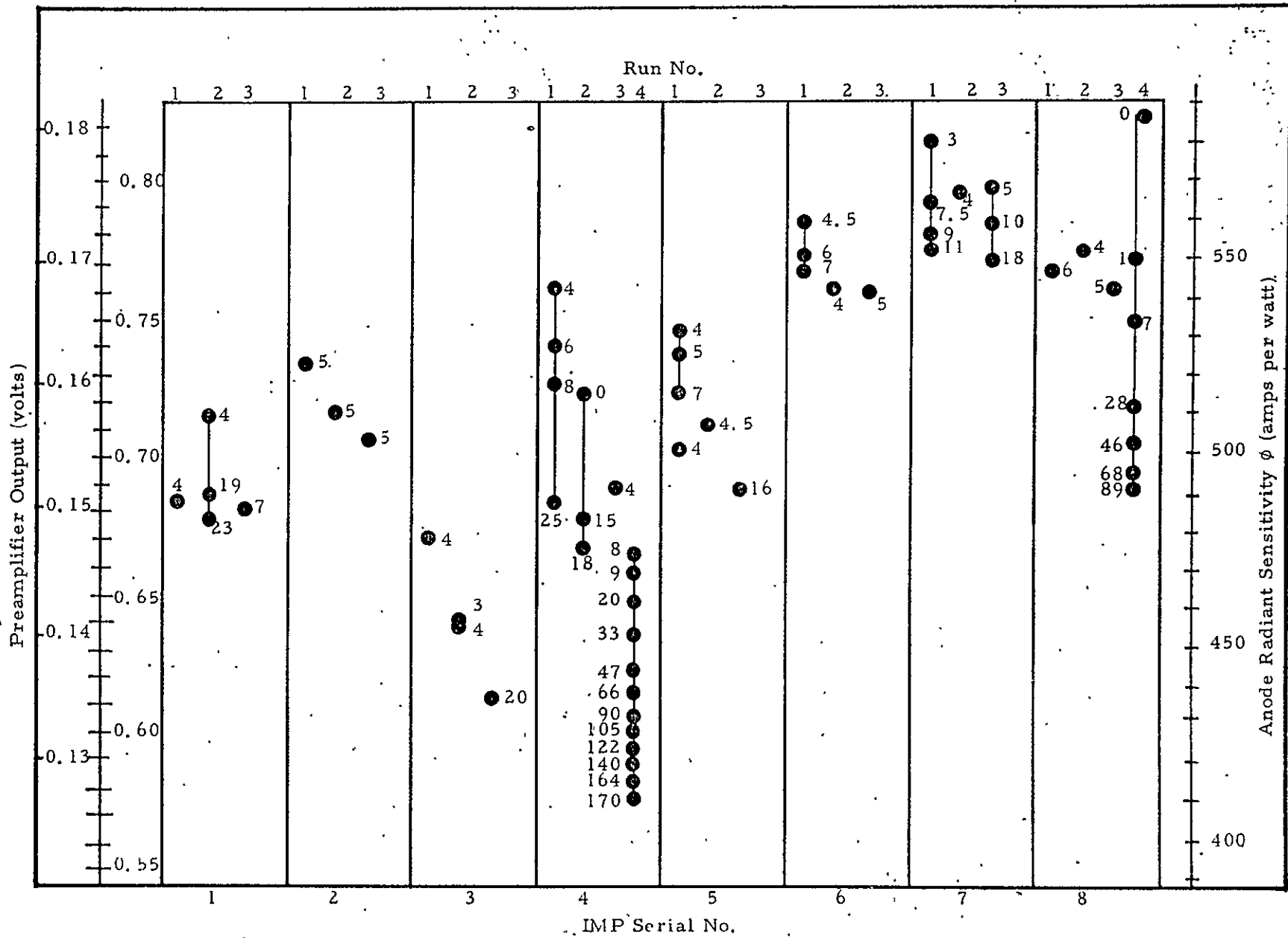


Figure 3-77. Engineering Model IMP Stability Tests

Table 3-28 summarizes the minimum anode radiant sensitivities and the ratio of signal to noise-in-signal for IMPs serial Nos. 1 through 8. All engineering model IMP units exceeded the specification requirements for signal to noise-in-signal ratio.

Table 3-28. Anode Radiant Sensitivity and Signal/Noise-in-Signal Ratio

IMP Serial-No.	Minimum	
	ϕ (amps/watt)	S/NS
1	482	32
2	503	30
3	437	36
4	411	34
5	591	35
6	541	35
7	550	35
8	491	35

Note: Anode radiant sensitivity still decreasing at conclusion of tests in all cases.

Redirected Measurements

Scope of the optical testing was redefined to determine whether the IMP units were useful for the VISSR program in spite of not meeting requirements of sensitivity and stability.

Anode Radiant Sensitivity. - It is possible to adjust the high voltage on the PMT and thus change the anode radiant sensitivity of the IMP to a proper value. However, it is meaningless to do this until you have reached some degree of stability at a meaningful radiant power level regime.

Stability Regime. - It was decided to modify the test setup and procedure to simulate more closely actual flight conditions. Primarily, this meant introducing a duty cycle corresponding to the angular subtense of the earth and the satellite spin period. The former is approximately 20° and the latter is 600 msec. The power level was to be left the same since it corresponded to

intermediate albedo levels for the system. If the IMP units met the stability requirements for this newly defined test, they might be useful for the VISSR program, but if they failed this test they would degrade the SMS/VISSR performance.

Test Set Modifications. - A 100-rpm synchronous motor with a single 20° sector chopper wheel was installed in the IMP test set as close to the final pinhole aperture as possible. This resulted in a trapezoidal input signal which was 33 msec long at the half-power points and about 20 msec across the top flat portion of the input signal. With this duty cycle and waveform it was no longer possible to measure the IMP response with conventional dc instruments nor could ac instruments be used. An oscilloscope did not have adequate accuracy to be useful. A sampling digital voltmeter (DVM) was obtained to read the dc signal level during the signal's 20-msec flat top. A synchronizing trigger was added to sense the phase of the chopper wheel and trigger the DVM to read at the proper time. The DVM used was a "successive approximation" type which took 1 msec to complete a reading. With a system bandwidth of 250,000 Hz, there are enough signal fluctuations in 1 msec that several hundred measurements would have to be made and averaged in order to get a single value good to better than $\pm 1/4\%$. This was done in the early measurements. Later, a 1-msec time constant filter was added to the input of the DVM to reduce the frequency bandwidth, noise fluctuations, and the number of readings required to get reasonable accuracy. This filter was removed and the chopper wheel stopped every time a noise reading was taken.

In practice, ten successive signal readings were found to be adequate to yield averaged measurements good to $\pm 0.1\%$ when the input filter was used. Care was taken to allow for at least 10 time constants of constant input signal amplitude before the DVM was triggered to read the dc signal. When data recording equipment was available, the readings were recorded automatically on punched tape for later computer averaging. Thermocouples were added to record the temperature of the IMP units during the test. No attempt was made to stabilize the IMP temperature except to isolate the test set from unreasonable heat sources and to allow thermal coupling to the ambient room environment.

Results of Flight Profile Measurements. - The stability of the anode radiant sensitivity is shown in Figure 3-78 for IMP No. 13. Measurements were repeated for IMP No. 8 and No. 4 and the results are plotted in Figures 3-75 and 3-76, respectively. These curves all indicate that a stabilized value is reached, with the signal within $\pm 3\%$ (approximate) of the stabilized value after 1 hour operation.

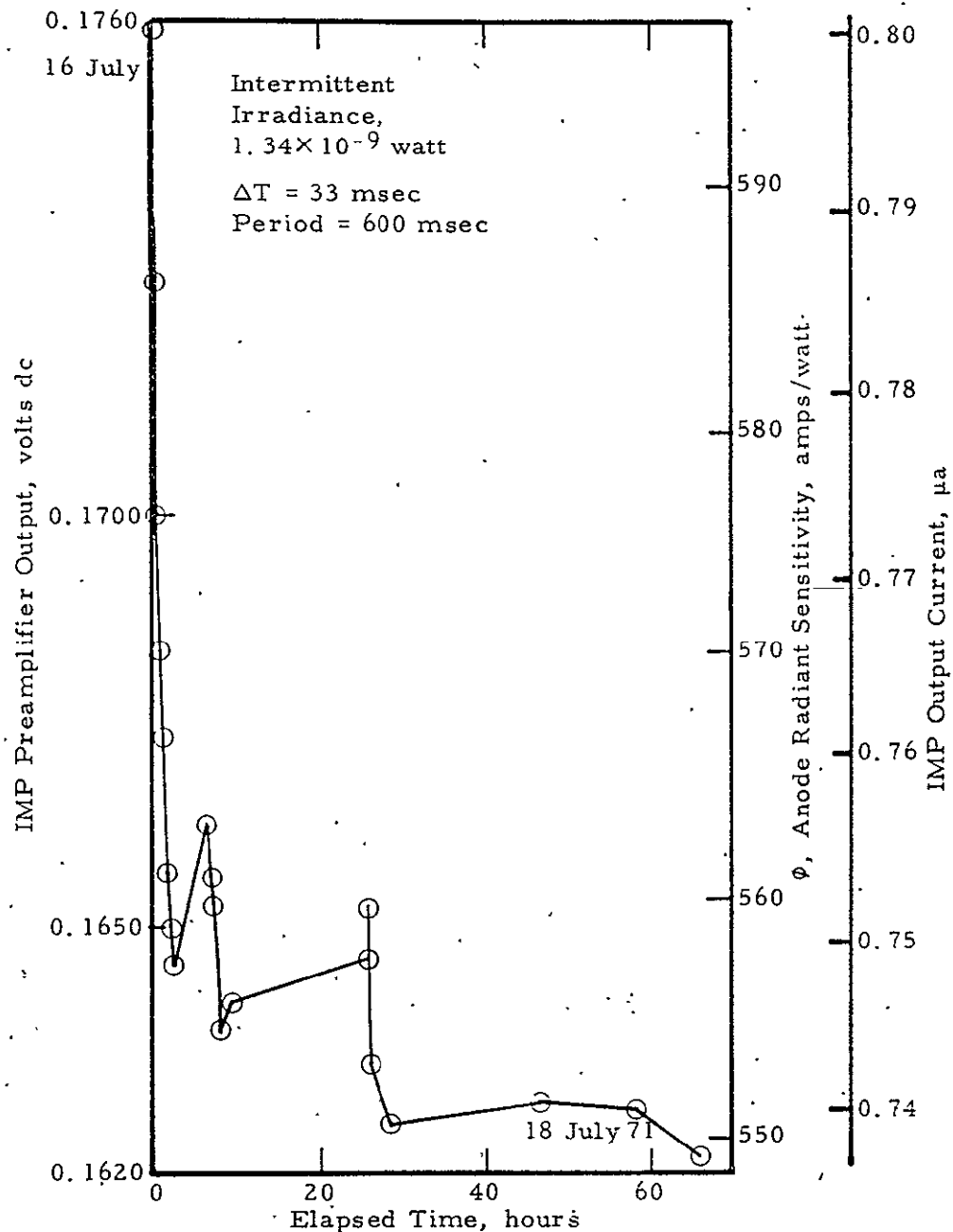


Figure 3-78. IMP Serial No. 13 Stability Tests

Figure 3-79 shows the response for IMP No. 9 which is a notable exception to the previous units. This unit took 16 hours before it was within $\pm 3\%$ of the stabilized value.

Figure 3-80 shows a summary of measured curves for the first eight IMP units (engineering units). Note that all units reached a stabilized value, and IMP units Nos. 4, 5, 6, 7, and 8 were within $\pm 3\%$ of that value in approximately 1 hour. IMP units Nos. 1, 2, and 3, however, required a longer time to stabilize than the 1-hour requirement as defined in the specification.

Figure 3-81 shows the results of those units which have been measured. Note that most units reached a stabilized value. The curves with questionable dips were checked for temperature changes during test, and for some, the dips are found by temperature correlation to be a nearly normal response of the unit to temperature changes. Notable exceptions to this: IMP units Nos. 33, 15, and 17 do not seem to reach a reliable stabilized value.

Among the IMP units which stabilized, the following do so to within $\pm 3\%$ in approximately 1 hour: Nos. 10, 11, 12, 13, 14, 16, 18, 19, 20, 24, 27, 28, 29, and 32. Those which do not reach to within $\pm 3\%$ of a stabilized value within 1 hour are IMP units: Nos. 9, 15, 17, 22, 23, 25, 26, and 33. Note that IMP unit No. 13 was measured on two separate occasions, and that the stabilized values differ by 4%, both at 75°F .

The stabilized values for the anode radiant sensitivity, as best as may be estimated between 75° to 77°F , are annotated on Figure 3-81 for each unit. Note that the stabilized sensitivity values vary from 634 to 439 amps/watt, values that are 9% to 38% too low.

The signal to noise-in-signal ratio was measured for all IMP units tested, and all meet or exceed the $S/N = 29$ value derived from the specification. Table 3-29 lists the S/N , sensitivity, and stabilization determinations for all units tested.

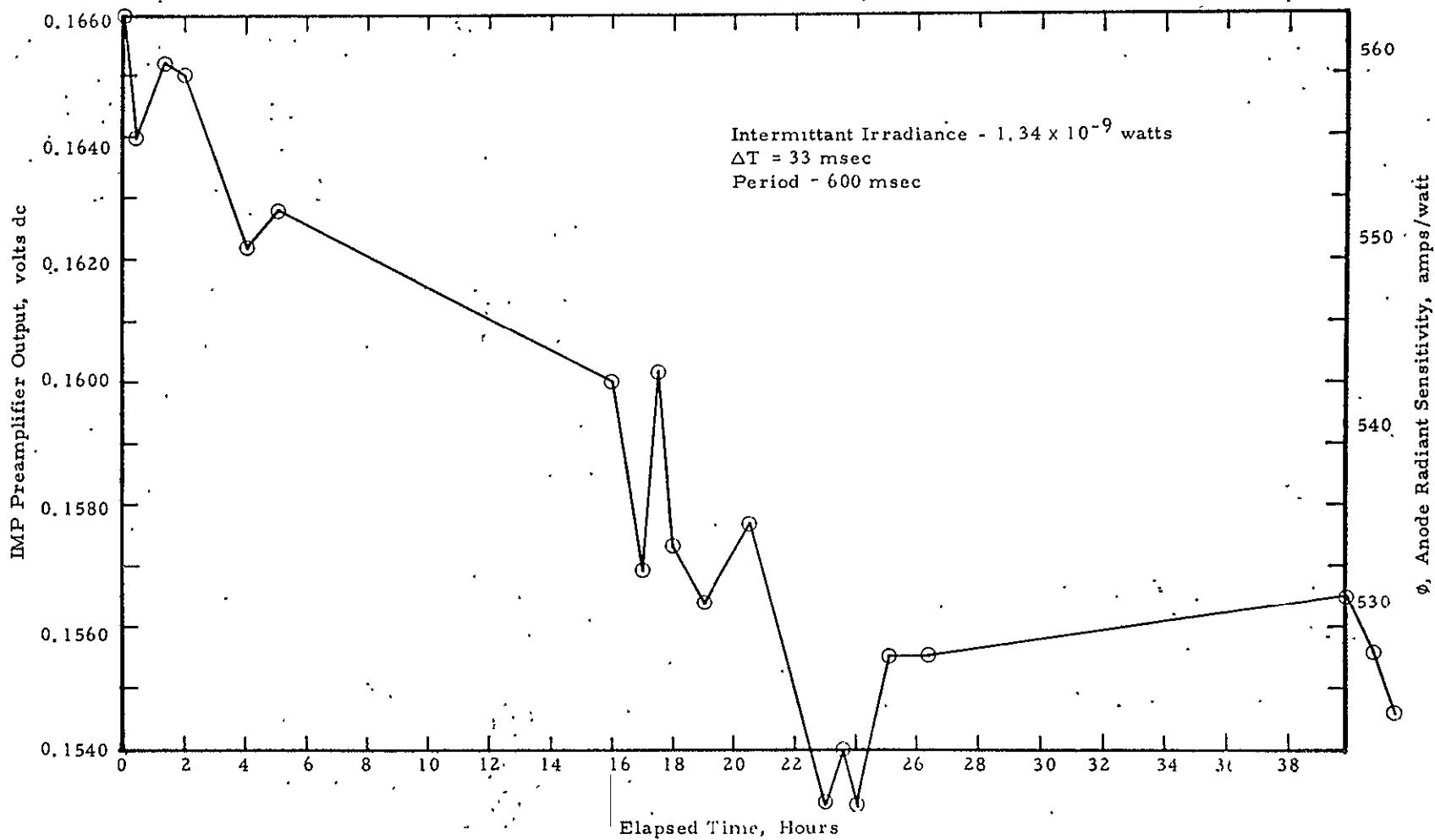


Figure 3-79. IMP Serial No. 9 Stability Tests

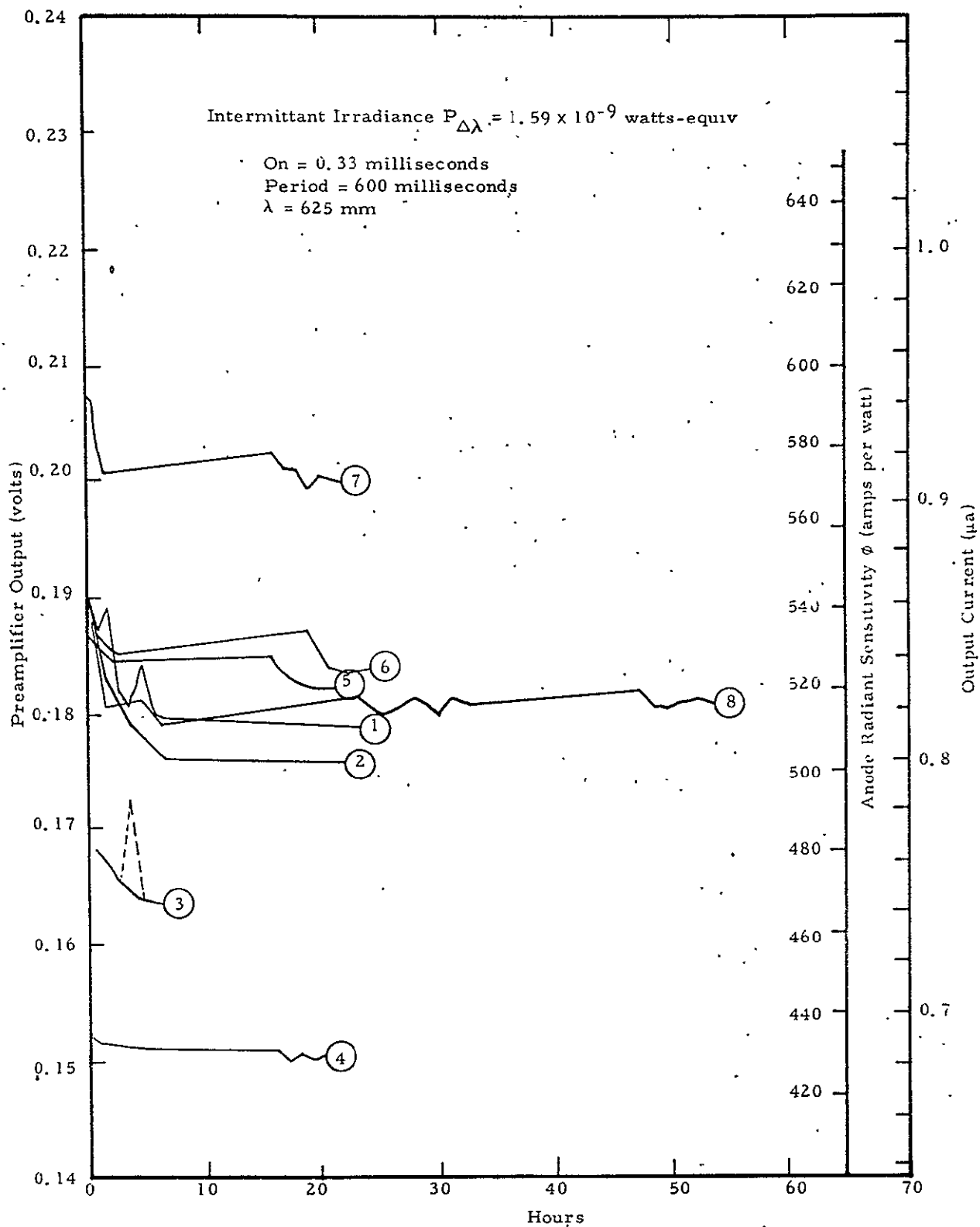


Figure 3-80. IMP Output vs Time - Engineering Model Units

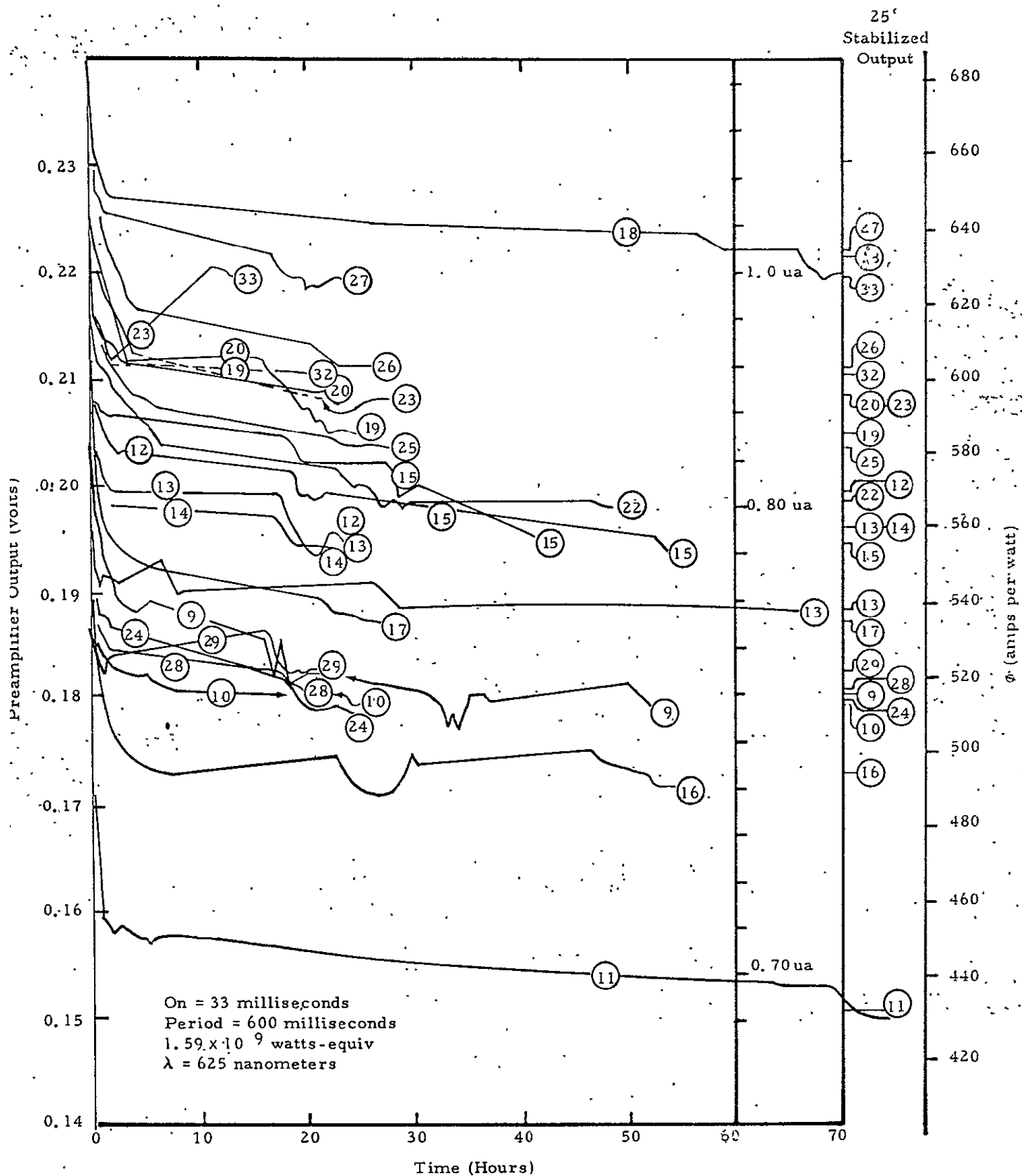


Figure 3-81. IMP Output vs Time - Flight Model Units

Table 3-29. Summary for Flight Profile Testing of
SMS/VISSR IMP Units

IMP Serial No.	Ø Intermittent	S/N During Initial Measurements (Spec = 29)	Stabilize in 1 Hour
1	512.	32	No
2	503	30	No
3	471	36	No
4	443	34	Yes
5	528	36	Yes
6	535	34	Yes
7	572	35	Yes
8	548	36	Yes
9	516	32	No
10	513	32	Yes
11	430	31	Yes
12	570	35	Yes
13	539	37	Yes
14	560	36	Yes
15*	556	37	No
16	494	35	Yes
17*	535	35	No
18	633	36	Yes
19	586	37	Yes
20	596	38	Yes
21	Not Measured		
22	566	37	No
23	596	38	No
24	514	37	Yes
25	581	39	No
26	603	35	No
27	634	41	Yes
28	517	30	Yes
29	521	34	Yes
30	Not Measured		
31	Not Measured		
32	601	35	Yes
33*	627	38	No
34 thru 38	Not Measured		

*Unit did not stabilize.

Stabilization Effects of Solar Scanning. - The effect on the stability of sensitivity due to scanning through the sun has been tested previously by the vendor. Single flashes, of a comparable power to the sun, indicated no serious degradation of sensitivity. With the failure of the IMP units to meet the steady-state stability specification on a long-term basis, it was deemed important to assess the significance of long-term solar flashing. A modification to the IMP test set was made so that a helium-neon laser would shine through the system into the IMP input in addition to the normal operation. A timed shutter for the laser was provided so that the laser would deliver a 1- to 2-msec burst once each 600 msec - synchronized with the chopper wheel. An optical filter was provided to reduce the laser intensity to 10^{-4} watt (effective) into the IMP. The true solar pulse is expected to be 10^{-4} watt (effective) and of 1-msec duration.

A test regime was established where the laser would flash once every 600 msec for a period of 30 seconds, then resume normal operation for 19-1/2 minutes. Near the end of each 600-msec scan, the partially recovered normal albedo signal level is measured and plotted. This cycle approximates the scanning when the $1/2^\circ$ wide sun is scanned in a 20° field of view, requiring 20 minutes. Thus the sun is scanned for $1/2^\circ \times 1/20^\circ \times 20 \text{ min} = 1/2 \text{ min} = 30 \text{ seconds}$.

Short duration tests were made on IMP units Nos. 4 and 8, with nominal results. A 30-hour continuous, round-the-clock, test was set up for IMP unit No. 15. It required continuous and rigorous attention as the laser had to be calibrated, activated and timed each 20 minutes, in addition to taking response readings of the IMP units. The IMP was prestabilized for 63 hours in a normal flight profile regime. A minimum of 20 hours of stabilized operation was desired. Figure 3-82 shows the data from this test. A stabilized sequence of values was reached after 5 hours. The values plotted are the apparent earth albedo measurement, using the calibrated lamp and the IMP test set at various times during the 20-minute test cycle. At 10 hours, the electrical power in the plant went off, and was off for 65 minutes before resuming the

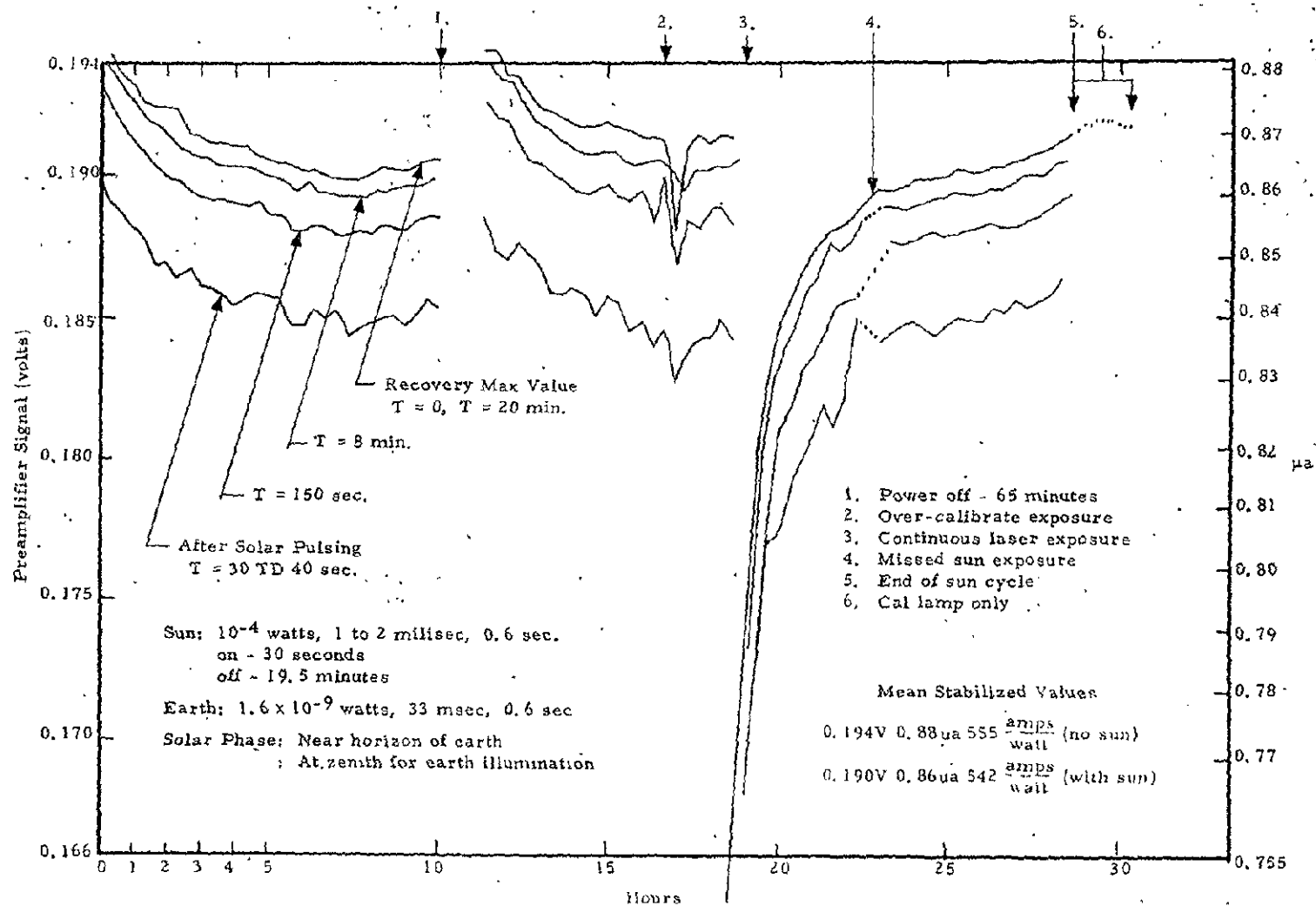


Figure 3-82. IMP Solar Flashing Tests

SRRC

test. Note in Figure 3-82 that during the 65-minute off period the IMP completely recovered. In another 5 hours of operation it again reached a stabilized sequence of values.

At 18.5 hours, the laser was inadvertently left on for an indefinite time — probably 2 to 10 seconds. The laser pulse to the IMP unit would then be on for 33 msec every 600 msec. The accumulative time would have been about 99 to 550 msec at 10^{-4} watt. Note the substantial but finite degradation of IMP response due to the excessive laser pulsing by -16%. However, the test continued normally immediately after the extra long laser burst, and previously stabilized sequence values were reached again in 6 hours. At the 28.66-hour point, the solar flashing was discontinued and normal flight profile operation continued for 1.66 hours — with surprisingly little recovery.

To summarize the results of the solar flashing test, it can be said that 1) there is a 2% drop in the recovery maximum value while solar flashing cycle continues, 2) stabilization decreasing or increasing takes place in about 5 or 6 hours, 3) during the time it takes to make one complete field-of-view picture (20 minutes), the sensitivity drops 2.75 to 3% after each solar flashing period — and then recovers nearly completely by the time another solar image is started again, and 4) there appears to be no significant permanent damage to the IMP due to solar flashing. (Steady sun on the IMP would require the satellite to stop spinning.)

OPTICAL SYSTEM TESTING

Hemispherical Scattering Analysis

The rationale behind the data reduction for the SBRC scatter goniometer equipment is given below. The geometry is shown schematically in Figure 3-83. Only a small portion of the ring formed by $d\theta$ is sampled.

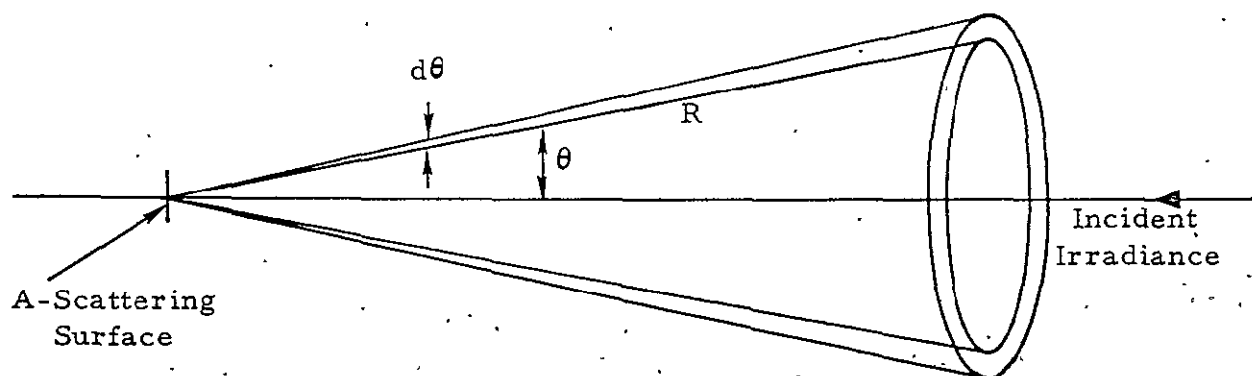


Figure 3-83. Scatter Measurement Geometry

Assuming scattering surface is an ideal diffuser with a reflectance of unity and is irradiated normally with a level of H (watts/cm²), the reflected radiance is

$$N = \frac{H}{\pi} \text{ (watts/cm}^2 \text{ sr)} \quad (3-52)$$

The power, P , reflected (scattered) from area A into solid angle with $d\theta$ width is

$$dP = \frac{H}{\pi} (A \cos \theta) \frac{2\pi R \sin \theta R d\theta}{R^2} \quad (3-53)$$

$$dP = HA \sin \theta \cos \theta d\theta$$

By integration with limits describing hemisphere

$$\int_0^P dP = HA \int_0^{\pi/2} \sin \theta \cos \theta d\theta \quad (3-54)$$

$$P = HA \sin^2 \theta \Big|_0^{\pi/2} = HA \quad (3-55)$$

Of course, this is the expected result since HA is the power incident on the surface with area 'A.'

In the experimental measurements, the scattering of a mirror surface is referenced to the scattering of BaSO₄ surface. The BaSO₄ surface is assumed to be an ideal diffuser with a reflectance of unity.

The mirror hemispherical scattering, HS, is defined as

$$HS = \frac{P_M(sc)}{P_{BaSO_4}(sc)} \quad 3-56$$

$$\text{where } P_{BaSO_4}(sc) = HA \int_0^{\pi/2} 2 \sin \theta \cos \theta d\theta \quad (3-57)$$

$$P_M(sc) = HA \int_0^{\pi/2} 2 \rho_\theta \sin \theta \cos \theta d\theta \quad (3-58)$$

Using equations 4-5, 4-6, and 4-7

$$HS = \frac{\int_0^{\pi/2} 2 \rho_\theta \sin \theta \cos \theta d\theta}{\int_0^{\pi/2} 2 \sin \theta \cos \theta d\theta} \quad (3-59)$$

$$HS = \int_0^{\pi/2} 2 \rho_\theta \sin \theta \cos \theta d\theta \quad (3-60)$$

To facilitate numerical integration of scattering data, we write

$$\sum_{i_0}^{i_{\max}} \Delta P_i = HA \sum_{i_0}^{i_{\max}} \Delta \sin^2 \theta_i, \quad i = 1, 2, 3 \dots i_{\max} \quad (3-61)$$

viz., a set of angles where

$$\Delta \sin^2 \theta_i = \sin^2 \theta_i - \sin^2 \theta_{i-1} = \frac{1}{i_{\max}} \quad (3-62)$$

Assume $i_0 = 1$, $i_{\max} = 20$, which gives $\Delta P = 0.05$.

These conditions result in

i	θ_i (degrees)	$\frac{\theta_i + \theta_{i-1}}{2} = \theta_{i \text{ av}}$ (degrees)
1	12.9	6.45
2	18.45	15.68
3	22.8	20.63
4	26.4	24.60
5	30	28.2
6	33.2	31.6
7	36.3	34.8
8	39.3	37.8
9	42.1	40.7
10	45.0	43.6
11	48.0	46.5
12	50.8	49.4
13	53.8	52.3
14	56.9	55.4
15	60.0	58.4
16	63.6	61.8
17	67.3	65.5
18	71.8	69.6
19	77.1	74.4
20	90.0	83.6

A set of scattering data consists of signals at each of the angles, $\theta_{i \text{ av}}$, for the BaSO_4 and mirror surface. The hemispherical scatter, HS, is calculated by

$$HS = \frac{1}{i_{\text{max}}} \sum_{i_0}^{i_{\text{max}}} \frac{S_M(\theta_{i \text{ av}})}{S_{\text{BaSO}_4}(\theta_{i \text{ av}})} \quad (3-63)$$

The above analysis assumes rotational symmetry for scattering about the surface normal. This condition has not been met by many of the mirror surfaces measured to date. For these cases we have assumed a linear interpolation, such that the average of two orthogonal sets of $S_M(\theta_{i \text{ av}})$ is used in equation 3-63 to obtain hemispherical scatter.

As indicated above, the BaSO_4 surface has been assumed to be an ideal diffuser (Lambertian) with a reflectance of unity. The Lambertian, or cosine, distribution property is checked in the following manner. If the surface is Lambertian, we have

$$\frac{\frac{1}{i_{\max}} \sum_{i_0}^{i_{\max}} S_{\text{BaSO}_4}(\theta_{i \text{ av}}) / S_{\text{BaSO}_4}(\max)}{\frac{1}{i_{\max}} \sum_{i_0}^{i_{\max}} \cos \theta_{i \text{ av}}} = 1.0$$

Actually, the ratio is

$$\frac{0.612}{0.664} = 0.923$$

Thus, for hemispherical scatter reference, the BaSO_4 is within 8% of being Lambertian. Grum⁶ reports the reflectance for BaSO_4 powder is ≥ 0.99 for the 0.55- to 0.80- μm spectral range. Thus, BaSO_4 powder surface closely approaches an ideal diffuser (Lambertian) with unity reflectance.

Scattering Measurements

Numerous scattering measurements have been made on VISSR optical components. The results of these measurements are summarized in Table 3-30.

SBRC and Perkin-Elmer scattering measurements do not correlate too well. The scatter data correlation is generally within a factor of two.

Significant efforts have been made to determine the cause of the inconsistencies. The initial effective spectral region used by SBRC was 0.45 to 0.73 μ . An additional Corning sharp-cut filter was added to change the spectral region to 0.55 to 0.73 μ . The PMT detector used determines the long-wavelength cutoff edge. This change in spectral band results in a change of scattering value of the order of 10%.

⁶F. Grum and G. Luckey, Appl. Opt. 1, 2289 (1968)

Table 3-30. Summary of Scattering Measurements - VISSR Optics

Scan	Primary	Secondary	Company	Coating	Scatter			Meas Date (1971)	
					HS (%) Avg	Scatter Max	Scatter Min		
002	004	004	TLI	None	1.88	3.5	0.16	7/6	
			TLI	None	4.1	8.0	0.37	7/2-7/3	
			TLI	None	0.59	1.84	0.2	7/3	
004	002	002	TLI	None	1.31	1.89	0.5	6/25-6/26	
			TLI	None	≥1.19	1.8	0.8	6/26	
			TLI	None	0.60			5/17	
004	002		TLI	None	1.26	2.7	0.8	7/17-7/19	
			TLI	None	1.80	5.5	1.0	7/16	
	002	002	TLI	None	1.73	3.5	0.23	7/31-8/2	
			TLI	None	0.51			8/2	
	002		TLI	None	0.77	1.40	0.30	8/6	
003	005	005	PE	None		0.68	0.63	6/25	PE Measurements
			PE	None		0.55	0.53	6/25	
			PE	None		0.73	0.53	6/25	
	005	005	PE	Al-SiO	1.9	2.5	1.0	7/29	Cursory Measurements Not Detailed
			PE	Al-SiO	1.3	2.8	1.26	7/28	
005	003	003	PE	None	0.56			9/1	PE Measurements
			PE	None	0.49			9/1	
			PE	None	1.1			8/12	
005	003	003	PE	None	0.44	0.59	0.29	8/13-8/17	
			PE	None	0.85	1.52	0.44	8/12	
			PE	None	0.73	0.82	0.66	8/12	

The Perkin-Elmer scattering measurement method uses an integrating sphere, and the VISSR mirrors are measured relative to an aluminized glass reference mirror. The reference mirror scattering was measured by H. Bennett of the Navy Ordnance Test Station, China Lake, California. Figure 3-84 compares SBRC and H. Bennett narrow-band spectral scattering.

Figure 3-84 shows that the scattering function for the glass reference mirror decreases with increasing wavelength. The Bennett data are fitted closely by a straight line. The SBRC scattering data tend to be less dependent on wavelength for longer wavelengths.

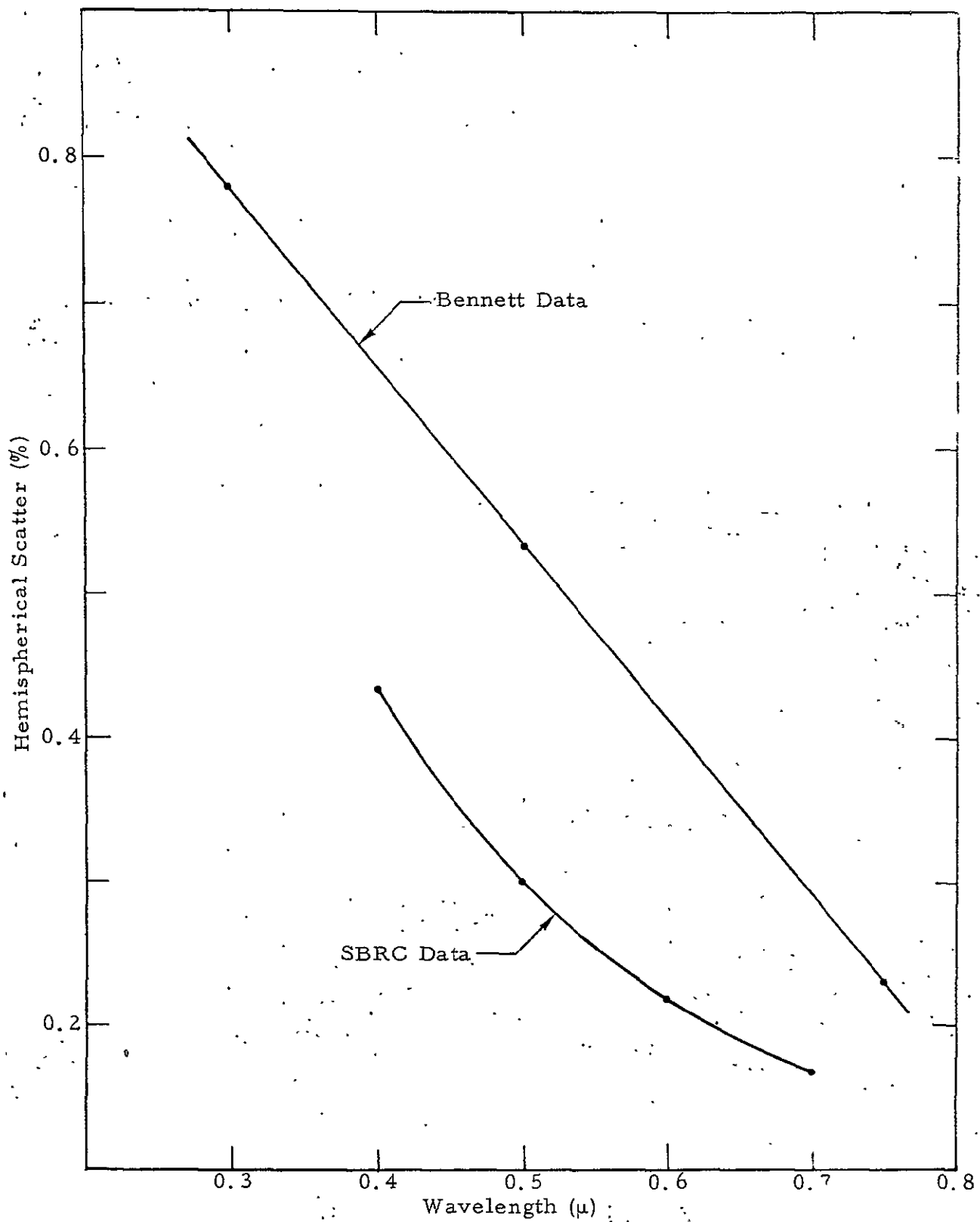


Figure 3-84. Hemispherical Scatter, Perkin-Elmer Reference Mirror No. 3

The hemispherical spectral scattering function for one of the VISSR Ni-Be test specimens was measured and plotted in Figure 3-85. The shapes of the two spectral scattering functions, represented in Figures 3-84 and 3-85, are within 10% of each other. The "shape" is determined by taking ratios of the two curves.

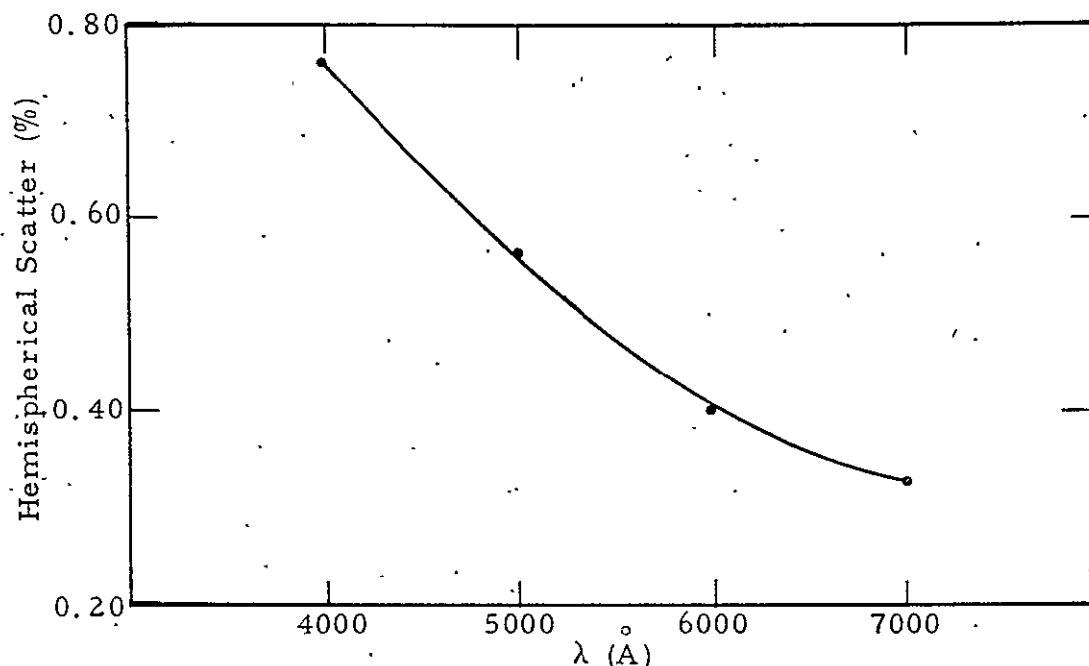


Figure 3-85. Hemispherical Scatter

Reflectance (Scattering) - Scan Mirror Serial No. 005

A diffuse reflectance (scattering) curve is given in Figure 3-86 for scan mirror serial No. 005 (Tinsley). The curve has been normalized to the BaSO_4 diffuse reflectance standard. The BaSO_4 surface is assumed to be an ideal diffuser with reflectance of unity and Lambertian scatter.

Reflectance (Scattering) - Anodized Beryllium

A sample of VISSR anodized beryllium was measured for hemispherical scatter. Its hemispherical scatter was 3.3%. Its reflectance (scattering) properties as a function of angle are illustrated in Figures 3-87 and 3-88. The incident radiant energy was normal to the anodized beryllium sample.

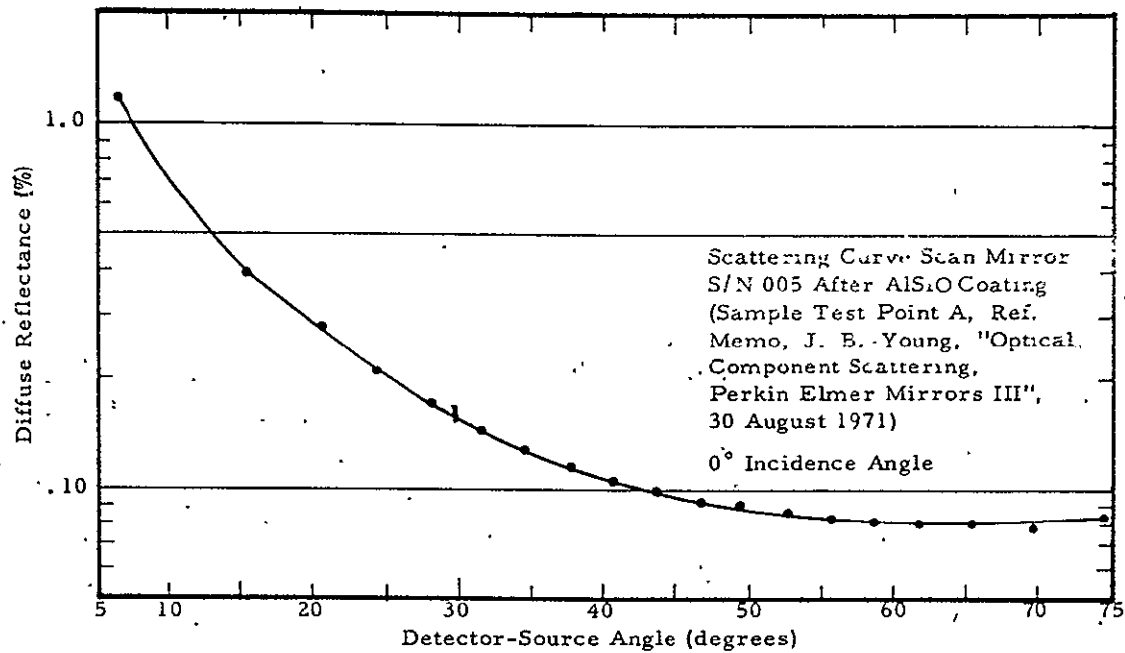


Figure 3-86. Scan Mirror Reflectance (Scattering)

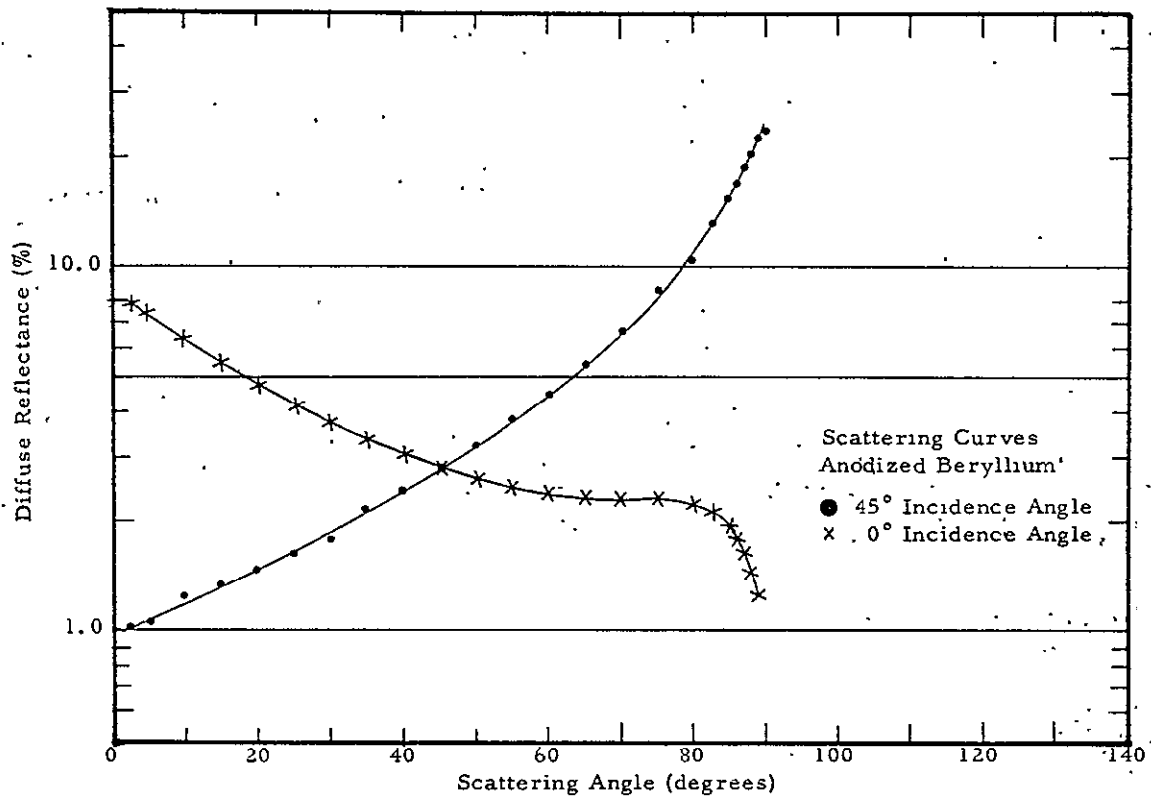


Figure 3-87. Anodized Beryllium Reflectance (Scattering)

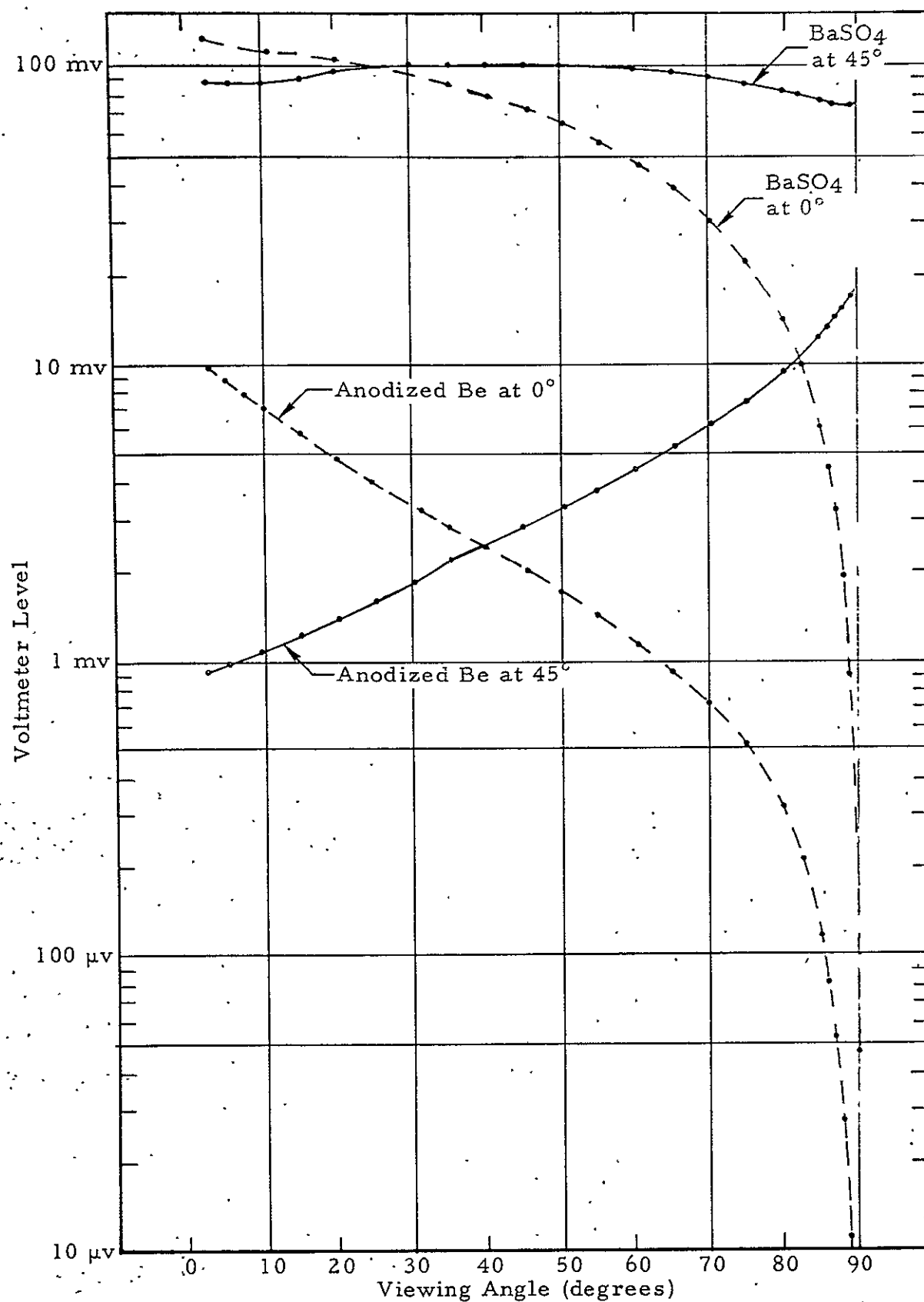


Figure 3-88. Diffuse Reflection of Anodized Beryllium

Reflectance (Scattering) - Radiation Cooler Honeycomb

Measurements were made of diffuse reflectance (scattering) for the radiation cooler honeycomb radiator on the protoflight model. Results for 0° incidence angle are shown in Figure 3-89 for both dull and gloss black finishes. The finish selected for use on the protoflight model is dull black (Cat-A-Lac).

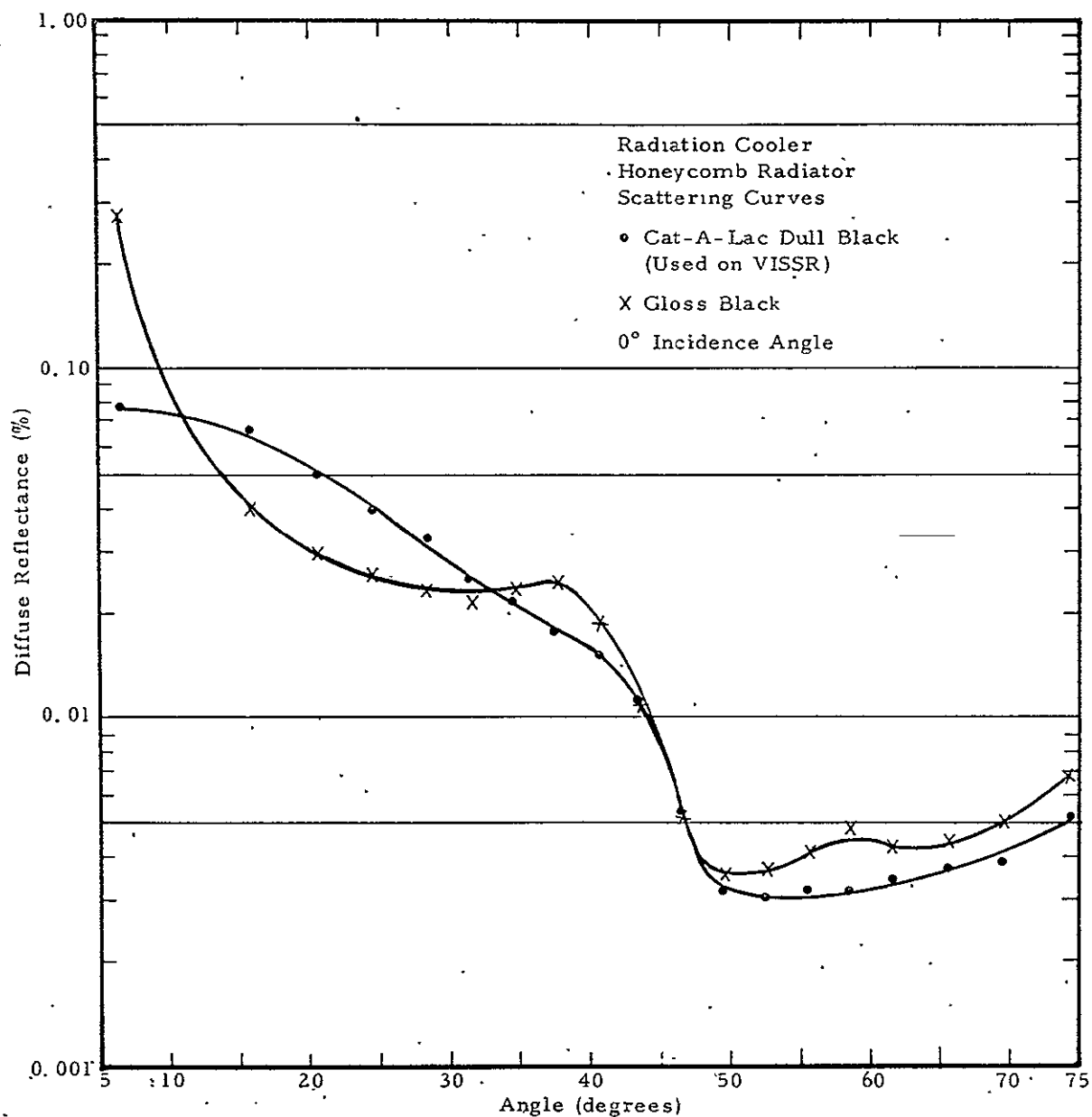


Figure 3-89. Radiation Cooler Honeycomb Reflectance (Scattering)

Reflectance (Scattering) - Cat-A-Lac Black Paint

The diffuse reflectance (scattering) for a flat sample surface painted with Cat-A-Lac black paint was measured for normally incident light at scattering angles from 6° to 75° . Reflectance as a function of angle is illustrated in Figure 3-90.

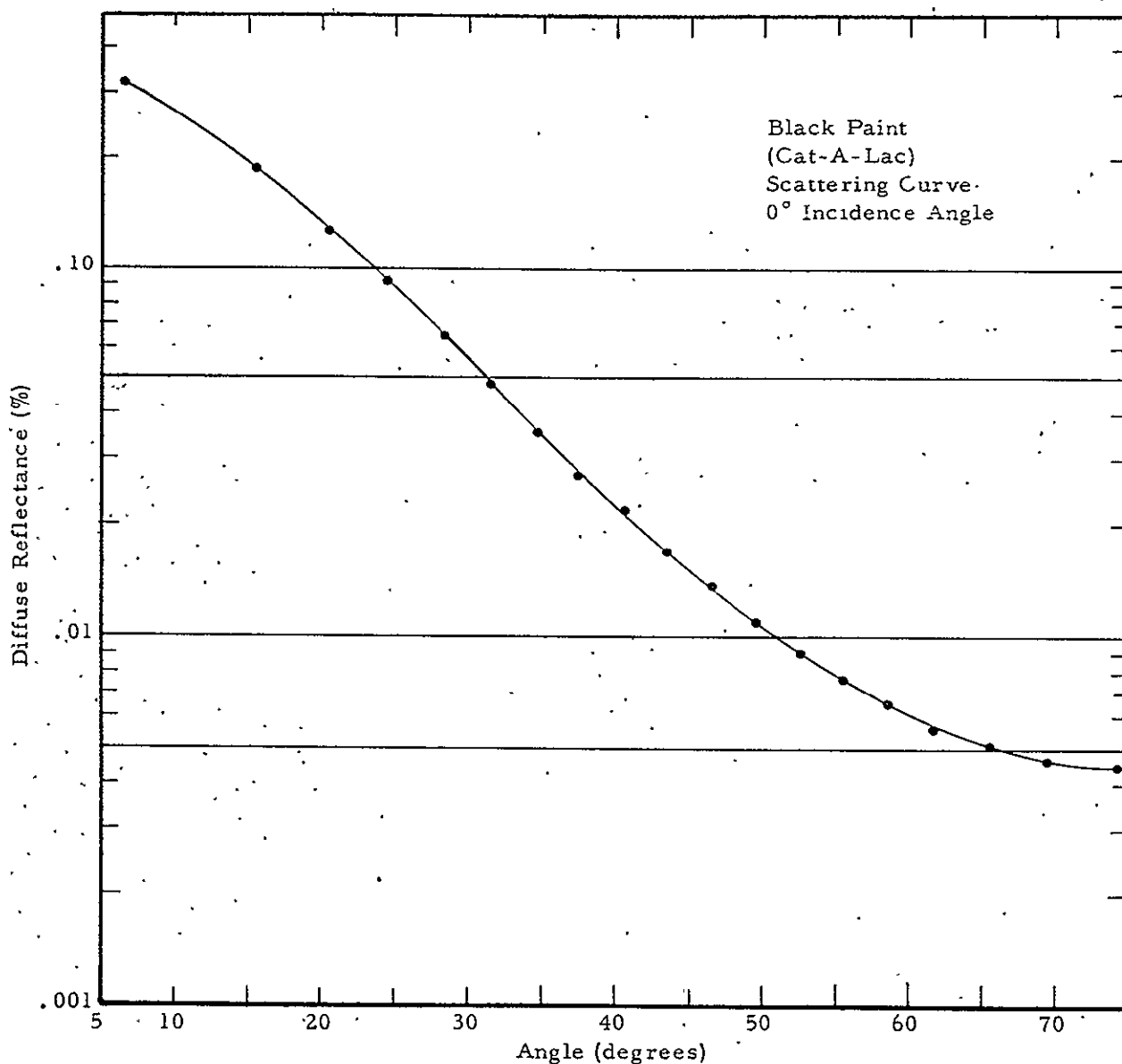


Figure 3-90. Cat-A-Lac Black Paint Reflectance (Scattering)

ENGINEERING MODEL OPTICAL SYSTEM MEASUREMENTS

Image Quality - Class II

The VISSR optical system was measured in Class II configuration. The optical system was assembled in a laboratory setup. The optical specification required that the optical vendor measure the system performance using two different optical testing methods. The optical vendor, Perkin-Elmer, chose: 1) interferometric measurement of wavefront, and 2) image blur - radiometric (encircled energy distribution).

The interferometric technique used a scatter plate interferometer operating at 0.6328 micron. The VISSR/SMS optical system is autocollimated with an optical test flat. The scatter plate is located at the focus of the VISSR optical system.

Figures 3-91 and 3-92 illustrate typical interferograms on-axis and 1.6 mr off-axis, respectively.

Since the test uses a double pass system, each fringe in the interferogram represents a $\lambda/4$ surface or $\lambda/2$ wavefront deformation. If the fringes are all straight and parallel, the system is perfect; any deviation from straightness or parallelism represents a system optical error.

The Class II wavefront deformation specification requires the assembled optical system to have a wavefront deformation less than $\lambda/2$ for all field angles of 1.6 mr or less where $\lambda = 0.6$ micron.

Figures 3-91 and 3-92 indicate that the Class II measured maximum wavefront deformation is of the order of $\lambda/2$.

Radiometric Tests - Class II

The radiometric tests were performed on the VISSR/SMS optical system with the optical axis horizontal. The scan mirror was at 45° to the optical axis. Energy from an auxiliary collimator filled the VISSR entrance aperture. Final alignment to the VISSR optics was performed in this configuration using a microscope to examine the image on-axis.



Figure 3-91. Interferograms, On-Axis,
Class II Test Configuration



Figure 3-92. Interferograms, 1.6 mr, Off-Axis,
Class II Test Configuration

The collimator source was a quartz arc lamp with a spectral output peaked at 0.58 micron. The source pinhole was 0.0004 inch (after a 10:1 reduction by a relay lens). The focal length of the collimator is 218 inches. Thus, the effective source diameter referred to the VISSR focal surface was 0.0002 inch.

A photometer was placed at the focus of the VISSR optical system. The photometer assembly consists of a relay lens (10X microscope objective), aperture field, quartz field lens, filter holder, and Model 2020 (Gamma Scientific) photometer with S-20 photomultiplier. The photometer assembly is mounted on a three-axis adjustable stage. A flip mirror is provided for use in visual examination of the images with an eyepiece. The aperture wheel contains twelve precision round apertures of specific sizes.

The microscope objective relays the image formed by the VISSR optical system onto the aperture wheel plane. The desired aperture is selected and positioned on the axis of the microscope manually. The quartz field lens images the relay lens (microscope objective) onto the S-20 PMT photocathode at about unity magnification.

Figure 3-93 illustrates several functions of fractional encircled energy versus angular diameter of circle (pinhole). Curve A is the VISSR optical system Class II specification requirements. Curve B is the Class II measurements. Curve C is the test equipment calibration function. The portion of the test equipment tested is the source optics and detector optics. Curve D is the Class II measurements corrected for effects of the test equipment.

The data reduction used root sum square (rss) subtraction. For example

$$\theta_{\text{CORR}} = \sqrt{\theta_{\text{M}}^2 - \theta_{\text{CAL}}^2}$$

where θ_{CORR} = corrected Class II angular diameter of encircled energy

θ_{M} = Class II angular diameter of encircled energy

θ_{CAL} = calibration of test equipment angular diameter of encircled energy

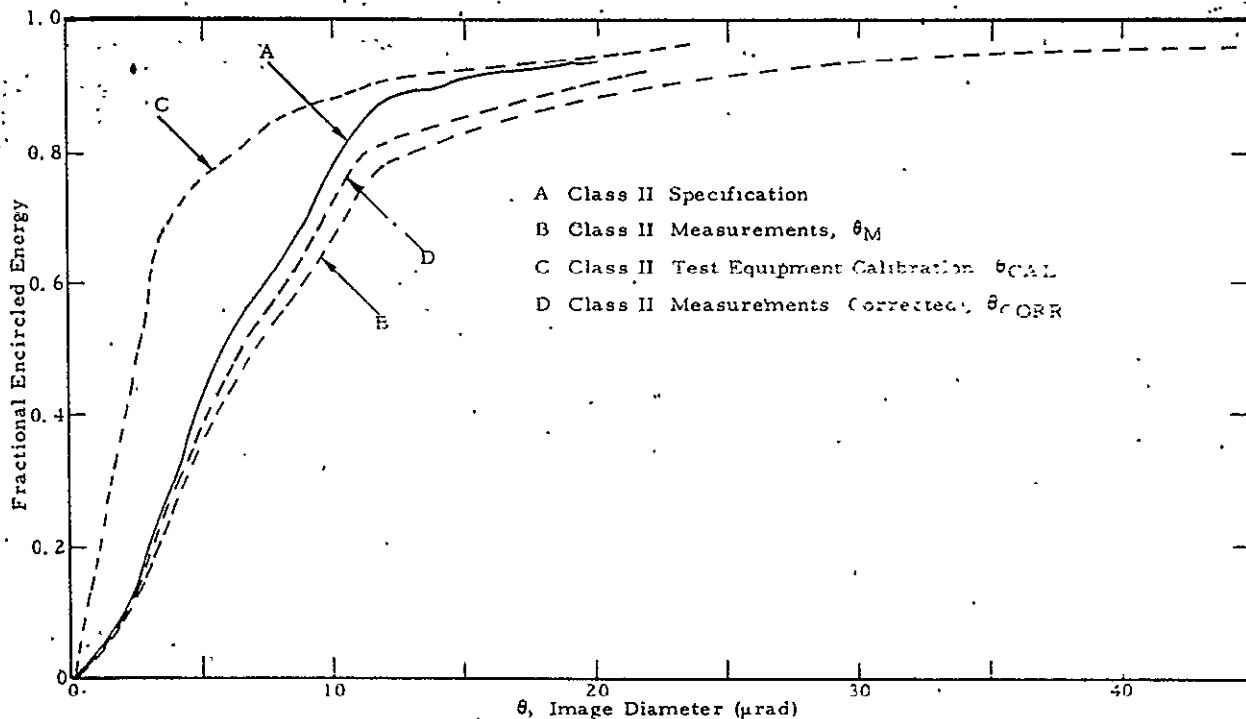


Figure 3-93. Fractional Encircled Energy as a Function of Blur Diameter, Class II Test Configuration

The corrected Class II measurements (Curve D) did not meet the VISSR image quality specification (Curve A). However, based on schedule considerations and the fact that the mirrors would be used in the engineering model of VISSR, the decision was made to accept the mirrors.

Assembly - Class I Measurements

Preliminary optical measurements of the VISSR optical system were made in Class I configuration. Class I configuration has VISSR mirrors mounted and aligned in VISSR beryllium hardware.

During the assembly phase, the scan mirror was measured after assembly in a Ritchey test configuration. An interferometer was placed at the center of curvature of a well figured sphere ($R = 300$ inches). The scan mirror was situated such that it folded the beam as shown in Figure 3-94.

The criterion for the scan mirror assembly was to obtain an interferogram equivalent to the ones obtained with scan mirror supported in a laboratory.

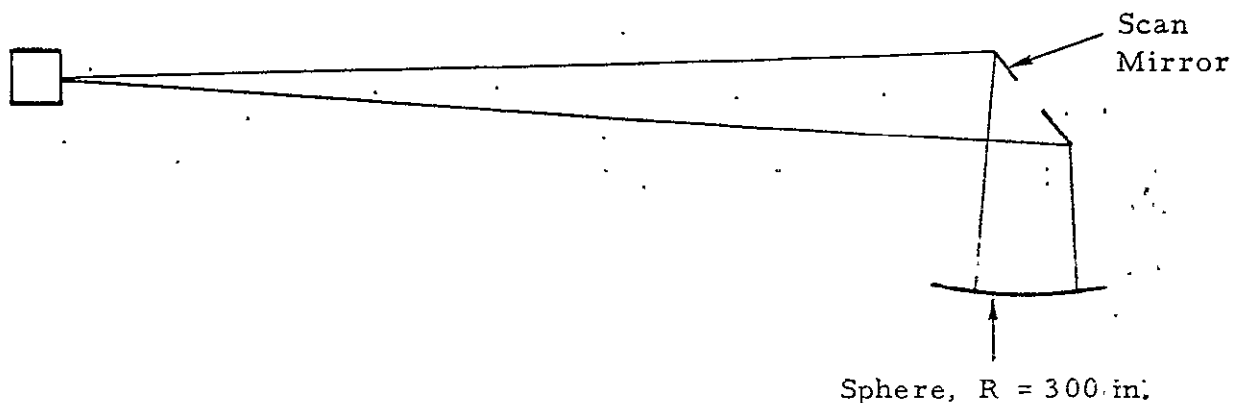


Figure 3-94. Ritchey Test, Scan Mirror

setup; i. e., minimum restraints. The interferogram indicated a scan mirror surface deviation from flatness of $< \lambda/5$.

Interferograms were taken of the primary mirror supported loosely in VISSR hardware and with it in turn supported firmly. No appreciable wavefront deformations were observed.

The same basic image quality measurements were made in Class I configuration as done in Class II configuration. The principal difference involved was that the SBRC collimator ($f/6$, EFL = 108.2 inches) was used rather than the Perkin-Elmer 218-inch focal length collimator.

Figures 3-95 and 3-96 illustrate typical interferograms on-axis and 1.6 mr off-axis, respectively, for Class I configuration.

The Class I wavefront deformation specification requires the assembled optical system to have a wavefront deformation less than $3\lambda/4$ for all field angles of 1.6 mr or less where $\lambda = 0.6$ micron.

Figures 3-95 and 3-96 indicate that the Class I measured maximum wavefront deformation is of the order of $\lambda/2$.

Figure 3-97 gives equivalent curves for Class I measurements as Figure 3-93 did for Class II measurements. Curve A is the VISSR optical system Class I specification requirements. Curve B is the Class I measurements. Curve C is the test equipment calibration function. Curve D is the Class I measurements corrected for effects of the test equipment.



Figure 3-95. Interferograms, On-Axis,
Class I Test Configuration



Figure 3-96.. Interferograms, 1.6 mr, Off-Axis,
Class I Test Configuration

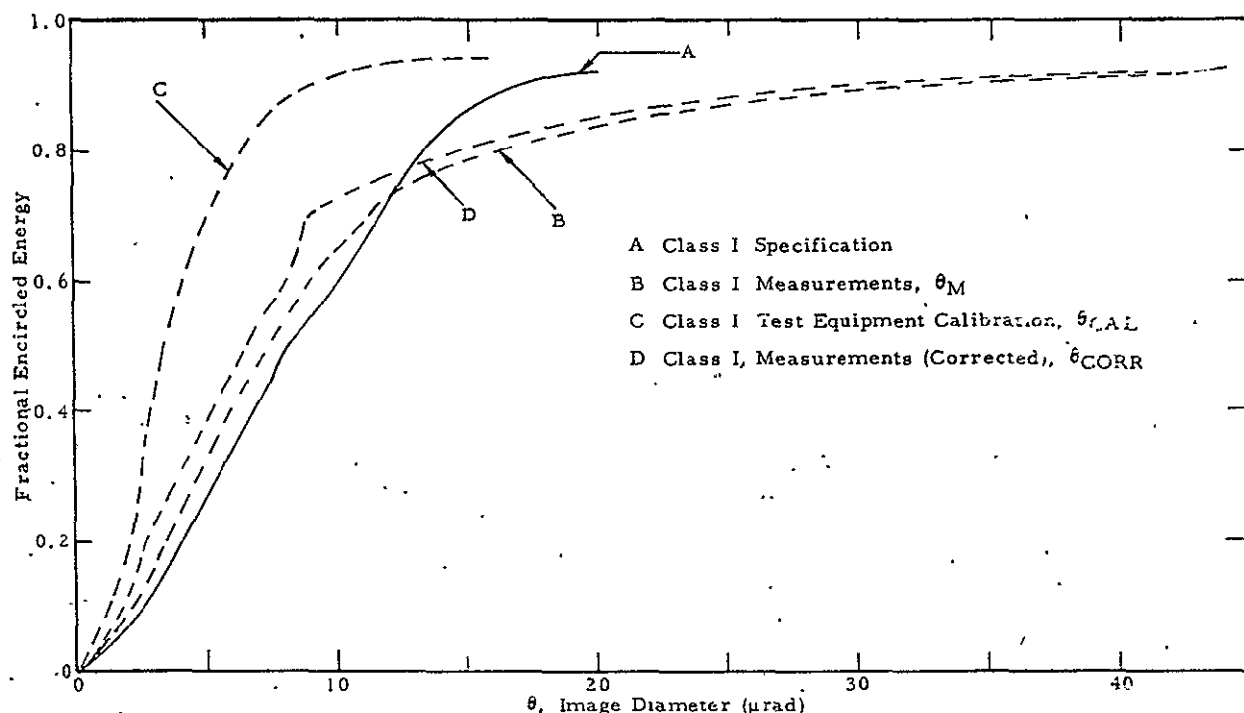


Figure 3-97. Fractional Encircled Energy as a Function of Blur Diameter, Class I Test Configuration

The corrected Class I measurements (Curve D) meet the VISSR image quality requirements (Curve A) for fractional encircled energy levels less than about 0.75. For values greater than 0.75, the Class I configuration deviates significantly from the specification.

In an effort to determine the possible cause of the Class I image measurement results, a function (θ_{CON}) was generated that converts corrected Class II into corrected Class I measurements. This function is given by

$$\theta_{CON} = \{[\mp\theta_{CORR}(\text{Class I})]^2 \pm [\theta_{CORR}(\text{Class II})]^2\}^{\frac{1}{2}}$$

Figure 3-98 illustrates the function θ_{CON} . Negative values of θ_{CON} indicate for those levels of fractional encircled energy that the Class I configuration image was smaller than Class II. The second curve labeled, $\theta_{CON}(\text{Spec})$, is the function required to convert the specification Class II values to Class I values.

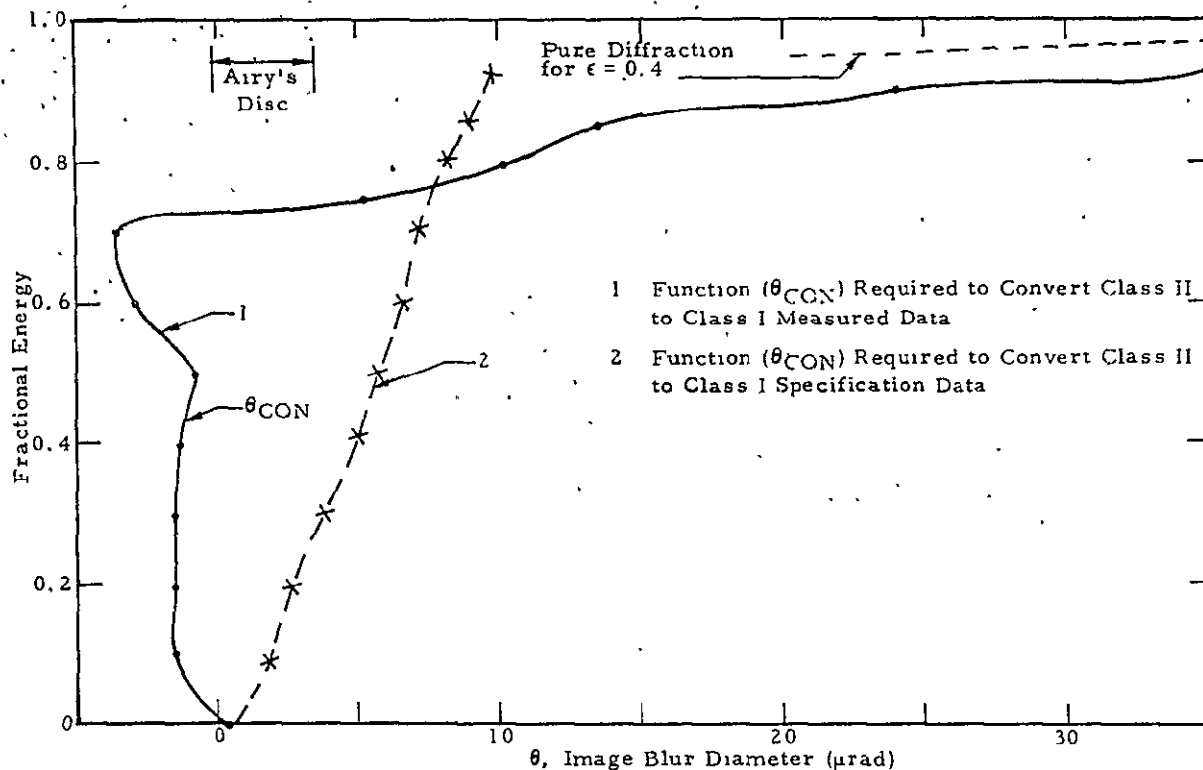


Figure 3-98. Function θ_{CON} Which Converts Class II Fractional Encircled Energy to Class I Fractional Encircled Energy Data

It appears that the alignment of the optical system was more optimum for the Class I configuration as compared to the Class II configuration. This could result in the improved "hard central core." During the VISSR design phase, it was assumed that mounting the optical system in VISSR beryllium hardware would result in some image degradation. However, a reasonable theory has not been found which would attribute the Class I image low level skirts to the VISSR mountings and yet permit the major portion of the energy to be contained in a small image.

It does appear possible that the measured low level skirts could be associated with scattering effects. The scattering effects might be associated with the test equipment.

ENGINEERING MODEL OPTICAL SYSTEM TESTS

General

Engineering Model optical alignment and tests have been completed during this reporting period. The following listed activities are discussed in detail.

1. Initial Channel Alignment of the VISSR per SBRC Procedure 19145.
2. Field-of-View Measurements, VISSR/SMS, per SBRC Procedure 19181.
3. Relative Spectral Response, VISSR/SMS, per SBRC Procedure 19147.
4. Primary Laboratory Modulation Transfer Function Measurements, VISSR/SMS, per SBRC Procedure 19146.
5. Reference Mirror Alignment Measurements per SBRC Procedure 19148.

Alignment and optical system measurements served the following purposes:

1. Permitted validation of test procedures prior to release so that corrected versions of these procedures will be available for testing the Prototype Model.
2. Disclosed VISSR optical problem areas and determined satisfactory solutions.
3. Defined VISSR optical parameters sufficiently accurate to uncover possible problem areas associated with subsequent environmental testing.
4. Provided data so that Engineering Model functioning can be compared to VISSR design parameters.

The stability of the 18-inch diameter SBRC collimator was not adequate to measure certain VISSR alignment parameters within the specified quantities. Measurements were made with the unmodified SBRC collimator because of

schedule constraints. Subsequently, the collimator base was modified to improve the measurement capability.

Relative spectral response data for the visible channels were correlated with the PMT relative spectral response data and disclosed that electronic channels were labeled differently from the optical components on the Engineering Model. Differences are tabulated as follows:

Electronic Channel No.	8	7	6	5	4	3	2	1
Optical Channel No.	1	2	3	4	5	6	7	8

All Engineering Model data contained in this section use the electronic channel identification number.

Initial Channel Alignment of the VISSR

During the channel alignment it was noted that the thermal detectors' array was rotated by 90° . Figure 3-99 indicates the correct thermal-to-visible channels alignment. Figure 3-100 illustrates the Engineering Model configuration.

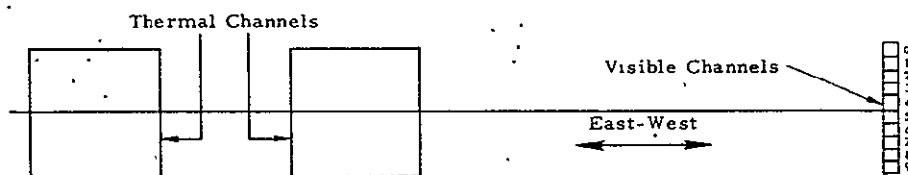


Figure 3-99. Proper Orientation of the Visible and Thermal IGFOVs

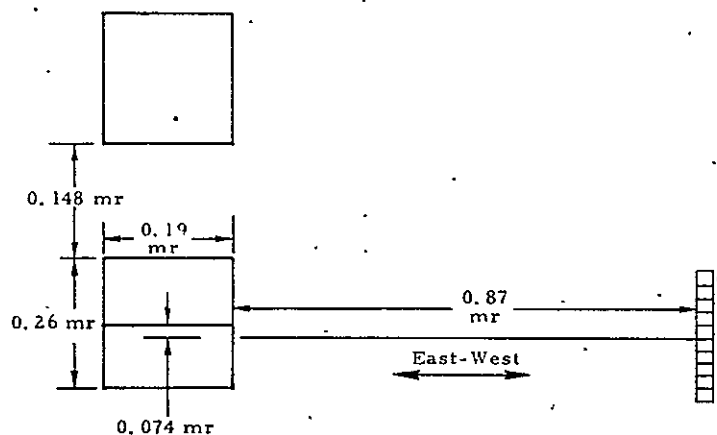


Figure 3-100. Orientation of the VISSR Engineering Model Visible and Thermal IGFOVs

The mechanism used to position the radiation cooler (including thermal detector) to the visible channel functioned adequately. However, it was a delicate, time consuming operation to tighten the radiation cooler without losing optical alignment in the process. The techniques used were adequate, but because of schedule considerations the thermal channel was not aligned to the values specified in SBRC Procedure 19145. Figure 3-100 illustrates the alignment achieved.

The two end illuminated fibers (0 and 9) were used as the visible channel alignment reference rather than Channels 4 and 5 as indicated in SBRC Procedure 19145. This change was appropriate because of effects associated with the SBRC collimator instability. It is expected that the alignment accomplished after modifications to the SBRC collimator have been completed will be made in accordance with the SBRC Procedure.

After optical alignment of the thermal detectors, the radiation cooler was removed and epoxied in accordance with the requirements of SBRC drawing 44345. After reassembly a check of optical alignment was made. It was found to be the same within 20 μ rad. The SBRC collimator instability resulted in data spread of the same order.

Field-of-View (FOV) Measurements

The VISSR Engineering Model FOV measurements were made in accordance with SBRC Procedure 19181 with the following exceptions.

A simpler technique (relative to paragraph 3.3.3, SBRC Procedure 19181) of aligning the alignment microscope to the SBRC collimator was used. SBRC collimator basic instability precluded exhaustive studies of other potential instability (paragraph 3.5.8). Indicated procedures for other instability parameters will be used during prototype measurements. The SBRC collimator will be modified and will have a significantly more stable platform. At the time the Engineering Model FOV measurements were made, the VISSR noise level was higher than expected and this limited the FOV "skirt" measurements. Figure 3-101 is a simplified block diagram of the FOV measurement equipment setup.

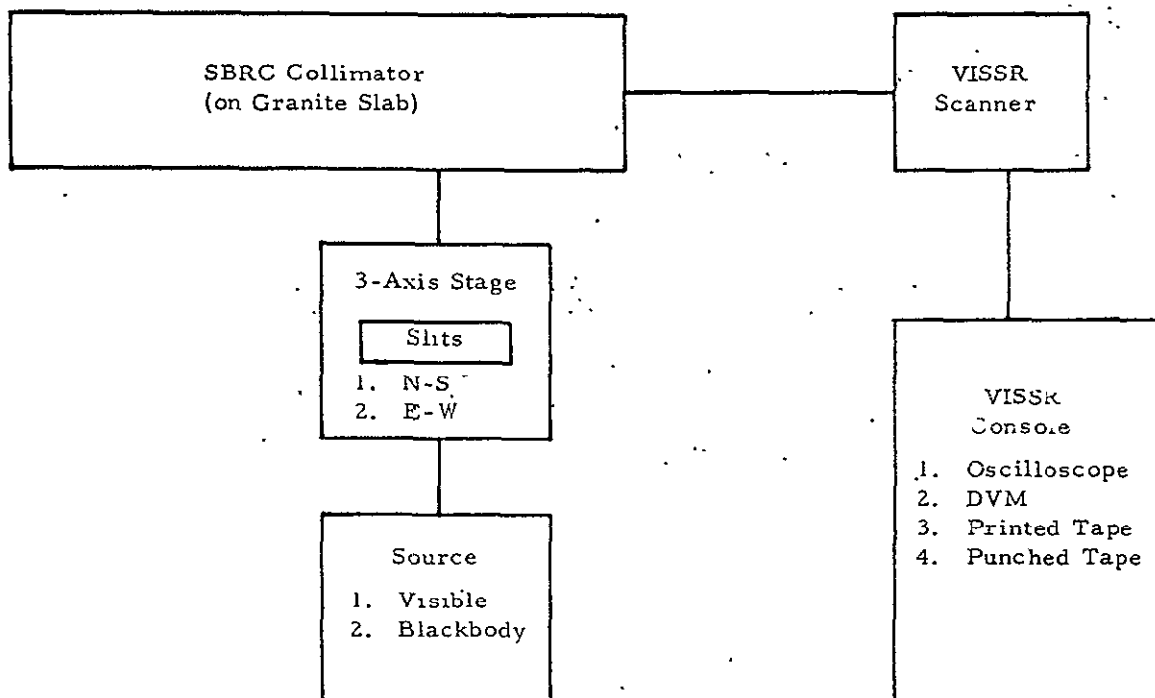


Figure 3-101. FOV Measurement Equipment Setup,
Simplified Block Diagram

Graphic and tabular data for Engineering Model FOV tests are contained in Part 1, Appendix B. Tables 3-31 and 3-32 summarize data pertinent to the FOV measurements. Parameters listed are: peak signal, noise, IFOV half-width, channel center and channel separation. Channel center and channel separation are referred to the center of IFOV array. The center of the IFOV array is defined on the system optical axis. It is centered between Channels 4 and 5 in the north-south direction and is midway between the east and west half-power points for Channels 4 and 5.

The major discrepancy found in the Engineering Model optical system tests is the apparent effective size of image. It is significantly larger than the Class I measurements indicate. This subject is discussed further in the section on modulation transfer function measurements.

Table 3-31. FOV Data, North-South Scan

Channel	Peak Signal (mv)	Noise (mv)	Half-Width (μ rad)	Channel Center (μ rad)	Channel Separation (Adjacent Channels) (μ rad)
1	270	0.40	24.0	94.7	26.8
2	306	0.46	24.4	67.9	26.9
3	345	0.61	22.7	41.0	27.6
4	297	0.32	26.8	13.4	26.8
5	358	0.44	24.0	13.4	
6	--	--	--	--	--
7	404	0.34	23.0	66.5	25.9
8	248	0.37	24.9	92.4	

Table 3-32. FOV Data, East-West Scan

Channel	Peak Signal (mv)	Noise (mv)	Half-Width (μ rad)	Channel Center (μ rad)	Channel Separation (Adjacent Channels) (μ rad)
1	217	0.30	24.0	+1.85	0.00
2	248	0.36	26.8	+1.85	0.93
3	276	0.69	24.9	+0.93	0.93
4	269	0.42	24.9	0.00	0.00
5	293	0.40	24.0	0.00	
6	--	--	--	--	--
7	325	0.44	24.9	-1.85	0.00
8	302	0.31	24.0	-1.85	

Relative Spectral Response

Relative spectral response (RSR) measurements were made for the VISSR/SMS Engineering Model scanner. A Perkin-Elmer Model 16U spectrophotometer (filter-grating monochromator) was used in conjunction with the SBRC collimator for these tests. Channel outputs were monitored on the VISSR console. Data were recorded on paper tape in a form appropriate for subsequent computer reduction. Figure 3-102 is a simplified block diagram of the RSR equipment setup.

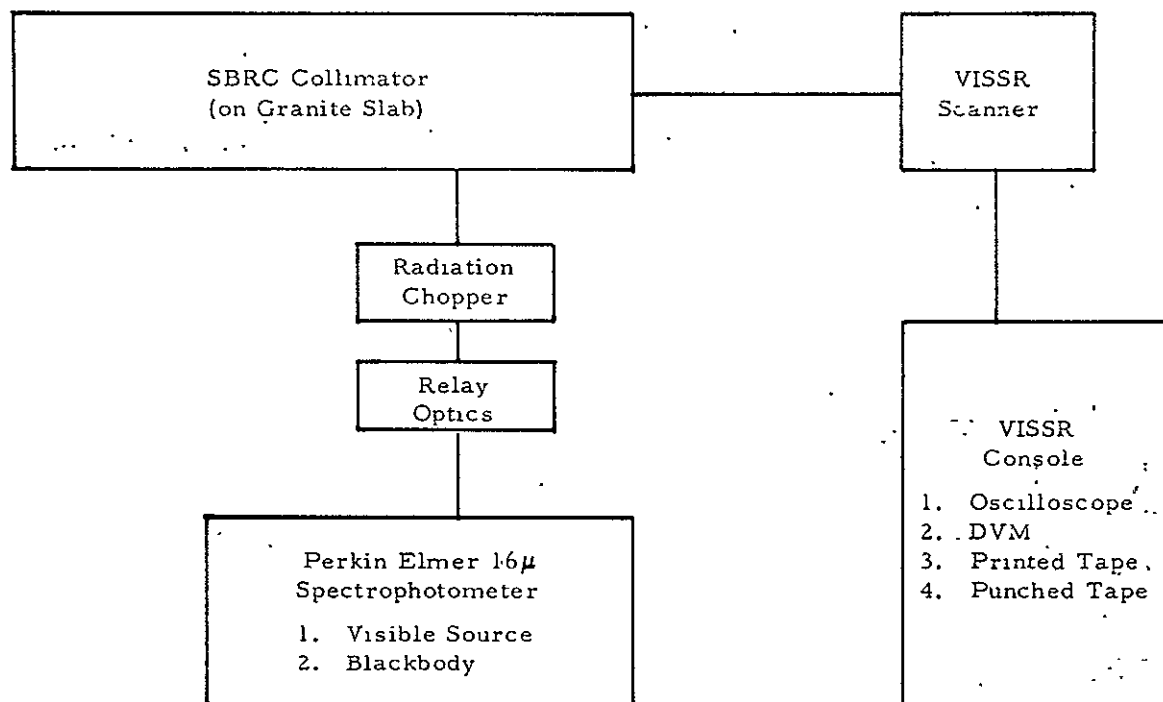


Figure 3-102. RSR Measurement Equipment Setup,
Simplified Block Diagram

Thermal Channels. - Thermal channel measurements were made using a globar radiant energy source for the spectrophotometer. A 101 ℓ/mm grating was used along with appropriate LWP filters. The following parameters are associated with the spectrophotometer for the thermal channel measurements:

1. Slit width 4 mm
2. Spectral slit width 0.12 μ
3. Globar source operating 1200°K
4. Chopping frequency 100 Hz with an electrical bandpass of 20 Hz

The relative spectral response was calculated using the following expression:

$$R(\lambda)_{\text{VISSR}} = \frac{S(\lambda)_{\text{VISSR}} \cdot \rho(\lambda)_{\text{16U}}}{\rho(\lambda)_{\text{Coll}} \cdot \rho(\lambda)_{\text{Relay}} \cdot S(\lambda)_{\text{TC}}} R(\lambda)_{\text{TC}}$$

where $R(\lambda)_{\text{VISSR}}$ = Relative spectral response of VISSR thermal channel
 $R(\lambda)_{\text{TC}}$ = Relative spectral response of PE16U radiation thermocouple
 $S(\lambda)_{\text{VISSR}}$ = VISSR signal as a function of wavelength
 $S(\lambda)_{\text{TC}}$ = Thermocouple signal as a function of wavelength
 $\rho(\lambda)_{\text{Coll}}$ = SBRC collimator (two mirrors) spectral reflectance
 $\rho(\lambda)_{\text{Relay}}$ = Relay optical system (two mirrors) spectral reflectance
 $\rho(\lambda)_{\text{PE16U}}$ = PE 16U thermocouple optics (two mirrors) spectral reflectance

NOTE: $R(\lambda)_{\text{TC}}$ is essentially constant over the $8 \leq \lambda \leq 14 \mu\text{m}$ region.

$\rho(\lambda)_{\text{PE16U}}$ spectral reflectance for spectrophotometer internal mirrors is flat over $8 \leq \lambda \leq 14 \mu\text{m}$ region.

$\rho(\lambda)_{\text{Coll}}$, $\rho(\lambda)_{\text{Relay}}$ employ Al with an overcoat of SiO. Spectral reflectance is assumed flat over $8 \leq \lambda \leq 14 \mu\text{m}$ region.

Results of the measurements for the two thermal channels are given in Figures 3-103 and 3-104.

Visible Channels. - Visible channel measurements were made using a tungsten filament source for the spectrophotometer. A 1440 ℓ/mm grating was used along with appropriate LWP filters. The following parameters are associated with the spectrophotometer for the visible channel measurements:

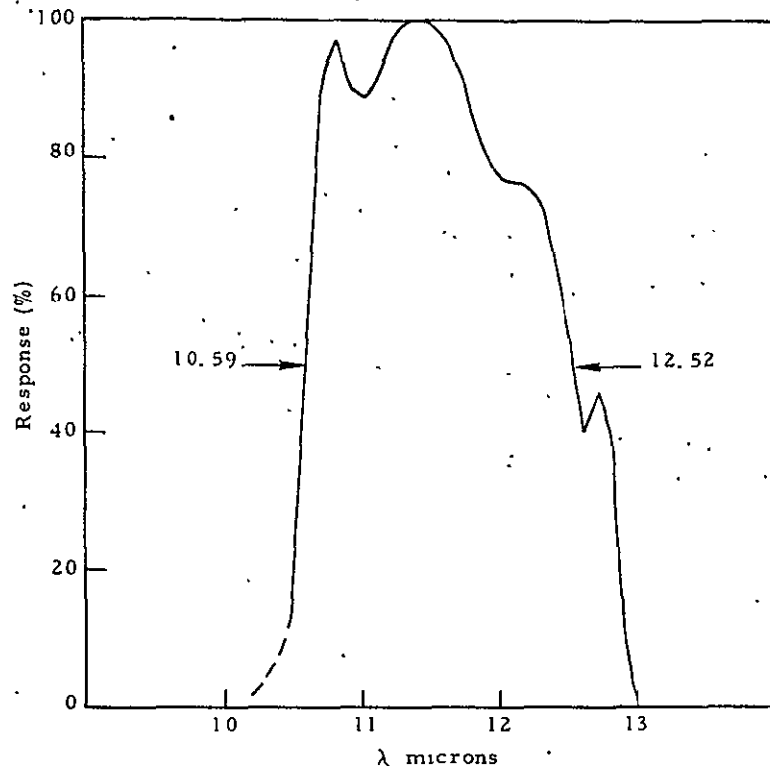


Figure 3-103. Thermal Channel 1 Relative Spectral Response

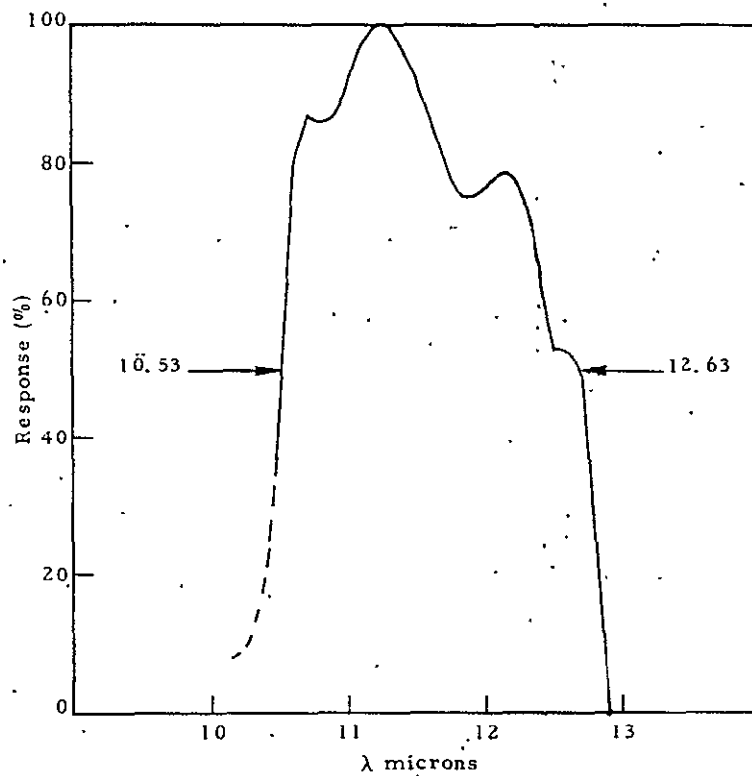


Figure 3-104. Thermal Channel 2 Relative Spectral Response

- | | |
|--|---|
| 1. Slit width | 2 mm |
| 2. Strip filament lamp
operating at | $\approx 2700^{\circ}\text{K}$ |
| 3. Grating | 1440 ℓ/mm |
| 4. Chopper frequency | 100 Hz with electrical bandpass of
20 Hz |
| 5. Spectral slit width | 0.004 μ |

The relative spectral response was calculated using the following expression:

$$\frac{R(\lambda)}{\text{VISSR}} = \frac{\frac{S(\lambda)}{\rho(\lambda)} \cdot \frac{\text{VISSR}}{S(\lambda)}}{\frac{\text{Coll}}{\text{SiPD}}} \cdot \frac{R(\lambda)}{\text{SiPD}}$$

where $\frac{R(\lambda)}{\text{VISSR}}$ = Relative spectral response of VISSR

$\frac{R(\lambda)}{\text{SiPD}}$ = Relative spectral response of silicon photodiode standard detector

$\frac{S(\lambda)}{\text{VISSR}}$ = VISSR signal as a function of wavelength

$\frac{S(\lambda)}{\text{SiPD}}$ = Silicon photodiode signal as a function of wavelength

$\frac{\rho(\lambda)}{\text{Coll}}$ = SBRC collimator (two mirrors) spectral reflectance

Graphic and tabular data for Engineering Model RSR tests are contained in Part 2, Appendix B.

Modulation Transfer Function Measurements

The modulation transfer function (MTF) was measured for both visible and thermal channels under ambient laboratory conditions. VISSR MTF was measured in two orthogonal directions corresponding to the east-west and north-south directions. Equipment and procedures used in these measurements are those defined in SBRC Procedure 19146. Figure 3-105 is a simplified block diagram of the MTF test setup.

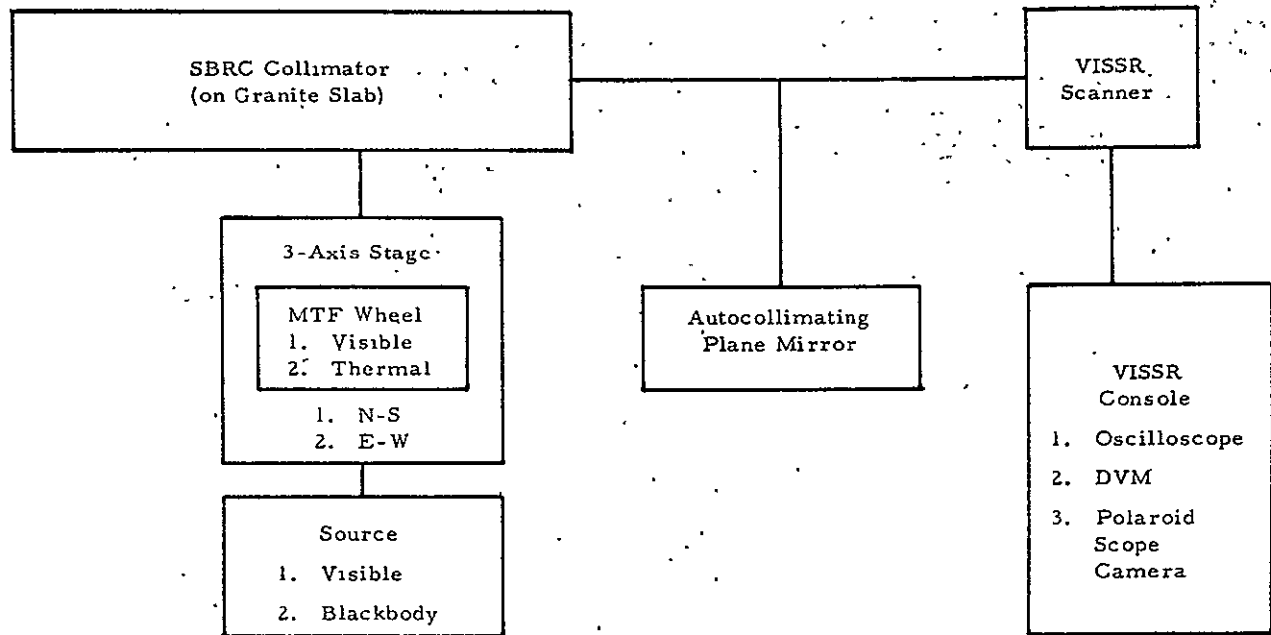


Figure 3-105. MTF Measurement Equipment Setup,
Simplified Block Diagram

The principal deviation from the procedure is with respect to data format. Oscilloscope traces of the MTF pattern were made rather than digital recording on tape with subsequent computer reduction. Oscilloscope traces will be used on following measurements.

Figures 3-106 and 3-107 illustrate modulation versus spatial frequency for the visible and thermal channels, respectively. The curves contained in these two figures are computed square-wave modulation with no modification due to electronics. Three computed curves are given for visible channel MTF. See Figure 3-106. These curves are Class I specification $+21 \mu\text{r}$ IGFOV, Class I specification $+25 \mu\text{r}$ IGFOV, and $25\text{-}\mu\text{r}$ diameter blur assuming cosine intensity distribution $+25 \mu\text{r}$ IGFOV. Two computed curves are given for thermal channel MTF. See Figure 3-107. These curves are diffraction $+200 \mu\text{r}$ IGFOV and diffraction $+250 \mu\text{r}$ IGFOV. Diffraction data were computed, based on an optical diameter of 16 inches with a 0.4-inch central obscuration. A wavelength of 11.5μ was used.

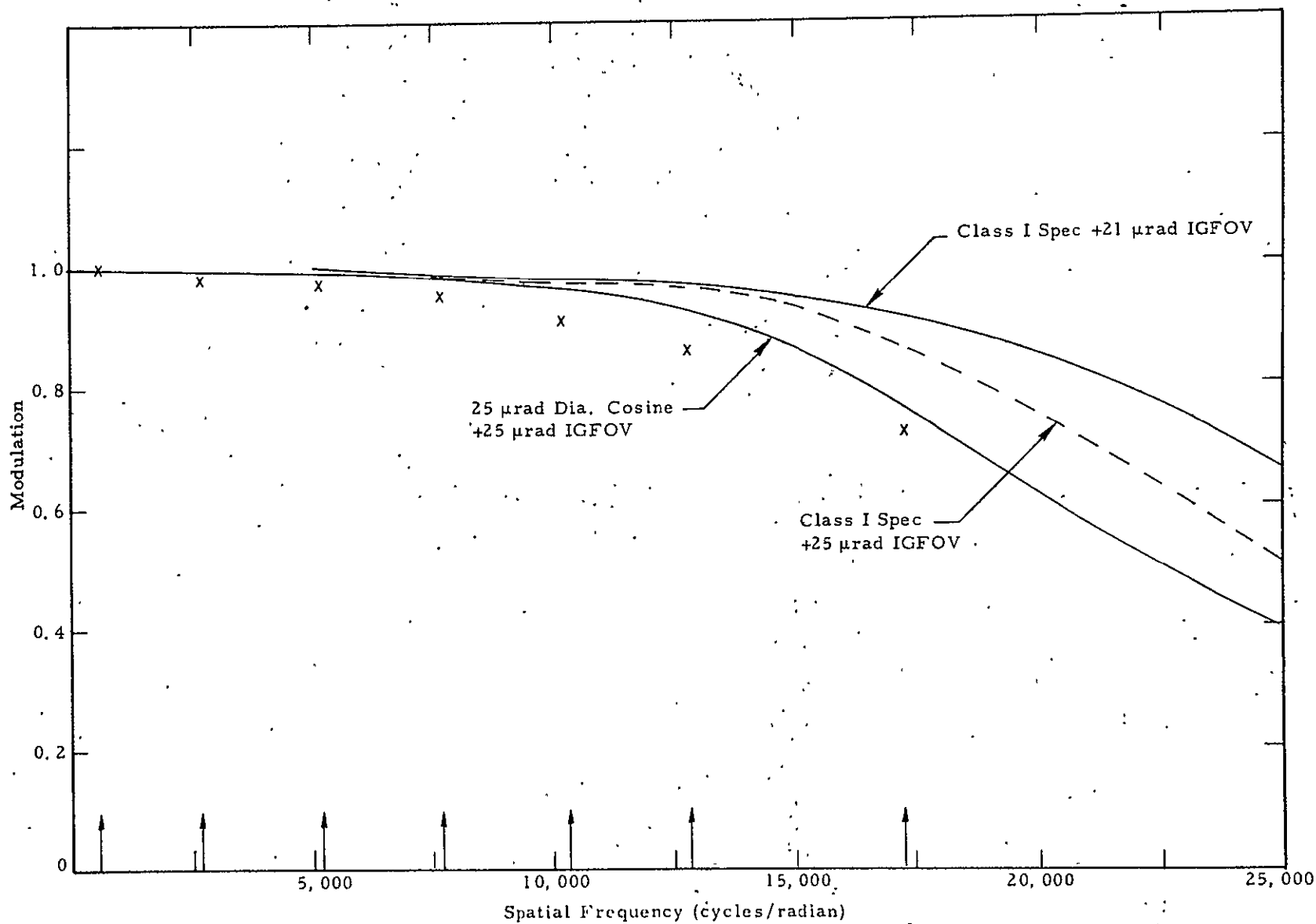


Figure 3-106. Visible Channel Modulation Transfer Function - Engineering Model

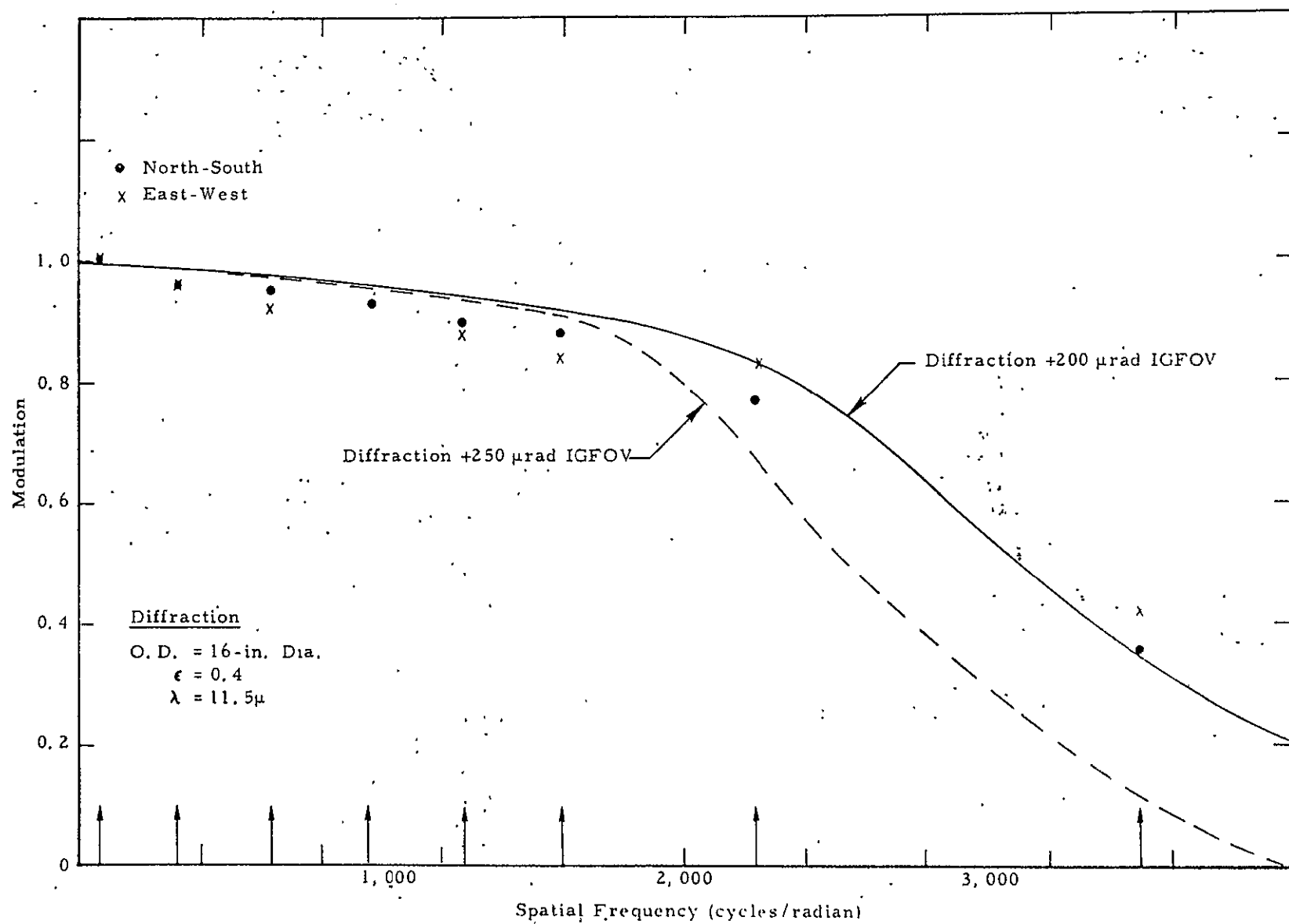


Figure 3-107. Thermal Channel Modulation Transfer Function

The spatial frequencies at which MTF values were measured are listed in Table 3-33 and are shown on Figures 3-106 and 3-107 as arrows perpendicular to the abscissa.

Table 3-33. Spatial Frequencies

Visible Channel (cycles/radian)	Thermal Channel (cycles/radian)
510	65.4
2550	318
5100	628
7640	955
10200	1272
12720	1590
17200	2230
25000	3500

Analysis of visible channel MTF and FOV data indicates an apparent image blur that is significantly larger than that measured on the Engineering Model optical system Class I acceptance tests. Engineering Model optical system tests are consistent with assuming an image of the order of 20 to 25 μ r in diameter with a cosine intensity distribution. In Class I acceptance tests, the measured image diameter containing 85% and 90% of the total energy was 20 and 30 μ r, respectively.

The VISSR Engineering Model fiber optics assembly has appreciable delamination effects in the fiber/epoxy/prism interface at the focal plane. Since this is the principal known difference between VISSR Engineering Model and the Protoflight optics and the Protoflight does not exhibit anomalous image degradation, it is presumed that the delamination causes the image degradation.

Reference Mirror Alignment Measurements

Objectives. - Alignment and measurement objectives are as specified in SBRC Procedure 19148. These objectives are:

The distance from the fiducial lines reference point on primary alignment reference mirror PARM-1 to the YZ plane and the distance from the fiducial lines reference point on primary alignment reference mirror PARM-2 to the XZ plane shall be measured and recorded with an accuracy of 0.003 inch (Paragraph 3.2.1).

The angular alignment of PARM-1 and PARM-2 to the VISSR mounting plane (XY) shall be measured and recorded with an accuracy of 0.001 radian (Paragraph 3.2.2).

The scan mirror angle with respect to VISSR optical axis shall be positioned to 45° location (nearest step) and measured with an accuracy of 10^{-5} radian (Paragraph 3.2.3).

The angular alignment of the VISSR optical axis (including the scan mirror) to PARM-1 will be measured with an accuracy of 10^{-5} radian (Paragraph 3.2.4).

The angular alignment of the VISSR optical axis (excluding scan mirror) to two nominally orthogonal primary alignment reference mirrors (PARM-1 and PARM-2) will be measured with an accuracy of 10^{-5} radian (Paragraph 3.2.5).

The angular alignment of secondary alignment reference mirror SARM-2 to PARM-2 will be measured with an accuracy of 10^{-5} radian (Paragraph 3.2.6).

Paragraph 3.2.1 Alignment Requirements. - The distance from the fiducial lines reference point on PARM-1 to the YZ plane is 0.024 inch. The PARM-1 cross hair is 0.024 inch on the -X axis side of the VISSR YZ plane. The corresponding distance of the PARM-2 alignment cross hair to the XZ plane is 0.041 inch. The PARM-2 cross hair is 0.041 inch on the -Y axis side of the VISSR XZ plane.

Paragraph 3.2.2 Alignment Requirements. - A difficulty became apparent in determining the angular alignment of PARM-1 and PARM-2 to the VISSR mounting surface. In the initial draft of SBRC Procedure 19148 it was assumed that the VISSR mounting surface, a plane formed by three mounting pads, was parallel to the VISSR cart surface. In actual practice VISSR mounting pads are seated on an intermediate Delrin mount. As a result, the mounting pads

are not necessarily parallel to the VISSR stainless steel ring. Measurements were made to reduce uncertainty in Engineering Model data. VISSR reference axes are illustrated in Figure 3-108.

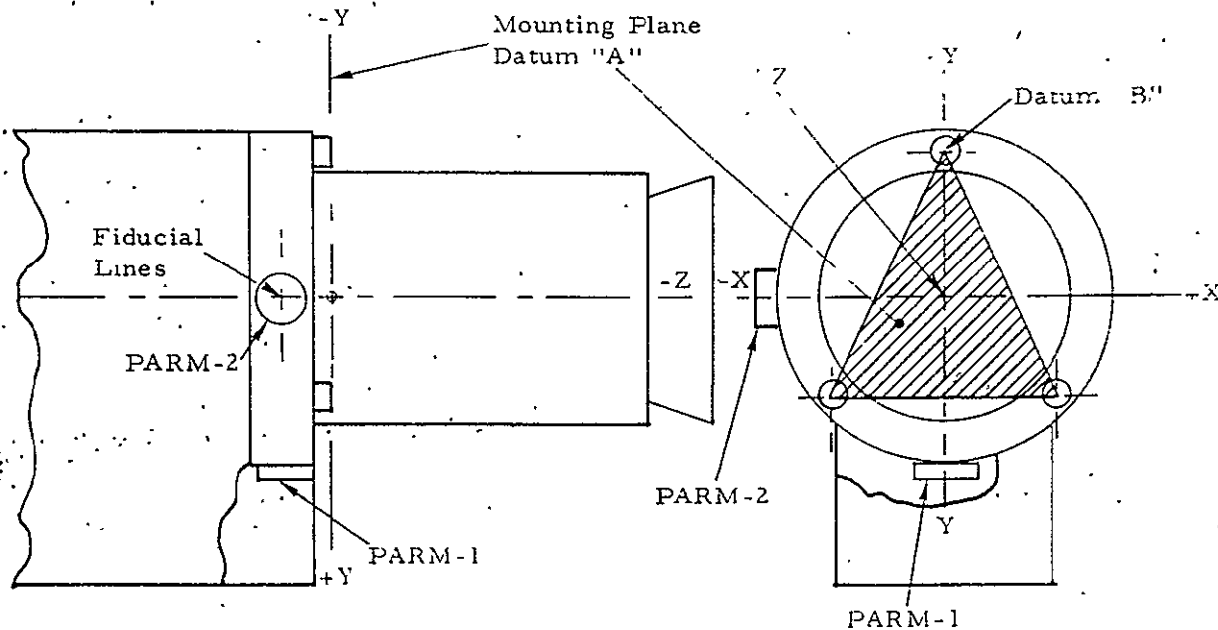


Figure 3-108. VISSR Reference Axes

The exterior angle formed by PARM-1 (nominally perpendicular to the Y axis) and the VISSR mounting plane, defined as XY plane, is $89^{\circ}54.8'$. See Figure 3-109.

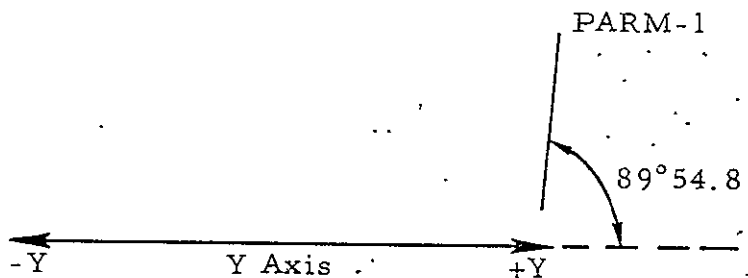


Figure 3-109. PARM-1 to Y Axis Alignment

The exterior angle formed by PARM-2 (nominally perpendicular to the X axis) and the VISSR mounting plane is $89^{\circ}59.7'$. See Figure 3-110.

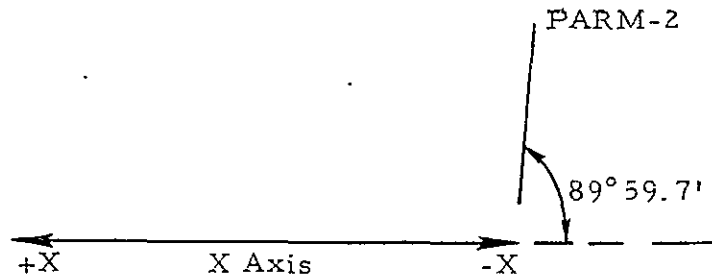


Figure 3-110. PARM-2 to X Axis Alignment

The measured angle formed by PARM-1 and the VISSR mounting plane exceeds fabrication tolerance of VISSR components. The measurement method necessitated by the Delrin intermediate mounts is believed to be causing the apparent discrepancy. Precision metal mounts will be substituted for the Delrin intermediate mounts during Prototype Model measurements.

Paragraph 3.2.3 Alignment Requirements. - The scan mirror angle with respect to the VISSR optical axis is 45° (to the nearest encoder step) when the redundant encoder is positioned at step +23. Scan mirror rotation toward encoder step +22 by $19 \mu\text{rad}$ would provide a true 45° angle with the VISSR optical axis.

With the primary encoder positioned to step -79, the scan mirror angle is 45° (to the nearest encoder step) with respect to the VISSR optical axis. Scan mirror rotation by $11.5 \mu\text{rad}$ toward encoder step -80 would provide a true 45° angle with the VISSR optical axis.

Paragraph 3.2.4 Alignment Requirements. - Angular alignment of the VISSR optical axis (including scan mirror) to PARM-1 was measured to the redundant optical encoder. With the redundant encoder set to +23 and using PARM-1 normal, the VISSR optical axis to PARM-1 normal has two angular components. In the VISSR YZ plane, the VISSR optical axis makes an angle

with the PARM-1 normal of 0.603 mrad with the VISSR optical axis pointing slightly toward the +Z axis. See Figure 3-111. In the VISSR XY plane, the VISSR optical axis makes an angle with the PARM-1 normal of 0.107 mrad with the VISSR optical axis pointing slightly toward the -X axis. See Figure 3-112.

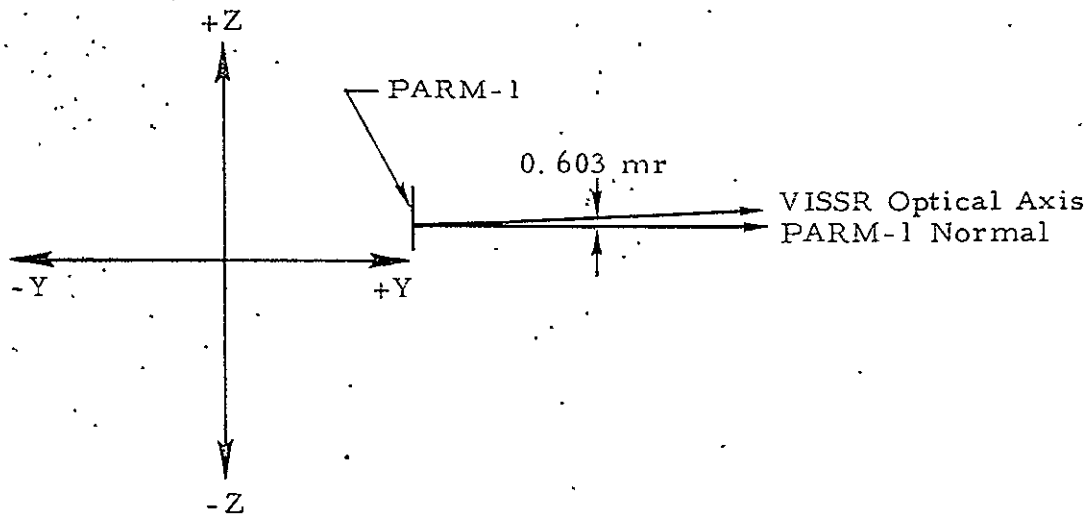


Figure 3-111. Alignment of VISSR Optical Axis to PARM-1 in YZ Plane

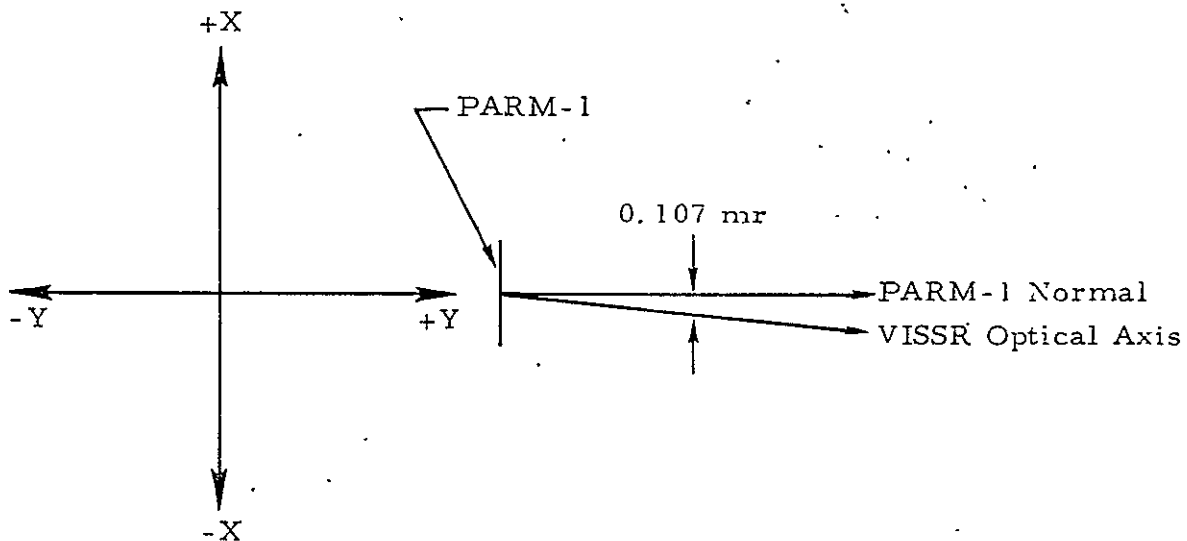


Figure 3-112. Alignment of VISSR Optical Axis to PARM-1 in XY Plane

Paragraph 3.2.5 Alignment Requirements. - The angular alignment of VISSR optical axis (excluding scan mirror) to two nominally orthogonal primary alignment reference mirrors was measured.

The angle between PARM-1 normal and the VISSR optical axis in the YZ plane is 0.656 mrad. The corresponding angle between PARM-2 normal and VISSR optical axis in the XZ plane is 0.456 mrad. See Figures 3-113 and 3-114.

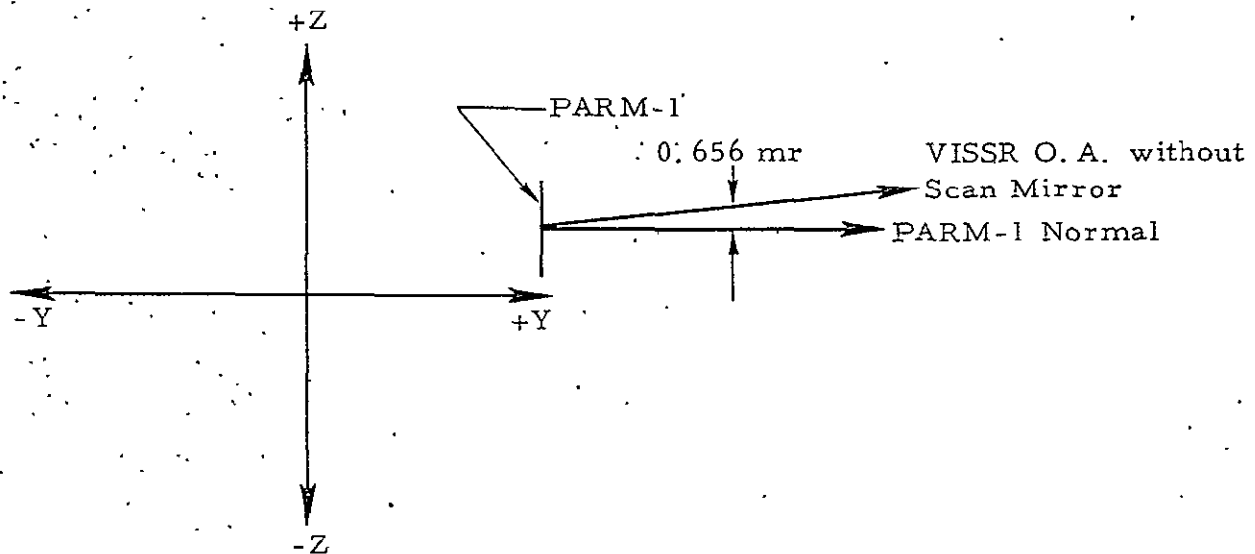


Figure 3-113. Alignment of VISSR Optical Axis (without Scan Mirror) to PARM-1 in YZ Plane

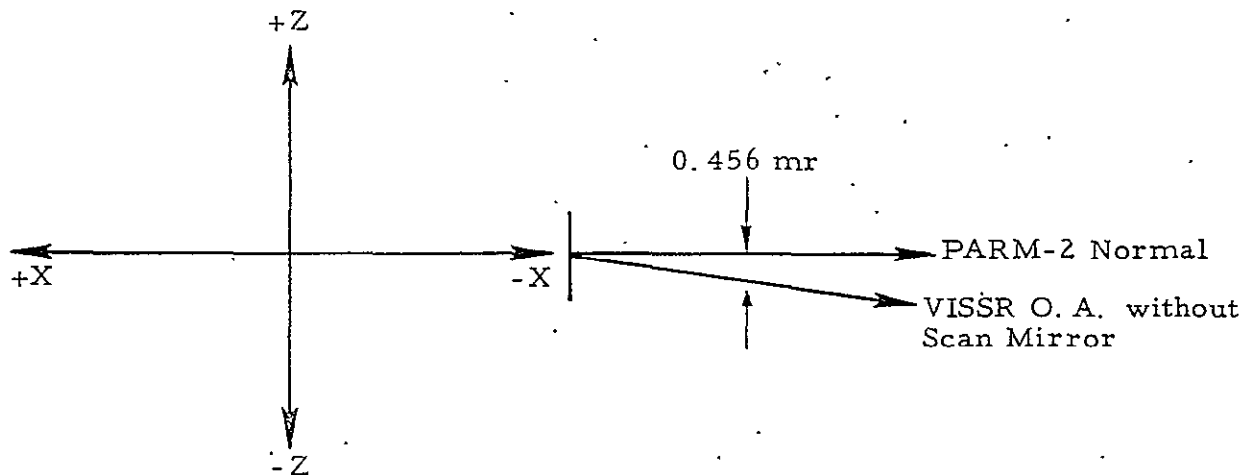


Figure 3-114. Alignment of VISSR Optical Axis (without Scan Mirror) to PARM-2 in XZ Plane

Paragraph 3.2.6 Alignment Requirements. - The angular alignment of the secondary alignment reference mirror (SARM-2) to PARM-2 was measured. Alignment in the XZ plane and XY plane is illustrated in Figures 3-115 and 3-116.

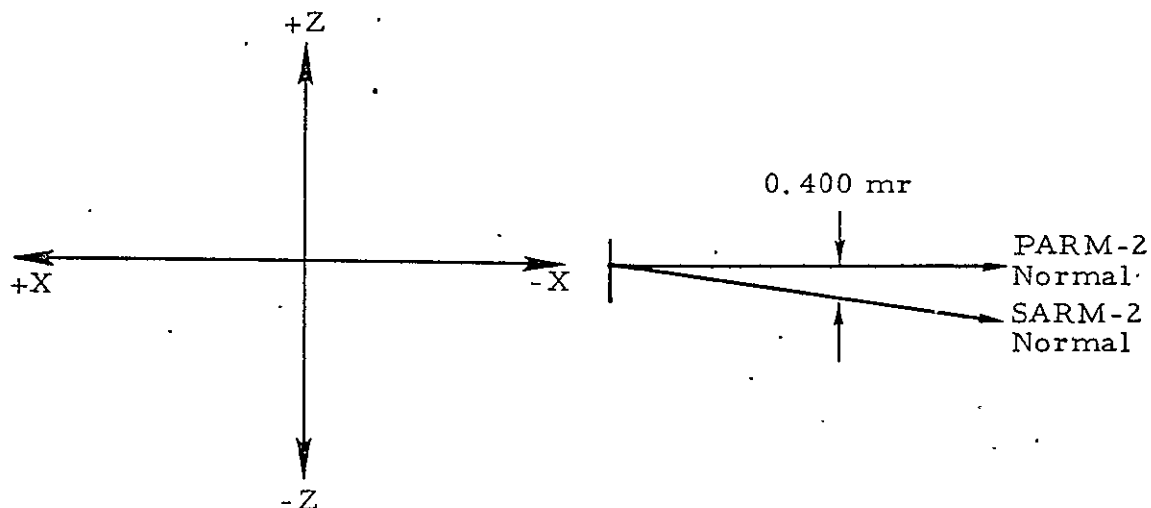


Figure 3-115. Alignment of SARM-2 to PARM-2 in XZ Plane

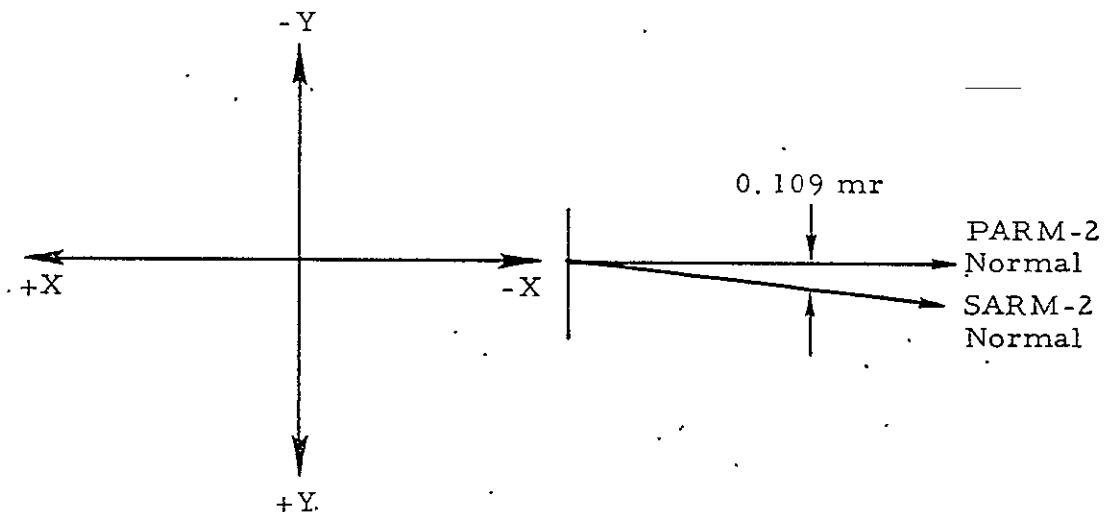


Figure 3-116. Alignment of SARM-2 to PARM-2 in XY Plane

Alignment Measurements After Environmental Testing

Check of optical alignment measurements was made on the VISSR Engineering Model after environmental testing. The measurements were made April 5-7, 1972. The coordinates used in summarizing the measurements are shown in Figure 3-108.

Angular alignment of the VISSR optical axis (including scan mirror to PARM-1) was measured for both the primary and redundant optical encoder. The primary encoder was set to -79. Figure 3-117 and Figure 3-118 illustrate optical alignment before and after environmental testing for the primary encoder.

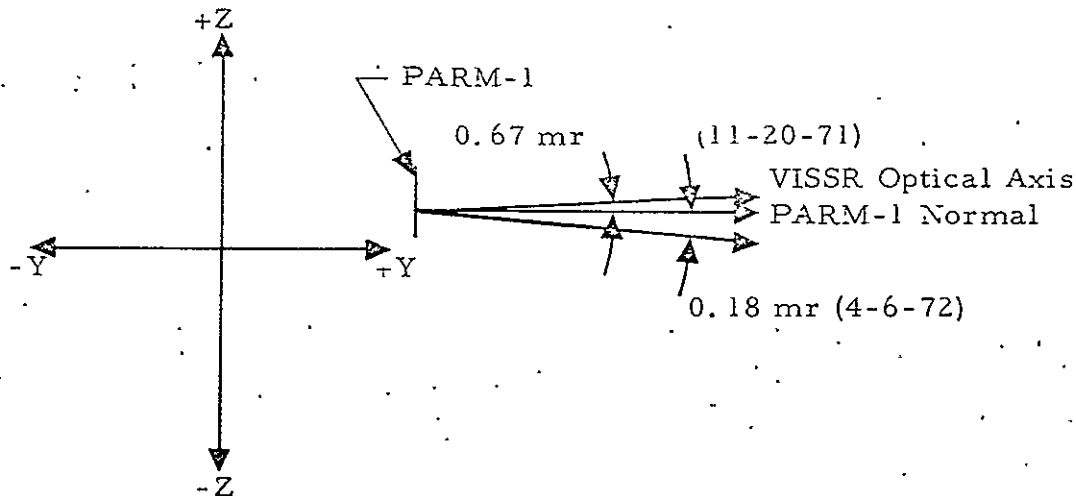


Figure 3-117. Alignment of VISSR Optical Axis to PARM-1 in YZ Plane - Primary Encoder

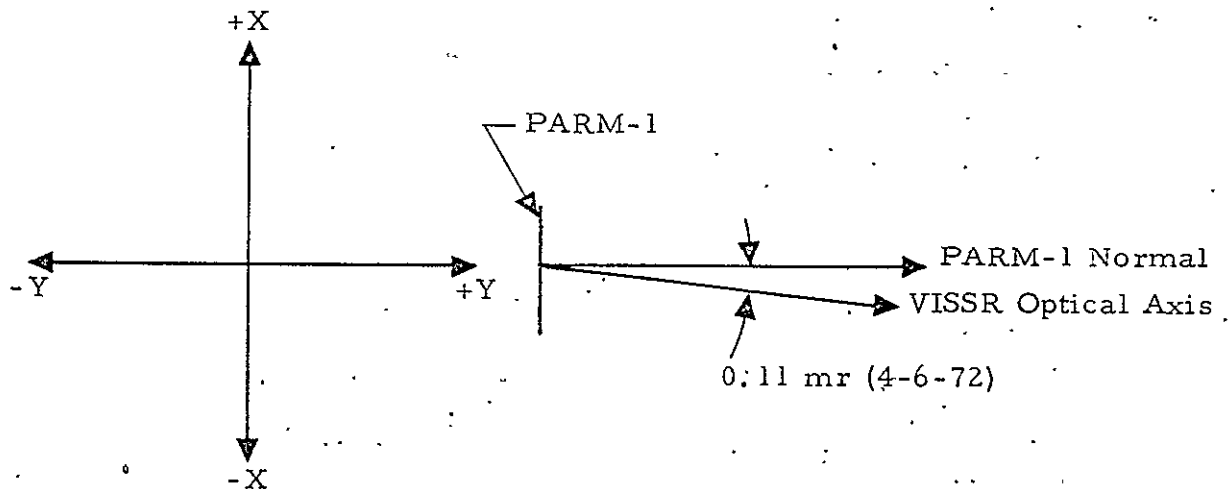


Figure 3-118. Alignment of VISSR Optical Axis to PARM-1 in XY Plane - Primary Mirror

In like manner the redundant encoder was set to +23. Figures 3-119 and 3-120 illustrate optical alignment before and after environmental testing for the redundant encoder.

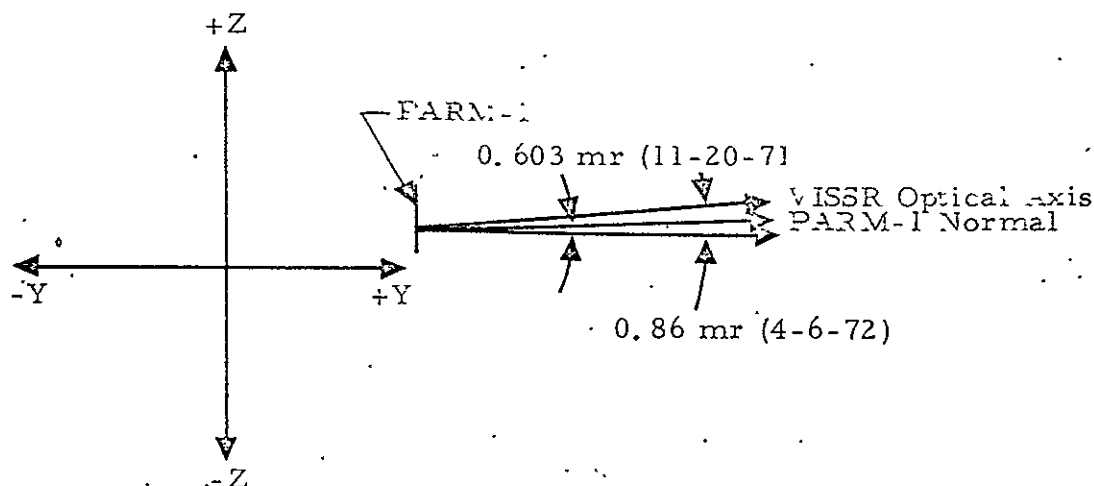


Figure 3-119. Alignment of VISSR Optical Axis to PARM-1 in YZ Plane - Redundant Encoder

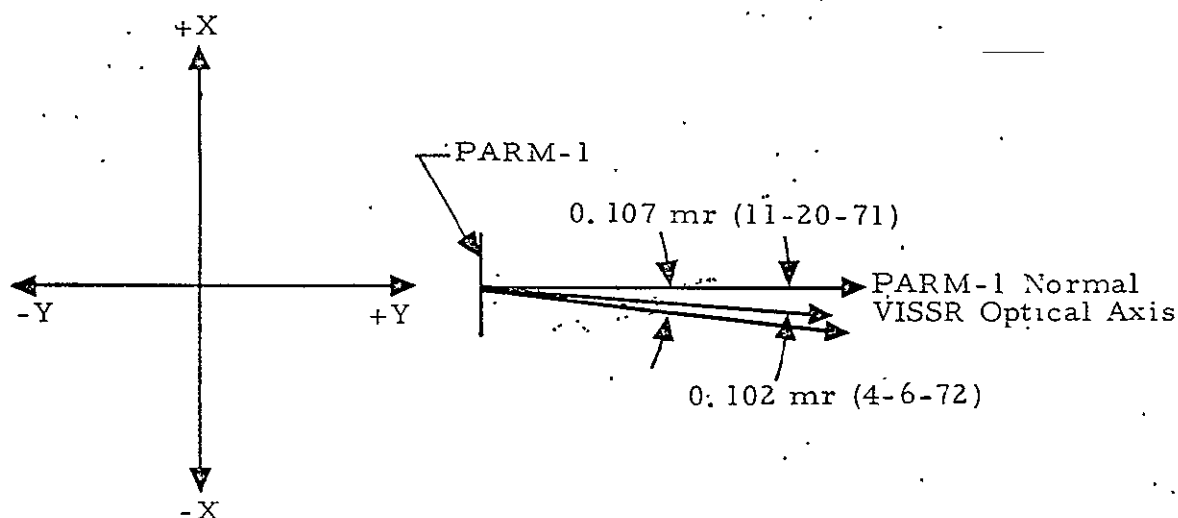


Figure 3-120. Alignment of VISSR Optical Axis to PARM-1 in XY Plane - Redundant Encoder

The alignment of VISSR optical axis via scan mirror compared to the optical axis excluding the scan mirror is illustrated in Figure 3-121. Primary encoder set at -79 was used.

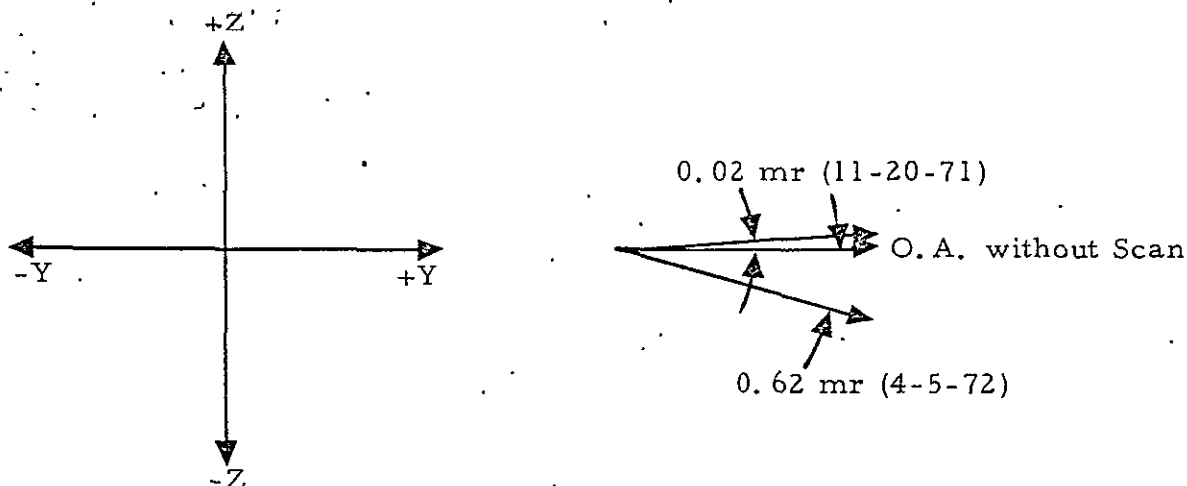


Figure 3-121. Alignment of VISSR Optical Axis With and Without Scan Mirror - Primary Encoder -79

The alignment of the VISSR optical axis, with scan mirror, compared to the optical axis excluding the scan mirror is illustrated in Figure 3-122. Redundant encoder set at +23 was used.

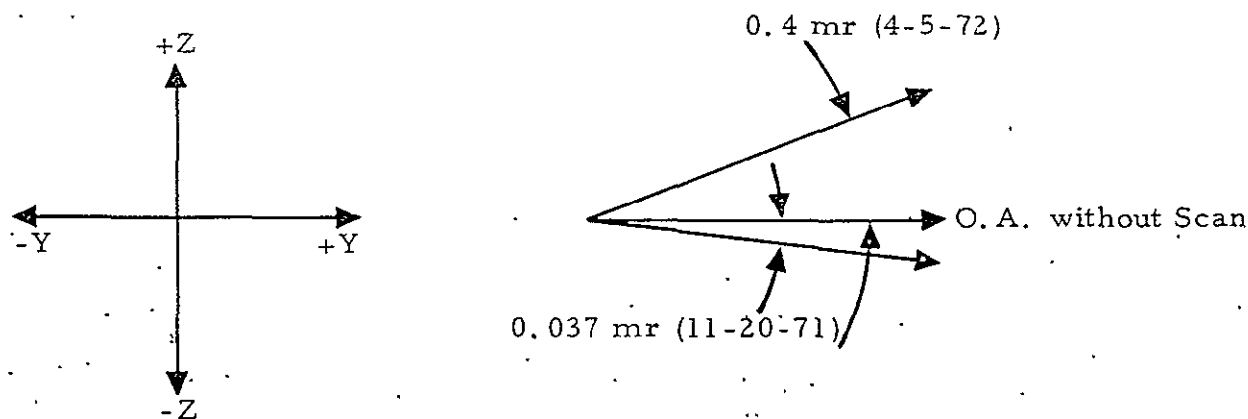


Figure 3-122. Alignment of VISSR Optical Axis With and Without Scan Mirror - Redundant Encoder +23

The optical alignment of thermal channel No. 1 with respect to VISSR optical axis (illuminated fibers) was measured and the results are graphically illustrated in Figures 3-123 and 3-124.

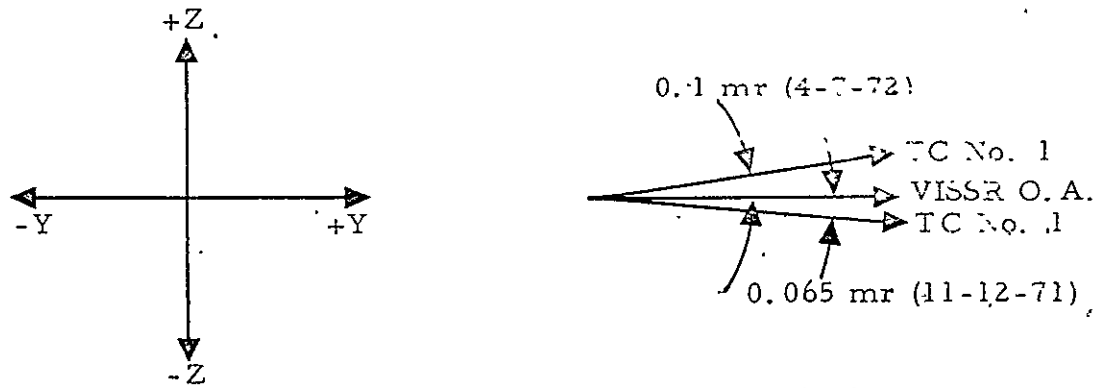


Figure 3-123. Optical Alignment of Thermal Channel No. 1 (TC No. 1) to VISSR Optical Axis - North-South Direction

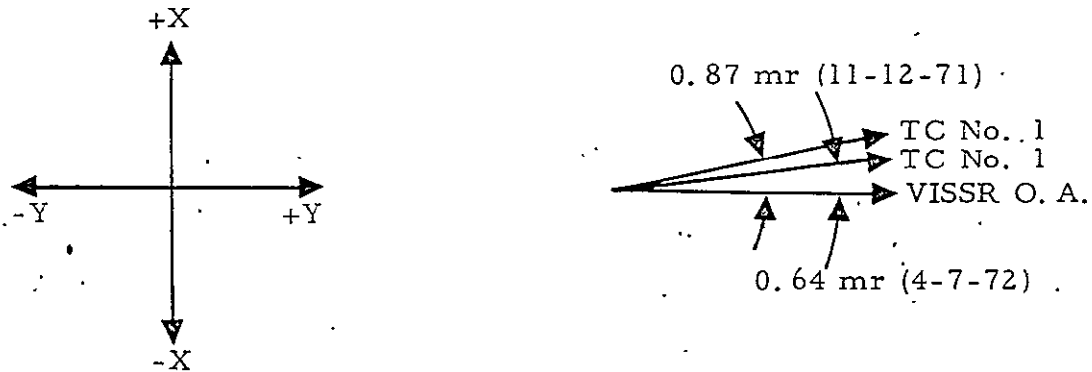


Figure 3-124. Optical Alignment of Thermal Channel No. 1 (TC No. 1) to VISSR Optical Axis - East-West Direction

The preceding optical alignment measurements indicate the following:

1. The alignment of the two scan mirror encoders with respect to the scan mirror changed by varying amounts.
 - a. RDN - Scan Mirror +0.44 mr
 - b. PRI - Scan Mirror -0.64 mr
2. The optical telescope (excluding scan mirror effects) and/or fibers with respect to primary alignment reference mirror (PARM-1) changed by -0.21 mr in the YZ plane.
3. Alignment of the thermal channel to visible channels changed by
 - a. +0.16 mr in the YZ plane
 - b. -0.23 mr in the XY plane

Probable mechanisms associated with alignment shifts are discussed as follows:

The encoder might move on its mounting bolt circle. Linear motions of 0.0011 to 0.0016 inch are required to account for the noted angular alignment changes. The encoders are not pinned and motion of this magnitude appears possible.

The telescope optical axis alignment change of 0.21 mr could be caused by secondary mirror tilt associated with linear shifts of less than 0.001 inch.

The thermal to visible channel alignment change of 0.2 mr appears too large to be associated with fiber motion which would require a linear motion of 0.023 inch. It seems unlikely that the effect is associated with radiation cooler since it was not vibrated, etc. However, a lateral shift in the thermal channel relay lenses could account for the alignment change. An alignment change of 0.23 mr is equivalent to a lateral motion of the relay lens of 0.004 inch. Relay lens assembly will be modified on the protoflight model to minimize the possible relay lens motion.

The simplified block diagram for equipment setup for alignment measurements is shown in Figure 3-125.

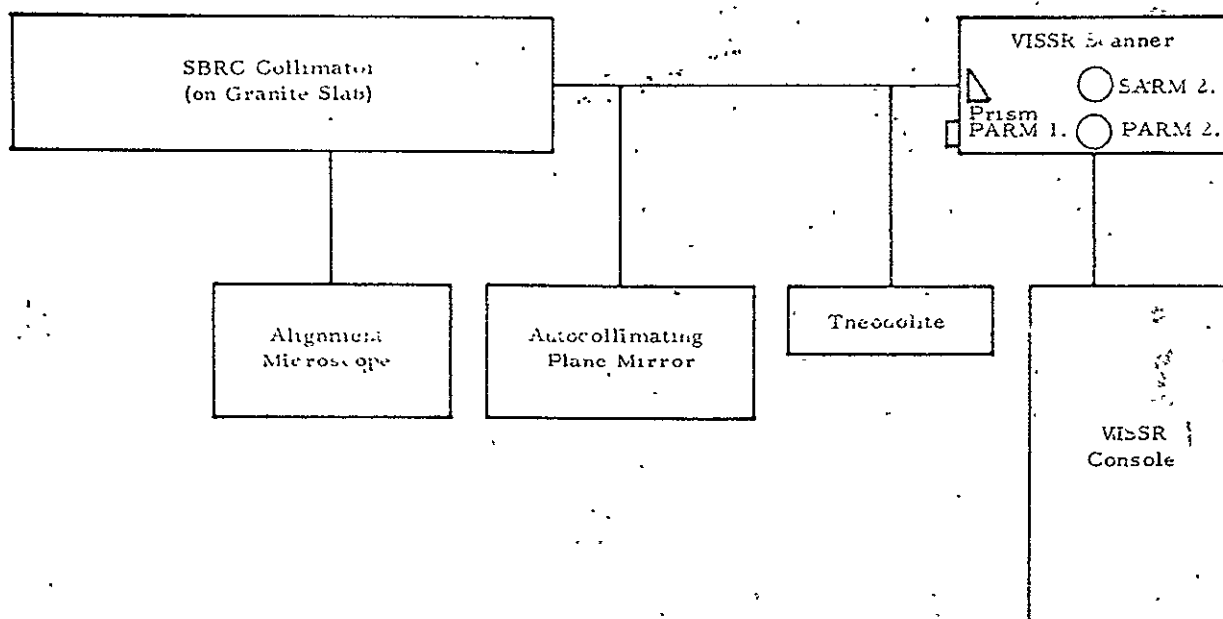


Figure 3-125. Reference Mirror Alignment Measurement Equipment Setup
Simplified Block Diagram

Scattering Light Measurements - Laser Source

During the initial VISSR engineering model solar calibration tests, the direct sun signal had very long skirts, and indeed, at times extended to the solar inflight calibrator signal. The probable cause of the skirts seemed to be scattering within the earth's atmosphere and thus not related to VISSR.

However, to verify this, an experiment was conducted in the laboratory with a small portion of the VISSR entrance aperture being irradiated with a laser beam. The laser was modulated with the Brower chopper at a frequency of 260 Hz. The signal from VISSR PMT preamplifier channel No. 1 was fed into the Princeton Applied Research HR8 lock-in voltmeter. A reference signal from the Brower chopper was also used. A neutral density filter attenuated the laser beam when it was focused directly on or near the VISSR IFOV. With the above experimental setup, the dynamic range was 5×10^8 . Noise corresponded to a relative signal level of 1.5 and was actually 1.5 μ v.

Figure 3-126 illustrates the signal falloff with angle. It is plotted as a function of scan mirror steps, where a step is equal to 0.192 mr.

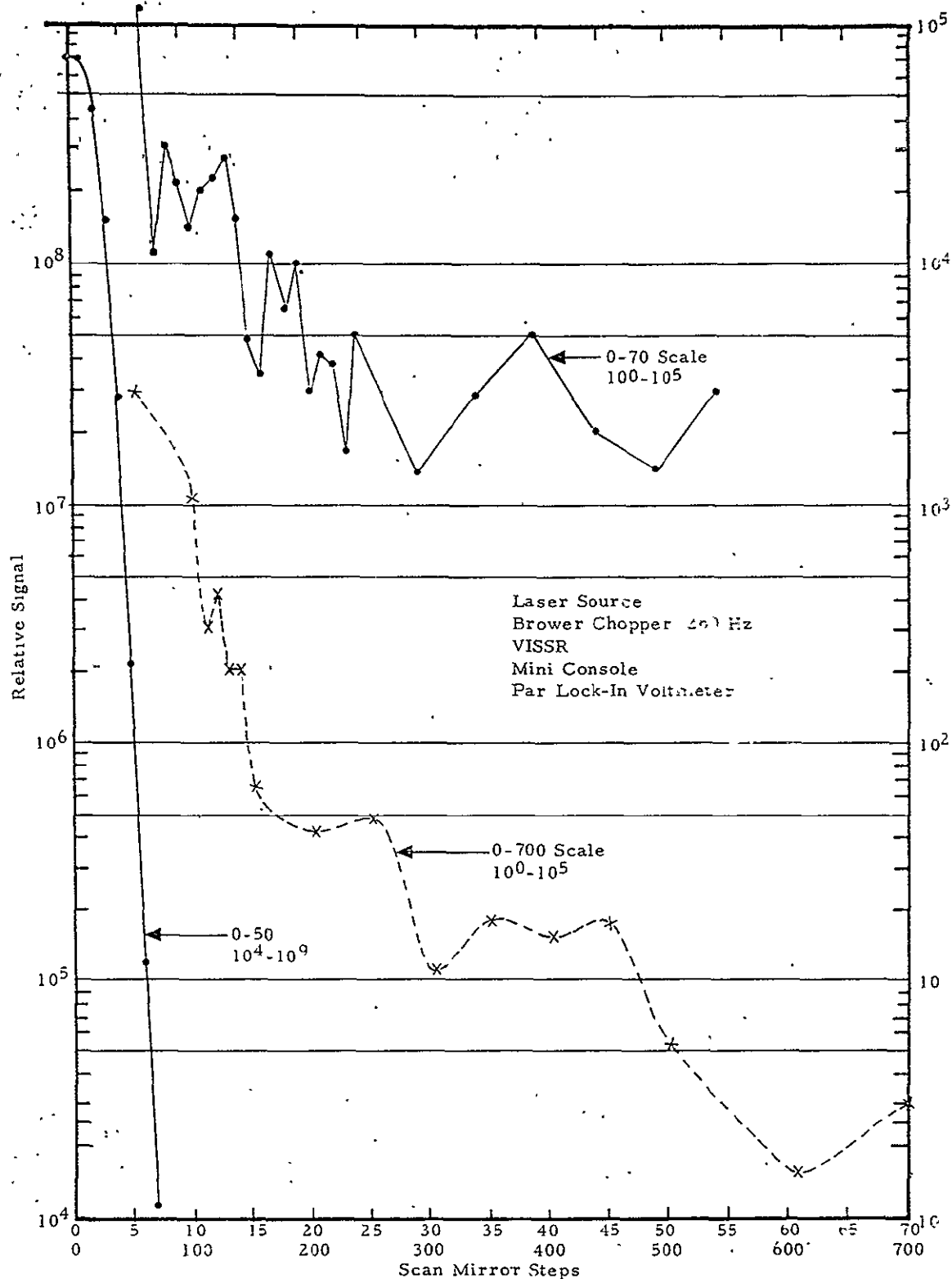


Figure 3-126. Scattered Light Using Laser Source

The graph shows that the solar calibration skirts are not due to VISSR. As indicated earlier, the probable cause is atmospheric scattering.

It should be noted that the above data do not eliminate the desirability of conducting additional scattering tests on the VISSR. Since the above measurements were made using a very small portion of the VISSR entrance aperture, they do not preclude spurious signals of solar origin.

Solar Inflight Calibrator Spurious Radiation

During the initial solar inflight calibrator calibration, a spurious signal was noted midway between the "direct" signal and the calibrator signal. Subsequent laboratory investigation using laser techniques identified the problem. Figure 3-127 illustrates the desired and spurious energy paths in P/N 46020 prism.

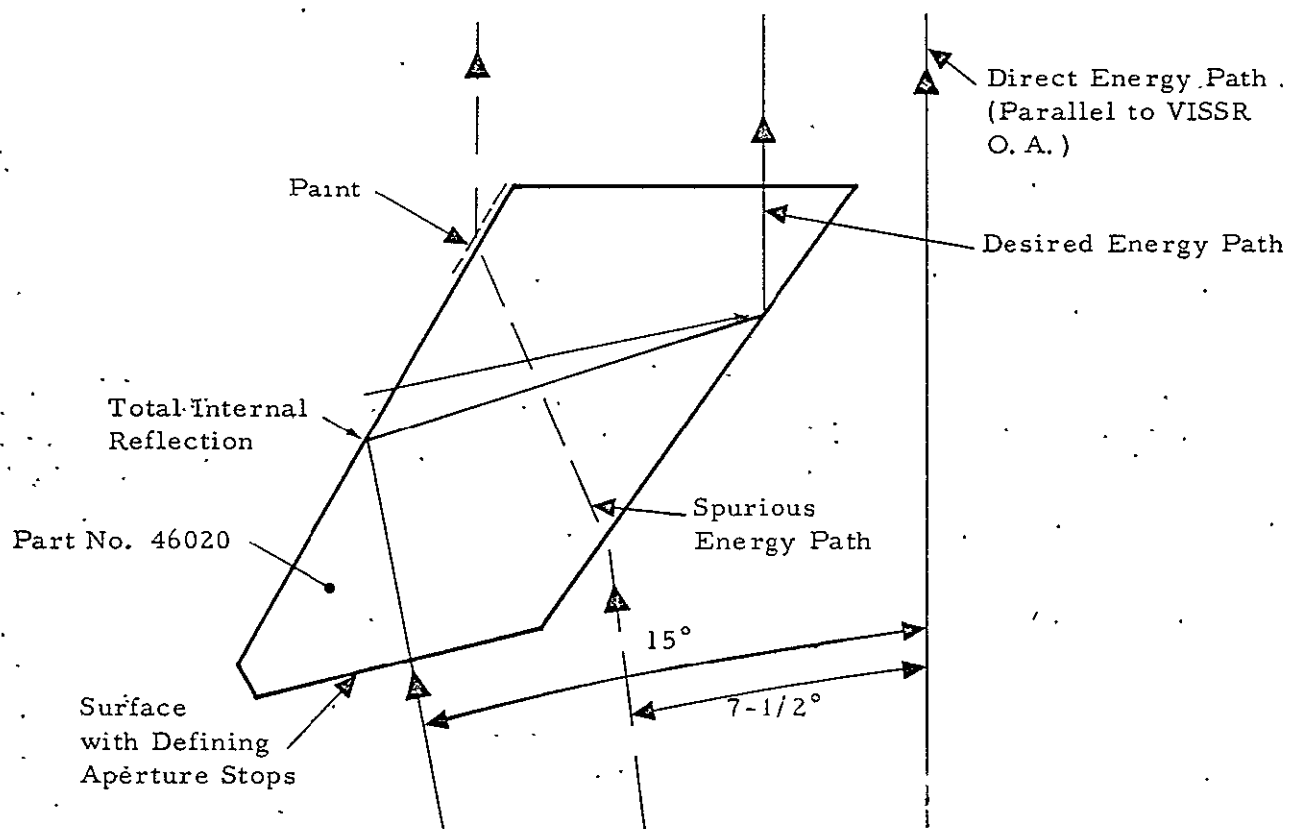


Figure 3-127. Desired and Spurious Energy Paths in P/N 46020 Prism

The spurious energy was blocked by painting the indicated surface with Cat-A-Lac black paint (see Figure 3-127) in the region indicated by dashed line.

Another spurious energy path was noted during this investigation. Energy reflected from the Dove prism base along side, was transmitted by the central aperture on Part No. 46020. This spurious energy path was nearly coincident angularly with the desired calibration energy transmitted by the Dove prisms.

Due to the angular subtense of the sun, the spurious signal would add to the desired calibration signal. Furthermore, the signal due to spurious energy would vary with the time of year. This is caused by the change of surface reflection with incidence angle. The average reflectance varies between 7 and 27%. The calibration signal would have then varied by 18%.

This effect was eliminated by placing thin metal baffles in close proximity to both of the Dove prism bases. Both modifications were made on the engineering model solar inflight calibrator assembly.

Anomalous Focus Shift

During the engineering model thermal vacuum testing, anomalous focus changes were observed for both the visible and thermal channels. This section summarizes the analysis completed in an effort to understand these effects.

Table 3-34 is a tabulation of optimum focal position as a function of temperature and calibration sequence and is based on a computer modeling transition time of:

- < 6 hours - has severe thermal gradients
- ≈ 24 hours - has small thermal gradients
- ≥ 48 hours - is a stabilized system

Refer to VISSR Project Memo 2640-0078, dated 11 July 1972, entitled "Thermal Settling Time in an Environmental Test Chamber."

Table 3-34. Tabulation of Focal Position as a Function of Temperature

Preliminary Calibration Sequence

Chamber Temperature (°C)	23		5		45		5		25
Transition* Time (Hrs)		4		51		42		30	
Focus Step									
Visible	220		152		273		194		245
Thermal	357		380						347

Final Calibration Sequence

Chamber Temperature (°C)	20		45		25		5		23
Transition* Time (Hrs)		150		25		25		24	
Focus Step									
Visible	222		266		170		136		230
Thermal			329		341		370		

*Transition time = time between starting a temperature change making measurements.

The relationship between defocusing, ΔF , and temperature for a two-mirror system is:

$$\Delta F = M^2 f_p \alpha_p \Delta T_p - M^2 S_{p-s} \alpha_{S_{p-s}} \Delta T_{S_{p-s}} + (M-1)^2 f_s \alpha_s \Delta T_s - S_{s-f} \alpha_{S_{s-f}} \Delta T_{S_{s-f}} \quad (3-64)$$

where ΔF = focal plane shift

M = system magnification

f_p = primary mirror focal length

f_s = secondary mirror focal length

S_{p-s} = Spacing - primary to secondary mirror

The saran (12.6μ) film is equivalent to the mylar (6.4μ) film in transmittance and has appreciably less scattering. In addition, its strength and mounting characteristics are equal or superior to the mylar film.

Based on the above data, saran film, 12.7μ thick; will be used as a cover for VISSR protective cover.

The effect of the plastic protective cover on the engineering model modulation was measured. The results are shown in Figure 3-146.

The 0.55 to 0.75 μ transmittance of the cover as measured during VISSR engineering model tests differs appreciably from laboratory spectrophotometer measurements. The transmittance values are 0.66 and 0.8, respectively. The cause of this discrepancy is not known at this time.

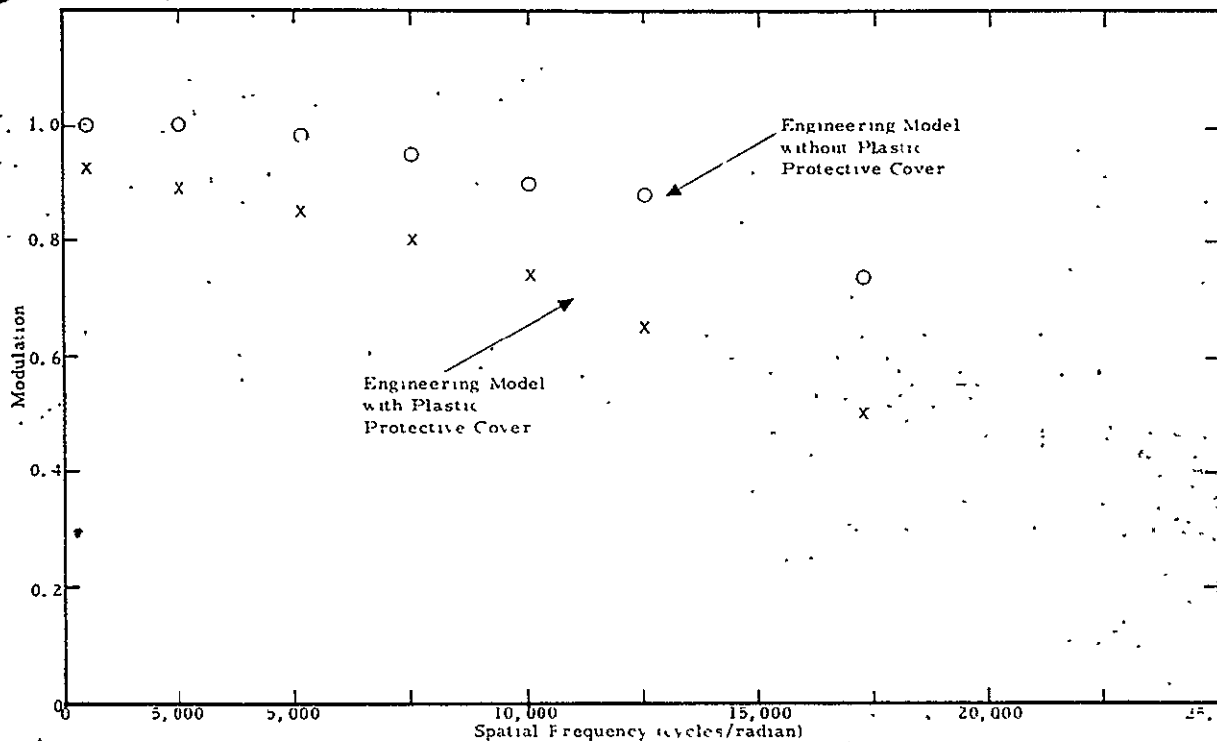


Figure 3-146. Engineering Model Modulation Modification upon Insertion of Plastic Protective Cover

S_{s-f} = Spacing - secondary to focal plane

α = thermal expansion coefficient

ΔT = temperature change

The equivalent expression for the VISSR relay lens system is

$$\Delta F_{\text{relay}} = \left(\frac{d_i}{d_o}\right)^2 [S_{Ti} \alpha_{Ti} \Delta T_{Ti} + S_{\text{cres}} \alpha_{\text{cres}} \Delta T_{\text{cres}}] + \left(\frac{d_i}{f_R}\right)^2 \left[f_R \alpha_R - \left(\frac{f_R}{\eta - 1}\right) \frac{\partial \eta}{\partial T} \right] \Delta T_R + S_{Be} \alpha_{Be} \Delta T_{Be} + (S \alpha \Delta T)_{\text{rad cooler}} \quad (3-65)$$

The above equation assumes that the VISSR relay lens system is replaced by an equivalent thin lens, where

d_i = image distance

d_o = object distance

f_R = focal length of relay lens

S = spacing (length)

η = refractive index of germanium

Subscripts for "S" refer to the controlling structural material.

The relationship between VISSR telescope change of focus, $\Delta F_{\text{telescope}}$, to VISSR relay system image plane, ΔF_{relay} , is

$$\Delta F_{\text{relay}} = M_R^2 \Delta F_{\text{telescope}} \\ \Delta F_{\text{relay}} = 0.032 \Delta F_{\text{telescope}} \quad (3-66)$$

The VISSR and VISSR calibrator material models are illustrated in Figures 3-128 and 3-129, respectively.

The required values for equations (3-64) and (3-65) are listed below:

VISSR Telescope. -

$M = -3.117$; $f_p = 36.8$ in.; $f_s = -13.7$ in.; $S_{p-s} = 27.5$ in.;

$S_{s-f} = 27.5$ in.; $S_{s-f} = 29.0$; $\alpha = 11.3 \times 10^{-6}$ in./in./°C

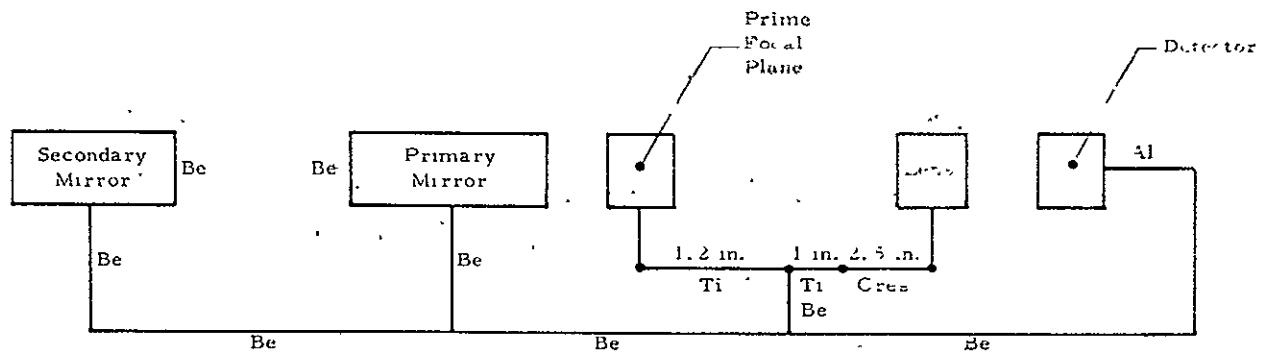


Figure 3-128. VISSR Material Model

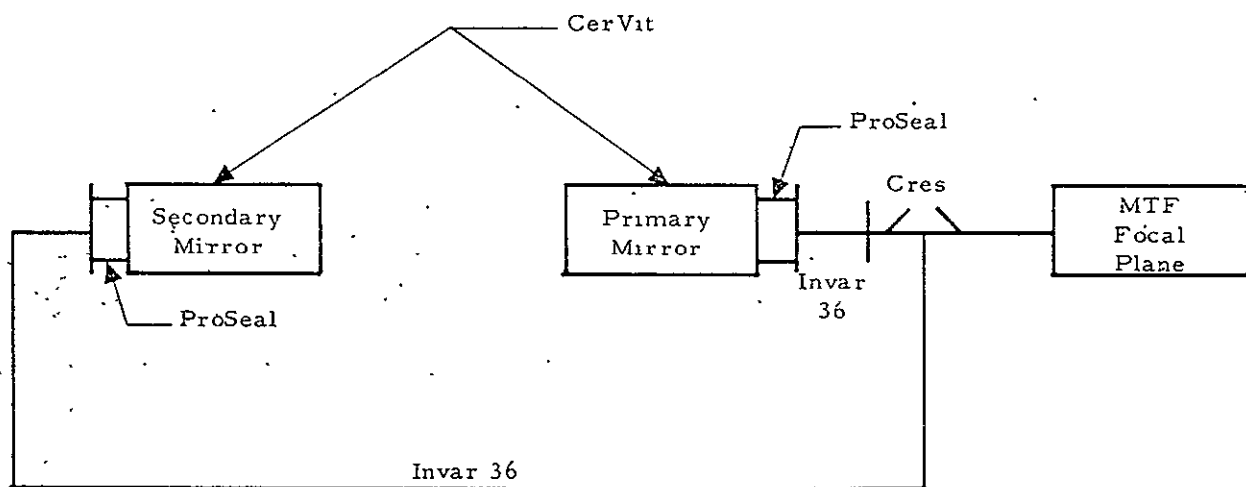


Figure 3-129. VISSR Calibrator Material Model

VISSR Relay System. -

$d_i = 0.846$ in.; $d_o = 4.71$ in.; $S_{Ti} = 2.2$ in.; $S_{cres} = 2.51$ in.;
 $f_R = 0.718$ in.; $\eta = 4.0$; $\frac{\partial \eta}{\partial T} = 300 \times 10^{-6} / ^\circ C$; $S_{Be} = 3.55$ in.;
 $S_{rad \text{ cooler}} = 2.69$ in.; $\alpha_{Ti} = 8.8 \times 10^{-6}$ in./in./ $^\circ C$;
 $\alpha_{cres} = 16 \times 10^{-6}$ in./in./ $^\circ C$; $\alpha_R = 6.0 \times 10^{-6}$ in./in./ $^\circ C$;
 $\alpha_{rad \text{ cooler}}$ - composite of Al and glass

VISSR Calibrator. -

$M = -3.91$; $f_p = 43.4$ in.; $f_s = -15.12$ in.; $S_{p-s} = 32.15$ in.;
 $S_{s-f} = 43.992$ in.

ProSeal Bonds. -

0.125-in. primary mirror, 0.015-in. secondary mirror
 $\alpha_p = \alpha_s = \pm 0.1 \times 10^{-6}$ in./in./ $^\circ C$; $\alpha_{S_{p-s}} = 1.3 \times 10^{-6}$ in./in./ $^\circ C$
 $\alpha_{S_{s-f}}$ is a composite; $\alpha_{ProSeal} = 1.8 \times 10^{-4}$ in./in./ $^\circ C$

The following relationships are useful in understanding the focusing effects.

1. VISSR calibrator serving as a radiant energy source

ΔF	Beam condition at calibrator exit aperture
Pos.	Diverging
0	Plane
Neg.	Converging
2. VISSR telescope with a plane wavefront incident on entrance aperture

ΔF	Image plane	Visible focus drive used to focus counter, N_V changes
Pos.	BFL increases	N_V decreases
Neg.	BFL decreases	N_V increases
3. With a "point source" radiating toward thermal channel relay lenses

ΔF	Image plane	Thermal focus drive used to focus counter, N_T changes
Pos.	BFL (or d_o) increases	N_T increases
Neg.	BFL (or d_o) decreases	N_T decreases

The above is graphically illustrated in Figure 3-130.

Equation (3-64) can be considered in terms of partial derivatives, such as, $\frac{\partial F_p}{\partial T}$, where

$$\frac{\partial F_p}{\partial T} = M^2 f_p \alpha_p \quad (3-67)$$

Table 3-35 lists VISSR telescope partial derivatives.

Table 3-35. VISSR Telescope Partial Derivatives

Element	$\frac{\partial F}{\partial T} \left(\frac{\text{inch}}{^\circ\text{C}} \right)$	$\Delta \frac{\partial F}{\partial T}$
Primary Mirror	0.00403	358 $\Delta \alpha_p$
Primary-Secondary Spacer	-0.0030	-267 $\Delta \alpha_{S_{p-s}}$
Secondary Mirror	-0.00069	-61 $\Delta \alpha_S$
Secondary to Focal Plane	-0.00033	-29 $\Delta \alpha_{S_{s-f}}$

The second partial derivatives of F with respect to T and α are used to obtain column 3 of Table 3-35.

Table 3-36 gives equivalent values for the VISSR calibrator.

Table 3-36. VISSR Calibrator Partial Derivatives

Element	$\frac{\partial F}{\partial T} \left(\frac{\text{inch}}{^\circ\text{C}} \right)$	$\Delta \frac{\partial F}{\partial T}$
Primary Mirror	± 0.000066	$\pm 660 \Delta \alpha_p$
Primary Secondary Spacer	-0.000689	-530 $\Delta \alpha_{S_{p-s}}$
Secondary Mirror	± 0.000013	$\pm 130 \Delta \alpha_S$
Secondary to Focal Plane Spacer	-0.000134	Composite
ProSeal Mounting Pads	+0.000386	2.15 $\Delta \alpha_{\text{ProSeal}}$

Using the preceding values for the calibrator and using $\alpha_p = -0.1 \times 10^{-6}$ in./in./ $^\circ\text{C}$

$$\begin{aligned} \Delta F_{\text{cal}} = & -66 \times 10^{-6} \Delta T_p - 689 \times 10^{-6} \Delta T_{S_{p-s}} + 13 \times 10^{-6} \Delta T_S \\ & - 134 \times 10^{-6} \Delta T_{S_{s-f}} + 386 \times 10^{-6} \Delta T_{\text{ProSeal}} \end{aligned} \quad (3-68)$$

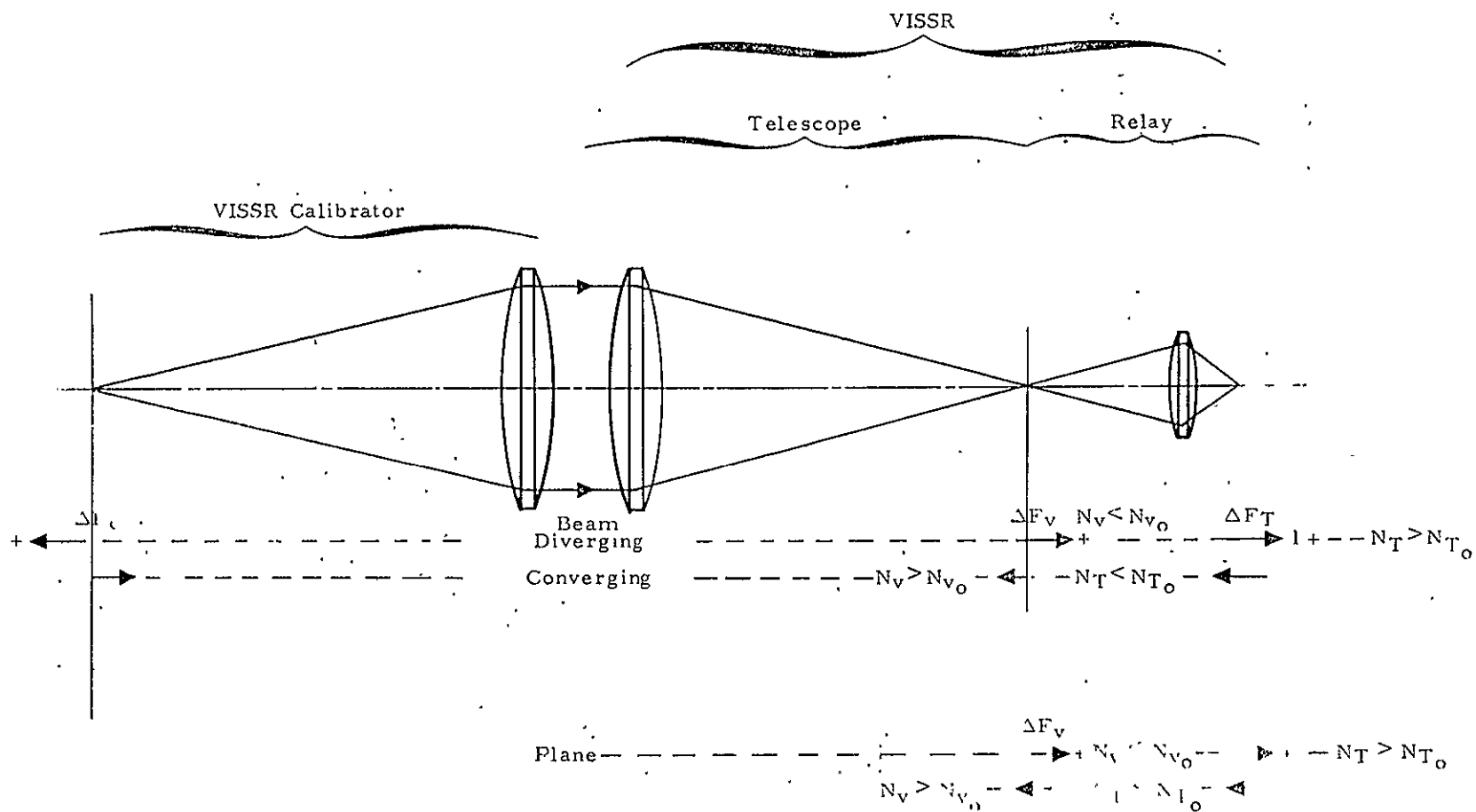


Figure 3-130. Graphic Illustrations of Focusing Effects

and if a calibrator with no temperature gradients is assumed,

$$\Delta F_{\text{cal}} = -490 \times 10^{-6} \Delta T \quad (3-69)$$

The equivalent change at VISSR focal plane is

$$\Delta F_v = \left(\frac{\text{EFL}_{\text{VISSR}}}{\text{EFL}_{\text{cal}}} \right)^2 \Delta F_{\text{cal}} \quad (3-70)$$

$$\frac{\Delta F_v}{\Delta T_{\text{cal}}} = 0.457 \Delta F_{\text{cal}} = -224 \times 10^{-6} \text{ in./}^\circ\text{C}$$

VISSR telescope, ΔF_v , is given by

$$\begin{aligned} \Delta F_v = & 4030 \times 10^{-6} \Delta T_p - 3000 \times 10^{-6} \Delta T_{S_{p-s}} - 690 \Delta T_S \\ & - 330 \times 10^{-6} \Delta T_{S_{s-f}} \end{aligned} \quad (3-71)$$

Of course, if VISSR telescope has no thermal gradients, $\Delta F_v = 0$ per equation (3-71).

Substitution of values into equation (3-65) for thermal relay

$$\begin{aligned} \Delta F_R = & -0.62 \times 10^{-6} \Delta T_{Ti} - 1.3 \times 10^{-6} \Delta T_{\text{cres}} \\ & - 93.6 \times 10^{-6} \Delta T_R - 40 \times 10^{-6} \Delta T_{\text{Be}} \end{aligned} \quad (3-72)$$

The term involving the radiation cooler is deleted since the detector stage is fairly well decoupled from VISSR ambient temperature. If we assume no thermal gradients for other terms, we have:

$$\Delta F_R = -136 \times 10^{-6} \Delta T_{\text{relay}} \quad (3-73)$$

The experimental data shown in Table 3-34 can be used to obtain experimental values of dF/dT , where

$$\frac{dF}{dT} = \frac{dN}{dT} \frac{dF}{dN} \quad (3-74)$$

$$(dF/dN)_v = -0.00046 \text{ in./step} \quad \text{visible channel}$$

$$(dF/dN)_T = 0.00025 \text{ in./step} \quad \text{thermal channel}$$

For the VISSR visible channel

$$\left(\frac{dF_v}{dT}\right)_{\text{average}} = -1040 \times 10^{-6} \pm 0.00023 \text{ in./}^\circ\text{C}$$

where data used for averaging was limited to transition times in excess of 40 hours. The tolerance is equivalent to an uncertainty of ± 0 steps for optimum focus.

Predicted $\frac{dF_v}{dT}$ is based on an isothermperature calibrator, VISSR with a 1°C temperature gradient between primary mirror and spacer, S_{p-s} (developed over a 20°C VISSR temperature change), and 5% difference in the VISSR beryllium housing with respect to VISSR mirrors.

$$\begin{aligned} \frac{dF}{dT} &= \left(\frac{dF_v}{dT}\right)_{\text{cal}} + \left(\frac{dF_v}{dT}\right)_{1^\circ\text{C}} + \left(\frac{dF_v}{dT}\right)_{5\sigma} \\ &= -124 \times 10^{-6} - 500 \times 10^{-6} - 150 \times 10^{-6} \\ &= -874 \times 10^{-6} \text{ in./}^\circ\text{C} \end{aligned} \quad (3-75)$$

In addition, Invar 36 has a $\pm 15\%$ thermal expansion coefficient spread from the nominal value used. The ProSeal band line is assumed to "track" the temperature of the Invar spacers S_{p-s} . It seems likely that the calibrator CerVit mirrors will have a thermal time constant considerably greater than any other item in the calibrator-VISSR configuration. Although mirror contributions are small due to very low expansion coefficient, the ProSeal is in intimate contact with these elements and will more likely track their temperature. Its contribution to $\frac{dF}{dT}$ is appreciable.

Within experimental accuracy and knowledge of specific elements, the "temperature-focusing anomalies" for the engineering model visible channel are explicable using the above first order equation analysis.

Greater uncertainty exists in the thermal channel temperature focusing effect. First, very little thermal channel data is available. Second, the available data is questionable due to thermal gradients.

Final calibration sequence data, Table 3-34, is used to obtain

$$\frac{dF_T}{dT} = \frac{329 - 370}{45 - 5} 0.00025 = -0.00051 \text{ in./}^\circ\text{C}$$

The engineering model thermal channel sensitivity was low. Due to low SNR, optimum focus has an uncertainty of ± 10 steps. Thus

$$\frac{dF_T}{dT} = -0.00051 \pm 0.00025 \text{ in./}^\circ\text{C}$$

This value can be separated into two components. One is due to VISSR calibrator-VISSR telescope effects and the second is due to VISSR relay system. Mathematically, this is expressed by

$$\frac{dF_T}{dT} = (0.032) \frac{dF_V}{dT} + \frac{dF_R}{dT} \quad (3-76)$$

Solving for dF_R/dT , we have

$$\frac{dF_R}{dT} = \frac{dF_T}{dT} - 0.032 \frac{dF_V}{dT}$$

$$\begin{aligned} \text{and } \frac{dF_R}{dT} &= -0.00051 - \left[(0.032) \left(\frac{266 - 130}{45 - 5} \right) (-0.00046) \right] \\ &= -0.00051 + 0.000047 \\ &= -0.00046 \text{ in./}^\circ\text{C} \end{aligned}$$

Based on equation (3-73)

$$\frac{dF_R}{dT} = -0.00014 \text{ in./}^\circ\text{C}$$

The above equations do not explain the thermal channel temperature focusing effects. Due to the scarcity of data and basic uncertainty associated with the available data, efforts toward resolution of the discrepancy are to be continued with the protoflight unit.

PROTOFLIGHT MODEL OPTICAL SYSTEM TESTS

Field-of-View (FOV) Measurements

FOV measurements were made for visible channels in accordance with SBRC Procedure 19181 with the following exceptions.

Although the SBRC collimator had been modified prior to protoflight FOV tests to produce a significantly more stable platform than used earlier (engineering model measurements), a basic instability was observed between the collimator and attached scanner and VISSR cart. During the course of the measurements, the protoflight VISSR and VISSR cart were observed to drift with respect to the collimator. The total drift during north-south run 1 amounted to an angular displacement of $3.5 \mu\text{r}$. The corresponding total drift for north-south run 2 was $21 \mu\text{r}$. For the east-west scans, the total drift for run 1 corresponded to an angular displacement of $8 \mu\text{r}$, and for east-west run 2 the total was $3 \mu\text{r}$. In all cases, the movement was monitored continuously using a pointing interferometer and also by a repeated check on the output of one of the VISSR channels (Channel 1). All reduced FOV data have been corrected for drift. The basic instability between the collimator and cart precluded exhaustive studies of other potential instability (paragraph 3.5.9, Procedure 19181).

In addition to instability in the collimator-cart system, the digital voltmeter used for reading VISSR channel voltage outputs had a zero offset which could not be removed by simple adjustment. Correction for offset was made during data reduction by subtraction of offset from channel output voltage readings.

Graphic and tabular data for protoflight model FOV tests are contained in Part I, Appendix C. Tables 3-37 through 3-40 summarize data pertinent to the FOV measurements. The peak signal value has noise removed and a voltage offset of 1.41 mv has been subtracted from the noise values.

For comparison purposes, a theoretical FOV curve calculated from Protoflight Class I Energy Spread Function (ESF) measurements is plotted

Table 3-37. FOV Data, North-South Scan, Run 1

Channel	Peak Signal (mv)	Noise (mv)	Half-Width (μ r)	Channel Center (μ r)	Channel Separation (Adjacent Channels) (μ r)
1	686	0.06	19.0	-84.6	24.4 24.6 25.7 27.4 24.6 24.3 24.2
2	676	0.06	20.6	-60.0	
3	698	0.06	20.3	-34.1	
4	689	0.06	22.1	-9.3	
5	511	0.07	22.6	+18.1	
6	581	0.07	20.1	+42.7	
7	691	0.07	20.9	+67.0	
8	615	0.07	20.0	+91.2	

Table 3-38. FOV Data, North-South Scan, Run 2

Channel	Peak Signal (mv)	Noise (mv)	Half-Width (μ r)	Channel Center (μ r)	Channel Separation (Adjacent Channels) (μ r)
1	685	0.12	21.0	-87.3	27.7 25.1 24.5 27.0 24.1 23.9 24.0
2	675	0.11	20.0	-59.6	
3	707	0.12	21.0	-33.5	
4	689	0.12	21.0	-9.0	
5	519	0.12	22.7	+18.0	
6	586	0.12	21.5	+43.9	
7	706	0.12	20.3	+67.8	
8	625	0.13	20.6	+91.8	

Table 3-39. FOV Data, East-West Scan, Run 1

Channel	Peak Signal (mv)	Noise (mv)	Half-Width (μ r)	Channel Center (μ r)	Channel Separation (Adjacent Channels) (μ r)
1	389	0.03	22.0	+1.75	0.30
2	377	0.02	22.0	-1.45	0.20
3	306	0.02	22.0	+1.25	2.00
4	116	0.02	22.0	-0.75	0.50
5	176	0.02	23.0	+0.75	0.30
6	292	0.03	22.3	+0.45	0.20
7	357	0.03	22.3	+0.25	0.20
8	334	0.03	22.0	+0.05	

Table 3-40. FOV Data, East-West Scan, Run 2

Channel	Peak Signal (mv)	Noise (mv)	Half-Width (μ r)	Channel Center (μ r)	Channel Separation (Adjacent Channels) (μ r)
1	388	0.03	24.0	+0.48	0.00
2	371	0.02	23.5	+0.48	0.30
3	209	0.02	24.3	+0.78	1.00
4	217	0.03	24.5	-0.23	0.45
5	181	0.03	24.1	+0.23	0.25
6	313	0.02	24.0	-0.02	1.00
7	354	0.03	24.3	-1.02	0.00
8	355	0.03	24.0	-1.02	

in Figure 3-131 with the data plot for protoflight FOV east-west, Channel 1, run 2.

Experimental setup used for FOV measurements is depicted in Figure 3-101.

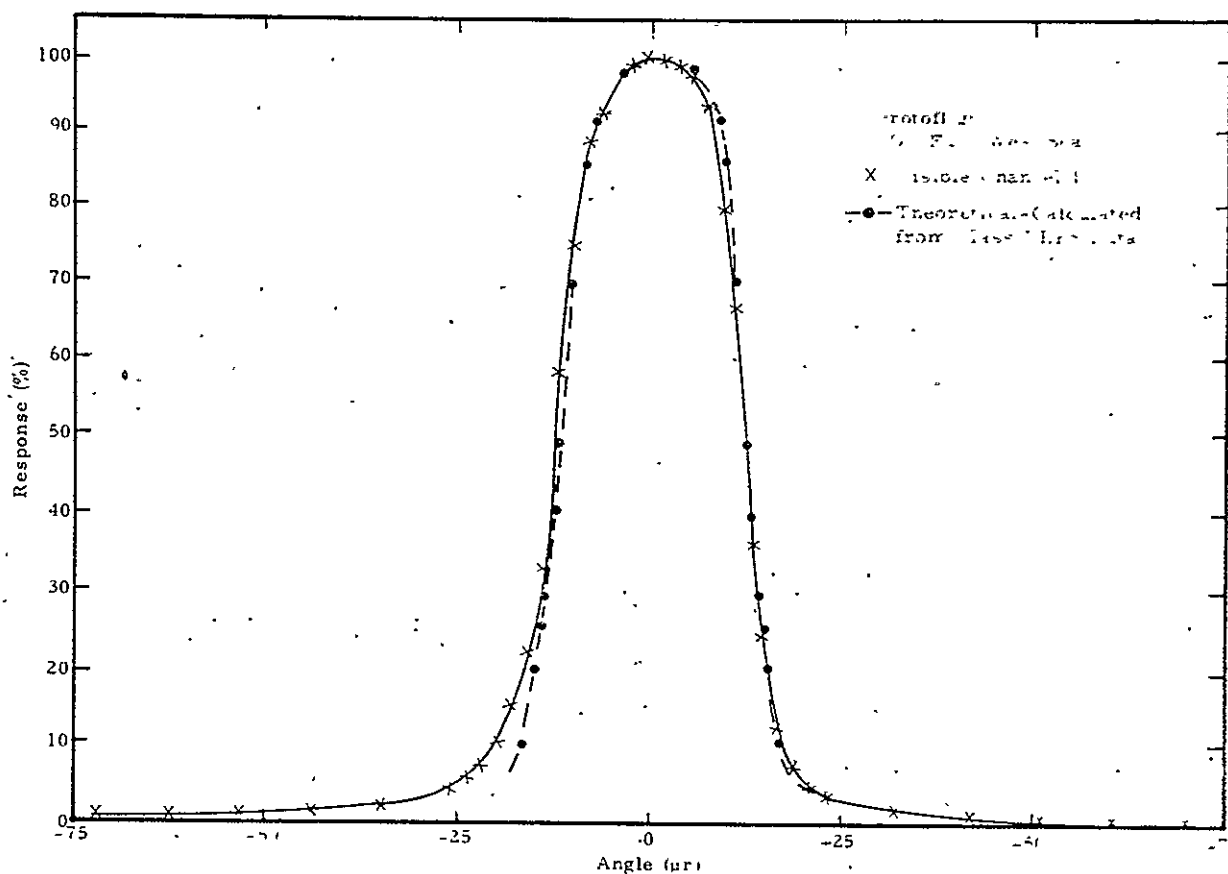


Figure 3-131. Theoretical versus Actual FOV

Relative Spectral Response

Relative spectral response (RSR) measurements were made for the VISSR/SMS protoflight model scanner visible channels in accordance with SBRC Procedure 19147. A Perkin-Elmer Model 16U spectrophotometer (filter-grating monochromator) was used in conjunction with the SBRC collimator for these tests. Characteristic parameters associated with the spectrophotometer are the same as those listed for engineering model measurements. Calculations were performed via computer using the same equation as for engineering model data. As the digital voltmeter used for reading

VISSR channel voltage outputs had a zero offset which could not be removed by simple adjustment, a correction was made during data reduction.

An apparent discontinuity for all RSR curves occurs at 0.8μ wavelength. This coincides with a point at which order filters were changed in the spectrophotometer and is not considered to be due to a defect in the VISSR optics.

Graphic and tabular data for protoflight RSR tests are contained in Part 2, Appendix C.

The experimental setup used for RSR measurements is depicted in Figure 3-102.

Modulation Transfer Function Measurements

The modulation transfer function (MTF) was measured for visible channels under ambient laboratory conditions. Measurements were made in two orthogonal directions corresponding to the east-west and north-south directions. Equipment and procedures used are those defined in SBRC Procedure 19146.

MTF data were recorded in the form of photographs of the oscilloscope traces for the eight visible channels. A sample of the reduced data is given in Figure 3-132 which illustrates modulation versus spatial frequency. Three computed curves (same as used for engineering model data) are included in the figure for purposes of comparison.

Reference Mirror Alignment Measurements

Reference mirror alignment measurements were made for the VISSR/SMS protoflight model scanner in accordance with SBRC Procedure 19148 with the following exceptions.

The depth-of-field of the alignment microscope as focused on the PARM-1 reference mirror resulted in an uncertainty in the Z-axis best-focus position measurement which made it difficult to repeat redundant encoder readings to primary encoder readings as required by paragraph 3.6.7 of the procedure. The difficulty was compounded by imperfect tracking of the X-Y micrometer microscope stage which produced a variation of the X-position

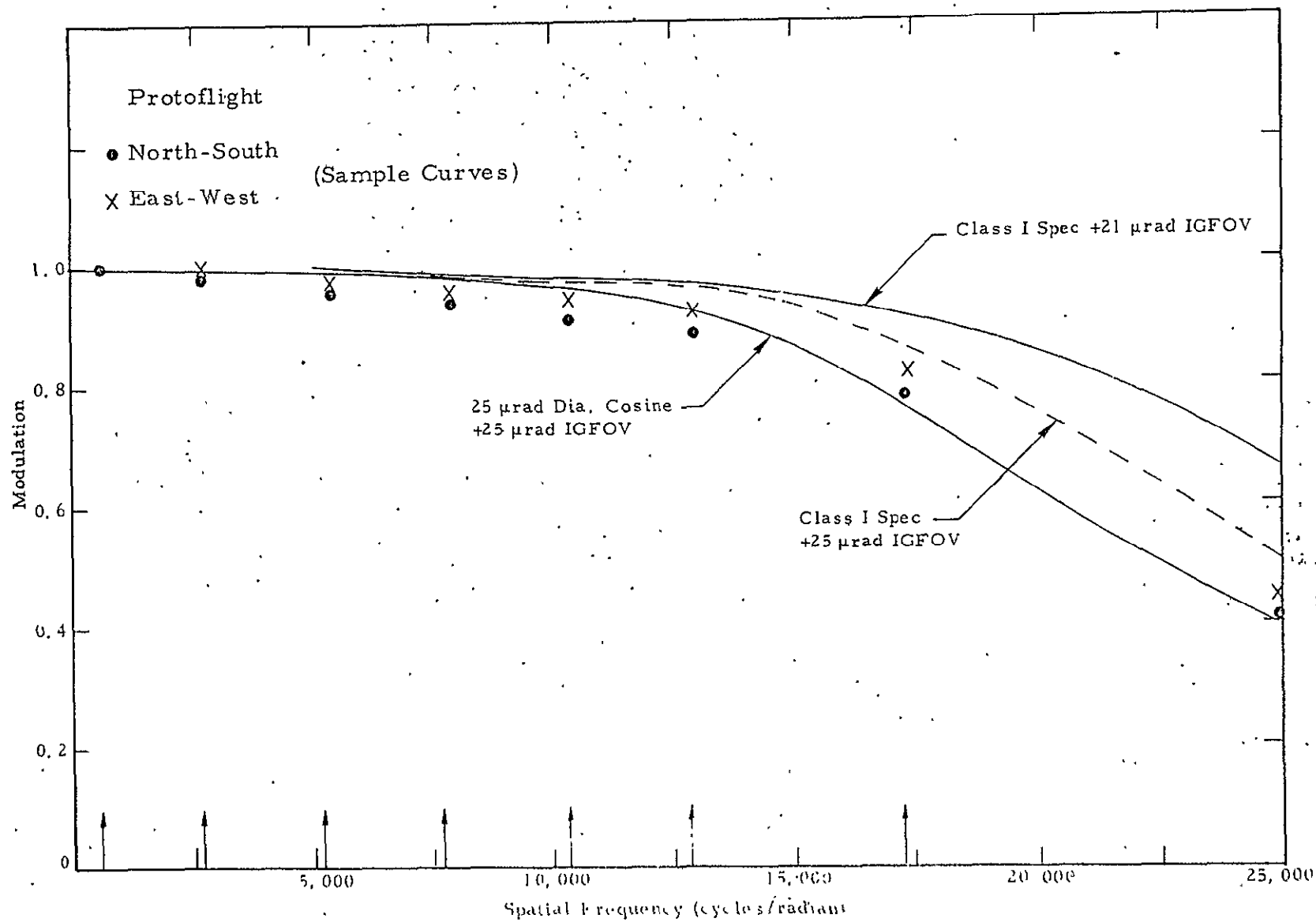


Figure 3-132. Visible Channel Modulation Transfer Function
Protoflight Model

readings with Z-axis movement. To alleviate this uncertainty, the alternate method was adopted of resetting the Z-axis stage to a single best-focus position determined by repetition of the Z-axis micrometer reading rather than operator judgment as to repetition of visual best focus. This deviation in method was likewise adopted for measurements called for by paragraphs 3.7.7, 3.8.7, 3.9.4, and 3.9.5 of the procedure. A modification to the microscope 3-axis stage has solved the problem with Z-axis tracking.

The following measurement results were obtained after the modification to the 3-axis stage and using the alternate method of achieving best focus as described above. Measurement objectives are the same as those described for the engineering model.

Paragraph 3.2.1 Alignment Requirements. - The distance from the fiducial lines reference point on PARM-1 to the Y-Z plane is 0.000 inch. The PARM-1 cross hair lies in the VISSR Y-Z plane. The corresponding distance of the PARM-2 alignment cross hair to the X-Z plane is 0.008 inch. The PARM-2 cross hair is 0.008 inch on the -Y axis side of the VISSR X-Z plane. VISSR reference axes are illustrated in Figure 3-108.

The exterior angle formed by PARM-1 (nominally perpendicular to the Y axis) and the VISSR mounting plane, defined as X-Y plane, is $89^{\circ}55.3'$. See Figure 3-133.

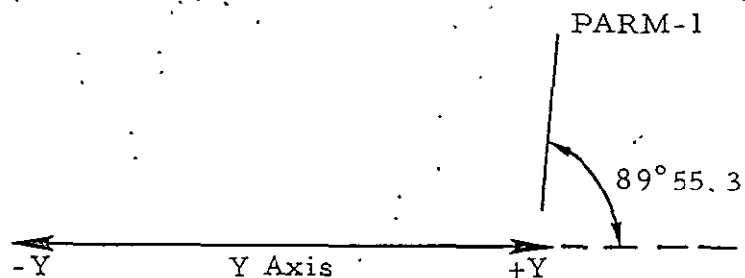


Figure 3-133. PARM-1 to Y-Axis Alignment

The exterior angle formed by PARM-2 (nominally perpendicular to the X-axis) and the VISSR mounting plane is $89^{\circ}44.8'$. See Figure 3-134.

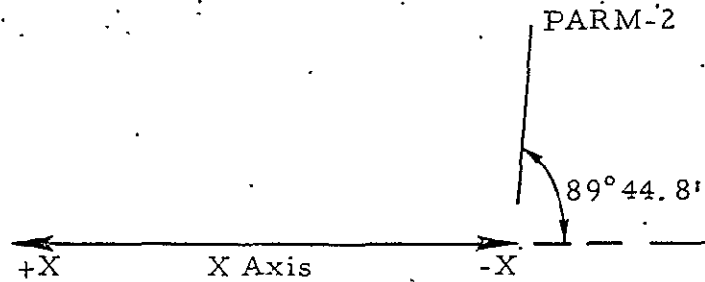


Figure 3-134. PARM-2 to X-Axis Alignment

Paragraph 3.2.3 Alignment Requirements. - The scan mirror angle with respect to the VISSR optical axis is 45° (to the nearest encoder step) when the redundant encoder is positioned at step +32. Scan mirror rotation toward encoder step +31 by $53 \mu r$ would provide a true 45° angle with the VISSR optical axis.

With the primary encoder positioned to step -60, the scan mirror angle is 45° (to the nearest encoder step) with respect to the VISSR optical axis. Scan mirror rotation by $31 \mu r$ toward encoder step -59 would provide a true 45° angle with the VISSR optical axis.

Paragraph 3.2.4 Alignment Requirements. - Angular alignment of the VISSR optical axis (including scan mirror) to PARM-1 was measured to the primary optical encoder. With the primary encoder set to -59 and using PARM-1 normal, the VISSR optical axis to PARM-1 normal has two angular components. In the VISSR Y-Z plane, the VISSR optical axis makes an angle with the PARM-1 normal of 0.031 mr with the VISSR optical axis pointing slightly toward the -Z axis. See Figure 3-135. In the VISSR X-Y plane, the VISSR optical axis makes an angle with the PARM-1 normal of 0.029 mr with the VISSR optical axis pointing slightly toward the +X axis. See Figure 3-136.

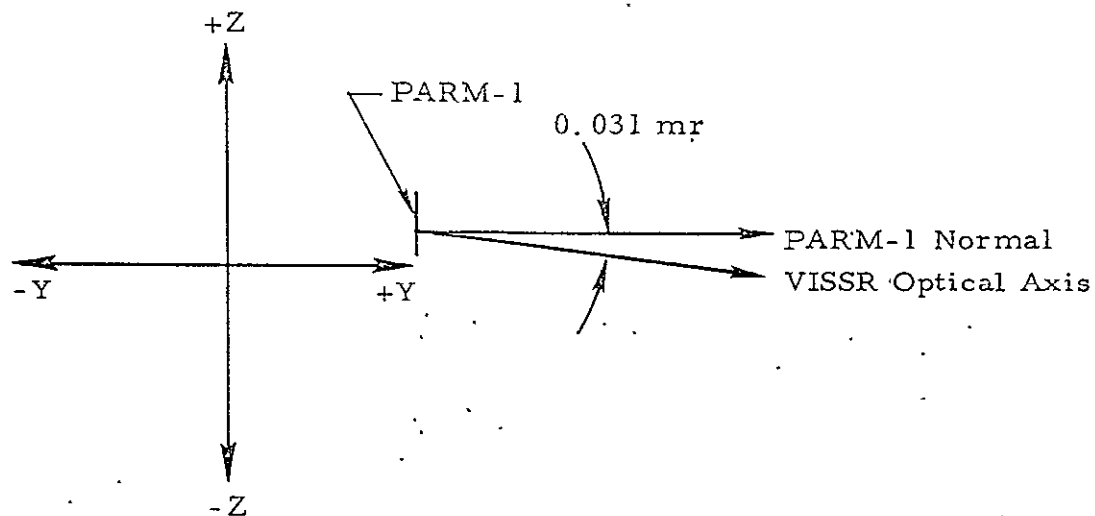


Figure 3-135. Alignment of VISSR Optical Axis to PARM-1 in YZ Plane

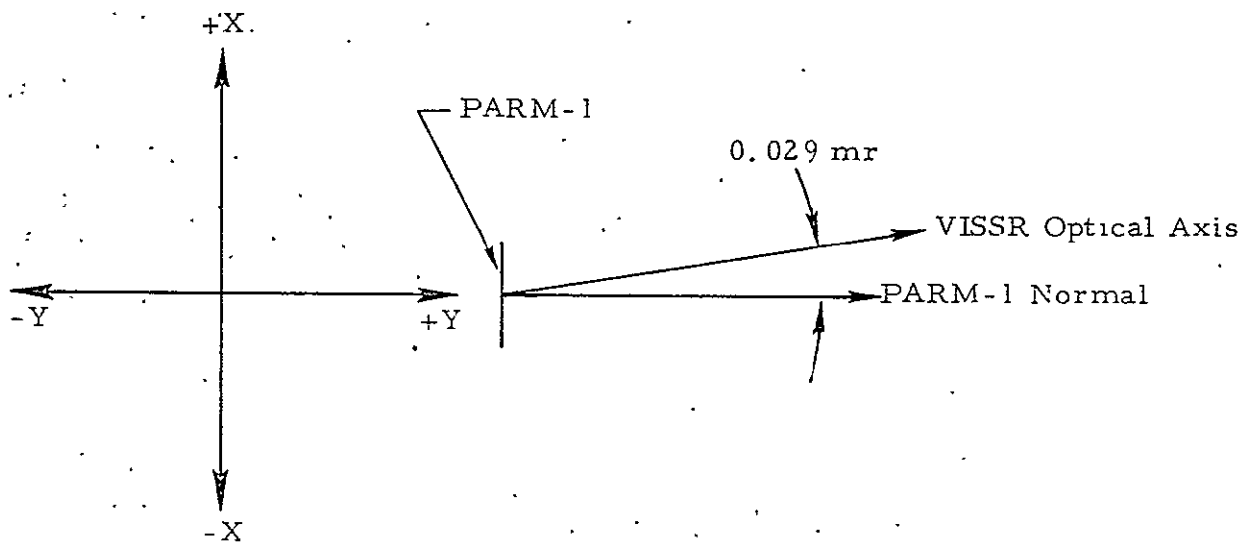


Figure 3-136. Alignment of VISSR Optical Axis to PARM-1 in XY Plane

Paragraph 3.2.5 Alignment Requirements. - The angular alignment of VISSR optical axis (excluding scan mirror) to two nominally orthogonal primary alignment reference mirrors was measured:

The angle between PARM-1 normal and the VISSR optical axis in the Y-Z plane is 0.381 mr. The corresponding angle between PARM-2 normal and VISSR optical axis in the X-Z plane is 4.87 mr. See Figures 3-137 and 3-138.

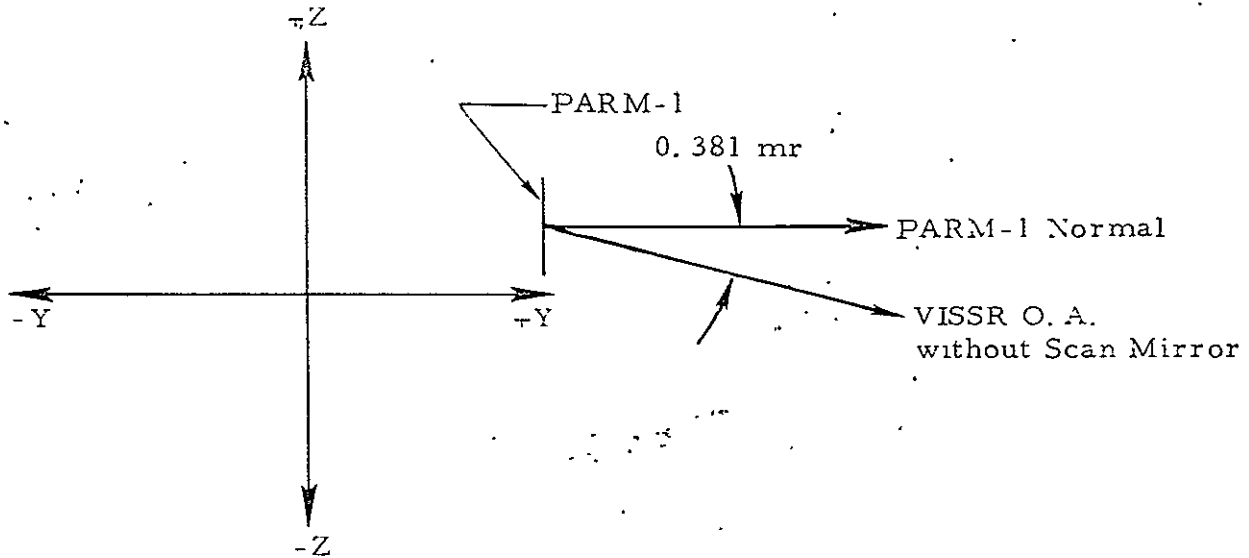


Figure 3-137. Alignment of VISSR Optical Axis (without Scan Mirror) to PARM-1 in Y-Z Plane

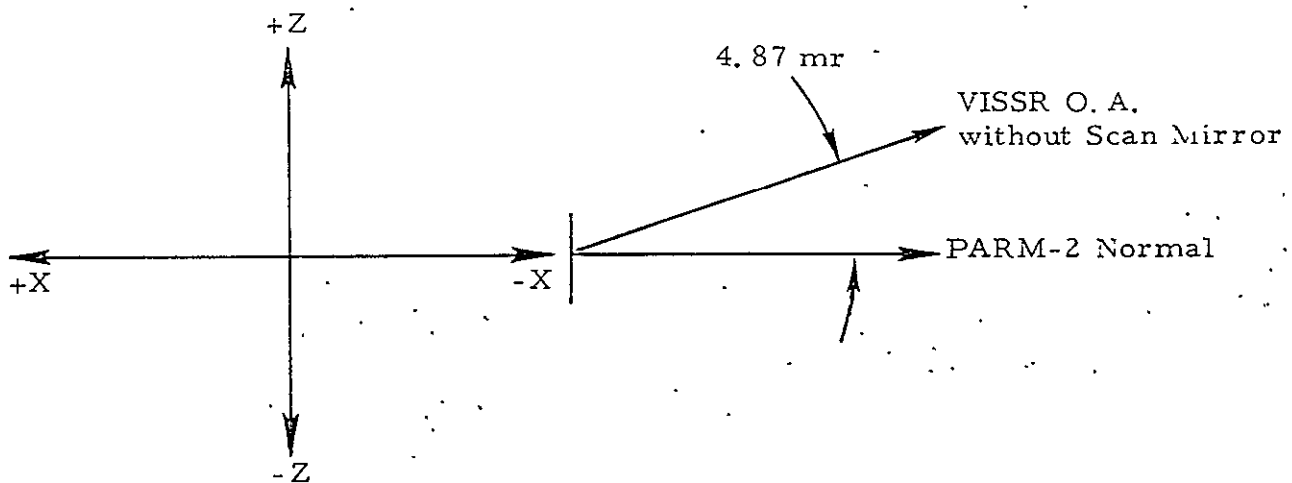


Figure 3-138. Alignment of VISSR Optical Axis (without Scan Mirror) to PARM-2 in X-Z Plane

Paragraph 3.2.6 Alignment Requirements. - The angular alignment of the secondary alignment reference mirror (SARM-2) to PARM-2 was measured. Alignment in the XZ plane and XY plane is illustrated in Figures 3-139 and 3-140.

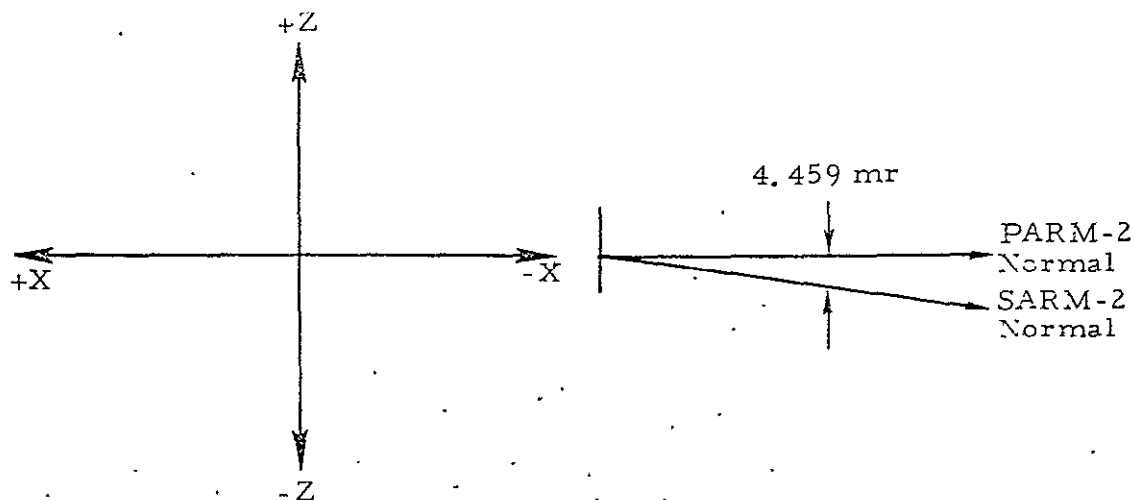


Figure 3-139. Alignment of SARM-2 to PARM-2 in XZ Plane

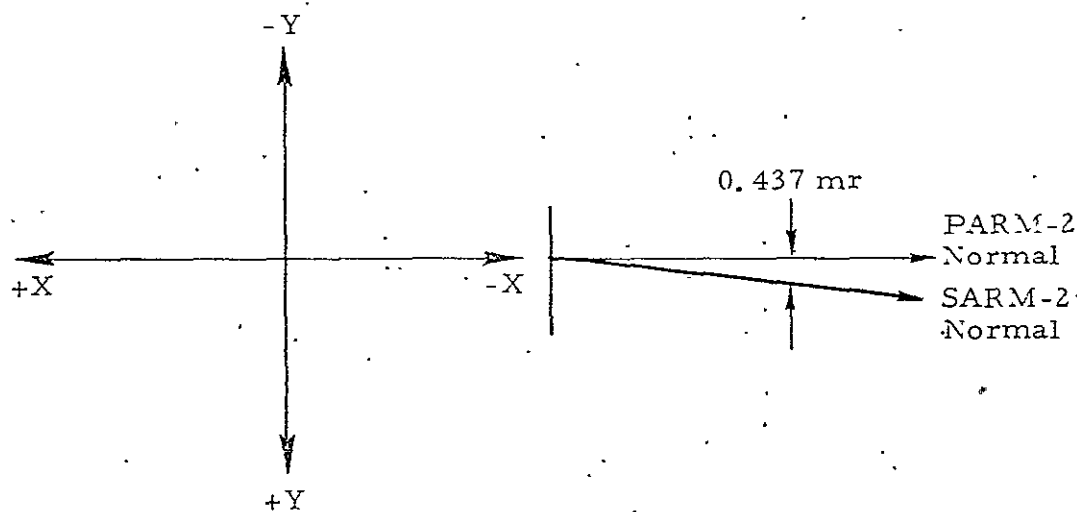


Figure 3-140. Alignment of SARM-2 to PARM-2 in XY Plane

Protective Plastic Cover for VISSR

The VISSR must be protected from various forms of contamination. One of the methods being evaluated is the use of a thin plastic film across the VISSR "entrance aperture." Such a cover used in conjunction with a dry nitrogen purge should reduce contaminants in the vicinity of scan mirror, telescope and aft optics assemblies.

Any plastic film being considered should be evaluated from the following aspects:

1. Absorption
2. Scattering
3. Mechanical strength
4. Mounting characteristics
5. Image degradation - uniformity

A preliminary survey indicated saran and mylar films were potential candidates for the cover. Mylar films, 6.4 and 12.7 μ thick, and saran film, 12.7 μ thick, were measured. Figures 3-141 and 3-142 illustrate transmittance of mylar films in the VISSR visible and infrared channels, respectively. Figures 3-143 and 3-144 are the equivalent transmittance data for saran plastic film.

Because of SBRC scattering, goniometer configuration limitations single-pass scattering in transmission could not be measured. Figure 3-145 schematic illustrates the two types of scattering measurement made.

Experimental arrangement (shown in A of Figure 3-145) measures film scattering in reflection. The arrangement shown in B of Figure 3-145 measures film scattering in reflection and transmission as modified by the mirror. The total scattering, $S(\text{total})$, for the B arrangement can be expressed by

$$S(\text{total}) = S_{R_1} + \rho_M S_{T_1} + S_{T_2} - \rho_M^2 S_{R_2} + S_M$$

where S_{R_1} = film scattering in reflection (first pass)

S_{T_1} = film scattering in transmission (first pass)

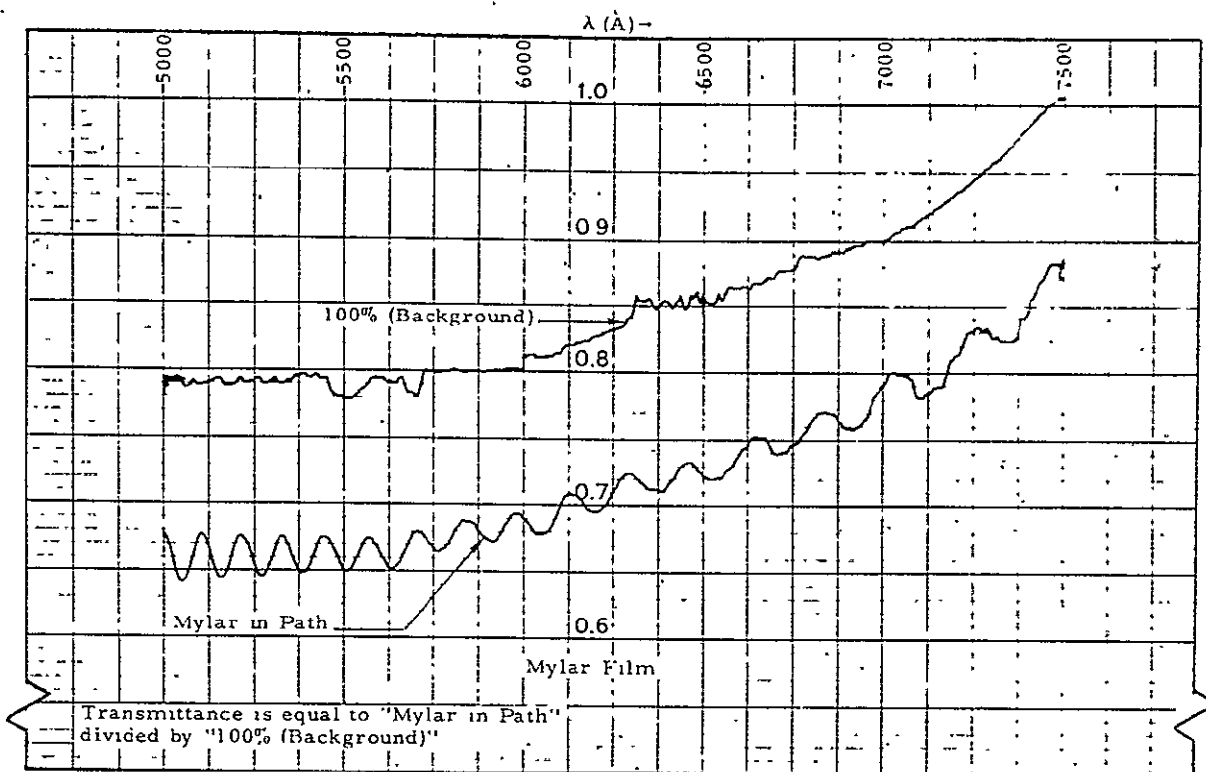


Figure 3-141. Spectral Transmittance of Mylar (0.00025 inch)

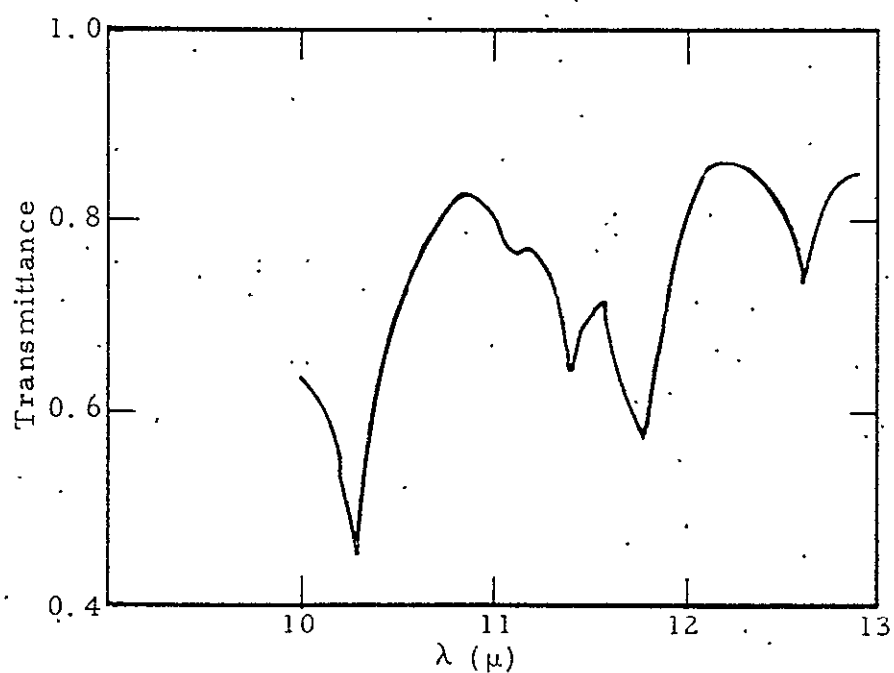


Figure 3-142. Spectral Transmittance of Mylar (0.00025 inch)

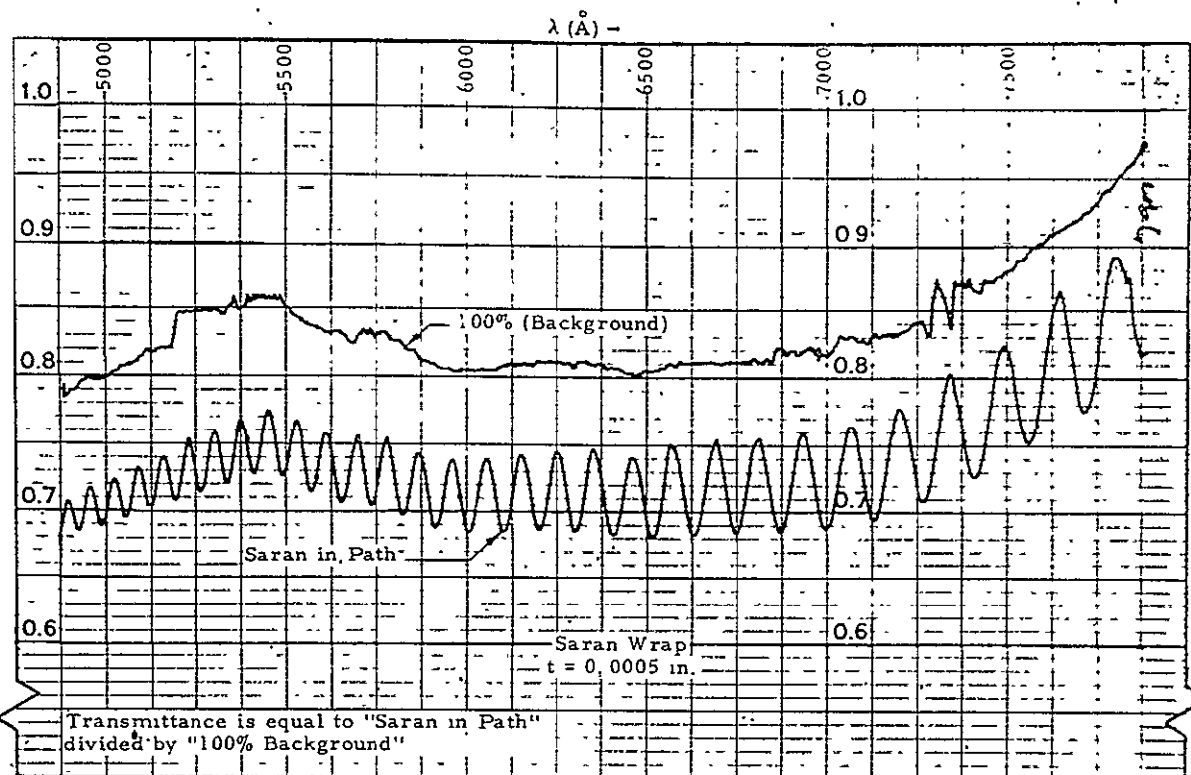


Figure 3-143. Spectral Transmittance of Saran (0.0005 inch)

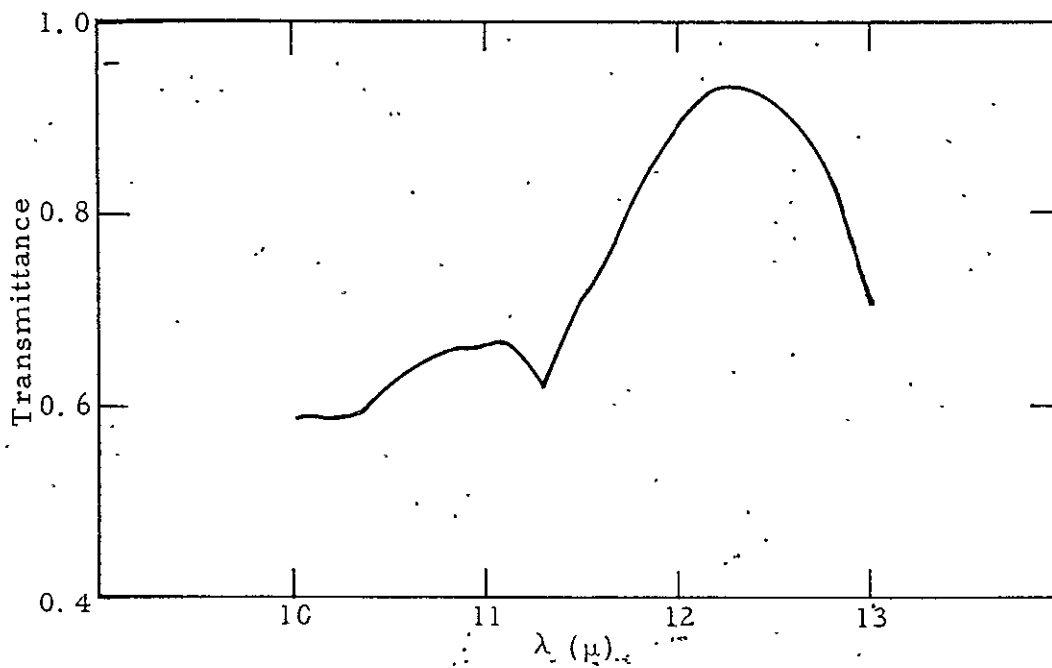


Figure 3-144. Spectral Transmittance of Saran (0.0005 inch)

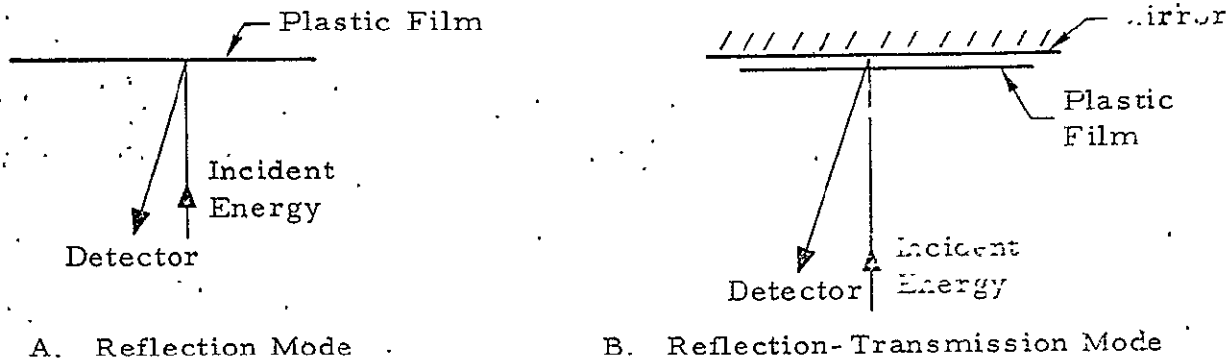


Figure 3-145. Plastic Film Measurement Setup

S_{T2} = film scattering in transmission (second pass - after energy is reflected off mirror)

S_{R2} = film scattering in reflection (second pass)

ρ_M = specular reflection of mirror

S_M = mirror scattering

Quantities $S(\text{total})$, S_{R1} , ρ_M , S_M are experimentally determined. It is assumed that $S_{T1} = S_{T2}$ and $S_{R1} = S_{R2}$. Therefore, S_{T1} is given by

$$S_{T1} = \frac{S(\text{total}) - S_M - (1 + \rho_M^2)S_{R1}}{(1 + \rho_M)}$$

The 12.7 μ saran film has hemispherical scatter, $S_{T1}(\text{saran})$, equal to

$$S_{T1}(\text{saran}) = \frac{2.47 - 0.01 - (1 + 0.80^2)0.72}{(1 + 0.80)} \\ = 0.71\%$$

The equivalent 6.4 μ mylar film hemispherical scatter, $S_{T1}(\text{mylar})$ is

$$S_{T1}(\text{mylar}) = \frac{6.22 - 0.01 - (1 + 0.80^2)1.21}{(1 + 0.80)} \\ = 2.4\%$$

NTTS

**Manual of Methods for Chemical Analysis of
Water and Wastes**
PB-259 973/ PAT 317 p. PC\$9.75/MF\$3.00

Item Number	Quantity		Unit Price*	Total Price*
	Paper Copy (PC)	Microfiche (MF)		

All prices subject to change. The prices above are accurate as of 6/77

Sub Total	
Additional Charge	
Enter Grand Total	

Foreign Prices on Request.